University of Southampton

# Marine Optics: Field Radiometry

by

Giuseppe Zibordi

Submitted in partial fulfillment of the requirements
for the Degree of Philosophy

School of Ocean and Earth Science
Southampton Oceanography Center
United Kingdom

February 2007

**Graduate School of the**

**National Oceanography Centre, Southampton**

This PhD dissertation by

*Giuseppe Zibordi*

has been produced under the supervision of the following persons

Supervisors

Dr. Simon Boxall

Prof. Ian Robinson

Chair of Advisory Panel

Dr. Duncan Purdie

# Abstract

UNIVERSITY OF SOUTHAMPTON
SCHOOL OF OCEAN AND EARTH SCIENCE

Doctor of Philosophy

## Marine Optics: Field Radiometry

by Giuseppe Zibordi

*In situ* optical radiometric methods for the determination of seawater apparent optical properties are comprehensively addressed with the final objective of quantifying measurement uncertainties for remote sensing applications. Emphasis is placed on the presentation and assessment of calibration and measurement protocols in combination with schemes for the minimization of instrument, deployment and environmental perturbing effects. Specific investigations deal with the determination of the uncertainties produced by the non ideal cosine response of irradiance sensors in the normalization of the water–leaving radiance, the quantification of the immersion factors for both in–water radiance and irradiance sensors, the estimate of perturbing effects by deployment superstructures, self-shading and surface roughness for in–water measurements. Applications of *in situ* optical radiometric measurements, including the development of algorithms for the determination of the concentration or the apparent optical properties of seawater optically significant constituents from remote sensing data, and additionally the validation of primary remote sensing radiometric products, are also addressed and discussed in relation to the uncertainty of radiometric data.

# Acknowledgements

I would like to thank Dr. Simon Boxall and Prof. Ian Robinson, my supervisors, for the unconditioned and continuous support provided during the development of this project. I also wish to thank the many collaborators and friends that during the last decade shared with me the interest and willingness to look at radiometric problems and ocean color remote sensing applications (in alphabetical order): Jean-François Berthon, Barbara Bulgarelli, Davide D'Alimonte, John-Piero Doyle, Scott McLean, Frèdèric Mèlin, Stanford Hooker, Dirk van der Linde, Giancarlo Maracci, Peter Schlittenhardt and Kenneth Voss.

*To Valentina and Francesco*

# Table of Contents

# List of Tables

# List of Figures

# Symbols

| Symbol | Quantity | Units |
|---|---|---|
| $a$ | Absorption coefficient | $\mathrm{m}^{-1}$ |
| $b$ | Scattering coefficient | $\mathrm{m}^{-1}$ |
| $c$ | Beam attenuation coefficient | $\mathrm{m}^{-1}$ |
| $d$ | Distance | m |
| $f$ | f-function | – |
| $f_0$ | value of $f$ for $\theta = 0$ | – |
| $f_c$ | Cosine error | % |
| $\bar{f}$ | Average cosine error | % |
| $\tilde{f}$ | Ratio term | – |
| $f_R$ | Sensor-to-instrument diameter | – |
| $k_{sun}$ | Parameter for self-shading computation | – |
| $k_{sky}$ | Parameter for self-shading computation | – |
| $n$ | Refractive index | – |
| $n_a$ | Refractive index of air | – |
| $n_d$ | Refractive index of a diffusing material | – |
| $n_g$ | Refractive index of the window | – |
| $n_m$ | Refractive index of medium $m$ | – |
| $n_w$ | Refractive index of water | – |
| $r$ | Radius | m |
| $r_{ag}$ | Reflectance of the air-window interface | – |

| | | |
|---|---|---|
| $r_b$ | Reflectance of the collector-detector interface | – |
| $r_c$ | Internal reflectance of the collector-air interface | – |
| $r_d$ | Detector reflectance | – |
| $r_e$ | External reflectance of the collector-air interface | – |
| $r_{mg}$ | Reflectance of the medium-window interface | – |
| $t_{ag}$ | Air-window transmittance | – |
| $t_d$ | Detector transmittance | – |
| $t_{mg}$ | Medium-window transmittance | – |
| $r_p$ | Reflectance of the plaque $p$ | – |
| $t_{wa}$ | Transmittance of the air-water interface | – |
| $t_{wg}$ | Water-window transmittance | – |
| $z$ | Water depth | m |
| $z_0$ | Upper extreme of the extrapolation interval | m |
| $z_1$ | Lower extreme of the extrapolation interval | m |
| $A$ | Active surface of the detector | $m^2$ |
| $C_E$ | Calibration coefficient for irradiance | W $m^{-2}$ $nm^{-1}$ $Counts^{-1}$ |
| $C_L$ | Calibration coefficient for radiance | W $m^{-2}$ $nm^{-1}$ $sr^{-1}$ $Counts^{-1}$ |
| $DN_a$ | Digital number for in–air measurements | Counts |
| $DN_w$ | Digital number for in–water measurements | Counts |
| $DN_m$ | Digital number for measurements in the medium $m$ | Counts |
| $D0$ | Digital number for the offset | Counts |
| $DN$ | Digital number for the signal | Counts |
| $E$ | Irradiance | W $m^{-2}$ $nm^{-1}$ |
| $E_c$ | Irradiance at the inner collector-air interface | W $m^{-2}$ $nm^{-1}$ |
| $E_d$ | Downward irradiance | W $m^{-2}$ $nm^{-1}$ |
| $\breve{E}_d$ | Above–water $E_d$ from in–water measurements | W $m^{-2}$ $nm^{-1}$ |
| $E_e$ | Irradiance at the external air-collector | W $m^{-2}$ $nm^{-1}$ |
| $E_i$ | Diffuse atmospheric irradiance | W $m^{-2}$ $nm^{-1}$ |
| $E_{0d}$ | Scalar upward irradiance | W $m^{-2}$ $nm^{-1}$ |

| | | |
|---|---|---|
| $E_{0u}$ | Scalar downward irradiance | W $m^{-2}$ $nm^{-1}$ |
| $E_u$ | Upward irradiance | W $m^{-2}$ $nm^{-1}$ |
| $\breve{E}_d$ | Simulated $E_d$ with an experimental cosine response | W $m^{-2}$ $nm^{-1}$ |
| $\tilde{E}_d$ | Simulated $E_d$ with an ideal cosine response | W $m^{-2}$ $nm^{-1}$ |
| $E_0$ | Standard Irradiance Values | W $m^{-2}$ $nm^{-1}$ |
| $E_D$ | Irradiance at the detector | W $m^{-2}$ $nm^{-1}$ |
| $E_s$ | Direct Sun irradiance | W $m^{-2}$ $nm^{-1}$ |
| $E_S$ | Extra-atmospheric sun irradiance | W $m^{-2}$ $nm^{-1}$ |
| $G$ | Geometric correction factor | – |
| $I_f$ | Immersion factor | – |
| $I_r$ | Diffuse to direct irradiance ratio | – |
| $K_d$ | Diffuse attenuation coefficient from $E_d$ | $m^{-1}$ |
| $K_l$ | Diffuse attenuation coefficient from $L_u$ | $m^{-1}$ |
| $K_u$ | Diffuse attenuation coefficient from $E_u$ | $m^{-1}$ |
| $K_{\Re}$ | Generic diffuse attenuation coefficient from $\Re$ | $m^{-1}$ |
| $L$ | Radiance | W $m^{-2}$ $nm^{-1}$ $sr^{-1}$ |
| $L_a$ | Generic in–air radiance | W $m^{-2}$ $nm^{-1}sr^{-1}$ |
| $L_i$ | Sky radiance | W $m^{-2}$ $nm^{-1}sr^{-1}$ |
| $L_m$ | Radiance detected in the medium $m$ | W $m^{-2}$ $nm^{-1}$ $sr^{-1}$ |
| $L_p$ | In–water radiance of the source $p$ | W $m^{-2}$ $nm^{-1}sr^{-1}$ |
| $L_u$ | Spectral upward radiance | W $m^{-2}$ $nm^{-1}sr^{-1}$ |
| $L_w$ | Generic in–water radiance | W $m^{-2}$ $nm^{-1}sr^{-1}$ |
| $L_W$ | Water leaving radiance | W $m^{-2}$ $nm^{-1}$ |
| $L_{WN}$ | Normalized water leaving radiance | W $m^{-2}$ $nm^{-1}sr^{-1}$ |
| $L_T$ | Total radiance above the sea surface | W $m^{-2}$ $nm^{-1}sr^{-1}$ |
| $Q$ | Q-factor | sr |
| $Q_n$ | Value of $Q$ for $\theta = 0$ | sr |
| $Q_0$ | Value of $Q_n$ for $\theta_0 = 0$ | sr |
| $R$ | Irradiance reflectance | – |

| | | |
|---|---|---|
| $R_c$ | Radius of the sensor aperture | m |
| $R_r$ | Instrument radius | m |
| $R_{rs}$ | Remote sensing reflectance | $\mathrm{sr}^{-1}$ |
| $R_\Phi$ | Responsivity of the detector | Counts $\mathrm{W}^{-1}$ |
| $T_0$ | Generic transmittance | – |
| $T_g$ | Window transmittance | – |
| $T_w$ | Water transmittance | – |
| $T_{ad}$ | Air-detector transmittance | – |
| $T_{ag}$ | Air-window transmittance | – |
| $T_{wd}$ | Water-detector transmittance | – |
| $T_{wg}$ | Water-window transmittance | – |
| $T_C$ | Collector transmittance | – |
| $\alpha$ | Ångström exponent | – |
| $\beta$ | Volume scattering function | $\mathrm{m}^{-1}\ \mathrm{sr}^{-1}$ |
| $\tilde{\beta}$ | Scattering phase function | $\mathrm{sr}^{-1}$ |
| $\gamma$ | Ångström coefficient | $\mu\mathrm{m}^{-1}$ |
| $\varepsilon_c$ | Irradance error for a non-ideal cosine response | – |
| $\lambda$ | Wavelength | nm |
| $\omega$ | Solid angle | sr |
| $\omega_0$ | Single scattering albedo | – |
| $\phi$ | Azimuth angle | degrees |
| $\psi$ | Scattering angle | degrees |
| $\varphi$ | Relative azimuth angle | degrees |
| $\rho$ | Reflectance | – |
| $\rho_b$ | Reflectance of the sea bottom | – |
| $\rho_d$ | Directional-directional reflectance | – |
| $\rho_h$ | Directional-hemispherical reflectance | – |
| $\rho_s$ | Sea-surface reflectance for $E_d$ | – |
| $\rho_0$ | Fresnel reflectance of the sea-surface | – |

| | | |
|---|---|---|
| $\theta$ | Zenith angle | degrees |
| $\theta_m$ | Half-angle field-of-view in the medium $m$ | degrees |
| $\sigma$ | Standard deviation | – |
| $\varphi$ | Relative azimuth | degrees |
| $\xi$ | Measurement repeatability | % |
| $\zeta$ | Variation coefficient | % |
| $\Upsilon$ | Radiant Energy | J |
| $\Phi$ | Radiant flux | W |
| $\Omega_a$ | Solid angle in air | sr |
| $\Omega_w$ | Solid angle in water | sr |
| $\Re$ | Generic radiometric quantity | |
| $\Im$ | Gothic R (air-water interface refraction) | – |
| $\langle \lvert \bar{f}_c \rvert \rangle$ | Average unsigned cosine error | [%] |
| $\langle \bar{f}_c \rangle$ | Average signed cosine error | [%] |

# Acronyms

| Acronym | Name |
|---|---|
| AAOT | Acqua Alta Oceanographic Tower |
| ADF | Angular Distribution Function |
| AERONET | Aersol Robotic Network |
| AERONET-OC | AERONET Ocean Color subnetwork |
| AOP | Apparent Optical Properties |
| CCD | Charge Coupled Device |
| CIE | Commission Internationale de l'Eclairage |
| CoASTS | Coastal Atmosphere and Sea Time Series |
| ComPACT | Compact Portable Advanced Characterization Tank |
| CZCS | Coastal Zone Color Scanner |
| DDAC | Distributed Active Archive Center |
| ESA | European Space Agency |
| FOV | Field-of-View |
| HPLC | High Performance Liquid Chromatography |
| IAPO | International Association on Physical Oceanography |
| IOP | Inherent Optical Properties |
| LoCNESS | Low Cost NASA Environmental Sampling System |
| ECPR | Electrically Calibrated Pyroelectric Radiometer |
| FEM | Finite-Elements Method |
| GSFC | Goddard Space Flight Center |

| | |
|---|---|
| JRC | Joint Research Centre |
| MC | Monte Carlo |
| MERIS | Medium Resolution Imaging Spectrometer |
| MFRCG | Modified Fresnel Reflectance Glint Correction |
| NIST | National Institute for Standards and Technology (USA) |
| MODIS | Moderate Resolution Imaging Spectrometer |
| NBS | National Bureau of Standards (USA) |
| NPL | National Physical Laboratory (UK) |
| NURADS | New Upwelling Radiance Distribution System |
| OCI-200 | Ocean Color Irradiance sensor – 200 series |
| OCR-200 | Ocean Color Radiance sensor – 200 series |
| OCR-507 | Ocean Color Radiometer – 500 series |
| PHOTRAN | Photon Transport (MC code) |
| RTE | Radiative Transfer Equation |
| SeaPRISM | SeaWiFS Photometer Revision for Incident Surface Measurements |
| SI | Sisteme Internationale |
| SIRREX | SeaWiFS Intercalibration Round Robin Experiment |
| TSM | Total Suspended Matter |
| WiSPER | Wire Stabilized Profiling Environmental Radiometer |

# Chapter 1

# Introduction

> *Optical oceanography considers the sea from an optical standpoint and is ... a special branch of oceanography. The subject is chiefly physical, and aspires to employ strict definitions of the quantities measured.*
>
> *Nils Jerlov, 1976.*

Marine optics investigates the interaction of light with seawater and makes use of optical radiometry for characterizing the radiance and irradiance fields. The principles of marine optical radiometry were already established in the 1930s. However, for several decades radiometric measurements were mostly qualitative because of the relatively poor technology available for the design of optical instruments, the low accuracy of calibration sources, and the lack of consolidated measurement protocols.

Quantitative marine optical radiometry grew significantly in the 1960s with the availability of new sensor technologies and accurate absolute calibration sources. Within the framework of the first satellite ocean color mission (i.e., the Coastal Zone Color Scanner (CZCS)), marine optical radiometry showed its relevance for oceanographic applications through the production of measurements for the development of algorithms linking satellite derived data to optically significant seawater components.

Further developments were driven by the need to reduce the uncertainties in field measurements for their application in advanced bio-optical modelling, in vicarious calibration of satellite sensors, and in validation of space derived radiometric products. The frameworks for these developments were the recent space missions for the global mapping of marine biomass (through the Sea-viewing Wide Field-of-view Sensor (SeaWiFS), the Moderate Resolution Imaging Spectroradiometer (MODIS), the Global Imager (GLI) and Medium Resolution Imaging Spectrometer (MERIS)).

In response to this need, the work presented herein addresses the major topics relevant to marine optical radiometry aiming at an assessment of the overall radiometric uncertainties. After a general introduction on marine optics and radiometry, the objective is pursued by: (*i*) addressing the problem of in-air absolute radiometric calibration, investigating non-cosine response of collectors for irradiance measurements and characterizing the *wet response* of in–water radiometers; (*ii*) discussing methods and requirements for the deployment of field radiometers and for data analysis; and (*iii*) investigating techniques for the removal of artifacts produced by instrument self-shading, deployment superstructures, bottom effects and surface roughness. The implication of radiometric uncertainty is then discussed through the application of quality assured data to the development of algorithms for the quantification of seawater constituents and the validation of satellite derived products.

The overall outcome represents a synthesis of the state of the art in marine optical radiometry resulting from the combination of pre-existing studies made by the author and new specific research aimed at resolving open issues. Each major topic is addressed in a separate chapter providing a view of the problem, and a review of the literature, as well as a description of the investigation and results.

# Chapter 2

# Marine Optics and Radiometry

> *Radiometry is a system of concepts, terminology, mathematical relationships, ... instruments, and units ... devised to describe and measure radiation and its interaction with matter.*
>
> *Ross McCluney, 1994.*

Optical radiometry is the science of measuring radiant energy in the spectral region of the electromagnetic spectrum ranging from the ultraviolet to the infrared. It had early developments in the 1730s with the work of Bauger and Lambert (Johnston, 2001) who attempted measurement of light with photometers (i.e., radiometers with sensitivity comparable to that of the human eye). These studies led to the formulation of basic theories like the law of addition, the inverse square law and the cosine law of illumination (Lambert, 1760). Despite the maturing of experimental know-how since these early studies, first results in measuring the marine light were not obtained until the 1920s with the design and application of underwater instruments (Atkins and Poole, 1933; Jerlov and Liljequist, 1938; Pettersson and Landberg, 1934) following the development of photoelectric cells. At the same time significant progress was

also made in understanding marine optical processes (Shuleikin, 1933), in producing theories to describe quantitatively the light field (Gershun, 1939) and in defining fundamental laws and methods for in-water optics (Le Grand, 1939). This rapid development was subsequently slowed for several decades by technical constraints in the production of absolute radiometric measurements (see the historical summaries in Tyler and Smith (1969) and Jerlov (1976)).

Starting from the 1960s, in conjunction with a reinvigorated theoretical effort (Jerlov, 1976; Tyler, 1977), marine optics took large benefit from quantitative radiometry due to technological developments in the production of absolute sources and light detectors. In the 1980s and 1990s, with the introduction and expansion of space technologies for the remote observation of the *color of the sea* to map the marine phytoplankton biomass at a global scale, marine optics gained a new impetus leading to the achievement of unprecedent accuracy in measurements and simulation of radiative processes (Kirk, 1994; Mobley, 1994; Spinrad et al., 1994).

This chapter, with the aim of underpinning the more technical information discussed later on, provides a general overview of optical radiometry and marine optics by supplying at first the physical definitions of radiometric quantities, hence an introduction to radiative processes, and finally a brief overview of marine radiometers.

## 2.1 Definitions

Terminology and notations describing the radiative transfer processes and relevant optical properties of media, may vary across the different fields of radiometry. Within marine optics, terminology generally makes reference to Morel and Smith (1982). These authors, following the basic rules given by the International System of Units

(Sisteme Internationale or SI) and the International Commission on Illumination (Commission Internationale de l' Eclairage or CIE), proposed: (*i*) fundamental terms for in-water optics by extending the terminology already proposed by the International Association on Physical Oceanography (IAPO) as published by Jerlov (1968, 1976); and, (*ii*) general terms already accepted and commonly used by the scientific community, such as those introduced by Preisendorfer (1960, 1976) to identify and distinguish *apparent* and *inherent* optical properties of natural waters.

### 2.1.1 Radiometric Quantities

Common radiometric quantities are the *radiant energy*, *radiant flux*, *irradiance* and *radiance*.

*Radiant energy*, $\Upsilon$, in units of J, is the fundamental radiometric quantity which indicates the amount of energy propagating onto, through, or emerging from a specified surface of given area in a given element of time.

*Radiant flux*, $\Phi$, in units of W, is the time rate flow of radiant energy

$$\Phi = \frac{d\Upsilon}{dt} \tag{2.1.1}$$

where $d\Upsilon$ is an element of radiant energy and $dt$ an element of time.

*Irradiance*, $E$, in units of W m$^{-2}$, is the area density of radiant flux

$$E = \frac{d\Phi}{ds_0} \tag{2.1.2}$$

where $d\Phi$ is the element of radiant flux and $ds_0$ is an element of area at the surface. Thus, irradiance is a function of position on a specified surface.

*Radiance*, $L$, in units of W $m^{-2}$ $sr^{-1}$, is the area and solid angle density of radiant flux

$$L = \frac{d^2\Phi}{d\omega ds} = \frac{d^2\Phi}{d\omega ds_0 cos\theta} \tag{2.1.3}$$

where $ds = ds_0 cos\theta$ is a quantity called projected area in the direction of propagation onto the plane perpendicular to this direction, $d\omega$ is an element of solid angle in the specified direction and $\theta$ is the angle between this direction and the normal to the surface at the specified point (see Fig. 2.1). Thus radiance is a function of both position and direction. The integral of all radiance elements over a solid angle $\Omega$, gives the irradiance.

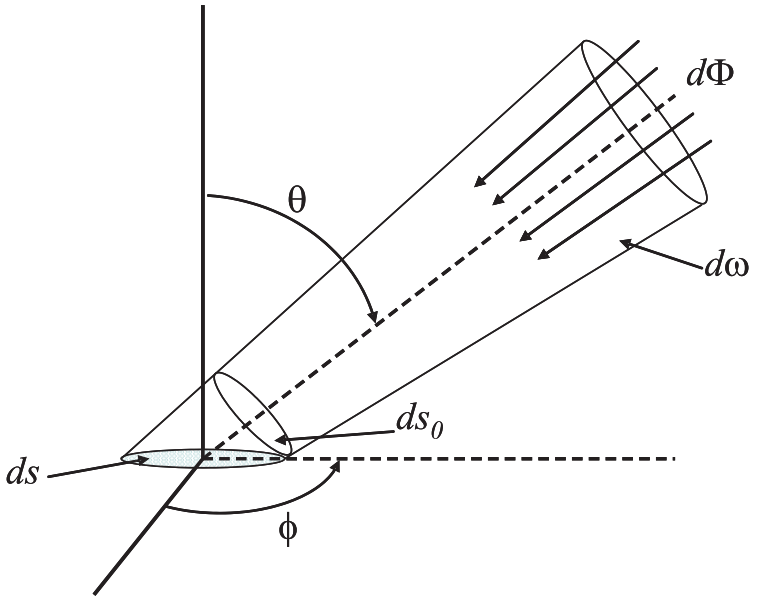


Figure 2.1: Concept of radiance.

The solid angle, which is a basic quantity in radiomery, is formed by the straight lines from a single point (the vertex) and it is defined as the area intercepted on the surface of a unit hemisphere centered at the vertex (Wyatt, 1978). Considering the element of solid angle $d\omega$ in units of sr in spherical coordinates on a unitary sphere,

with $\phi$ and $\theta$ indicating the azimuth and zenith angles,

$$d\omega = \frac{ds}{r^2} = sin\theta d\theta d\phi, \tag{2.1.4}$$

the solid angle $\Omega$ is determined by integrating $d\omega$ according to

$$\Omega = \int_0^{2\pi} \int_0^{\theta} sin\theta d\theta d\phi = 2\pi(1 - cos\Theta) \tag{2.1.5}$$

where $\Theta$ is half-angle of the circular cone defining $\Omega$.

Irradiance and radiance are commonly expressed as spectral quantities. *Spectral irradiance*, $E(\lambda)$, in units of W $m^{-2}$ $nm^{-1}$, is the spectral concentration of irradiance

$$E(\lambda) = \frac{dE}{d\lambda} = \frac{d^2\Phi}{ds_0 d\lambda}. \tag{2.1.6}$$

*Spectral radiance*, $L(\lambda)$, in units of W $m^{-2}$ $sr^{-1}$ nm $^{-1}$, is the spectral concentration of radiance

$$L(\lambda) = \frac{dL}{d\lambda} = \frac{d^3\Phi}{d\omega ds_0 cos\theta d\lambda}. \tag{2.1.7}$$

The fundamental relationship linking $E(\lambda)$ and $L(\lambda)$ for a point at the surface on which they are defined is

$$E(\lambda) = \int_\Omega L(\theta, \phi, \lambda) cos\theta d\omega. \tag{2.1.8}$$

When considering the whole hemispherical solid angle, i.e., $\Omega = 2\pi$,

$$E(\lambda) = \int_0^{2\pi} \int_0^{\pi/2} L(\theta, \phi, \lambda) cos\theta sin\theta d\theta d\phi. \tag{2.1.9}$$

If $L(\theta, \phi, \lambda)$ is constant (i.e., isotropic) over the range of integration, then

$$E(\lambda) = \pi L(\lambda). \tag{2.1.10}$$

Relevant to marine optics is the law of *radiance invariance at an interface*. This describes the change in radiance distribution across two media of refractive indices

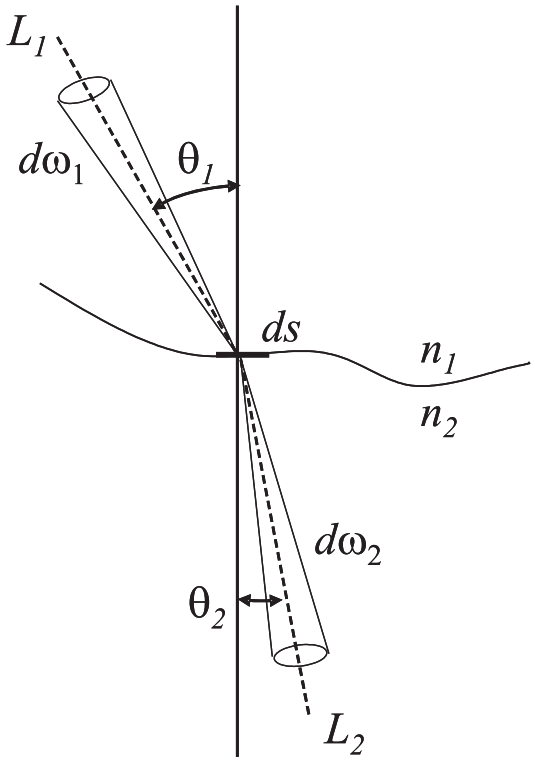


Figure 2.2: Geometry of light refraction.

$n_1$ and $n_2$, assuming radiance is not absorbed or scattered at the interface between the two media. Explicitly, if $\rho$ is the reflectance for the given angle of incidence at the interface for the radiance $L_1$ in the medium with refractive index $n_1$, then the fraction of radiance that enters the medium with refractive index $n_2$ is $L_2 = (1-\rho)L_1(n_2^2/n_1^2)$. Following McCluney (1994) and making reference to Fig. 2.2, this can be demonstrated by introducing the elements of flux $d\Phi_1$ and $d\Phi_2$ for the radiance terms $L_1$ and $L_2$

$$d\Phi_1 = L_1\ cos\theta_1\ ds\ d\omega_1 = L_1\ ds\ cos\theta_1\ sin\theta_1\ d\theta_1\ d\phi \tag{2.1.11}$$

and

$$d\Phi_2 = L_2\ cos\theta_2\ ds\ d\omega_2 = L_2\ ds\ cos\theta_2\ sin\theta_2\ d\theta_2\ d\phi. \tag{2.1.12}$$

The element of transmitted flux is then

$$(1-\rho)d\Phi_1 = (1-\rho)L_1 ds cos\theta_1 sin\theta_1 d\theta_1 d\phi. \tag{2.1.13}$$

Being $(1-\rho)d\Phi_1 = d\Phi_2$ for conservation of energy,

$$\frac{(1-\rho)\ L_1\ cos\theta_1\ sin\theta_1\ d\theta_1}{L_2\ cos\theta_2\ sin\theta_2\ d\theta_2} = 1. \tag{2.1.14}$$

Now differentiating Snell's law with respect to angles (Snell's law provides the relationship linking the angle of incidence and refraction for rays crossing media with different refractive indices),

$$\frac{sin\theta_1}{sin\theta_2} = \frac{cos\theta_1\ d\theta_1}{cos\theta_2\ d\theta_2} = \frac{n_2}{n_1}. \tag{2.1.15}$$

Combining (2.1.15) with (2.1.14)

$$\frac{(1-\rho)L_1}{n_1^2} = \frac{L_2}{n_2^2}. \tag{2.1.16}$$

This relationship states that when ignoring reflection losses (i.e., $\rho = 0$), the ratio $L/n^2$ remains invariant for a light beam crossing the interface between two media with different refractive indices.

Specific spectral radiometric quantities of relevance for marine optics are the *upwelling radiance* $L_u(z,\lambda)$ at depth $z$ and wavelength $\lambda$, the *downward irradiance* $E_d(z,\lambda)$, and the *upward irradiance* $E_u(z,\lambda)$. Additional radiometric quantities are the *scalar upward* and *downward irradiance* $E_{0u}(z,\lambda)$ and $E_{0d}(z,\lambda)$ which result from the integral of radiance contributions over a hemispheric surface (different from the plane surface considered in Eq. 2.1.8 for irradiance). These latter quantities, in units of W $m^{-2}$ $nm^{-1}$, indicate the volume density of radiant flux. They are related to $E_d(z,\lambda)$ and $E_u(z,\lambda)$, and sometimes are used to describe the in-water light fields

(Aas and Højerslev, 1999; Voss, 1989). They however are not considered in the following chapters focussed on the marine radiometric quantities more strictly related to remote sensing applications.

### 2.1.2 Optical Properties of Seawater

Following Preisendorfer (1960, 1976), the optical properties of seawater are divided into *inherent* and *apparent*. Inherent optical properties (IOP's) are those depending on the medium only and not on the illumination conditions. Apparent optical properties (AOP's) are those depending on both IOP's and illumination conditions.

**a. Inherent Optical Properties**

The most common IOP's are the spectral *absorption coefficient*, *scattering coefficient*, *beam attenuation coefficient*, *single scattering albedo*, *volume scattering function*, *back-scattering coefficient*, *scattering phase function*.

The *absorption coefficient*, $a(\lambda)$ in units of $\mathrm{m}^{-1}$, is the absorbance (i.e., the ratio of the absorbed to incident spectral radiant flux of a narrow collimated monochromatic beam in a elementary volume of a given medium) per unit distance.

The *scattering coefficient*, $b(\lambda)$ in units of $\mathrm{m}^{-1}$, is the scatterance (i.e., the ratio of the scattered to incident spectral radiant flux of a narrow collimated monochromatic beam in a elementary volume of a given medium) per unit distance.

The *beam attenuation coefficient*, $c(\lambda)$ in units of $\mathrm{m}^{-1}$, is given by

$$c(\lambda) = a(\lambda) + b(\lambda). \tag{2.1.17}$$

The *single scattering albedo*, $\omega_0(\lambda)$, is dimensionless and given by

$$\omega_0(\lambda) = b(\lambda)/c(\lambda). \tag{2.1.18}$$

The *volume scattering function*, $\beta(\psi, \lambda)$ in units of $\mathrm{m}^{-1}$ $\mathrm{sr}^{-1}$, is the scattered intensity per unit incident irradiance per unit volume with $\psi$ indicating the angle of scattering with respect to the direction of the incident light. The scattering coefficient, $b(\lambda)$, is obtained by integrating $\beta(\psi, \lambda)$ over all directions

$$b(\lambda) = \int_{\Omega} \beta(\psi, \lambda) d\omega = 2\pi \int_{0}^{\pi} \beta(\psi, \lambda) sin\psi d\psi. \tag{2.1.19}$$

When restricting the integration of $\beta(\psi, \lambda)$ to the interval $\pi/2 \leq \psi \leq \pi$, the result provides the *back-scattering coefficient*, $b_b(\lambda)$ in units of $m^{-1}$.

Additional relevant IOP is the *scattering phase function*, $\widetilde{\beta}(\psi, \lambda)$ in units of $sr^{-1}$, which provides the angular distribution of the scattered light and is given by

$$\widetilde{\beta}(\psi, \lambda) = \beta(\psi, \lambda)/b(\lambda). \tag{2.1.20}$$

**b. Apparent Optical Properties**

Frequently measured and applied AOP's are the spectral *irradiance reflectance*, *remote sensing reflectance*, *normalized water-leaving radiance*, *diffuse attenuation coefficient* and the so called *Q-factor*.

The dimensionless *irradiance reflectance* at depth $z$, $R(z, \lambda)$, defined as the ratio of upward to downward irradiance, is given by

$$R(z, \lambda) = E_u(z, \lambda)/E_d(z, \lambda) \tag{2.1.21}$$

The value of $R(z, \lambda)$ at the so called depth z=$0^-$ just below the water surface, i.e., $R(0^-, \lambda)$, has particular relevance in marine optics and is determined using $E_u(0^-, \lambda)$ and $E_d(0^-, \lambda)$ obtained from the extrapolation to $z$=$0^-$ of the log-transformed $E_u(z, \lambda)$ and $E_d(z, \lambda)$ measured at multiple depths $z$, respectively.

The *remote sensing reflectance*, $R_{rs}(\lambda)$ in units of $\mathrm{sr}^{-1}$, is defined as

$$R_{rs}(\lambda) = L_W(\lambda)/E_d(0^+, \lambda) \tag{2.1.22}$$

where $L_W(\lambda)$ is the so called *water-leaving radiance* in units of W m$^{-2}$ nm$^{-1}$ sr$^{-1}$, i.e., the radiance leaving the sea and quantified just above the surface, and $E_d(0^+, \lambda)$ the above water downward irradiance. In practice $L_W(\lambda)$ is determined as

$$L_W(\lambda) = 0.543 \cdot L_u(0^-, \lambda) \tag{2.1.23}$$

where the factor 0.543 (Jerlov and Nielsen, 1974) accounts for the reduction in radiance from below to above the water surface (mostly due to the change in the refractive index at the air–water interface), and $L_u(0^-, \lambda)$ is the upwelling radiance just below the water surface extrapolated from log-transformed $L_u(z, \lambda)$ values at multiple depths $z$.

The *normalized water leaving radiance*, $L_{wn}(\lambda)$ in units of W m$^{-2}$ nm$^{-1}$ sr$^{-1}$, is then defined as

$$L_{wn}(\lambda) = R_{rs}(\lambda) E_S(\lambda) \tag{2.1.24}$$

with $E_S(\lambda)$ average extra-atmospheric sun irradiance.

This *normalization* process removes from $L_W(\lambda)$ the effects of illumination condition dependent from the sun zenith angle and the atmospheric transmittance (Mueller and Austin, 1995). Specifically, for both remote sensing reflectance and normalized water-leaving radiance, the minimization of the effects of illumination condition is obtained through normalization with respect to the above-water downward irradiance.

The *diffuse attenuation coefficient*, $K_d(\lambda)$ in units of m$^{-1}$, indicates the extinction of irradiance in the water column and is determined as the slope term from the regression of the log-transformed $E_d(z, \lambda)$ as a function of depth $z$.

The *Q-factor*, $Q(\theta, \phi, z, \lambda)$ in units of sr, quantifies the light distribution in the water and is the ratio of the upward irradiance to the upwelling radiance in the generic

direction $(\phi, \theta)$. Commonly used quantity in marine optics is $Q_n(0^-, \lambda)$, the Q-factor at nadir view and depth $0^-$, defined as

$$Q_n(0^-, \lambda) = E_u(0^-, \lambda)/L_u(0^-, \lambda). \tag{2.1.25}$$

## 2.2 Radiative Transfer

Early studies on radiative transfer processes in generic absorbing and scattering media are dated back to the 1880s (Lommel, 1889). However, even though extensive treatises were written in the 1950s (Chandrasekhar, 1950; Sobolev, 1956), the first comprehensive work addressing radiative transfer in natural waters came when Preisendorfer (1960) combined theories on extintion processes with Gershun's studies (Gershun, 1939) on in-water geometric optics. Since then various solutions of the radiative transfer equation have been proposed and applied to marine and lake waters. Treatises on radiative transfer in seawater are given in Preisendorfer (1976), Shifrin (1988) and Mobley (1994). Thus, the only general concepts are mentioned here.

### 2.2.1 The Radiative Transfer Equation

Light processes in a medium are mostly governed by absorption and scattering, and can be described through the integral-differential equation of radiative transfer. In a plane parallel medium, excluding inelastic processes, the radiative transfer equation is given by

$$cos\ \theta \frac{dL(z, \phi, \theta, \lambda)}{dz} = -c(z, \lambda)L(z, \phi, \theta, \lambda) + \int_{4\pi} \widetilde{\beta}(z, \phi', \theta', \lambda) \longrightarrow \theta, \phi) L(z, \phi', \theta', \lambda) d\omega' \tag{2.2.1}$$

where $d\omega' = sin\theta' d\theta' d\phi'$, $c$ is the beam attenuation coefficient, and $\widetilde{\beta}$ is the scattering phase function. The first term on the right side represents the loss by scattering and absorption of radiance $L$ in the direction $(\theta, \phi)$, while the second term provides the gain in radiance due to scattering contributions from all other directions $(\theta', \phi')$ into the direction $(\theta, \phi)$. Comprehensive presentation of the various solutions proposed for the radiative transfer equation are given in Lenoble (1986) and Walker (1994), while Mobley et al. (1993) presented a comprehensive intercomparison of various computer codes applied to simulate the underwater light field.

### 2.2.2 Monte Carlo Methods

Relevant for studies related to radiometric measurements, is the capability of producing numerical solutions of the radiative transfer equation which allows for simulating processes in three dimensional systems including complex geometries, like those involving the use of instruments having various shapes or of generic deployment platforms. This can be accomplished with Monte Carlo methods based on the concept that, by knowing the probability of occurrence of each individual event in a sequence, the probability of occurrence of the whole sequence of events can be determined. In the case of marine processes the different events are represented by following the history of a very large number of photons beginning with their entry at the top of the atmosphere, travelling a given distance before interacting with the medium (i.e., air or water) and then being absorbed or scattered (Mobley, 1994). If the photon is absorbed, it is removed from the process. If it is scattered, its scattering angle is determined through the scattering phase function, the new travel distance to

next interaction is computed, and the process is repeated. This solution, called *Forward Monte Carlo* because the photons are traced forward in time, is however very inefficient. In fact, most of the photons generated in the simulation process never reach the sensor and are consequently lost. Because of this, *Backward Monte Carlo* methods were introduced to more efficiently address radiative transfer processes in atmosphere-ocean systems. These methods trace the photon path back from the detector to the source as a time-reversal problem. Computational efficiency is optimized by assuming each photon is a *packet of photons* whose weight, initially assumed 1, is decreased after each interaction with the medium. Specific examples of application of Monte Carlo methods to marine radiometric problems are the studies on self-shading of underwater sensors (Doyle and Voss, 2000; Gordon and Ding, 1992; Leathers et al., 2001; Piskozub et al., 2000) and on shadowing perturbations by deployment platforms (Doyle and Zibordi, 2002; Gordon, 1985; Zibordi et al., 1999). This latter case is analyzed in Chapter 7.

## 2.3 Marine Radiometers

A modern radiometer is composed of at least three basic components: (*i*) the optics which collect the light through an aperture, spectrally filter or disperse the light, and focus it on a field stop; (*ii*) the detector which transduces the light received through the field stop into an electrical signal; (*iii*) the analog to digital converter which translates the analog output of the detector (typically a voltage or a current) into a digital number. The major characteristics identifying the performance of a radiometer are: (*i*) the responsivity defined as the output per input of incident light; (*ii*) the detectivity defined as the responsivity divided by the root mean square (rms)

noise of the detector output; (*iii*) the operational range defined by the maximum incident radiation saturating the detector's output.

Commercial instruments for marine optical radiometry embrace a wide range of technical specifications and can be separated into two major groups: in– and above–water systems. In–water systems provide radiance and irradiance measurements at different depths (fixed in case of moorings or continuous in the case of winched or free-fall systems) commonly used for the determination of the subsurface values of the various seawater apparent optical properties. Above–water systems generally provide measurements of the total radiance leaving the sea and of the diffuse radiance from the sky, and are commonly used to determine the normalized water-leaving radiance or alternatively the remote sensing reflectance.

This section provides general introductory elements on a sample of commercial radiometers widely used in marine optics. No insight is given on *recent* systems like the New Upwelling Radiance Distribution System (NURADS), a unique $2\pi$ imaging system used to map the in water radiance field (Voss and Chapin, 2005), or the hyperspectral above–water radiometers used to produce high resolution spectra of $L_{wn}(\lambda)$ (Ruddick et al., 2006). It is however emphasized that the principles and methods discussed in the following chapters equally apply to these recent systems as to the more *classical* radiometers.

### 2.3.1 In-water radiometers

The first successful in-water measurement of light is dated back to the early 1920s (Shelford and Gail, 1922). Since then, technological developments led from the deployment of a single sensor at a fixed depth to the capability of in-water profiling

with a suite of multiple sensors for a comprehensive characterization of the spectral light field in the water column.

The in–water radiometric measurement methods currently adopted by the scientific community are mostly derived from that proposed by Smith and Baker (1984, 1986). This method, which combines achievements of former experimental studies (Dera et al., 1972; Jerlov, 1968), has significantly influenced the design of in-water radiometers in the last two decades. Basically, the method requires measurements to be collected in the water column at different depths, in combination with above-water downward irradiance data. The in–water radiometric measurements are used to extrapolate values to $0^-$ depth (i.e., just below the water surface). Above–water downward irradiance data are used to minimize the effects of illumination changes on in–water radiometric measurements during data collection.

### a. Wire Stabilized Profiling Environmental Radiometer

The Wire Stabilized Profiling Environmental Radiometer (WiSPER) is an example of in–water optical profiler (see Fig. 2.3). This is a winched system deployed through a custom-built profiling rig which provides $L_u(z,\lambda)$, $E_u(z,\lambda)$ and $E_d(z,\lambda)$ in seven spectral bands 10 nm wide in the 400–700 nm interval (Zibordi et al., 2004c). The system is equipped with OCI-200 and OCR-200 ocean color radiometers manufactured by Satlantic Inc.(Halifax, Canada): an OCR-200 with in-water 20 degrees full-aperture field-of-view for $L_u(z,\lambda)$ measurements; two OCI-200 with independent collectors for each channel for $E_d(z,\lambda)$ and $E_u(z,\lambda)$ measurements; and an additional OCI-200 operating in air for above–water $E_d(0^+,\lambda)$ measurements. System control and data logging are ensured through RS-232 or RS-422 serial links. A detailed description of in–water methods is given in Chapter 6.

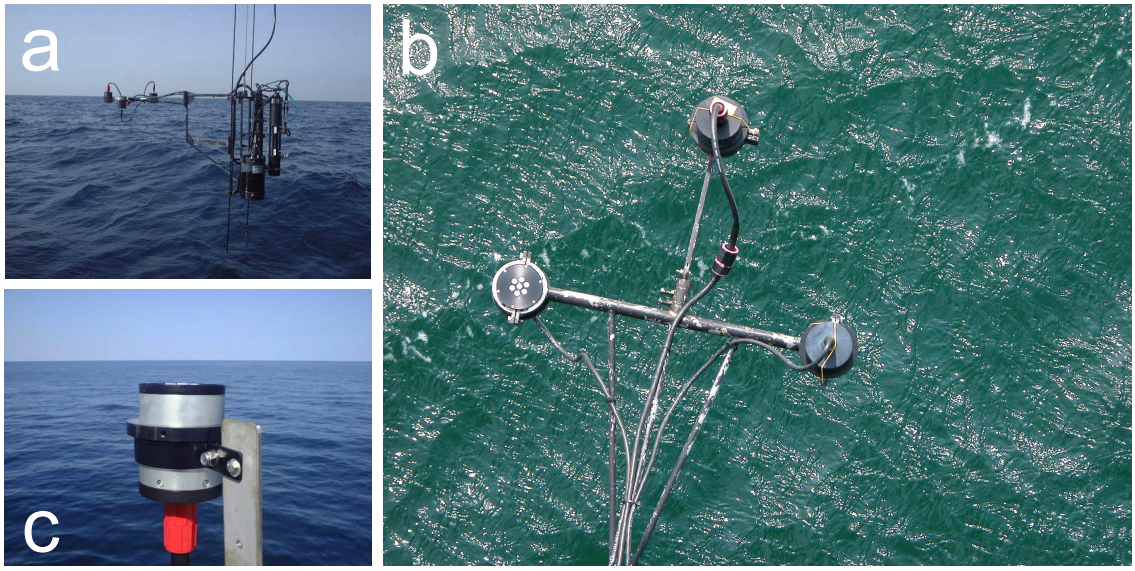


Figure 2.3: The WiSPER system: *a.* view of the WiSPER profiling rig before deployment (two taut wires anchored between the deployment platform on a fixed oceanographic tower and a weight on the sea bottom maintain stable the system during deployment); *b.* close view of the three in–water sensor heads for $L_u(z,\lambda)$, $E_u(z,\lambda)$ and $E_d(z,\lambda)$ measurements; *c.* close view of the in-air sensor head for $E_d(0^+\lambda)$ measurements.

### b. The micro-Profiler

The micro-Profiler (microPro) system manufactured by Satlantic Inc. is an example of a tethered free-fall instrument (see Fig. 2.4). It can be deployed at some distance from superstructures (generally ships) and produces profile data at 6 Hz sampling rate with a minimum deployment speed of 0.2-0.3 m $s^{-1}$. The profiler is equipped with three OCR-507 radiometers, two attached on the fins and one on the nose, which provide the capability of measuring $L_u(z,\lambda)$, $E_d(z,\lambda)$ and $E_u(z,\lambda)$, respectively, in seven spectral bands 10 nm wide in the 400-700 nm range. An additional in-air OCR-507 radiometer is used to produce $E_d(0^+\lambda)$ data. Tilt sensors provide information on the system stability during profiling.

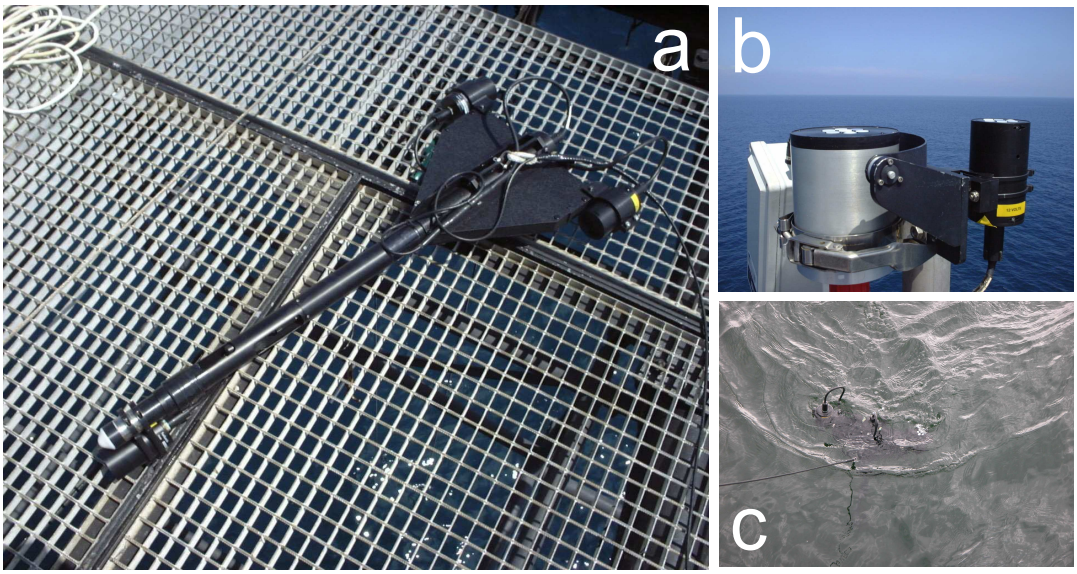


Figure 2.4: The microPro system: *a.* view of the profiler before deployment; *b.* close view (device on the right) of the in-air sensor head for $E_d(0^+\lambda)$ measurements (the device on the left is an in–air OCI-200 sensor head equipped with a shadow-band radiometer used to collect total and diffuse downward irradiance data); *c.* view of microPro at the sea surface just before its release.

Peculiarity of this system is its reduced size and the small cross section of radiometers which minimize the self-shading perturbations (Gordon and Ding, 1992). In particular the diameter of the OCR-507 radiometers is only 2.5 inch, approximately 2/3 of the OCI-200 or OCR-200 radiometer series installed on WiSPER. System control and data logging are ensured through RS-232 and RS-422 serial links.

### 2.3.2 Above-Water Radiometers

Above–water radiometry, when compared to the more consolidated and widely used in–water radiometry, is a relatively new technique in marine optics. Early above–water radiometric methods were reported by Morel (1980), and, Carder and Steward (1985). Extensive use of above-water radiometry started in the second half of the

1990s. Relevant contributions to the refinement of the early methods came with the theoretical work of Mobley (1999) and the experimental activities of Hooker et al. (2002b, 2004) and Zibordi et al. (2002b, 2004d). Almost all published methods address the production of water-leaving radiance data, $L_W$, from measurements of the total radiance from the sea, $L_T$, (which includes water–leaving, sky–glitter and sun–glint contributions) and of the diffuse radiance from the sky (i.e., sky radiance), $L_i$.

### a. The SeaWiFS Surface Acquisition System

The SeaWiFS Surface Acquisition System (SeaSAS) is an example of manned above water radiometer system (see Fig. 2.5). This, manufactured by Satlantic Inc., was designed to measure the total radiance from the sea, $L_T(\varphi, \phi, \lambda)$, at relative azimuth $\varphi$ with respect to the sun azimuth and viewing angle $\theta$, and the sky radiance, $L_i(\varphi, \theta', \lambda)$, at viewing angle $\theta'$, with seven-channel OCR-200 radiometers having 6 degrees full-angle field-of-view (Hooker et al., 2004). A separate sensor (an OCI-200 not shown in Fig. 2.5) is used to measure the above water downward irradiance, $E_d(0^+, \lambda)$, as required for the minimization of perturbations produced by changes in illumination conditions during measurements. The system is equipped with tilt sensors to accurately determine the pointing geometry and to monitor the stability of the frame hosting the radiometers. The system is manually operated and data are commonly acuired with $\theta = 40$ degrees and $90 \leq \varphi \leq 135$ degrees. System control and data logging is ensured through RS-422 serial link.

Figure 2.5: The SeaSAS: view of the radiometers for $L_T(\lambda, \theta, \phi)$ (left unit) and $L_i(\lambda, \theta', \phi)$ (right unit) measurements.

### b. The SeaWiFS Photometer Revision for Incident Surface Measurements

The SeaWiFS Photometer Revision for Incident Surface Measurements (SeaPRISM) is an example of autonmous above–water radiometer systems (see Fig. 2.6). This, manufactured by CIMEL Electronique (Paris, France), measures: (*i*) the direct sun irradiance, $E_s(\phi_0, \theta_0, \lambda)$, as a function of sun azimuth, $\phi_0$, sun zenith, $\theta_0$, and wavelength, $\lambda$, as required for the retrieval of the atmospheric optical thickness; (*ii*) the sky radiance, $L_i(\phi, \theta, \lambda)$, in a wide range of angles identified by the azimuth plane, $\phi$, and by the viewing angle, $\theta$, as required for the retrieval of the atmospheric scattering phase function; and (*iii*) the total radiance above the sea surface, $L_T(\varphi, \theta, \lambda)$, and the sky radiance, $L_i(\varphi, \theta', \lambda)$, with the specific geometry required for the retrieval of

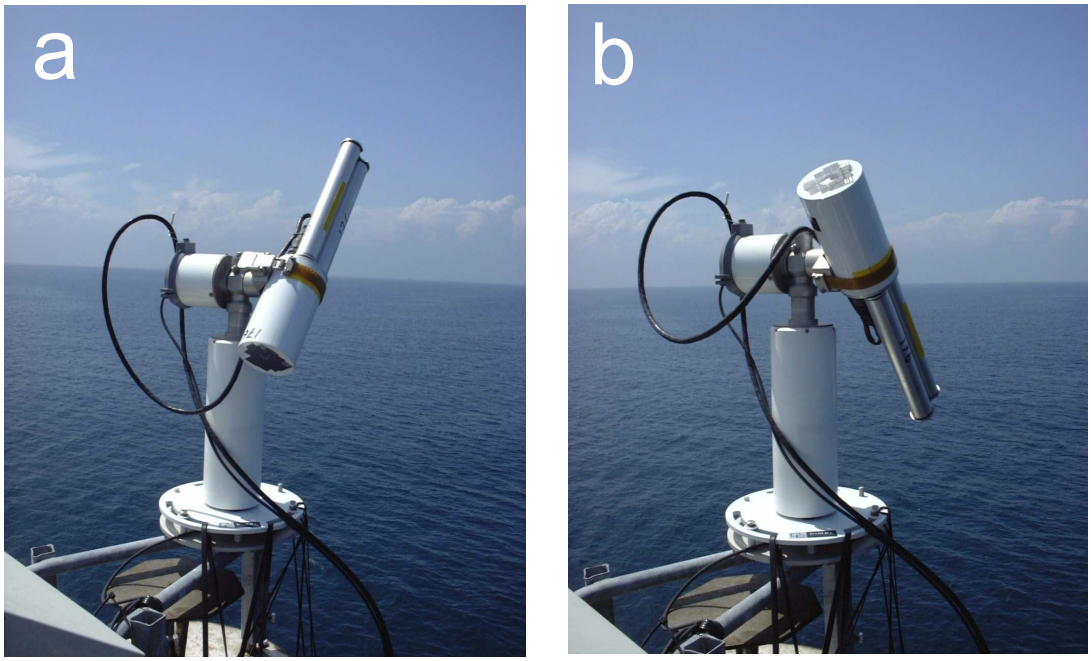


Figure 2.6: The SeaPRISM system: *a.* view during the execution of $L_i(\phi, \theta', \lambda)$ measurements; *b.* view during the execution of $L_T(\varphi, \theta, \lambda)$ measurements.

the water-leaving radiance, $L_W(\lambda)$ (Hooker et al., 2004; Zibordi et al., 2004a). Measurements are performed with a 1.2 degrees full-angle field-of-view in eight channels within the 340–1020 nm spectral range suitable for atmospheric aerosol measurements and ocean color applications.

Independent sun– , sky– , and sea–viewing scenarios identify the data collection sequences for direct sun irradiance, sky radiance and sea radiance respectively. An autonomous transmission capability, relying on collection systems onboard geostationary satellites, permits near real time data handling within the framework of the ocean color component (Zibordi et al., 2006c) of the Aerosol Robotic Network (AERONET-OC) of SeaPRISM system. More details on above–water methods are given in Chapter 6.

## 2.4 Summary

Terminology used in marine optical radiometry to identify seawater optical properties follows the general separation between inherent (i.e., absorption coefficient, $a$; scattering coefficient, $b$; and volume scattering function, $\beta$) and apparent (i.e., irradiance reflectance, $R$; normalized water-leaving radiance, $L_{wn}$; remote sensing reflectance, $R_{rs}$; diffuse attenuation coefficient, $K_d$) optical properties. The former depend on the properties of the medium only, while the latter depend on both the illumination conditions and the properties of the medium.

Marine optical radiometry had early experimental developments in the 1920s and the understanding of marine optical processes significantly grew in the following decades. In contrast, comprehensive descriptions of the in-water radiative transfer processes were only formulated in the 1960s and coincided with the assessment of quantitative in-water radiometry.

Instruments for marine optical radiometry embrace a wide range of technical specifications and can be separated into two major groups: in– and above–water systems. In–water systems provide radiance and irradiance measurements at different depths and are commonly used for the determination of the subsurface values of the various seawater apparent optical properties. Above–water systems generally provide measurements of the total radiance leaving the sea and of the sky radiance, commonly used to determine the normalized water-leaving radiance or alternatively the remote sensing reflectance.

The efficacy of state of the art radiometers in support of marine optics is dependent on a comprehensive understanding of calibration requirements, measurement protocols and uncertainties, which are all addressed in the following chapters.

# Chapter 3

# Absolute Radiometric Calibration

*Radiometry (or spectroscopy) is concerned with the transfer of optical radiation between a target source and its associated background, through the intervening medium, to a receiver or detector of optical radiant energy. The problem is to determine the quantity and quality of energy or flux flowing in a beam of radiation.*

*Clair Wyatt, 1978.*

[1]Measurement is the process by which different states of a physical quantity are compared. Absolute measurements are possible through comparisons with a standard of the given physical quantity. Thus, the absolute calibration of measuring instruments in principle allows for determining physical quantities independently of the particular instrument applied in the data collection.

Accurate absolute calibration of field radiometers is a major requirement to support development of bio-optical algorithms for natural waters, vicarious calibration of space data (i.e., the indirect calibration of data using *in situ* measurements) and

[1]The material presented and discussed in this chapter was partly published in Voss and Zibordi (1989).

validation of ocean color remote sensing radiometric products resulting from the atmospheric correction of top-of-the-atmosphere radiances (Sturm and Zibordi, 2002; Zibordi et al., 1990). Specifically, some space agencies have defined a maximum 5% uncertainty for top-of-atmosphere radiance corrected for atmospheric perturbations. This threshold was chosen to guarantee the determination of the concentration of chlorophyll *a*, $Chla$, – which is a proxy for phytoplankton biomass – with uncertainties of approximately 35% in oceanic waters (McClain et al., 2004). This means that when vicarious calibration processes are applied, or the accuracy of space derived products is assessed, the overall uncertainty budget of *in situ* measurements should be below 5%. This is possible when each factor contributing to the overall uncertainty budget (including calibration terms, deployment perturbations and environmental effects) has an uncertainty typically lower than 1%.

Early steps in defining standards for radiometric calibrations are associated with the National Physical Laboratory (NPL) in England and later on with the U.S. National Bureau of Standards (NBS), currently National Institute for Standards and Technology (NIST). These studies led to the development of a primary standard, the Electrically Calibrated Pyroelectric Radiometer (ECPR) having 1% uncertainty in the measurement of radiant power from 0.1 to 100 mW over the wavelength range of 0.25–10 $\mu$m (Hengstberger, 1989). This primary standard is now used for the absolute calibration of secondary standards commonly applied for the absolute calibration of field radiometers. The widely applied secondary standard is the FEL 1000 W tungsten quartz halogen lamp available since 1980 as a revision of a former 1000 W lamp introduced in 1965. This lamp produces a known and constant quantity of flux, used for absolute irradiance calibrations in the 250–2400 nm spectral range, with an

uncertainty within 1.5% (at three standard deviations, $3\sigma$) in the 400–700 nm range.

The issue of absolute calibration is separately addressed in this chapter with a view to identify uncertainties required to consequently address the overall uncertainty budget of marine optical radiometric measurements and of derived quantities.

## 3.1 Measurement equation

Absolute calibration of radiometers requires the definition of the mathematical transformation for converting the sensor output signal into the appropriate input radiometric quantity. Kaostkowsky and Nicodemus (Wyatt, 1978) introduced the concept of the *measurement equation* (also called *system performance equation*). This yields the sensor output for a specific source configuration, to support design of calibration experiments, to quantify measurement uncertainties and to determine the calibration coefficients for the reduction of field data into radiometric quantities.

In the current analysis a radiometer is considered an almost ideal system with linear response in the range of operation and with narrow spectral bandpass allowing for the assumption of a monochromatic light detector. Under these conditions the measurement equation for any radiometric quantity $\Re(\lambda)$ (i.e., $E(\lambda)$ or $L(\lambda)$) at center-wavelength $\lambda$ is

$$\Re(\lambda) = C_{\Re}(\lambda) I_f(\lambda)(DN(\lambda) - D0(\lambda)) \tag{3.1.1}$$

where $C_{\Re}(\lambda)$ is the in-air absolute calibration coefficient, $I_f(\lambda)$ is the so-called *immersion factor* accounting for the change in response of the sensor when immersed in water with respect to in air, $DN(\lambda)$ is the digital output for a given input signal and $D0(\lambda)$ is the dark value measured by obstructing the entrance optics.

The basic step of any absolute radiometric calibration is a measure of the flux from a standard source whose characteristics are known. It is however required that, due to possible nonlinear response of radiometers, these are calibrated over their range of operation. This is generally obtained by adjusting the calibration flux to match the measurement range of the radiometer by changing the distance between the detector and the source. Then, by applying the inverse square law, the standard irradiance value $E_0(\lambda)$ at distance $d_0$ (provided with the calibrated source) is scaled to an irradiance flux $E(\lambda)$ at distance $d$ according to

$$E(\lambda) = E_0(\lambda)\frac{d_0^2}{d^2} \tag{3.1.2}$$

The in-air absolute calibration of irradiance and radiance sensors is addressed in the following sections. The more specific problem of characterizing the immersion factor, $I_f(\lambda)$, for in-water sensors is presented and discussed in Chapter 5.

## 3.2 Irradiance calibration

The in-air absolute calibration of an irradiance sensor is performed using an irradiance standard, $E_0(\lambda)$, (for instance a FEL 1000 W calibrated lamp). The procedure requires that the lamp is positioned at distance $d$ on axis and normal to the faceplate of the irradiance sensor (see Fig. 3.1). The lamp alignment needs to be checked via a laser and a lamp grid. A precision shunt in series with the lamp is required to monitor the stability of the current flowing in the lamp filament. The minimization of stray lights can be obtained by using baffling curtains and placing equipment like power supplies, digital voltmeters and computers, outside the calibration area. After warming up the lamp for several minutes (i.e., at least 30 min for a FEL 1000 W),

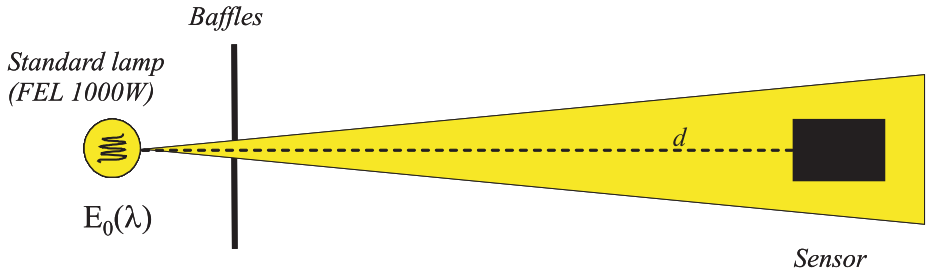


Figure 3.1: Schematic of the measurement configuration for irradiance calibration.

values of $DN(\lambda)$ and $D0(\lambda)$ for the individual sensor channels are recorded for a defined period (averaging of measurements minimize the effects of sensor noise) and from these, the irradiance calibration values, $C_E(\lambda)$, are produced according to

$$C_E(\lambda) = I_f(\lambda)\frac{E(\lambda)}{DN(\lambda) - D0(\lambda)} \tag{3.2.1}$$

where $I_f(\lambda) = 1$ and $E(\lambda)$ is determined with Eq. 3.1.2.

## 3.3 Radiance calibration

The in-air absolute calibration of a radiance sensor can be performed using integrating spheres with calibrated radiance, $L(\lambda)$, or systems composed of an irradiance standard $E_0(\lambda)$ (i.e., a FEL 1000 W) and a reflectance standard (i.e., a plaque with calibrated directional-directional reflectance). The adoption of the lamp-plaque system may help in reducing the relative uncertainties between radiance and irradiance calibrations, when using the same source (i.e., the lamp) for both types of calibration. Because of this, the latter calibration method is that considered in the following brief overview. The calibration procedure requires that the lamp is positioned at distance $d$, on axis and normal to the center of the plaque. The radiance sensor should be installed to view the plaque at 45 degrees with respect to the lamp illumination axis (see

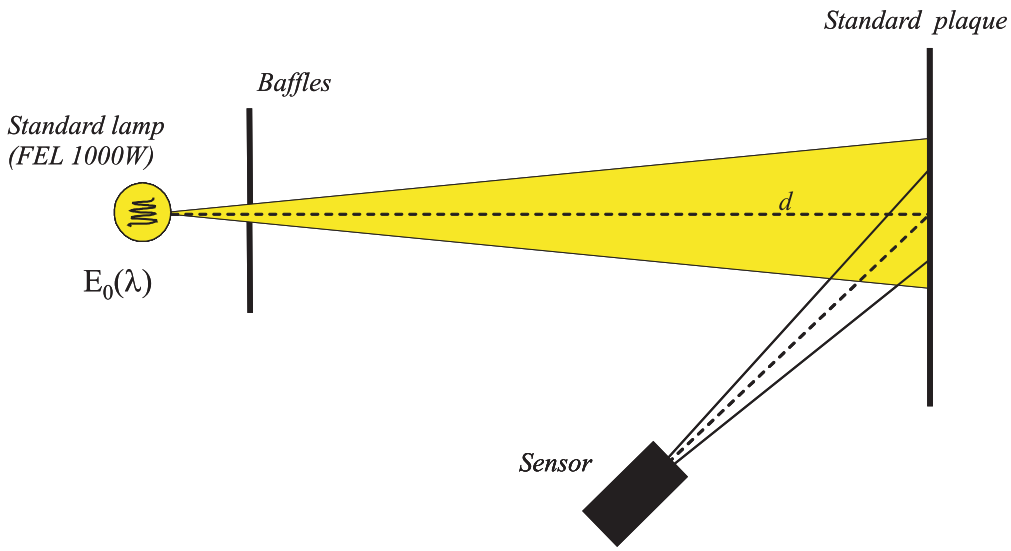


Figure 3.2: Schematic of the measurement configuration for radiance calibration.

Fig. 3.2). This is a suitable compromise which avoids looking at the plaque with normal view and thus obstructing the light field reaching the sensor. The lamp-plaque distance needs to be at least 1 m to minimize inhomogeneities in the light field at the plaque surface. In fact it must be recalled that the inhomogeneity of the radiance at the plaque is a function of the lamp-plaque distance, sensor-plaque distance and sensor field-of-view and orientation (this latter is even more relevant for multi-aperture radiometers whose individual sensors look at different portions of the plaque during the calibration). The lamp-plaque-radiometer alignment needs to be checked via a laser and a lamp grid. Similar to the irradiance calibration system, a precision shunt in series with the lamp provides the capability of checking the value and the stability of the current flowing in the lamp filament. Stray light minimization is again an important factor to reduce calibration uncertainties. After warming up the lamp, $DN(\lambda)$ and $D0(\lambda)$ values for the individual sensor channels are recorded for a defined period and from these, radiance calibration values, $C_L(\lambda)$, are produced

according to

$$C_L(\lambda) = I_f(\lambda)\frac{L(\lambda)}{DN(\lambda) - D0(\lambda)} \tag{3.3.1}$$

with $I_f(\lambda) = 1$ and $L(\lambda) = E(\lambda)\rho_d(\lambda)\pi^{-1}$, where $\rho_d(\lambda)$ is the directional-directional reflectance of the plaque for the specific viewing configuration and $E(\lambda)$ is determined using Eq. 3.1.2.

In general, instead of the directional-directional values $\rho_d(\lambda)$, the plaque reflectance is specified as directional-hemispherical $\rho_h(\lambda)$ (McCluney, 1994). In such a case, if the plaque cannot be assumed Lambertian and thus $\rho_d(\lambda) \neq \rho_h(\lambda)$, a correction factor needs to be applied to $\rho_d(\lambda)$. For instance, the values of $\rho_h(\lambda)$ commonly provided with Spectralon plaques manufactured by Labsphere (North Sutton, New Hampshire) require typical corrections ranging from 1.01 to 1.02.

## 3.4 Uncertainties on absolute calibration

Extended analysis of calibration uncertainties were made within the framework of the Seventh SeaWiFS Intercalibration Round Robin Experiments (SIRREX-7) (Hooker et al., 2002a). Specific efforts were addressed to the evaluation of uncertainties of lamp fluxes (based on multiple measurements performed on a set of lamps), calibration repeatability (as affected by power supply and lamp stabilities, and radiometer alignment) and plaque reflectance (due to spatial inhomogeneity and uncertainty in directional-directional reflectance). Results suggested different uncertainties ranked as primary (minimum), secondary (average) and tertiary (high) based on the difficulty of reducing the size of uncertainties from different individual sources. These values are given in Tab. 3.1 and vary from 1.1% to 3.4% for irradiance and from 1.5% to 6.3% for radiance (assuming 1% uncertainty for the lamp flux). In the following

chapters the values of 1.5 and 2.1% (Zibordi et al., 2002b), are applied as typical irradiance and radiance uncertainties, respectively. They were derived by simply accounting for the uncertainties of lamp flux and plaque reflectance, and fall within the ranges given by Hooker et al. (2002a).

In the evaluation of the absolute calibration uncertainties for field instruments, it is also important to consider the capability of tracing changes in the sensitivity of sensors over time. This requires regular pre– and post–deployment calibrations and, whenever possible through the use of portable sources, monitoring of the sensitivity change of radiometers during field activities (Hooker and Aiken, 1998).

Table 3.1: Estimated uncertainties in irradiance ($\varepsilon_E$) and radiance ($\varepsilon_L$) calibration coefficients (after Hooker et al. (2002a)).

| Ranking | Minimum | Typical | Maximum |
|---|---|---|---|
| $\varepsilon_E$ [%] | 1.1 | 2.3 | 3.4 |
| $\varepsilon_L$ [%] | 1.5 | 2.7 | 6.3 |

## 3.5 Summary

Absolute calibration is a fundamental step for any quantitative analysis of marine radiometric quantities. Irradiance and radiance in–air absolute calibrations are commonly carried out with a reference FEL 1000 W lamp, and with a reference FEL 1000 W lamp in combination with a reference reflectance plaque, respectively. Uncertainties of in–air absolute calibration of irradiance sensors may vary from 1.1 to 3.4 %, while for radiance they may vary from 1.5 to 6.3%. Critical to any field measurement process is the capability of producing pre- and post-measurement calibrations of radiometers to track sensitivity changes with time.

# Chapter 4

# Cosine Response

*Measurements of irradiance and its attenuation with depth are one of the most important aspects of oceanographic research. These measurements are generally made onboard a research vessel. Many conditions have to be satisfied so that this can be done properly: the diurnal irradiance must be stationary during the measurement, the irradiance collector must have suitable geometry and properties and the spectral characteristics of the measuring device must be known.*

*Jerzy Dera, 1992.*

[1]The development of bio-optical algorithms and the validation of ocean color remote sensing radiometric products rely on the knowledge of the *in situ* normalized water-leaving radiance, $L_{wn}(\lambda)$, (or alternatively the remote sensing reflectance, $R_{rs}(\lambda)$) at specific center-wavelengths, $\lambda$, in the visible and near infrared. The normalized water-leaving radiance, as already outlined in Chapter 2, can be determined from the water-leaving radiance, $L_W(\lambda)$, divided by the total downward irradiance,

[1]The material presented and discussed in this chapter is mostly published in Zibordi and Bulgarelli (2007).

$E_d(0^+, \lambda)$ (Mueller and Austin, 1995). As a consequence, the accuracy of $L_{wn}(\lambda)$ mostly depends on the accuracy of $L_W(\lambda)$ and $E_d(0^+, \lambda)$.

Given the need to produce highly accurate *in situ* data for ocean color calibration and validation activities (McClain et al., 2004), various studies and experiments have incrementally investigated the absolute accuracy of the required radiometric measurements (Hooker et al., 2002a; Zibordi et al., 2003b). However, no major work has evaluated the actual uncertainties induced in $E_d(0^+, \lambda)$ by the non ideal cosine response of irradiance sensors. In reply to this lack of knowledge, the following elements are presented and discussed here: (*i*) the characterization of the angular response of different irradiance sensors pertaining to the same class of *in situ* radiometers commonly used for $E_d(0^+, \lambda)$ measurements; (*ii*) the effects of non cosine response on $E_d(0^+, \lambda)$; and (*iii*) correction schemes for minimizing the related errors in determining $E_d(0^+, \lambda)$, and consequently $L_{wn}(\lambda)$.

## 4.1 Background

The optics of an irradiance sensor consists of a diffuser (so called *collector*) collecting the directional radiance contributions as a function of the incidence angle and ideally exhibiting a cosine response. Real collectors, nevertheless, have angular responses which deviate from the cosine law. This deviation, called the *cosine error*, is one of the major sources of uncertainty in irradiance measurements and induces errors which depend on wavelength, sun zenith (i.e., geographic position, season and time) and atmospheric optical conditions (i.e., cloudiness, aerosol type and load).

The cosine error of a sensor is conveniently described by its normalized angular

response – the response divided by the cosine of the angle of incidence and by the response at normal incidence – and commonly exhibits the largest values at high angles. The atmospheric scientific community has extensively investigated the effects of cosine errors on irradiance measurements, aiming at increasing the accuracy of radiation measurements from networks of instruments. This was mostly suggested by the need to support the creation of a global radiation climatology and to quantify trends (de La Casiniére et al., 1995; Grainger et al., 1993; Michalsky et al., 1995; Seckmeyer and Bernhard, 1993). Within such a framework, various studies showed cosine errors varying between a few, and several tens percent at 80 degrees incidence angle (Groebner, 2003; Nast, 1983; Seckmeyer and Bernhard, 1993).

A commonly accepted method for the characterization of the angular response of irradiance sensors relies on the use of an optical bench equipped with a rotating platform and a light source. While keeping the source-collector distance constant, the instrument is rotated at discrete steps so that the light beam of the source is received by the instrument collector at given incidence and azimuth angles (an alternative scheme allows for the movement of the lamp instead of the instrument). During such a characterization, a relatively small indetermination in the incidence angle can lead to an appreciable uncertainty in the quantification of the cosine error. For instance indeterminations of 0.5 degrees may produce uncertainties of approximately 1–5% in the estimate of the cosine error for an incidence angle of 50–80 degrees, respectively.

While adopting the same general method, individual investigators used various light sources and laboratory set-ups to characterize cosine errors. Nast (1983) used a halogen lamp installed on a swivel arm whose tilting allowed for varying the angle of incidence at the collector surface. A 5 mm aperture in front of the lamp acted as a

point source that, by means of lens, was converted to a parallel light beam producing a light spot of 200 W $m^{-2}$ in front of the collector. Seckmeyer and Bernhard (1993) used a 1000 W tungsten lamp in front of a radiometer mounted on two translation stages on top of a rotary stage. Harrison et al. (1994) used a 300 W axial xenon arc light source. The output beam of the source was projected through a 5 m long black-walled tube with internal baffles, to an enclosed black-walled working cavity in which the instrument was rotated. Groebner (2003) used a 1000 W quartz-halogen lamp installed on an arm 1 m long rotating in front of the sensor being characterized.

Several methodologies for minimizing the effects of cosine errors on ultraviolet (UV) irradiance measurements were proposed. Most of them assume that: (*i*) the sensor angular response is independent of the azimuth angle; and (*ii*) the sky radiance distribution is isotropic (Blumthaler et al., 1996; Groebner et al., 1996). Specifically, making use of the former assumptions and knowing the angular response of a sensor, Seckmeyer and Bernhard (1993) proposed a general analytical methodology for the minimization of the effects of cosine errors by weighting the error on direct and diffuse irradiances with the ratio of the direct to the total component of the downward irradiance.

Several investigators showed that the correction for UV measurements may vary from a few to tens of percent, depending on the measurement conditions and the characteristics of the sensor (Bais et al., 1998; Feister et al., 1997; Seckmeyer and Bernhard, 1993). The minimization of the effects of cosine errors in irradiance measurements outside the UV spectral region requires, however, investigations on consequences of non isotropic distribution of the sky radiance (Zibordi and Voss, 1989) in view of addressing the high accuracy requirements for ocean color applications.

## 4.2 Experimental characterization

Irradiance radiometers analyzed within the framework of this study, include two OCI-200 and one OCR-507. The analysis was restricted to in-air instruments and to the 412-683 nm spectral range. The OCI-200 and OCR-507 series of seven-channel radiometers belong to the same class of optical instruments and are widely used by the ocean color community to support remote sensing applications. The two series of instruments have different diameter (3.5 and 2.5 inches, respectively) and different output signals (analog and digital, respectively), but have identical optics design characterized by separate irradiance collectors and detectors for each sensor. The sensors (see inset *a* in Fig. 4.1) are distributed on the faceplate of the radiometer, with one sensor placed in the center and six sensors circularly positioned around it. The adoption of an independent collector for each channel, different from the alternative design based on a single diffuser for multiple channels (Morrow et al., 1994), exhibits the possibility of minimizing spectral asymmetries in the angular response. Conversely, it has the drawback of introducing discontinuities in the measured irradiance spectrum, if the cosine errors across the various sensors are different and not correlated. The sample of radiometers included in this analysis was composed of instruments manufactured from 1998 to 2002. Two of the radiometers (the OCI-200 s/n 129 and the OCR-507 s/n 045) were never used in the field, while the other (the OCI-200 s/n 099) was quite extensively deployed. At a visual inspection, none of the collectors exhibited defects on the external surface. The nominal center-wavelengths, identical for the different radiometers, are 412, 443, 490, 510, 555, 665 and 683 nm.

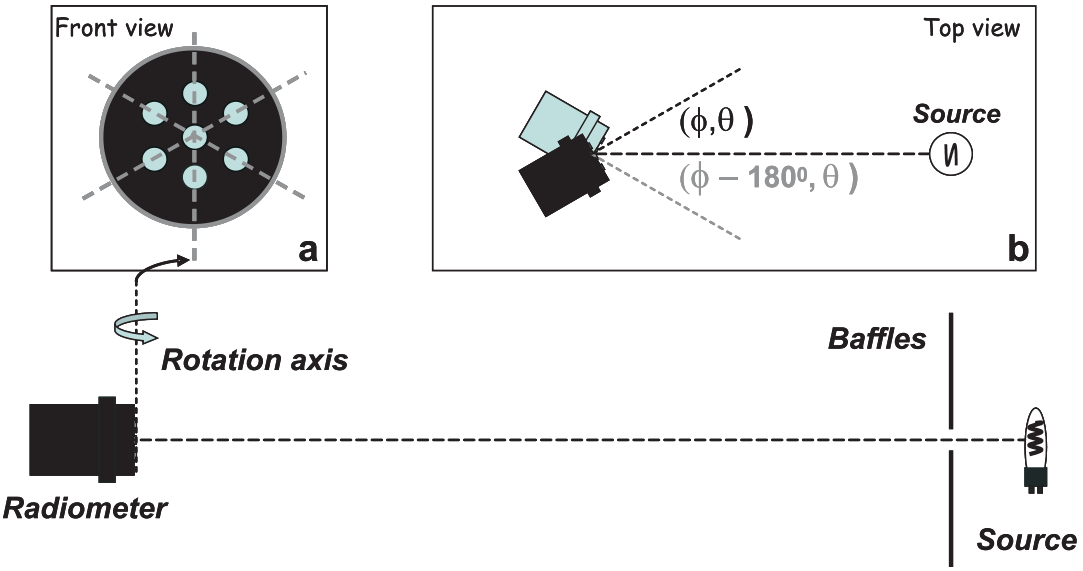


Figure 4.1: Schematic of the measurement configuration for the characterization of cosine response. Inset (it a) displays the front view of the OCI-200 and OCR-507 radiometers, while inset (it b) displays the top view of the measurement system and highlights the viewing geometry.

The cosine error of each irradiance sensor, determined from the angular response to a directional source, was measured with a 1000 W FEL lamp positioned at 90 cm distance from the collector and by rotating the instrument with respect to the optical axis of the collector itself (see Fig. 4.1). The instrument mounting consists of an X-Y translation unit installed on a rotary stage. The alignment was made with a laser. The uncertainty in the alignment of the source and sensor optics, was estimated lower than 0.5 degrees. The source and the radiometer were operated in two adjacent black-walled work-areas inter-communicating through a circular aperture. This assignment constrains the light source onto the radiometer faceplate and then minimizes the background light in the instrument work-area.

Measurements were generally taken in two azimuth planes, $\phi$, at a number of angles $\theta$, between the direction of the incident light and the direction perpendicular

to the horizontal plane of the collector. The cosine error, $f_c(\phi, \theta, \lambda)$, is computed as a percentage at the center-wavelength $\lambda$ of each channel, using

$$f_c(\phi, \theta, \lambda) = 100[\frac{E(\phi, \theta, \lambda)}{E(\phi, 0, \lambda)cos\theta} - 1] \tag{4.2.1}$$

where $E(\phi, \theta, \lambda)$ is the measurement taken at azimuth $\phi$ and incidence angle $\theta$, and $E(\phi, 0, \lambda)$ is the measurement taken at $\theta = 0$, with $E(\phi, 0, \lambda)cos\theta$ indicating measurements for an ideal cosine response. When $f_c(\phi, \theta, \lambda)$ is assumed independent of the azimuth, it is defined as $f_c(\theta, \lambda)$.

Because the OCI-200 and OCR-507 radiometers have multiple apertures distributed over a circular area, for each radiometer repeated measurement sequences were required for the characterization of all collectors. A reduction in the number of measurement sequences was obtained by taking simultaneous measurements for rows of collectors. This was made by choosing the rotation axis of the radiometer (i.e., the axis tangent to the faceplate of the radiometer and laying on the plane identifying the angle $\theta$) coincident with the symmetry axis of three of the seven collectors (see Fig. 4.1). This solution ensured the collector-source distance is kept constant at different angles $\theta$ for the three collectors aligned with respect to the rotational axis. Measurement sequences were then performed for the three different rows of aligned collectors: for each radiometer this resulted in three characterizations of the sensor located in the center of the faceplate and one characterization of the angular response of each of the six sensors symmetrically positioned around the central one.

For each row of collectors, measurements were taken in two different azimuth planes (i.e., $\phi$ and $\phi - \pi$) for the same angles $\theta$ in the 0-85 degrees range. Specifically, the radiometer rotation from 0 up to 85 degrees was made with incremental angles of 10 degrees from 0 up to 60 degrees, and of 5 degrees above. Each single measurement

at given $\phi$ and $\theta$, resulted from the averaging of approximately 500 consecutive values taken at 6 Hz. The radiometer rotation was made manually and this restricted the number of angular characterizations to three (i.e., one row of sensors per instrument) per hour.

The data defining the experimental angular response of sensors, as determined during a measurement sequence at discrete incidence angles in the 0-85 degrees range for the azimuth planes $\phi$ and $\phi - \pi$, were fitted as a function of $\theta$ to a third order polynomial function assuming independence from $\phi$. The resulting fits were then used to describe the continuous angular response of the radiometers and to determine cosine errors, $f_c(\theta, \lambda)$, for incidence angles within 0–90 degrees. Fitting of data taken in the two opposite azimuth planes (i.e., $\phi$ and $\phi - \pi$) ensures minimization of uncertainties in the determination of the angular response specifically due to: alignment or levelling inaccuracies of the irradiance sensor, non-homogeneity or asymmetry of the collector, sensitivity to polarization and instability of the source during a measuring sequence. In this analysis a cumulative estimate of the effects of these sources of uncertainty was made using replicate measurements at various azimuth planes. Results are presented in Fig. 4.2 for the 683 and 412 nm center-wavelengths corresponding to the sensors positioned in the center of the faceplate of the OCI-200 and of the OCR-507 radiometers, and for which multiple characterizations of cosine errors were made. The uncertainties were determined as the standard deviation, $\sigma$, of the three curves of cosine errors independently produced with the three sequences of angular measurements performed in six different azimuth planes. Uncertainties are generally lower than 0.5% below 65 degrees and higher than 1% above 80 degrees.

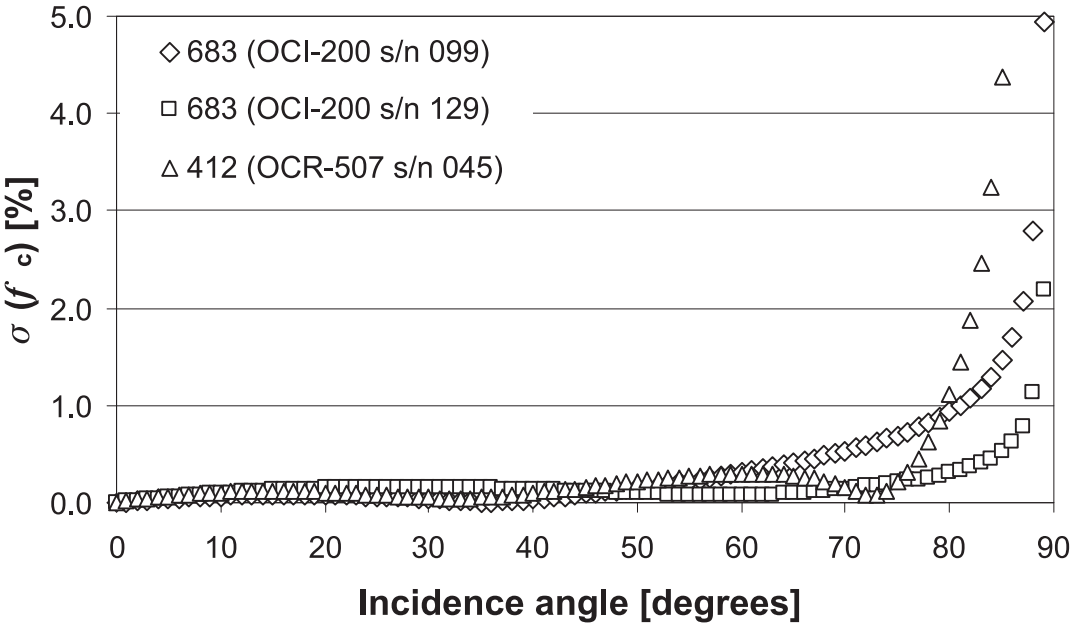


Figure 4.2: Standard deviation, $\sigma$, of cosine errors $f_c(\theta, \lambda)$ determined for multiple characterizations of the same sensors.

An additional uncertainty, not included in the former analysis and only applicable to those sensors asymmetrically positioned with respect to the center of the radiometer faceplate, is due to the adoption of off-axis geometries for the cosine error determination. In fact because of the measurement configuration, all the sensors not located in the center of the radiometer faceplate receive the light from the source with a constant tilt of approximately 1 degree with respect to the rotation axis. Combining this tilt with the value of the incidence angle at the center of the radiometer faceplate, the resulting angle does not exhibit any appreciable deviation from the actual incidence angle itself above 10 degrees (while below 10 degrees the dependence of measurements on the incidence angle is assumed negligible). This suggests that the determination of the angular response for the off-axis sensors of the considered radiometers should

not be markedly affected by additional measurement uncertainties when compared to the on-axis sensor. An experimental estimate of this source of uncertainty was made by comparing the cosine error determined for the same collectors operated off-axis (as during the regular measurement) and on-axis after their alignment with the aid of the X-Y translation unit. Results showed differences within the variations observed for the on-axis measurements. The former results suggest that the uncertainty in the experimental determination of the cosine error can be reasonably assumed lower than 0.5% below 65 degrees incidence angles and up to 1% between 65 and 80 degrees.

### 4.2.1 Inter-channel variability

The inter-channel variability of $f_c(\theta, \lambda)$ exhibits quite diverging results with $\lambda$ as $\theta$ increases. These are mostly explained by the different geometries (thickness and shape) and materials used for the various collectors at the different center-wavelengths, and are similar to those presented by various authors for a variety of in-air irradiance sensors (Bernhard and Seckmeyer, 1997; Groebner, 2003; Nast, 1983). Fig. 4.3 summarizes the average cosine errors $\bar{f}_c(\theta, \lambda)$ for the radiometers considered in the study. These values were determined by averaging the experimental angular responses of the different sensors at each center-wavelength. Results show $\bar{f}_c(\theta, \lambda)$ values generally lower than $\pm 3\%$ below 80 degrees incidence angle. Some of these values are higher than the limits given by current ocean optics protocols which require deviations lower than 2% between 0–65 degrees and 10% above (Mueller and Austin, 1995). In particular, large deviations varying from approximately 4% (absolute) at 50 degrees to 20% (absolute) at 80 degrees, are observed at the 412 and 443 nm center-wavelengths, which are relevant for the accuracy assessment of atmospherically corrected data used for the determination of pigments concentration and colored dissolved organic matter

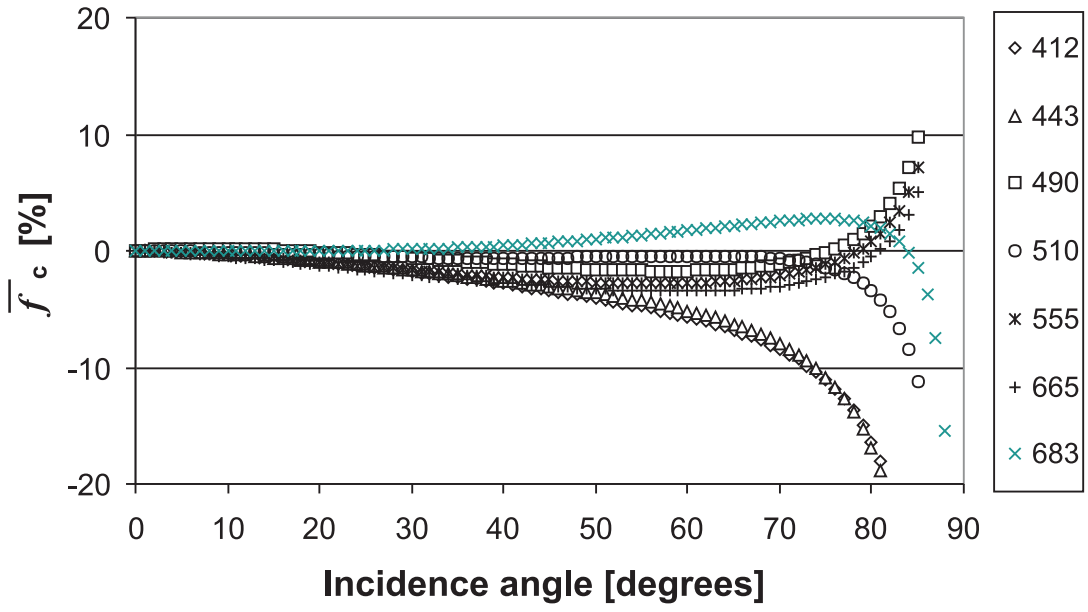


Figure 4.3: Average cosine errors $\bar{f}_c(\theta, \lambda)$ determined at various center-wavelengths.

(D'Alimonte and Zibordi, 2003; D'Alimonte et al., 2004). An index of the quality of the cosine response of irradiance sensors can be computed following the DIN 5032 standard from the German Institute of Standardization (1978) by integrating the absolute $\bar{f}_c(\theta, \lambda)$ values between 0 and 85 degrees with

$$\langle |\bar{f}_c(\lambda)| \rangle = \int_0^{85} |\bar{f}_c(\theta, \lambda)| sin(2\theta) d\theta. \tag{4.2.2}$$

Values of $\langle |\bar{f}_c(\lambda)| \rangle$ determined with the average cosine errors $\bar{f}_c(\theta, \lambda)$ presented in Fig. 4.3, are given in Tab. 4.1. They vary from 0.9% at 683 nm to 4.4% at 412 nm and are within the range of those determined for commercial UV instruments (Bernhard and Seckmeyer, 1997; Groebner, 2003). Clearly the $\bar{f}_c(\theta, \lambda)$ curves shown in Fig. 4.3, and the $\langle |\bar{f}_c(\lambda)| \rangle$ values given in Tab. 4.1, highlight the existence of

markedly different inter-channel angular responses for the sensors of the considered radiometers.

Table 4.1: Average values of $\langle|\bar{f}_c(\lambda)|\rangle$ for the radiometers included in the analysis.

| $\lambda$ | 412 | 443 | 490 | 510 | 555 | 665 | 683 |
|---|---|---|---|---|---|---|---|
| $\langle\|\bar{f}_c(\lambda)\|\rangle$ [%] | 4.4 | 4.2 | 1.1 | 0.7 | 2.0 | 2.5 | 0.9 |

### 4.2.2 Intra-channel Variability

The intra-channel variability of cosine errors for the considered three radiometers is revealed in Fig. 4.4 for the 443, 555 and 665 nm center-wavelengths. Results suggest that differences in $f_c(\theta, \lambda)$ among radiometers of the same class cannot be simply attributed to measurement uncertainties or diffuser aging. In fact at various wavelengths the two new radiometers (i.e. OCI-200 s/n 129 and OCR-507 s/n 045) exhibit differences larger than the expected measurement uncertainties. It is then supposed that slight differences in the optical properties of the materials used for manufacturing the diffusers (which are composed of multiple layers of acrylic substances) or mechanical differences introduced in the manufacturing process, are the major sources of the intra-channel variability. The standard deviations of $f_c(\theta, \lambda)$ for individual collectors at each center-wavelength, are plotted in Fig. 4.5 and summarize the intra-channel variability. These values are generally lower than 2% up to 50 degrees incidence angle while they may exhibit values as high as 6% at 80 degrees.

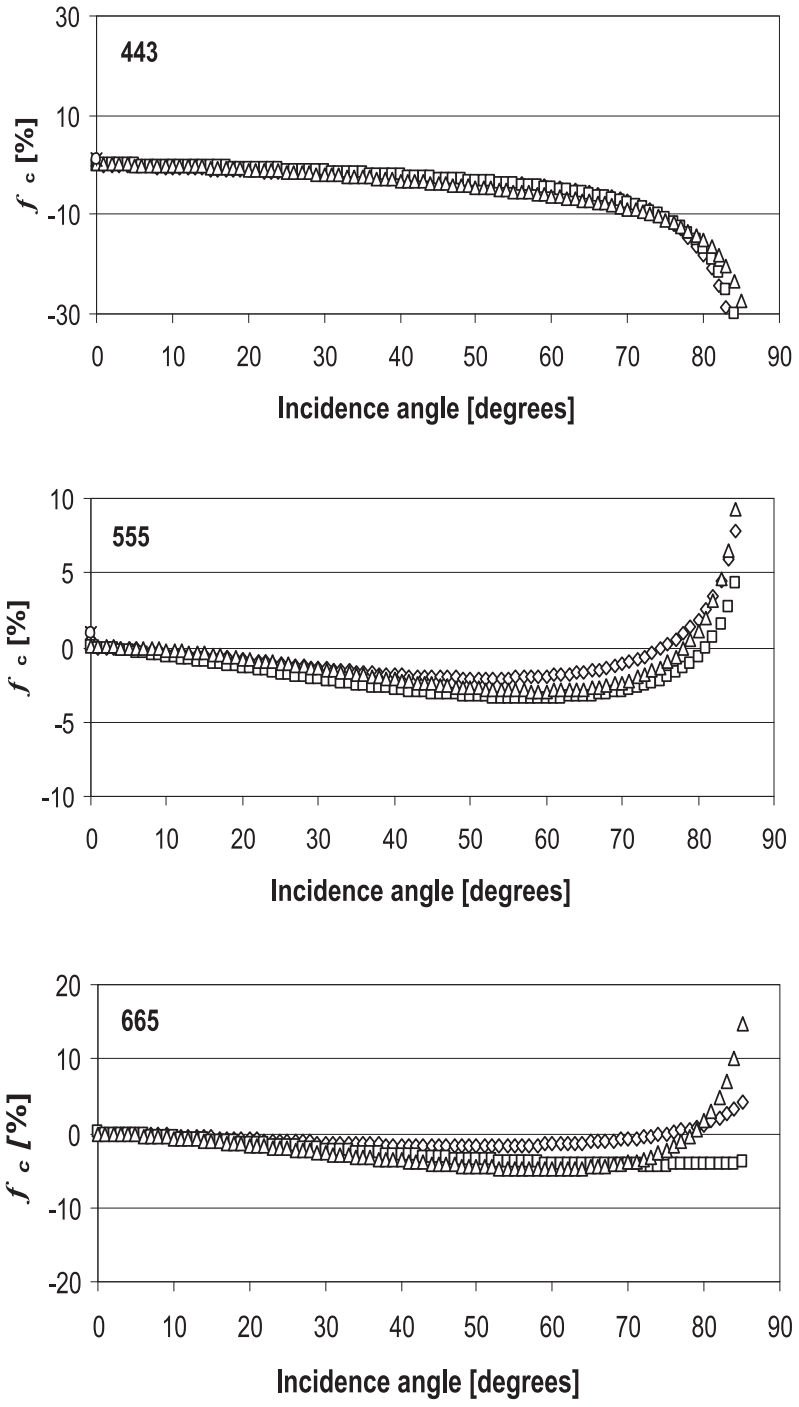


Figure 4.4: Intra-channel cosine errors $f_c(\theta, \lambda)$ at the reference center-wavelengths 443, 555 and 665 nm (different symbols indicate different radiometers: $\diamondsuit$ for OCR-507 s/n 045; $\square$ for OCI-200 s/n 099; $\triangle$ for OCI-200 s/n 129).

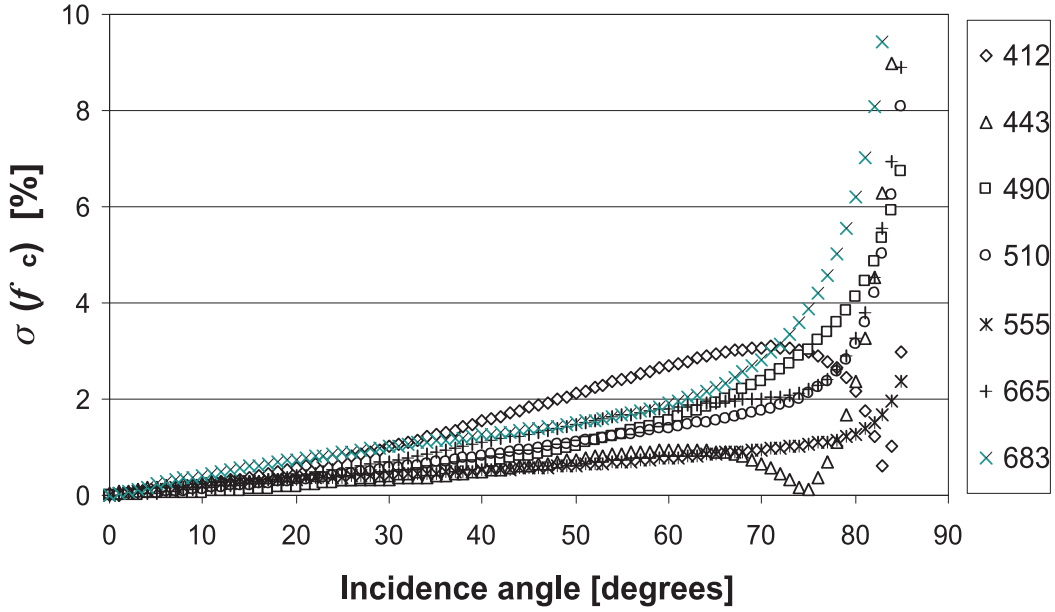


Figure 4.5: Standard deviation, $\sigma$, of intra-channel cosine errors $f_c(\theta, \lambda)$.

## 4.3 Minimization of uncertainties

The average experimental cosine errors $\bar{f}_c(\theta, \lambda)$ determined for the sample radiometers included in this analysis exhibit quite large variations as a function of the incidence angle $\theta$ and wavelength $\lambda$. It is then of general interest to evaluate the expected errors in absolute irradiance measurements as a function of wavelength, sun zenith and atmospheric conditions as produced by a different aerosol type and load.

Theoretical errors were determined through irradiance simulations made with the Finite-Element Method (FEM) highly accurate radiative transfer code (Bulgarelli et al., 1999). Simulated data were then used to benchmark a simple analytical correction scheme commonly applied to UV measurements by assuming an isotropic distribution of sky radiance.

### 4.3.1 Simulation of cosine error effects in $E_d(0^+, \lambda)$

Simulations were performed for clear sky conditions, which are those of major interest for ocean color applications, using published atmospheric (Bulgarelli and Zibordi, 2003) and seawater (Bulgarelli et al., 2003) models. Continental and maritime atmospheres were diversified by the aerosol type, whose single scattering albedo was defined spectrally varying (IAMAPRC, 1984). The scattering phase function was described by the Two-Terms-Henyey-Greenstein analytical function (Kattawar, 1975) with factors $a$=0.973, $g_1$=0.833 and $g_2$=0.671 for maritime aerosol, and $a$=0.990, $g_1$=0.729 and $g_2$=0.698 for continental aerosol (Bulgarelli and Zibordi, 2003).

The irradiance error $\varepsilon_c(\theta_0, \lambda)$ was computed for the center-wavelengths $\lambda$ of the considered radiometers and sun zeniths $\theta_0$ corresponding to the incidence angles chosen for laboratory measurements, as

$$\varepsilon_c(\theta_0, \lambda) = 100[\frac{\breve{E}_d(0^+, \lambda)}{\tilde{E}_d(0^+, \lambda)} - 1] \tag{4.3.1}$$

where $\breve{E}_d(0^+, \lambda)$ and $\tilde{E}_d(0^+, \lambda)$ indicate simulated downward irradiances computed using the experimental angular response and the ideal cosine response, respectively. It is clarified that, while Eq. 4.3.1 provides the percent error in irradiance data as a function of sun zenith, Eq. 4.2.1 provides the percent deviation from cosine response as a function of the incidence angle.

Simulated values of $\varepsilon_c(\theta_0, \lambda)$ are presented in Fig. 4.6 and Fig. 4.7 for maritime and continental aerosols as computed using extreme values of aerosol optical thickness, $\tau_a(\lambda)$, representing very clear and hazy atmospheres. These atmospheric optical conditions were defined by choosing specific values of the coefficient, $\gamma$, and exponent, $\alpha$, of the Ångström law (Ångström, 1961) for $\tau_a(\lambda)$ computations: specifically, $\gamma$=0.02

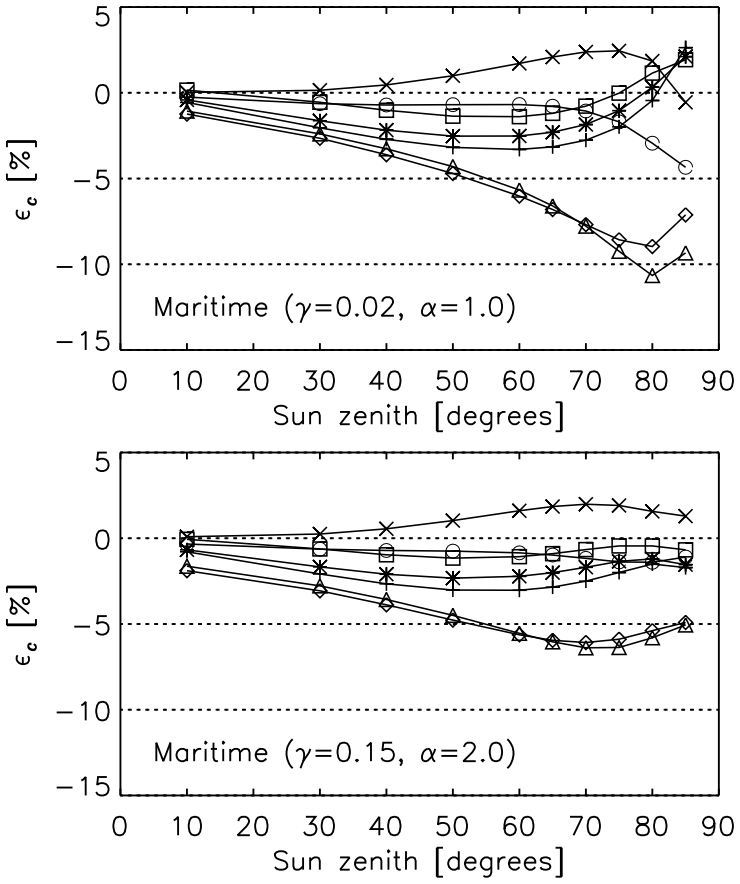


Figure 4.6: Simulated $\varepsilon_c(\theta_0, \lambda)$ for maritime aerosol, as a function of sun zenith. Values in brackets indicate the Ångström coefficient and exponent, respectively. Symbols $\diamondsuit$ indicate data at the 412 nm center-wavelength, $\triangle$ at 443 nm, $\square$ at 490 nm, $\bigcirc$ at 510 nm, $*$ at 555 nm, $+$ for 665 nm, $\times$ at 683 nm.

and $\alpha$=1.0 were used to represent a very clear atmosphere while $\gamma$=0.15 and $\alpha$=2.0 were chosen for a hazy atmosphere.

Data in Fig. 4.6 and Fig. 4.7 show that $\varepsilon_c(\lambda, \theta_0)$ varies with $\theta_0$ and exhibits values generally within $\pm$3%. An exception are data at 412 and 443 nm which may reach -10% at 80 degrees during very clear sky conditions. Variations in $\varepsilon_c(\theta_0, \lambda)$ with $\theta_0$ result from a combination of cosine error effects on direct and diffuse irradiance contributions. Specifically, results show that changes in $\varepsilon_c(\theta_0, \lambda)$ as a function of $\theta_0$

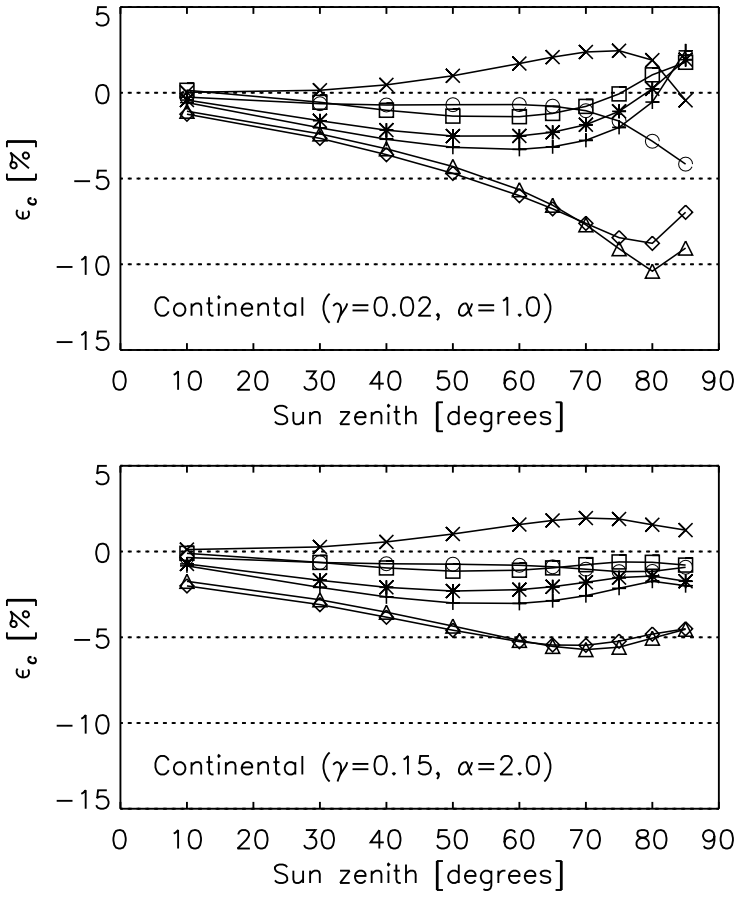


Figure 4.7: Simulated $\varepsilon_c(\theta_0, \lambda)$ for continental aerosol, as a function of sun zenith. Values in brackets indicate the Ångström coefficient and exponent, respectively. Symbols $\diamondsuit$ indicate data at the 412 nm center-wavelength, $\triangle$ at 443 nm, $\square$ at 490 nm, $\bigcirc$ at 510 nm, $*$ at 555 nm, $+$ for 665 nm, $\times$ at 683 nm.

largely follow the variations of $\bar{f}_c(\theta, \lambda)$ as a function of $\theta$ up to approximately 70-80 degrees. Above these angles, $\varepsilon_c(\theta_0, \lambda)$ tends to decrease due to an increase in the relative weight of the diffuse with respect to the direct irradiance.

The comparison of data simulated assuming maritime and continental aerosols indicate that differences in $\varepsilon_c(\theta_0, \lambda)$ due to changes in aerosol type are generally within 0.3% with extreme values in the range of 0.4–0.8 % above 60 degrees at 412

and 443 nm. On the other hand, differences are more pronounced when considering changes in $\tau_a(\lambda)$ for the same aerosol type as implicitly shown by the two extreme cases considered. This suggests that relatively accurate minimizations of the effects of cosine error in irradiance measurements can be computed without an accurate knowledge of the aerosol type, as long as $\tau_a(\lambda)$ is accurately accounted for.

The diffuse to direct irradiance ratio, $I_r(\theta_0, \lambda)$, is an alternative to $\tau_a(\lambda)$ for the determination of $\varepsilon_c(\theta_0, \lambda)$. In fact $I_r(\theta_0, \lambda)$ is already applied for cosine error corrections in the UV spectral region (Bais et al., 1998; Seckmeyer and Bernhard, 1993), and moreover it is a quantity of relevance in marine optics being used for self-shading and superstructure corrections of in–water radiometric data (Doyle and Zibordi, 2002; Zibordi and Ferrari, 1995). In addition, when compared to $\tau_a(\lambda)$, the quantity $I_r(\theta_0, \lambda)$ provides the advantages of being easily collectable in the field by the same radiometers used for irradiance measurements and of better describing the diffuse irradiance in presence of clouds. It is however stated that, if $I_r(\theta_0, \lambda)$ is determined with the same radiometer used for measuring $E_d(0^+, \lambda)$, the effects of the nonideal cosine response could affect $I_r(\theta_0, \lambda)$ itself.

In anticipation of investigating the applicability of an operational correction scheme for $E_d(0^+, \lambda)$ data collected in the visible and near infrared with the considered radiometers, values of $\varepsilon_c(\theta_0, \lambda)$ simulated for maritime aerosols are shown in Fig. 4.8 as a function of $I_r(\theta_0, \lambda)$ for discrete values of $\theta_0$ at 443, 555 and 665 nm. The plotted values computed using various $\tau_a(\lambda)$ ranging within the identified cases of very clear and hazy atmospheres, display: (*i*) a large dependence of $\varepsilon_c(\theta_0, \lambda)$ on $\theta_0$ and $\lambda$; (*ii*) a slight dependence of $\varepsilon_c(\theta_0, \lambda)$ on $I_r(\theta_0, \lambda)$ at fixed $\theta_0$ and $\lambda$; and (*iii*) an expected convergence of $\varepsilon_c(\theta_0, \lambda)$ to a single value at $I_r(\theta_0, \lambda) \to \infty$ for each $\lambda$. The values of

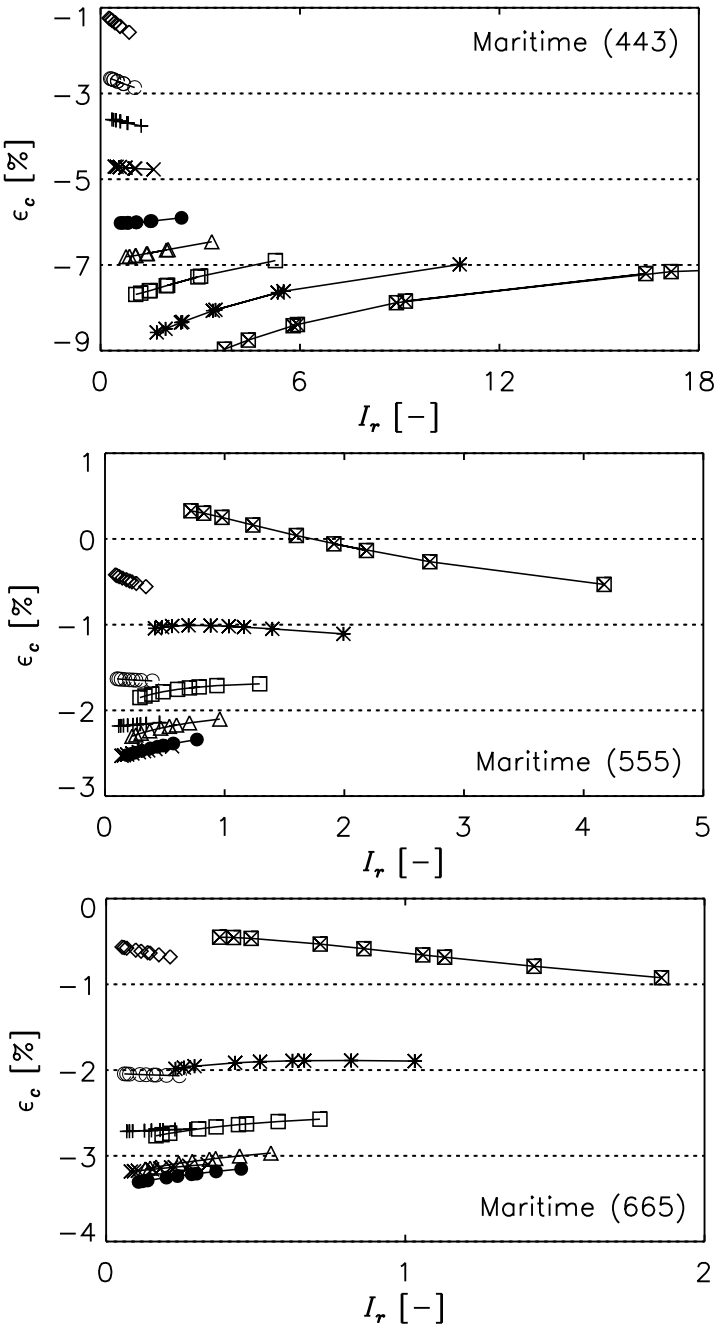


Figure 4.8: Simulated $\varepsilon_c(\theta_0, \lambda)$ as a function of $I_r(\theta_0, \lambda)$ at the reference center-wavelengths 443, 555 and 665 nm for maritime aerosol (symbols indicate different sun zeniths in degrees: $\diamondsuit$ for 10; $\bigcirc$ for 30; $\dot{+}$ for 40; $\times$ for 50; $\bullet$ for 60; $\triangle$ for 65; $\square$ for 70; $*$ for 75; $\boxtimes$ for 80).

$\varepsilon_c(\theta_0, \lambda)$ determined with $\tau_a >> 1$ for simulated overcast sky conditions (i.e., equivalent to $I_r(\theta_0, \lambda) \rightarrow \infty$ ) are presented in Tab. 4.2 and vary from 0.8 % at 683 nm to -3.9% at 412 nm.

Table 4.2: Simulated $\varepsilon_c(\lambda, \theta_0)$ for overcast sky.

| $\lambda$ | 412 | 443 | 490 | 510 | 555 | 665 | 683 |
|---|---|---|---|---|---|---|---|
| $\varepsilon_c(\lambda, \theta_0, \tau_a)$ [%] | -3.9 | -3.7 | -0.7 | -0.7 | -1.8 | -2.3 | 0.8 |

### 4.3.2 Analytical correction scheme for $E_d(0^+, \lambda)$

The use of a simple analytical correction scheme for $E_d(0^+, \lambda)$ measurements, based on the knowledge of the cosine error, of the irradiance ratio, and assuming isotropic the distribution of sky radiance, was investigated and benchmarked with data obtained from simulations performed with the FEM code choosing a maritime aerosol. Specifically, following Seckmeyer and Bernhard (1993) the error in irradiance measurements, here denoted with $\varepsilon'_c(\theta_0, \lambda)$, was estimated according to

$$\varepsilon'_c(\theta_0, \lambda) = \langle \bar{f}_c(\lambda) \rangle \frac{I_r(\theta_0, \lambda)}{I_r(\theta_0, \lambda) + 1} + f_c(\theta, \lambda) \frac{1}{I_r(\theta_0, \lambda) + 1} \tag{4.3.2}$$

where the two terms on the right side of Eq. 4.3.2 account for the effects of cosine error on diffuse and direct irradiance, respectively, with

$$\langle \bar{f}_c(\lambda) \rangle = \int_0^{90} \bar{f}_c(\theta, \lambda) sin(2\theta) d\theta. \tag{4.3.3}$$

Note that, when compared to Eq. 4.2.2, the quantity $\langle \bar{f}_c(\lambda) \rangle$ indicates the integral of the signed $\bar{f}_c(\lambda, \theta)$ function over 0–90 degrees. It is also recalled that Seckmeyer and Bernhard (1993) developed their correction scheme using the direct to total irradiance ratio instead of the diffuse to direct ratio applied here.

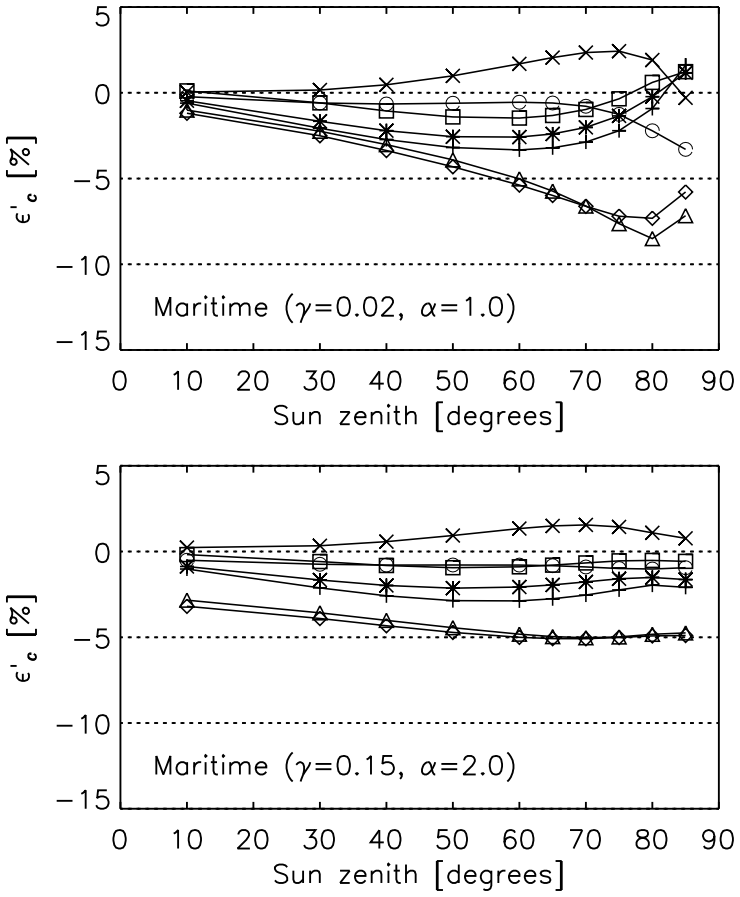


Figure 4.9: Values of $\varepsilon'_c(\theta_0, \lambda)$ as a function of sun zenith, computed with $\tau_a(\lambda)$ for very clear ($\gamma$=0.02 and $\alpha$=1.0) and hazy ($\gamma$=0.15 and $\alpha$=2.0) atmospheres. Symbols $\diamondsuit$ indicate data at the 412 nm center-wavelength, $\triangle$ at 443 nm, $\square$ at 490 nm, $\bigcirc$ at 510 nm, $*$ at 555 nm, $+$ for 665 nm, $\times$ at 683 nm.

Values of $\varepsilon'_c(\theta_0, \lambda)$ computed using the same $I_r(\theta_0, \lambda)$ resulting from the simulation of data presented in Fig. 4.6, are given in Fig. 4.9. The differences between $\varepsilon'_c(\theta_0, \lambda)$ and $\varepsilon_c(\theta_0, \lambda)$ are shown in Fig. 4.10, and exhibit values generally well below 1% (absolute), an exception are data at 412 nm and 443 nm which may display values of 1–2% (absolute) during both clear and hazy sky conditions.

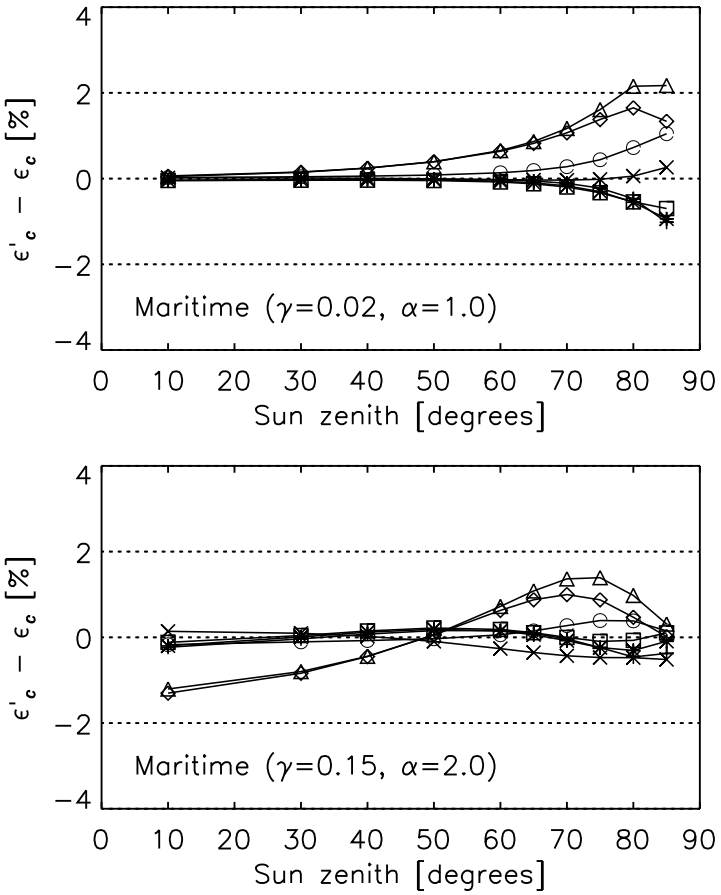


Figure 4.10: Differences between the values of $\varepsilon'_c(\theta_0, \lambda)$ and $\varepsilon_c(\theta_0, \lambda)$ displayed in Fig. 4.9 and 4.6 for very clear ($\gamma$=0.02 and $\alpha$=1.0) and hazy ($\gamma$=0.15 and $\alpha$=2.0) sky conditions. Symbols $\diamondsuit$ indicate data at the 412 nm center-wavelength, $\triangle$ at 443 nm, $\square$ at 490 nm, $\bigcirc$ at 510 nm, $*$ at 555 nm, $+$ for 665 nm, $\times$ at 683 nm.

## 4.4 Discussion on corrections

The former analysis supports the need for implementing a correction scheme for the minimization of the effects of cosine errors in irradiance measurements when highly accurate data are required. Possible correction schemes include:

1. A look-up table whose elements, resulting from simulations performed with a radiative transfer code, are indexed by $\lambda$ (related to a specific average cosine

error function $\bar{f}_c(\theta, \lambda)$), $\theta_0$ and $I_r(\theta_0, \lambda)$.

2. An analytical relationship relying on the assumption of isotropic distribution of the sky radiance and requiring knowledge of $\bar{f}_c(\theta, \lambda)$, $\theta_0$ and $I_r(\theta_0, \lambda)$.

Uncertainties in the determination of the correction values through a look-up table generated with a radiative transfer code can be mostly attributed to: (*i*) intra-channel variability of $f_c(\theta, \lambda)$; (*ii*) uncertainty in the determination of $f_c(\theta, \lambda)$; (*iii*) uncertainty in the value of $I_r(\theta_0, \lambda)$; *iv.* adoption of a single aerosol type. For the specific case study, the uncertainty in $\varepsilon_c(\theta_0, \lambda)$ has been estimated assuming the following individual values for the different sources: (*i*) 3.0% as determined with 3.0% (absolute) average intra-channel variability in $f_c(\theta, \lambda)$ derived from the standard deviation of $\bar{f}_c(\theta, \lambda)$; (*ii*) 0.5% (absolute) as determined with 0.5% average uncertainty in $f_c(\theta, \lambda)$; (*iii*) 0.2% assuming 20% uncertainty in $I_r(\theta_0, \lambda)$; and (*iv*) 0.3% as resulting from the analysis of the effects of aerosol type. From these, the total uncertainty in $\varepsilon_c(\theta_0, \lambda)$ is slightly higher than 3% (as given by the quadrature sum of individual uncertainties). This estimated maximum value would however become approximately 0.6% by minimizing the effects of intra-channel uncertainties (i.e., using collector specific $f_c(\theta, \lambda)$ instead of the average $\bar{f}_c(\theta, \lambda)$ for theoretical computations of $\varepsilon_c(\theta_0, \lambda)$).

When considering the correction scheme based on the use of a simple analytical relationship, the former uncertainties would increase by an amount varying with the amplitude of the cosine error and of the irradiance ratio. In the case of the considered radiometers the added uncertainty (a bias) is generally well below 1%, but it may reach values of 1–2% at certain sun zenith angles for the center-wavelengths at 412 and 443 nm which exhibit the largest cosine errors.

## 4.5 Summary

The accuracy of the normalized water-leaving radiance $L_{wn}(\lambda)$, extensively used for ocean color bio-optical algorithms and the validation of remote sensing products, relies on the accuracy of the above-water downward irradiance $E_d(0^+, \lambda)$ generally applied to normalize the water-leaving radiance $L_W(\lambda)$ needed for the computation of $L_{wn}(\lambda)$. Accurate measurements of $E_d(0^+, \lambda)$ require small values of the cosine error of irradiance sensors, in addition to an accurate absolute calibration. In view of exploring the uncertainties in $L_{wn}(\lambda)$ due to errors in the determination of $E_d(0^+, \lambda)$, the cosine error was investigated for a sample of commercial multi-collector radiometers belonging to the same class of instruments specifically used to support ocean color calibration and validation activities. The analysis of inter-channel cosine errors showed values generally within ±3% below 80 degrees incidence angle within the 412-683 nm spectral range. Extreme values of 4–20% (absolute) at 50–80 degrees incidence angle were estimated for the channels at the center-wavelengths 412 and 443 nm. The additional analysis of intra-channel errors, likely produced by differences in the manufacturing of collectors, showed values generally lower than 2% for incidence angles up to 50 degrees and increasing up to 6% at 80 degrees for some center-wavelength.

A theoretical analysis of the effects of cosine errors for the considered radiometers exhibited errors in above-water downward irradiance varying as a function of sun zenith, wavelength and aerosol optical thickness. Results displayed errors generally within ±3% with extreme values of approximately 4–10% (absolute) at 40–80 degrees sun zenith for the channels at the center-wavelengths 412 and 443 nm. This suggests that when highly accurate irradiance data are required, the adoption of a correction

scheme for the minimization of the effects of cosine errors is recommended. Such a correction is even more needed in the presence of appreciably different inter-channel cosine errors which may amplify uncertainties in $E_d(0^+, \lambda)$ spectral ratios and thus in the $L_{wn}(\lambda)$ (or $R_{rs}(\lambda)$) spectral ratios used for the development of bio-optical algorithms.

The application of a correction method relying on radiative transfer simulations and knowledge of the cosine response of individual collectors, showed the possibility of minimizing the effects of cosine errors with an estimated uncertainty of 0.6% (by knowing the cosine response of each individual collector). When applying a correction scheme based on a simple analytical relationship relying on the assumption of isotropic distribution of the sky radiance, the latter uncertainty would increase by a bias generally lower than 1% (absolute), with extreme values of 1–2% (absolute) at some sun zenith angle for the channels at 412 and 443 nm.

The foregoing analysis represents a new outcome in the investigation of uncertainties in marine optical radiometry. The results demonstrate the importance of accurately considering cosine errors in the uncertainty budget of normalized water-leaving radiance. This emphasizes that the effects of cosine errors need to be investigated for each series of irradiance sensors used to support satellite ocean color applications like vicarious calibration or validation activities, which require highly accurate measurements.

# Chapter 5

# Immersion Factors

*Visibility underwater is restricted in a manner somewhat analogous to the obscuration produced by dense haze or fog in the atmosphere, but the nature of image transmission by water differs importantly from that by the atmosphere because of the vastly greater space-rate of thermodynamically non-reversible energy transformation, i.e. the transformation of light into heat, chemical potential energy (as in photosynthesis), etc.*

*Seibert Duntley, 1962.*

[1]The absolute calibration of a light sensor is made in air using a standard source. When the sensor is operated in water, the calibration coefficient determined in air needs to be corrected for the change in response produced by the different refractive index of the intervening medium in contact with the entrance optics. In the case of an in-water sensor designed for irradiance measurements, the change in the absolute response is primarily caused by a change in the reflectance and transmittance of the water-collector with respect to the air-collector interfaces. In the case of an in-water

[1]The material presented and discussed in this chapter was mostly published in Zibordi (2006); Zibordi and Darecki (2006); Zibordi et al. (2004b).

sensor designed for radiance measurements, the change in response characterizing in-water measurements is mostly due to a change in the field-of-view and in the reflectance and transmittance of the water-window with respect to the air-window interfaces. These changes in the sensor's response are accounted for through a spectral multiplication factor, the so-called *immersion factor*, $I_f(\lambda)$, introduced in Chapter 3 and required to properly apply the in-air absolute calibration of the sensor when operated underwater. This chapter presents and discusses state of the art methods for the determination of the immersion factors for both irradiance and radiance sensors, based on pre-existing and new research made by the author.

## 5.1 Immersion factor for irradiance sensors

Early studies on immersion effects for irradiance sensors were carried out by Atkins and Poole (1933). They made an attempt to describe the internal and external reflection factors for an opal glass diffuser. To experimentally estimate these reflection contributions, they used a gas-filled lamp as a light source to vertically illuminate a diffuser when it was dry and wet, i.e., in-air and in-water covered with different depths of distilled water, respectively. They proposed a constant immersion factor of 1.09 for opal glass diffusers to compensate for instrument sensitivity loss when operated in the water with respect to in the air.

Later, Berger (1958) presented: (*i*) a discussion on the immersion effects in the presence of a thin layer of water producing direct reflections between the external surface of the diffuser and the water subsurface (a perturbing effect in the characterization of the immersion factor); and (*ii*) a description of a simple method to

determine experimentally the immersion factor of disk-shaped diffusers based on a wide blackened funnel to hold pure water above the diffuser with a water depth of at least 0.9 times the radius of the diffuser. Notable contributions from Berger (1958) included observations and theoretical data on the immersion effects for different diffusers made of silicate and plastic glass showing a wide range of variations for the immersion factor. Data from Berger (1961) were later used by Westlake (1965) to extensively describe the reflection-refraction processes occurring at the air-diffuser and at the water-diffuser interfaces in the presence of thin or deep layers of water. Westlake (1965) presented estimates of the different contributions of internal and external reflection and suggested a constant immersion factor of 1.19 for opal glass, significantly higher than that proposed earlier by Atkins and Poole (1933).

A comprehensive description of a protocol for the experimental characterization of the immersion factor of in-water irradiance collectors, was given by Smith (1969). The protocol, which included vertical measurements in-air and in-water with different depths of water above the diffuser, suggested the use of a collimated beam as a light source to avoid changes in the energy falling on the collector when different water depths were used. Smith (1969) presented a spectral characterization of the immersion factor of a cosine collector made of clear Plexiglas bonded together with translucent Plexiglas (with the latter in contact with water). Smith determined immersion factors almost linearly varying with wavelength from 1.34 to 1.22, in the spectral interval 400-750 nm (as summarized in Tyler and Smith (1969)) and explained this spectral dependence as a function of the absorbance of the collector.

Contemporaneously to Smith's work, an alternative method for the characterization of the immersion factor of irradiance sensors was independently developed and

applied by Aas (1969). He made use of a lamp as a light source and introduced a geometric correction factor that, as a function of the lamp collector distance, water depth, and water refractive index, minimizes the effects due to variations in the energy falling on the collector as a function of changes in water depth. This basic method was then implemented by Petzold and Austin (1988) and applied by Mueller (1995) for the determination of $I_f(\lambda)$ for collectors made of Plexiglas and Teflon for several radiometers. Mueller reported $I_f(\lambda)$ values almost linearly decreasing with wavelength and ranging, on the average, from 1.38 to 1.32 in the spectral interval 406–670 nm. Aas' method was later adopted by the marine optics community (Mueller and Austin, 1995) and applied by instrument manufacturers to produce immersion factors commonly assumed to be specific for each class of instruments. This approach, based on the use of immersion factors for classes of instruments but not for each individual instrument, led to inconsistencies in measurements (Bulgarelli et al., 2003; Dierssen and Smith, 1996; Zibordi and Berthon, 2001). This finding further confirmed the recommendation from Mueller (1995) that accurate in-water radiometry requires an experimental characterization of each individual irradiance collector.

Building on this work, the need for an extensive characterization of the immersion factors of the widely used OCI-200 radiometers (Hooker and Maritorena, 2000; Zibordi et al., 2002b) was clear, and thus undertaken within the framework of a round-robin experiment (*The Eighth SeaWiFS Intercalibration Round-Robin Experiment* (SIRREX-8)) with the participation of various institutions (Zibordi et al., 2004b). Key novel objectives of this unique experiment were: (*i*) an investigation of interlaboratory uncertainties in the characterization of $I_f(\lambda)$; and (*ii*) the sensor-to-sensor variability of $I_f(\lambda)$ for the series of radiometers considered.

### 5.1.1 Characterization of $I_f$ for irradiance sensors

The refractive index of the diffuser material, $n_d(\lambda)$, used for manufacturing irradiance collectors is always larger than the refractive index of water, $n_w(\lambda)$, and of air, $n_a$. Being $n_w(\lambda) > n_a$, the Fresnel reflectance of the external water–diffuser interface is smaller than that of the air–diffuser interface. Consequently, the transmission of light through the external interface of the diffuser is larger in water than in air. Similarly, the internal diffuser–water interface reflects less of the internal diffuse light, when compared to the corresponding diffuser–air interface. Then because of the much larger amount of light transmitted back into the water with respect to the increased amount of light transmitted into the diffuser, there is a decrease in the net irradiance measured by the detector when the instrument is in water with respect to in air.

#### *a. Measurement method*

The methodology proposed in the literature (Aas, 1969; Petzold and Austin, 1988) for determining $I_f(\lambda)$ for in-water irradiance collectors is based on using irradiances measured by the sensor in the air and below the water surface when vertically illuminated by the same point source.

A schematic of the major reflection–refraction processes occurring within the diffuser and at the diffuser interfaces, and of the measurement geometry commonly applied for $I_f(\lambda)$ characterization, are given in Fig. 5.1. Specific geometric quantities relevant for the determination of $I_f(\lambda)$ are the distance between the diffuser and the source, $d$, and the water depth above the diffuser, $z_i$.

The schematic of the measurement setup currently in use at the Joint Research Centre (JRC) of the European Commission for $I_f(\lambda)$ characterization, is shown in

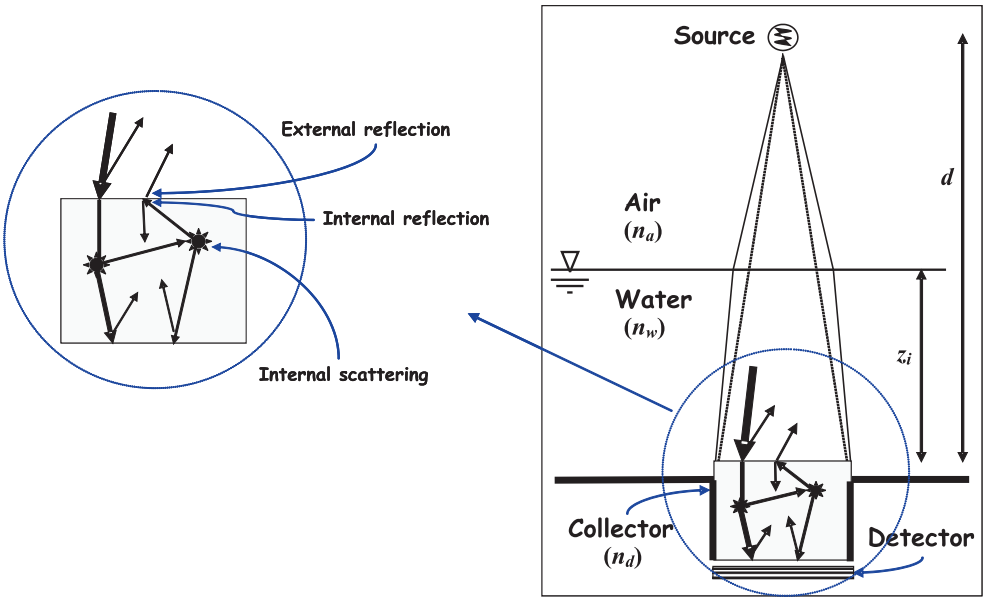


Figure 5.1: Schematic of the measurement geometry for the laboratory characterization of $I_f(\lambda)$ and of the reflection-refraction processes (see the inset) occurring at inside and outside the medium-diffuser interface of an irradiance collector (the thickness of lines indicate the relevance of the light contributions). The dashed black lines departing from the source show the in-air illumination geometry, while the continuous black lines indicate the illumination geometry with water depth $z_i$ above the collector at distance $d$ from the source (after Zibordi et al. (2004b)).

Fig. 5.2. The system is primarily composed of: (*i*) a water vessel with bottom shaped to accommodate one radiometer kinematically mounted with the collectors facing its internal side; (*ii*) a point source constituted of a lamp (i.e., a 1000 W tungsten-halogen lamp) and a lamp-screen with primary baffle; and (*iii*) a monitoring radiometer pointing at the source. All the different components of the system are installed on a vertical optical bench to facilitate the repositioning of each part at different distances. The alignment of the optical components is accomplished using a laser temporarily inserted in the support of the monitoring radiometer. A shunt resistor, in series with the lamp, is an additional means to monitor the stability of the

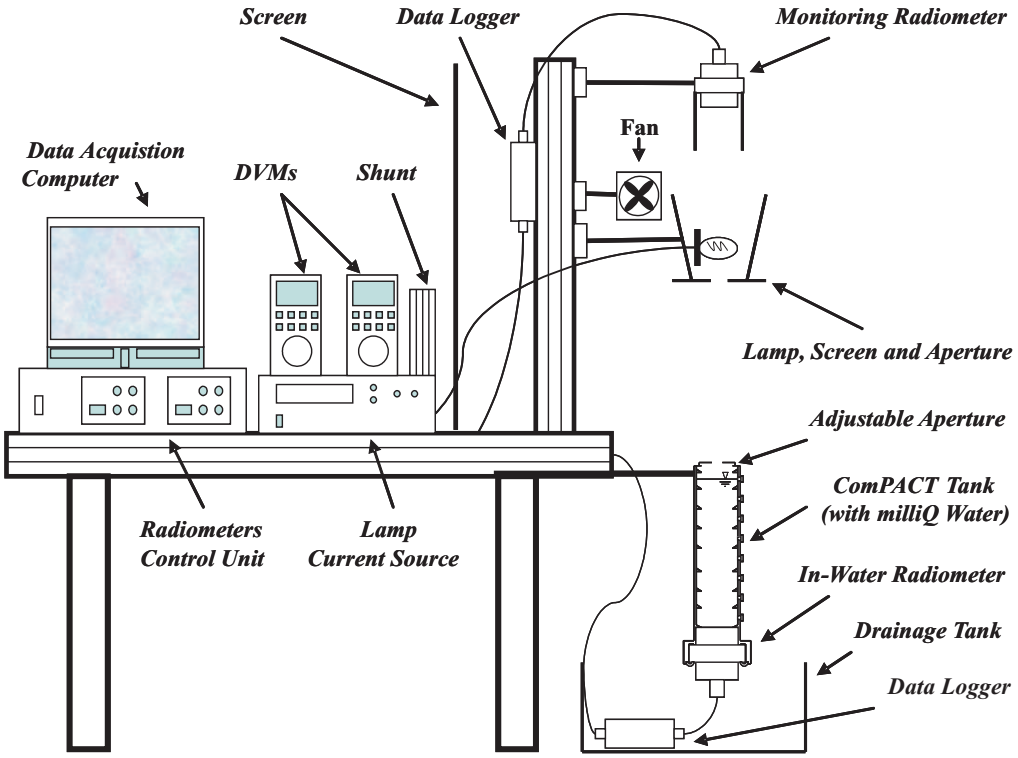


Figure 5.2: Schematic of a measurement setup for the characterization of $I_f(\lambda)$ of irradiance sensors (after Zibordi et al. (2003b)).

source. The rotational orientation of the radiometers, ensuring accurate repositioning during successive characterizations, is achieved using the flat edge of D-shaped collars attached to the radiometers. The water vessel, called Compact Portable Advanced Characterization Tank (ComPACT), can be filled with approximately 3 liters of water. This makes practical using pure water for each characterization. The ComPACT vessel, anodized dull black, has internal baffling designed to minimize any light reflection from the inside walls. A series of tapped holes, equally spaced along the vertical side of the water vessel, provide an accurate control of the water level within the tank (Zibordi et al., 2003b). During a measurement sequence the in-water data are collected for different water depths, $z_i$, by incrementally reducing the water level.

***b.*** $I_f$ ***determination***

The in-air $E(0^+, \lambda)$ and in-water $E(z_i, \lambda)$ values are determined from data computed with $I_f(\lambda)$=1, corrected for the dark or background signal, normalized with respect to measurements from the radiometer monitoring the source, and averaged for sampling interval $\Delta t$. The normalization, applied to reduce uncertainties caused by possible changes in the flux of the light source during the measurement sequence, is obtained by dividing each data record by the temporally matched data from the monitoring radiometer, and then by multiplying the resulting value by the monitoring radiometer data taken at initial time $t_0$ corresponding to the start of the measurement sequence. The subsurface in-water irradiance, $E(0^-, \lambda)$, is computed from the least-squares fit of $\ln E(z_i, \lambda)/G(z_i, \lambda)$ v.s. $z_i$. Where $\ln E(z_i, \lambda)$ is the logarithm of in-water irradiance data corrected by the measurement perturbations induced by the finite distance between an ideal point source and the collector, and $G(z_i, \lambda)$ is the so-called geometric correction factor. In agreement with Aas (1969), the $G(z_i, \lambda)$ values for the irradiance source $E(z_i, \lambda)$ at distance $d$ from the collector, are computed with

$$G(z_i, \lambda) = \left[1 - \frac{z_i}{d}\left(1 - \frac{1}{n_w(\lambda)}\right)\right]^{-2} \tag{5.1.1}$$

Once the in-air $E(0^+, \lambda)$ and the in-water subsurface $E(0^-, \lambda)$ irradiances have been determined, the immersion factor $I_f(\lambda)$ is given by

$$I_f(\lambda) = \frac{E(0^+, \lambda)}{E(0^-, \lambda)} t_{wa}(\lambda) \tag{5.1.2}$$

where $t_{wa}(\lambda)$ is the transmittance of the air–water interface to downward irradiance. This is computed from Fresnel reflectance for a vertically incident light beam and given by

$$t_{wa}(\lambda) = \frac{4n_w(\lambda)}{[1 + n_w(\lambda)]^2}. \tag{5.1.3}$$

where values of $n_w(\lambda)$ in the spectral range 400–700 nm for pure water and pure seawater (i.e., with a salinity of 0 PSU and 35 PSU, respectively, both at a temperature of 20 °C), can be obtained by

$$n_w(\lambda) = 1.31891 + \frac{6.31446}{\lambda - 139.596} \tag{5.1.4}$$

and

$$n_w(\lambda) = 1.32483 + \frac{6.53318}{\lambda - 139.589}. \tag{5.1.5}$$

The coefficients given in (5.1.4) and (5.1.5), were computed by fitting tabulated data from Austin (1976) with $\lambda$ in nm (Zibordi et al., 2003a). Equivalent equations were already proposed by Petzold and Austin (1988) for pure water at 22 °C and by Mueller and Austin (1995) for pure seawater at 16 °C.

Sample data produced in agreement with the described methodology are displayed in Fig. 5.3. They highlight the relevance of the geometric correction $G(z_i, \lambda)$ of the irradiance data taken with different water depths.

The elements used to evaluate the quality of the data applied for the determination of $I_f(\lambda)$ are: $(i)$ the standard deviation, $\sigma$, for the data collected in air or at each specific water depth during the defined sampling interval; $(ii)$ the negative values of slopes from the least-squares fit used to compute $E(0^-, \lambda)$, which are denoted here as $K(\lambda)$; and $(iii)$ the percent difference between the actual values $E(z_i, \lambda)/G(z_i, \lambda)$ and the fitted $E(0^-, \lambda)exp[-K(\lambda)z_i]$ values at each depth $z_i$. A high $\sigma$ value suggests changes in the measurement conditions during one step of the data collection (i.e., due to an instability of the water surface or the presence of large particles floating above the collectors). As a consequence of using a light source that approximates a direct beam illuminating the diffusers, the $K(\lambda)$ value is a function of the water absorption and scattering, and of the optical-mechanical setup. Significant differences

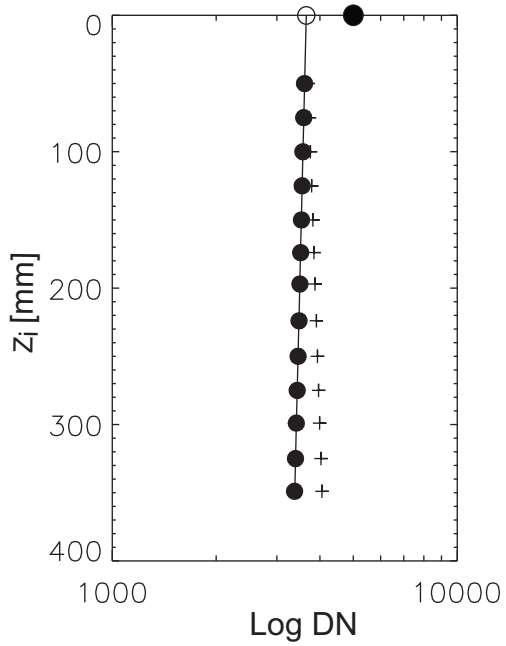


Figure 5.3: Sample data (in relative units expressed in digital numbers DN), used for $I_f(\lambda)$ characterization of an OCI-200 at the 555 nm center wavelength. Symbols + indicate actual measurements at different water depths. Symbols • at depth $z_i > 0$ indicate data corrected for geometric effects (through the $G$ factor). The symbol ● at zero depth indicates the in-air measurement to be divided by the subsurface extrapolated value highlighted by the symbol ○ (after Zibordi et al. (2004b)).

in $K(\lambda)$ among successive measurement sequences, therefore, imply changes in water quality or in the geometry of the system. Significant changes in the percent difference between $E(z_i, \lambda)/G(z_i, \lambda)$ and the fitted $E(0^-, \lambda)exp[-K(\lambda)z_i]$, at a specific depth $z_i$, may indicate an incorrect determination of the depth $z_i$ or changes in the optical setup during the measurement sequence.

### 5.1.2 Discussion on $I_f(\lambda)$ for irradiance sensors

SIRREX-8, was so far the most comprehensive experiment investigating the methods for the characterization of $I_f(\lambda)$ even though only focussing on the widely used seven-channel OCI-200 series of radiometers (Zibordi et al., 2004b). It is recalled that

the seven channels are associated with independent diffusers manufactured by layering different acrylic materials and that each diffuser has scattering and absorption properties optimized for the specific center-wavelength.

A total of nine OCI-200 radiometers (four $E_u$ sensors with s/n 048, 098, 109, 130, and five $E_d$ with s/n 015, 040, 050, 071, 097) all having the same nominal center-wavelengths (i.e., 412, 443, 490, 510, 555, 665, and 683 nm), were included in the experiment. The selected radiometers were manufactured between September 1994 and July 1999 and represent about 10% of the total production of in-water OCI-200 series radiometers for that period.

***a. Intra- and inter-laboratory analysis***

Inter-laboratory analysis of $I_f(\lambda)$ data for the nine radiometers was supported by measurements performed by three different laboratories: the Center for Hydro-Optics (San Diego, California); Satlantic Inc. (Halifax, Nova Scotia); and the Joint Research Centre (Ispra, Italy). $I_f(\lambda)$ data from the so-called *reference radiometer* (a radiometer frequently characterized to track changes in the measurement setup at each participating laboratory) provided an intercomparison among the different laboratories and supported an intra-laboratory analysis of the measurement repeatability. $I_f(\lambda)$ data from all the radiometers, in addition to providing intercomparability among the different laboratories, permitted an analysis of the dispersion of $I_f(\lambda)$ data across the OCI-200 sample radiometers (Zibordi et al., 2004b).

The uncertainty due to measurement repeatability was quantified through $\xi(\lambda)$ given by two times the standard deviation $\sigma(\lambda)$ divided by the average $\bar{I}_f(\lambda)$ of independent $I_f(\lambda)$ measurements, and expressed as a percentage, i.e., $\xi(\lambda) = 200[\sigma(\lambda) \backslash \bar{I}_f(\lambda)]$

($\xi(\lambda)/2$ is commonly called variation coefficient). The uncertainty due to method precision was then determined by $\xi^A(\lambda)$, computed in agreement with the defined $\xi(\lambda)$, but using the standard deviation and the average $\bar{I}_f^A(\lambda)$ of the $\bar{I}_f(\lambda)$ values from all three laboratories.

The $I_f(\lambda)$ intra-laboratory analysis based on data from the reference radiometer, showed a spectrally averaged uncertainty in repeatability $\xi(\lambda)$ varying from 0.3% to 0.6% across the different laboratories.

The intra-laboratory analysis based on the data from all radiometers, indicated the dispersion of $I_f(\lambda)$ values across the various instruments. This dispersion, defined by the standard deviation, exhibited spectrally averaged values of 2.2% for all three laboratories. Instrument-to-instrument variability, however, was quite spectrally pronounced. Data from all three laboratories displayed high variability in $I_f(\lambda)$ at 665 and 490 nm with dispersion of 5% and 3%, respectively.

The inter-laboratory comparison showed spectrally averaged values of 1.2% for uncertainties in method precision, $\xi^A(\lambda)$. The relative inter-laboratory uncertainties determined by the percent difference between $\bar{I}_f(\lambda)$ for each laboratory and $\bar{I}_f^A(\lambda)$, showed spectrally averaged values ranging from –0.5% to +0.6%.

***b. Uncertainties***

The analysis of SIRREX-8 data showed that the uncertainties in the characterization of $I_f(\lambda)$ for irradiance collectors, excluding any contribution from the optical–mechanical setup, are mostly sensitive to: (*i*) the use of tap water versus seawater; (*ii*) the presence of dust particles or slicks by contaminants at the water surface (i.e., silicon grease released by connectors, soap used in some laboratories to reduce the water surface tension); and (*iii*) the level of water purity.

Additional elements, which could become a source of uncertainty, if improperly handled, are: (*iv*) the assumption of a point source for the lamp; (*v*) the optical load of the radiometer (i.e., the perturbation induced in measurements by the high reflectance of diffusers); (*vi*) the stability of the light source; and (*vii*) the water temperature.

All these sources of uncertainty may produce additive effects increasing or reducing, in an almost unpredictable way, the total uncertainty in $I_f(\lambda)$.

Specifically, the use of tap water versus seawater introduces a negative bias in the absolute characterization of immersion factors. This bias is of the same order of the difference in refractive indexes of pure water and pure seawater (i.e., about 0.5% in the 400–700 nm spectral range) as confirmed through experimental determinations (Zibordi et al., 2003b).

The presence of particles or slicks at the water surface can produce an underestimate of subsurface irradiance that leads to an underestimate of $I_f(\lambda)$, almost constant across the visible spectrum. Surface skimming and care in the use of parts of the setup which may cause contamination, can easily minimize the effects of this potential source of uncertainty. An extreme case of surface contamination by floating particles creating a homogeneous layer at the water surface, showed a spectrally averaged overestimate of 1.6% in $I_f(\lambda)$.

The use of soap may efficiently reduce surface tension in seawater and, thus, in moving particles away from the surface area directly associated with the optical measurements. However, due to the lack of investigation, this solution has to be applied with caution because soap slicks may affect the surface transmittance and thereby produce an overestimate of $I_f(\lambda)$.

The purity of water is the most difficult accomplishment in $I_f(\lambda)$ characterization especially when large volumes of water are required. While absorption processes do not significantly affect the determination of the subsurface irradiance, the presence of scattering elements may produce an underestimate of $I_f(\lambda)$ because of an increase in the subsurface irradiance $E(0^-, \lambda)$ induced by an increase in the irradiance contribution reflected back into the water by the water-air interface. The analysis of $I_f(\lambda)$ data generated with specific experiments (Zibordi et al., 2003b), showed that perturbations due to scattering are more pronounced in the blue part of the spectrum and decrease toward the red (in agreement with theoretical expectations).

The use of a point source, (i.e., a lamp), at a finite distance from the collector, induces different illumination conditions on the collector as a function of the changing water depth, which leads to an overestimate of $I_f(\lambda)$. Combining the use of small filament lamps with increased distances between the lamp and collector, in addition to the use of the geometric correction model for in-water radiometric data as proposed by Aas (1969), minimizes the uncertainties in determining $I_f(\lambda)$. A specific experiment showed that with a lamp filament of $4 \times 8$ mm at two distances from the collector (at 86 cm and at 100 cm), the difference in $I_f(\lambda)$ values computed by applying the geometric factor $G(z, \lambda)$, was within the intra-laboratory measurement repeteability (i.e., approximately $\pm 0.5\%$).

The number, size and high reflectance of the irradiance collectors, are additional perturbation elements in the characterization of $I_f(\lambda)$. In fact, the collectors, at close distance to the water surface (i.e., within a few centimeters) induce an overestimate in the in-water irradiance. This is caused by multiple reflections between the immersed collectors and the air-water surface, resulting in an underestimate of $I_f(\lambda)$.

Berger (1958) showed that the perturbation becomes negligible when the water depth is greater than the critical depth $z_c \approx 0.9\ R_c$, where $R_c$ is the radius of the collector. Assuming that for OCI-200 radiometers the perturbation is produced by the area covered by all seven diffusers (i.e., a circular area of radius $R_c \approx 2.0$ cm) a depth $z_c \approx$ 1.8 cm satisfies the requirement for minimizing the perturbation. A specific measurement sequence including in-water data collected with 1 cm increments between 5 and 1 cm, in addition to regular depth measurements beyond 5 cm, showed an average $I_f(\lambda)$ underestimate ranging from 0.2% in the blue up to 0.9% in the red (Zibordi et al., 2004b). In agreement with expectations, the latter values decreased below the intralaboratory measurement repeatability when only data at depths $z_i \geqslant 2$ cm (i.e., $z_i > z_c$) were included in $I_f(\lambda)$ computations.

Monitoring the stability of the source, either by using a shunt resistor in series with the lamp or a radiometer directly looking at the source, is a good practice to ensure detection (with the shunt only) and minimization (with the monitoring radiometer) of any change in the illumination conditions during each measurement sequence. During SIRREX-8, the high stability of the source used at all three laboratories induced differences generally lower than 0.1% in $I_f(\lambda)$ values computed by normalizing and by not normalizing the in-air and in-water irradiance data, with respect to the data from the monitoring radiometer.

Changes in the water temperature that affects the seawater refractive index are also a source of uncertainty. An estimate of the effects induced by a change in the water refractive index associated with a 4 °C variation in water temperature, suggests variations within 0.1% in the $I_f(\lambda)$ value.

All the above sources of uncertainty can be easily minimized by creating a good

point source and monitoring its stability, avoiding collection of data affected by the optical load of collectors, keeping the surface free of particles and slicks, and finally using the purest water possible. Under the same conditions of water purity, the use of seawater is preferred over the use of fresh water because of the slight difference in the refractive index (i.e., approximately 0.5% in the spectral range 400–700 nm). The production of large quantities of pure seawater requires, however, much more effort than the production of large quantities of pure (i.e., milliQ) water, so the requirement of determining highly accurate immersion coefficients for marine radiometers suggests the use of pure water with the application of a correction factor for seawater to account for differences in the refractive indices (Zibordi et al., 2003b).

### *c. Typical values for the OCI-200 series of radiometers*

Spectral $I_f(\lambda)$ values for each of the nine OCI-200 radiometers included in SIRREX-8 and the resulting average $I_f(\lambda)$ values are presented in Fig. 5.4. Although most of the data show good agreement among different sensors, there are notable outliers at 490 and 665 nm, which are associated with one specific radiometer (i.e., the $E_d$ s/n 015). Additional radiometers exhibiting relevant differences from the average are $E_u$ s/n 048 and $E_d$ s/n 050 at 665 nm, and $E_d$ s/n 040 at 683 nm. All these radiometers are the oldest among those included in the experiment, but a visual inspection indicated no significant damage of the collectors.

Removing the $E_d$ s/n 015 data, the dispersion of the $I_f(\lambda)$ values defined by $2\sigma$ reduces 3.0 % and 5.5 % to 0.9 % and 3.0 % at 490 and 665 nm.

Excluding $E_d$ s/n 015 and partitioning the radiometers in two subsets of new ($E_d$ s/n 097, $E_d$ s/n 098, $E_u$ s/n 109, and $E_u$ s/n 130) and old ($E_d$ s/n 040, $E_u$ s/n 048,

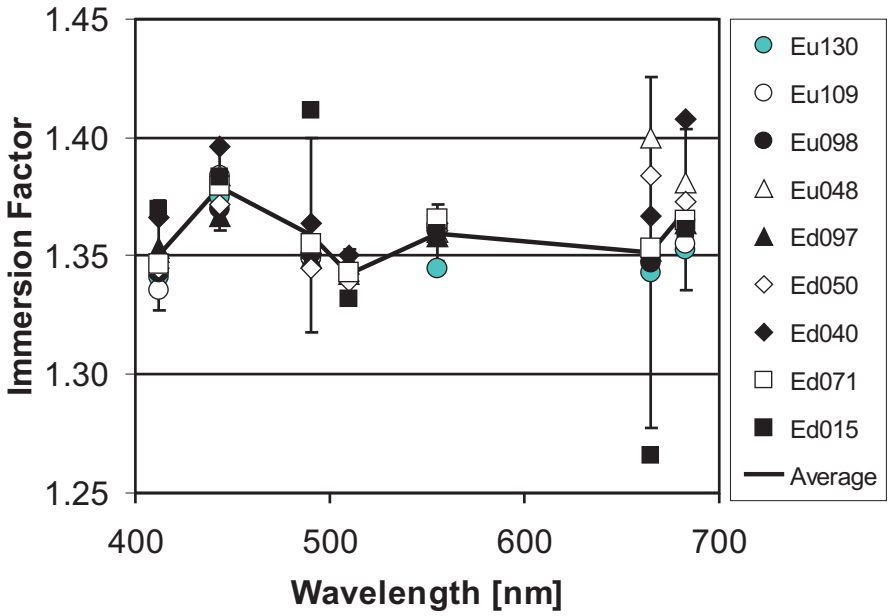


Figure 5.4: The spectral $I_f(\lambda)$ data determined for the nine OCI-200 radiometers included in the SIRREX-8 experiment. The continuous thick line highlights the spectrally averaged $I_f(\lambda)$ values and the bars indicate $2\sigma$ (after Zibordi et al. (2004b)).

$E_d$ s/n 050, and $E_d$ s/n 071) devices, the $I_f(\lambda)$ values show a general increase with aging. Composing the subsets, the average increase from new to older is 0.9%, with individual extreme values up to 2% in the red. Even though any final conclusion cannot be drawn from these results because of the small statistical representation of the samples, it suggests some difference over time in the manufacturing process of collectors or changes of the optical features with aging (probably due to their use), which is more pronounced in the red part of the spectrum (i.e., at 665 and 683 nm).

The typical $I_f(\lambda)$ (i.e, $I_f^T(\lambda)$) values proposed for seawater and computed excluding $E_d$ s/n 015, are given in Tab. 5.1 together with their estimated maximum uncertainties and average $I_f(\lambda)$ values for the old (i.e, $I_f^O(\lambda)$) and new (i.e, $I_f^N(\lambda)$) subsets of radiometers. The maximum estimated uncertainties provided in Tab. 5.1

Table 5.1: The typical immersion coefficients resulting from SIRREX-8 for the OCI-200 series of radiometers. $I_f^O(\lambda)$ data are for the subset of old radiometers, $I_f^N(\lambda)$ data are for the subset of new radiometers, $I_f^T(\lambda)$ data are for the whole set of trusted radiometers (i.e., $E_d$ s/n 015 excluded). The maximum uncertainties are the sum of average intra-laboratory measurement repeatability and $I_f(\lambda)$ dispersion values across the considered OCI-200 radiometers ($E_d$ s/n 015 excluded).

| $\lambda$[nm] | $I_f^O$ | $I_f^N$ | $I_f^T$ | *Maximum Uncertainties* [%] |
|---|---|---|---|---|
| 412 | 1.360 | 1.349 | 1.355 | ±2.1 |
| 443 | 1.388 | 1.381 | 1.385 | ±2.1 |
| 490 | 1.362 | 1.354 | 1.358 | ±1.5 |
| 510 | 1.351 | 1.350 | 1.350 | ±1.4 |
| 555 | 1.371 | 1.363 | 1.367 | ±2.3 |
| 665 | 1.384 | 1.355 | 1.370 | ±3.4 |
| 683 | 1.391 | 1.367 | 1.379 | ±3.1 |

confirm the need for determining the $I_f(\lambda)$ values for each single diffuser when the intended use of radiometers requires an highly accurate absolute calibration.

### *d. Spectral dependence*

Smith (1969), Petzold and Austin (1988) and Mueller (1995) observed an almost linear change of $I_f(\lambda)$ as a function of $\lambda$, with some deviation from linearity in the blue. Such a linear dependence was not observed in the current $I_f(\lambda)$ spectral measurements for the OCI-200 series of radiometers. The explanation for this is given by differences in the optical design of the radiometers involved in the various studies. The instruments analyzed by the aforementioned authors all had a single collector, while the OCI-200 series of radiometers has multiple collectors (one per spectral channel) designed to ensure optimum scattering and absorption performances at a specific center-wavelength. This is supported by the absorbance measurements made

on sample OCI-200 collectors at six different center-wavelengths (412, 443, 490, 555, 665, and 683 nm). The net-absorbance (i.e., the difference between the absorbance measured in transmission mode and the absorbance measured in reflection mode) and the reflection-absorbance (i.e., the absorbance measured in reflection mode), obtained with a dual beam spectrometer equipped with an integrating sphere, are plotted in Fig. 5.5. For each collector, the net-absorbance is quite linear as a function of wavelength, with some change in slope below 420 nm. The different collectors show very large relative differences appearing as an offset with some slight change in slope. Because of this, the spectral shape of the net-absorbance resulting from values associated with each collector (i.e., the encircled numbers in Fig. 5.5) indicates a dependence that is not linear with wavelength.

The comparison of Fig. 5.4 with Fig. 5.5 suggests high values of spectral net-absorbance and low values of spectral reflection-absorbance in correspondence to high $I_f(\lambda)$ values. Starting from this observation, a qualitative explanation of the $I_f(\lambda)$ spectral dependence can be constructed from the approximate model describing the irradiance $E_D(\lambda)$ (see Fig. 5.6) received by the detector on the back of the collector

$$E_D(\lambda) = \{E_e(\lambda)[1 - r_e(\lambda)] + E_c(\lambda)r_c(\lambda)\}T_C(\lambda)[1 - r_b(\lambda)] \tag{5.1.6}$$

where $E_e(\lambda)$ is the irradiance incident at the external surface of the collector, $r_e(\lambda)$ is the external reflectance of the medium–collector interface, $T_C(\lambda)$ is the collector transmittance that only depends on the diffuser material, $r_b(\lambda)$ is the reflectance of the collector–detector interface that does not depend on the refractive index of the external medium, and $E_c(\lambda)r_c(\lambda)$ identifies the diffuse irradiance reflected by the internal collector-medium interface with $r_c(\lambda)$ producing much higher effects than $r_e(\lambda)$ on $E_D(\lambda)$ (Westlake, 1965).

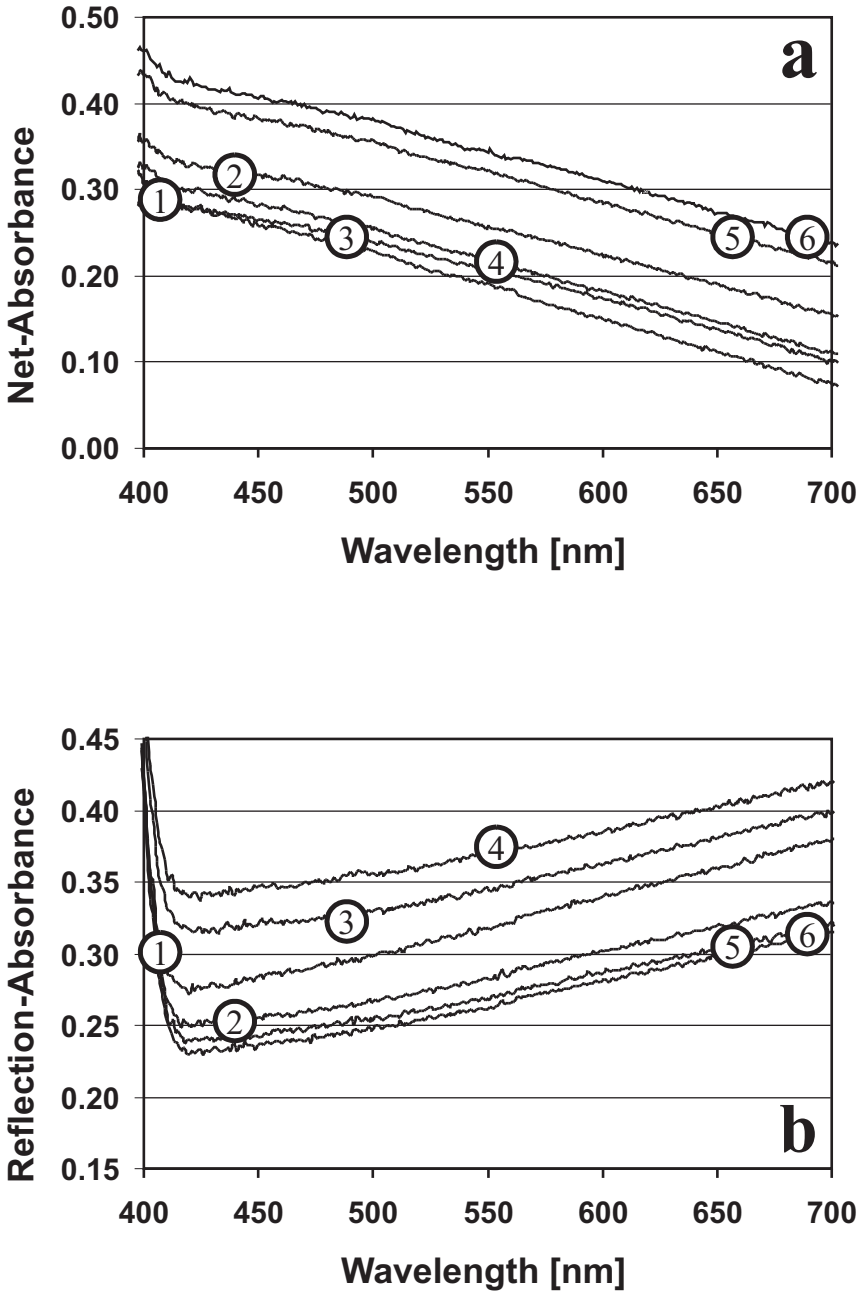


Figure 5.5: The net-absorbance (a) and reflection-absorbance (b) of a sample of OCI-200 collectors. The encircled numbers highlight the nominal center-wavelength: 1=412 nm, 2=443 nm, 3=490 nm, 4=555 nm, 5=665 nm, and 6=683 nm (after Zibordi et al. (2004b)).

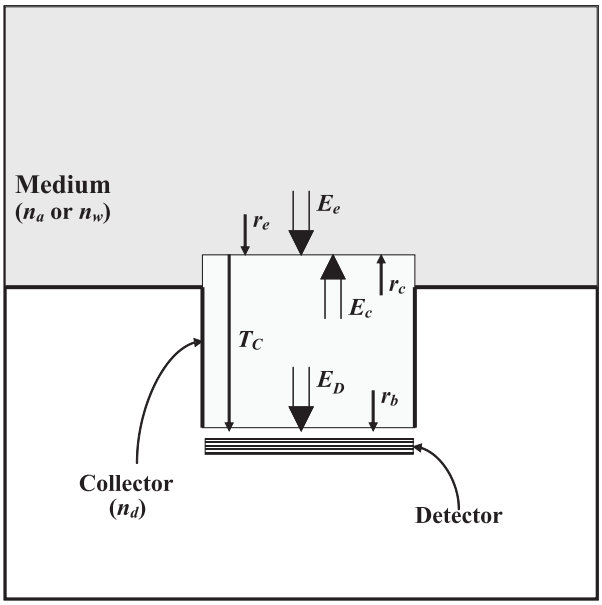


Figure 5.6: Schematic of the reflectance and transmittance elements presented in Eq. 5.1.6 for irradiance sensors (after Zibordi et al. (2004b))

When the medium in contact with the diffuser varies, by neglecting changes in $r_e(\lambda)$, changes in $E_c(\lambda)r_c(\lambda)$ explain variations in $I_f(\lambda)$ (i.e. when $E_c(\lambda)r_c(\lambda)$ increases, $E_D(\lambda)$ increases and $I_f(\lambda)$ decreases). Assuming as a first approximation that $E_c(\lambda)r_c(\lambda)$ is inversely related to the reflection-absorbance, the $I_f(\lambda)$ spectral shape inversely follows the reflection-absorbance spectral dependence. The expected linear dependence with wavelength is very evident in $I_f(\lambda)$ from in-water radiometers equipped with a single diffuser (Mueller, 1995; Smith, 1969). Different, in the case of the OCI-200 radiometers such a spectral dependence is not shown due to the difference in the reflection-absorbance among diffusers optimized for various center-wavelengths, as resulting from slightly different optical characteristics of the various diffusers. These different optical characteristics may create different spectral dependence of $r_e(\lambda)$, $r_b(\lambda)$, $r_c(\lambda)$ and $T_C(\lambda)$ among diffusers and consequently, induce

slightly different spectral dependence of $I_f(\lambda)$ on the reflection-absorbance for each diffuser. This leads to the generic spectral dependence observed between the OCI-200 $I_f(\lambda)$ and the reflection-absorbance spectral values, but does not permit any quantitative comparison between the two as a function of $\lambda$. This finding suggests it is inappropriate, for the OCI-200 series of radiometers, to use the defined typical $I_f(\lambda)$ values to extrapolate data at different center-wavelengths.

## 5.2 Immersion factor for radiance sensors

A comprehensive description of an analytical method for the determination of the immersion factor of radiance sensors was first presented by Austin (1976). His study led to the proposal of a basic relationship adopted by the marine optics community (Mueller and Austin, 1995). However, the applicability of this relationship to actual radiometers and its accuracy, was not previously investigated (or are not reported).

In the last decade various intra- and inter-laboratory experiments addressed the uncertainties of the specific terms relevant to the absolute calibration of radiance and irradiance sensors for ocean color field measurements (for instance see Hooker et al. (2002a); Johnson et al. (1999); Zibordi et al. (2003a)). These activities, however, left the immersion factor for in–water radiance sensors –whose value has been computed for three decades with the basic relationship proposed by Austin (1976) – as a relevant quantity for which the uncertainties were not yet assessed. To fill this gap, Austin's method has been investigated to quantify its accuracy when applied to a class of radiometers extensively used by the ocean optics community.

### 5.2.1 Theoretical determination of $I_f(\lambda)$ for radiance sensors

Equivalent to irradiance sensors, assuming the absolute calibration of a radiance sensor is made in air, the value of the immersion factor $I_f(\lambda)$ is then equal to 1 for in–air measurements and it is greater than 1 for in–water measurements. This corrects for the reduction of the sensor's radiometric response due to the spectral refractive index of water $n_w(\lambda) > n_a$ and resulting from two major effects: (*i*) the relative change in the solid angle field-of-view, and (*ii*) the relative change in reflectance and transmittance of the optical window (hereafter simply called window) of refractive index $n_g(\lambda)$ in contact with the intervening medium (i.e., air or water).

Figure 5.7 displays the schematic of the most relevant reflection and transmission processes contributing to the change of the sensor's response for the class of radiometers considered in this analysis. Specifically, symbols $t_{ag}(\lambda)$ and $r_{ag}(\lambda)$ indicate the spectral transmittance and reflectance of the air-window interfaces while $t_{mg}(\lambda)$ and $r_{mg}(\lambda)$ indicate the spectral transmittance and reflectance of the intervening medium-window interfaces (i.e., the air–window or the water–window). The additional symbols $t_d(\lambda)$ and $r_d(\lambda)$ indicate the spectral transmittance and reflectance of the detector, respectively. The symbol $T_g(\lambda)$ indicates the internal spectral transmittance of the window.

#### *a. Background*

The theoretical method proposed by Austin (1976) for the determination of the immersion factor of radiance sensors was developed assuming a narrow field-of-view (i.e., the instrument field-of-view approaches 0 degrees) and negligible effects of the internal optics (i.e., the reflectance and transmittance of the inner window interfaces

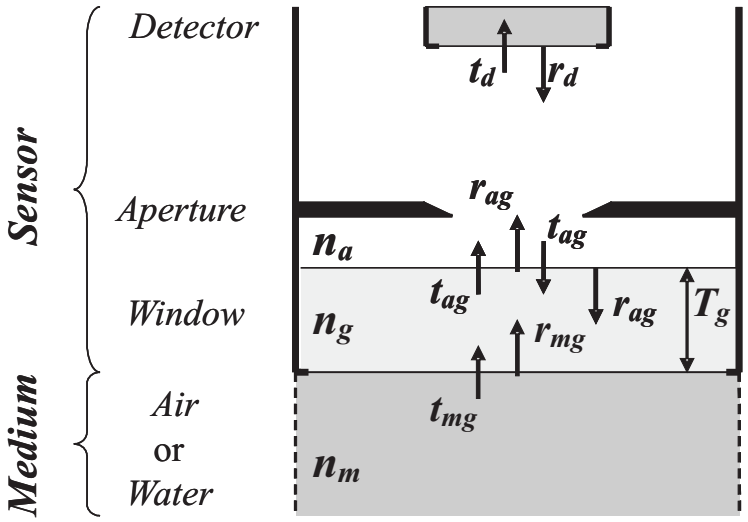


Figure 5.7: Schematic of the major transmission/reflection processes relevant to the determination of $I_f$ for radiance sensors (after Zibordi (2006)).

and of the detector, when considering the sensor illustrated in Fig. 5.7).

With these assumptions, referencing Austin (1976), the spectral radiant flux $\Phi_m(\lambda)$ received by the sensor looking at the radiance $L_m(\lambda)$ detected in a medium $m$ of refractive index $n_m$ through the window of refractive index $n_g(\lambda)$, is given by

$$\Phi_m(\lambda) = L_m(\lambda) A \Omega_m(\lambda) t_{mg}(\lambda) T_o(\lambda) \tag{5.2.1}$$

where $A$ is the active surface area of the detector (assumed non reflective), $\Omega_m(\lambda)$ is the solid angle defined by the sensor half-angle field-of-view $\theta_m(\lambda)$ varying with the refractive index of the medium, $t_{mg}(\lambda)$ is the transmittance of the window in contact with the intervening medium, $T_o(\lambda)$ is the transmittance of any other optical component (assumed invariant regardless of $n_m(\lambda)$) affecting the radiant flux.

The radiant flux can also be written as

$$\Phi_m(\lambda) = \frac{DN_m(\lambda)}{R_\Phi(\lambda)} \tag{5.2.2}$$

where $DN_m(\lambda)$ is the output of the radiometer in digital counts and $R_\Phi(\lambda)$ is the spectral responsivity of the detector in units of Counts $W^{-1}$ (Zissis, 1993), an invariant for the instrument and thus not depending on the intervening medium.

From equations 5.2.1 and 5.2.2, using subscripts $a$ and $w$ for air and water, the in–water radiance $L_w(\lambda)$ can be related to the in–air radiance $L_a(\lambda)$ through

$$L_w(\lambda) = L_a(\lambda)\frac{\Omega_a}{\Omega_w(\lambda)}\frac{t_{ag}(\lambda)}{t_{wg}(\lambda)}\frac{DN_w(\lambda)}{DN_a(\lambda)} \tag{5.2.3}$$

where $t_{ag}(\lambda)$ and $t_{wg}(\lambda)$ are the transmittances of the air–window and water–window interfaces, respectively.

From Eq. 5.2.3 and following its definition, $I_f(\lambda)$ is represented as

$$I_f(\lambda) = \frac{\Omega_a}{\Omega_w(\lambda)}\frac{t_{ag}(\lambda)}{t_{wg}(\lambda)} \tag{5.2.4}$$

where the term $\Omega_a/\Omega_w(\lambda)$ accounts for the change in the field-of-view and $t_{ag}(\lambda)/t_{wg}(\lambda)$ accounts for the change in transmittance of the medium-window interface when operated in water with respect to air.

With the condition of small $\theta_m(\lambda)$, the solid angle field-of-view is approximated by $\Omega_m(\lambda) = (\pi/4)\theta_m^2(\lambda)$ (Slater, 1980), with $m$ indicating either air $a$ or water $w$, and, $\Omega_m(\lambda)$ given in units of sr and $\theta_m(\lambda)$ in units of rad. By then applying Snell's law to the air-water interface with the condition of small $\theta_m(\lambda)$, leading to $\theta_w(\lambda) = \theta_a/n_w(\lambda)$, the correction term for the change in the field-of-view becomes

$$\frac{\Omega_a}{\Omega_w(\lambda)} = n_w^2(\lambda) \tag{5.2.5}$$

known as the $n_w^2$ *law of radiance.*

The transmittance of the medium-window interface, with the assumption of small $\theta_m(\lambda)$ and $n_m(\lambda)$ refractive index of the intervening medium, is given by

$$t_{mg}(\lambda) = 1 - \frac{[n_m(\lambda) - n_g(\lambda)]^2}{[n_m(\lambda) + n_g(\lambda)]^2}. \tag{5.2.6}$$

Using Eq. 5.2.6, the correction term for the change in transmittance of the medium–window interface is given by

$$\frac{t_{ag}(\lambda)}{t_{wg}(\lambda)} = \frac{[n_w(\lambda) + n_g(\lambda)]^2}{n_w(\lambda)[1 + n_g(\lambda)]^2}. \tag{5.2.7}$$

From equations 5.2.5 and 5.2.7, Eq. 5.2.4 can be re-written as

$$I_f(\lambda) = \frac{n_w(\lambda)[n_w(\lambda) + n_g(\lambda)]^2}{[1 + n_g(\lambda)]^2}. \tag{5.2.8}$$

Equation 5.2.8 is adopted by the ocean optics community for the determination of the immersion factor of in–water radiance sensors.

***b. Model revision***

To determine the uncertainties affecting $I_f(\lambda)$, when applied to actual radiance sensors having optical design matching the schematic in Fig. 5.7, the reflectance $r_{ag}(\lambda)$ and $r_{wg}(\lambda)$ of the inner window interface (where $r_{ag}(\lambda) = (1 - t_{ag}(\lambda))$ and analogously $r_{wg}(\lambda) = (1 - t_{wg}(\lambda))$ ) and the reflectance $r_d(\lambda)$ of the detector, were included in the revision of Austin's model. Equation (5.2.4) was then rewritten as

$$I_f(\lambda) = \frac{\Omega_a}{\Omega_w(\lambda)} \frac{t_{ag}(\lambda)}{t_{wg}(\lambda)} \frac{T_{ag}(\lambda)}{T_{wg}(\lambda)} \frac{T_{ad}(\lambda)}{T_{wd}(\lambda)} \tag{5.2.9}$$

where, without making explicit the dependence on $\lambda$,

$$T_{mg} = t_{ag} T_g + r_{ag} r_{mg} t_{ag} T_g^2 \tag{5.2.10}$$

indicates the additional transmittance of those optical components affecting the radiant flux received by the detector when the first order reflectance of the inner window surfaces is accounted for (with $m$ indicating either $a$ or $w$), and

$$T_{md} = t_d + r_d r_{ag} t_d + r_d t_{ag}^2 r_{mg} T_g^2 t_d + r_d t_{ag}^2 r_{ag} r_{mg}^2 T_g^4 t_d \tag{5.2.11}$$

indicates the further additional transmittance of those optical components affecting the radiant flux received by the detector when its first order reflectance $r_d$ is accounted for.

Using Eq. 5.2.10, after simplification, the term $T_{ag}/T_{wg}$ becomes

$$\frac{T_{ag}}{T_{wg}} = \frac{1 + T_g r_{ag}^2}{1 + T_g r_{ag} r_{wg}} \tag{5.2.12}$$

and similarly using (5.2.11), the term $T_{ad}/T_{wd}$ becomes

$$\frac{T_{ad}}{T_{wd}} = \frac{1 + r_d r_{ag} + r_d t_{ag}^2 r_{ag} T_g^2 + r_d t_{ag}^2 r_{ag}^2 T_g^4}{1 + r_d r_{ag} + r_d t_{ag}^2 r_{wg} T_g^2 + r_d t_{ag}^2 r_{ag} r_{wg} T_g^4}. \tag{5.2.13}$$

For an ideal sensor with $r_d = 0$ the term $T_{ad}/T_{wd} = 1$. It is to be noted that the high power terms in Eq. 5.2.13, have a weak effect on the determination of $I_f(\lambda)$ and they can be neglected for practical uses of Eq. 5.2.9.

### *c. Comparison between theoretical determinations*

The adoption of Eq. 5.2.9 in alternative to Eq. 5.2.8 was investigated in the 400-700 nm spectral range for Fused Silica windows (i.e., synthetic molten amorphous quartz glass windows currently used in most of the in–water radiometers) with $T_g(\lambda)$=0.99 and assuming $r_d(\lambda)$=0.15. Under the condition of small angle approximation (i.e., with $\Omega_a/\Omega_w(\lambda) = n_w^2(\lambda)$), the comparison showed an increase of 0.6 % in $I_f(\lambda)$ computed with the newly proposed relationship, with approximately 85% of the increase due to the detector reflectance. This result indicates that the determination of $I_f(\lambda)$ through Eq. 5.2.8 for radiometers with non-negligible reflectance of the detector, may lead to an appreciable negative bias in the absolute calibration of the in–water radiance data.

By accounting for the actual solid angle field-of-view computed from

$$\Omega_m(\lambda) = 2\pi[1 - \cos\theta_m(\lambda)] \tag{5.2.14}$$

with $\theta_m(\lambda)$ half-angle field-of-view in the medium $m$ (where $m$ indicates either $a$ or $w$), and additionally determining $r_{mg}(\lambda)$ and $t_{mg}(\lambda)$ by averaging their directional values over the solid angle $\Omega_m(\lambda)$, a spectrally averaged decrease of approximately 0.2% in $I_f(\lambda)$ with respect to the small angle approximation (largely due to the exact computation of $\Omega_m(\lambda)$) was observed. This leads to a net negative difference of approximately 0.4% between the $I_f(\lambda)$ values determined with the relationships linked to the basic and the extended sensor models, for the considered class of radiometers. The immediate conclusion from this result based on a theoretical analysis is that, for the specific class of sensors considered, the current theoretical relationship used for the determination of $I_f(\lambda)$ is still adequate for most of the ocean color applications which commonly face an overall uncertainty of approximately 4-5% in the determination of the water-leaving radiance (see Chapter 6).

### 5.2.2 Characterization of $I_f(\lambda)$ for radiance sensors

In order to assess the validity of the revised relationship for the theoretical computation of the immersion factor, a method for experimentally determining $I_f(\lambda)$ was conceived and applied to various radiometers from the same class of in–water instruments manufactured with optical windows having different refractive indices $n_g(\lambda)$. The method relies on performing in–water and in–air radiance measurements of a stable source, keeping constant the sensor-source distance.

The schematic of the measurement system realized for the experimental determination of the immersion factor is shown in Fig. 5.8. It is composed of: ($i$) a water

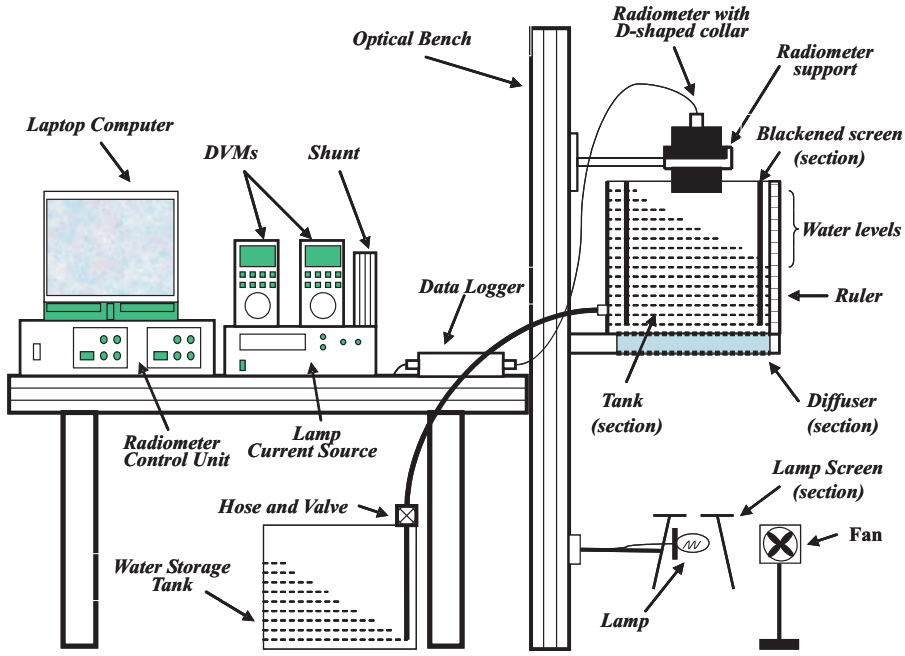


Figure 5.8: Set-up used for the experimental characterization of $I_f(\lambda)$ for radiance sensors (after Zibordi (2006)).

vessel made of Plexiglas with the lateral walls internally screened with a cylindrical tube painted dull black (so called *blackened screen*); (*ii*) a support to hold the radiometer within the vessel with the optics facing the source; (*iii*) a diffuse light source constituted of a diffuser located in air just underneath the water vessel and illuminated from below by a 1000 W tungsten-halogen lamp. The diffuser is made of a multilayer of three white flashed opal glasses manufactured by Shott AG (Grünenplan, Germany) and one blue glass. The blue element is included to reduce the light flux in the green and red part of the spectrum and ultimately to make more comparable the relative output of the radiometer at the different channels (this solution compensates for the relatively higher flux of the lamp in the green-red with respect to the blue, and makes the spectral flux distribution of the diffuse source more similar to that of the sun for which the gain setting of radiometers is optimized). The lamp is screened to

reduce the background light, and an adjustable aperture is used to optimize the size of the light cone illuminating the diffuser. All the various components of the measurement system are installed on a vertical optical bench to facilitate the accurate repositioning of each part at different distances. The stability of the source is tracked by monitoring the voltages across its terminals and across a precision shunt in series with it. The water depth reading is made through a ruler fixed inside the vessel and located between the Plexiglas wall and the blackened screen. A storage tank is used to temporarily accumulate the water for its reuse during successive measurement sequences. The employ of pure water (Milli-Q) is recommended by the need to perform measurements in a very reproducible manner and using a medium with well defined optical properties (i.e., $n_w(\lambda)$).

***a. The measurement method***

The quantities relevant to the experimental determination of $I_f(\lambda)$ are shown in Fig. 5.9 together with a schematic of the water vessel. Specific geometric quantities are the distance between the window and the diffuser, $d$, and the distance between the window and the water surface, $z_i$. Specific physical quantities are the water transmittance $T_w(d, z_i, \lambda)$ in the pathlength $d - z_i$, the radiance of the source, $L_p(\lambda)$, and, the transmittance of the air-water interface, $t_{aw}(\lambda)$.

***b. $I_f$ determination***

The spectral subsurface radiance, $L_p(0^-, \lambda)$, is determined from data taken with the instrument submersed in the water at distance $d$ from the source, computed with $I_f(\lambda)$ =1, corrected for the average background signal and averaged over the interval $\Delta t$. The above-water radiance value, $L_p(0^+, \lambda)$, is computed as the intercept of the

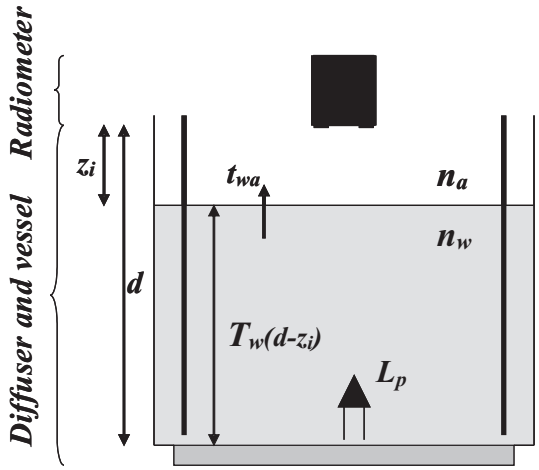


Figure 5.9: Schematic of the water-vessel and of the major reflection/transmission processes relevant to the determination of $I_f(\lambda)$ (after Zibordi (2006)).

least squares regression – as a function of $z_i$ – of the $L_p(i,\lambda)$ values given by

$$L_p(i,\lambda) = L_p(d,z_i,\lambda)\frac{T_w\,(d,0,\lambda)}{T_w\,(d,z_i,\lambda)} \tag{5.2.15}$$

where $L_p(d,z_i,\lambda)$ is determined from data taken with the radiometer operated in air with water layers of depth $d - z_i$, corrected for the average background signal, and averaged over the interval $\Delta t$. Thus $L_p(i,\lambda)$ indicates values of $L_p(d,z_i,\lambda)$ normalized with respect to the in–water optical path-length $d$ (i.e., at $z_i = 0$) using the term $T_w(d,0,\lambda)/T_w(d,z_i,\lambda)$ (this term differs most from 1 in the red).

The transmittance $T_w(d,z_i,\lambda)$ is computed according to

$$T_w(d,z_i,\lambda) = e^{-c(\lambda)(d-z_i)} \tag{5.2.16}$$

where $c(\lambda)$ is the spectral beam attenuation coefficient of pure water resulting from the sum of the absorption (Pope and Fry, 1997) and scattering (Morel, 1974) coefficients. The determination of $T_w(d,z_i,\lambda)$ using $c(\lambda)$ leads to an overestimate of the attenuation in the blue and green spectral regions where the scattering is more sizeable than the

absorption. However, due to the small optical pathlength, the use of Eq. 5.2.16 does not have any appreciable effect in the computation of $I_f(\lambda)$.

The least squares regression of $L_p(i,\lambda)$ values applied in the computation of $L_p(0^+,\lambda)$, in alternative to the use of a single $L_p(i,\lambda)$ value, minimizes the uncertainties in $L_p(0^+,\lambda)$ due to the inaccuracy in $T_w(d,z_i,\lambda)$ and, the inhomogeneity or deviation from the Lambertian response of the diffuse light source. However, $L_p(0^+,\lambda)$ could be computed from the least-squares fit – as a function of $z_i$ – of the $L_p(d,z_i,\lambda)$ log-transformed values. This solution, different from that applied in the current analysis to fully account for the involved physical processes, does not require the a-priori knowledge of $T_w(d,z_i,\lambda)$ to determine $L_p(0^+,\lambda)$.

Accounting for the decrease in radiance from below– to above–water quantified by $[\Omega_w(\lambda)/\Omega_a]t_{wa}(\lambda)$, the experimental immersion factor is given by

$$I_f(\lambda) = \frac{L_p(0^+,\lambda)}{L_p(0^-,\lambda)} \frac{\Omega_a}{\Omega_w(\lambda)} \frac{1}{t_{wa}(\lambda)}. \tag{5.2.17}$$

Figure 5.10 displays data at 665 nm obtained from a sequence of above– and in–water radiance measurements processed according to the proposed scheme. The data, presented in relative units as a function of the distance between the optical window and the water surface $z_i$, depict the actual time averaged measurements $L_p(d,z_i,\lambda)$ and the corresponding $L_p(i,\lambda)$ values used for the determination of the above–water value, $L_p(0^+,\lambda)$. The data at $z_i$=0 indicate the values used for the computation of $I_f(\lambda)$: (*i*) the above-water $L_p(0^+,\lambda)$ value; and, (*ii*) the subsurface $L_p(0^-,\lambda)$ value multiplied by $(\Omega_w(\lambda)/\Omega_a)t_{wa}(\lambda)$ to account for the decrease in radiance from below– to above–water. The plot in Fig. 5.10, exhibiting almost a constant value for the $L_p(i,\lambda)$ data, qualitatively demonstrates the appropriateness of the applied processing.

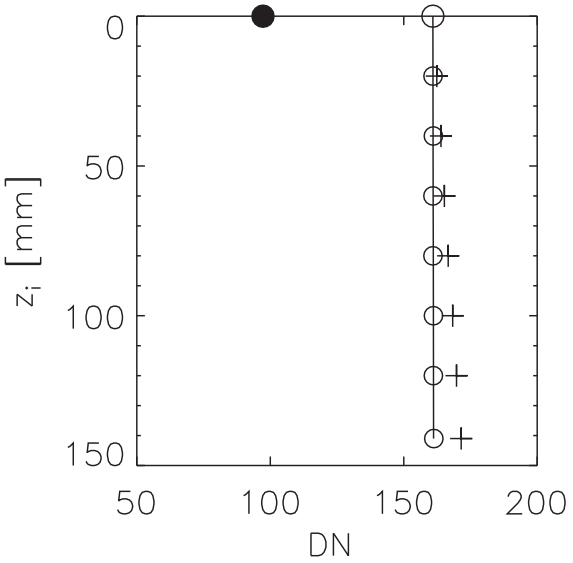


Figure 5.10: Data in relative units (DN) from a measurement sequence at 665 nm, as a function of the distance of the optical window from the water surface $z_i$, relevant to the determination of $I_f$ are $L_p(0^-)(\Omega_w/\Omega_a)t_{wa}$ shown by symbol ●, $L_p(0^+)$ shown by symbol ◯, actual time averaged $L_p(d,\, z_i)$ measurements shown by symbols + and corresponding $L_p(i)$ values shown by symbols ○ (after Zibordi (2006)).

### 5.2.3 Discussion on $I_f(\lambda)$ for radiance sensors

The assessment of the new relationship (i.e., Eq. 5.2.9) proposed for the computation of $I_f(\lambda)$, was made by comparing theoretical and experimental values determined with radiometers having optical design matching with the schematic in Fig. 5.7.

Experimental $I_f(\lambda)$ values were determined with OCR-200 and OCR-507 seven channel radiometers largely used within the ocean optics community. These two series of radiometers, which mostly differ by their output (analog for the OCR-200 and digital for the OCR-507) and size (diameter of 3.5 inches for the OCR-200 and of 2.5 inches for the OCR-507), have equivalent optics and detectors, and are considered to belong to the same class of in–water optical instruments.

The OCR-200 radiometers have windows made of Optical Crown Glass, or Fused

Silica when manufactured after mid-2001 (the use of Fused Silica was mostly introduced to support applications in the ultraviolet spectral region). The OCR-507 radiometers all have windows made of Fused Silica. In addition to the window (serving all sensors on each radiometer), the optics of an individual sensor is composed of: *i.* a detector comprising an interference filter with 10 nm spectral band in the 400-700 nm range; and *ii.* an aperture that, in conjunction with the active circular area of the detector, defines the solid angle field-of-view. It is considered a reasonable assumption that all the apertures of a single radiometer, symmetrically distributed in a circular area of approximately 2 cm radius, are equal in air with a half-angle field-of-view $\theta_a$ of 13 degrees. This defines an in–water half-angle field-of-view $\theta_w(\lambda)$ of approximately 10 degrees, slightly varying with $n_w(\lambda)$ as a function of wavelength.

The sample radiometers included in the study were manufactured in the period 1995-2002. They comprise both Optical Crown Glass and Fused Silica windows and have the same nominal center-wavelengths 412, 443, 490, 510, 555, 665 and 683 nm. The relatively small number of radiometers used for the experimental determination of the immersion factor was supported by: ($i$) the results obtained from the comparison of the relationships derived from the basic and extended sensor models showing that, for the considered case study and for a given medium, the values of $I_f(\lambda)$ almost entirely (i.e., by more than 99%) depend on the refractive index of the window; and ($ii$) the high precision in manufacturing optics implying a high repeatability of the optical properties of commercial windows. This suggested that, unlike previous studies on the immersion factor of irradiance sensors which required a relatively large number of instruments to reach any general conclusion due to differences in the geometric and optical features of basic components (Zibordi et al., 2004d), a few instruments

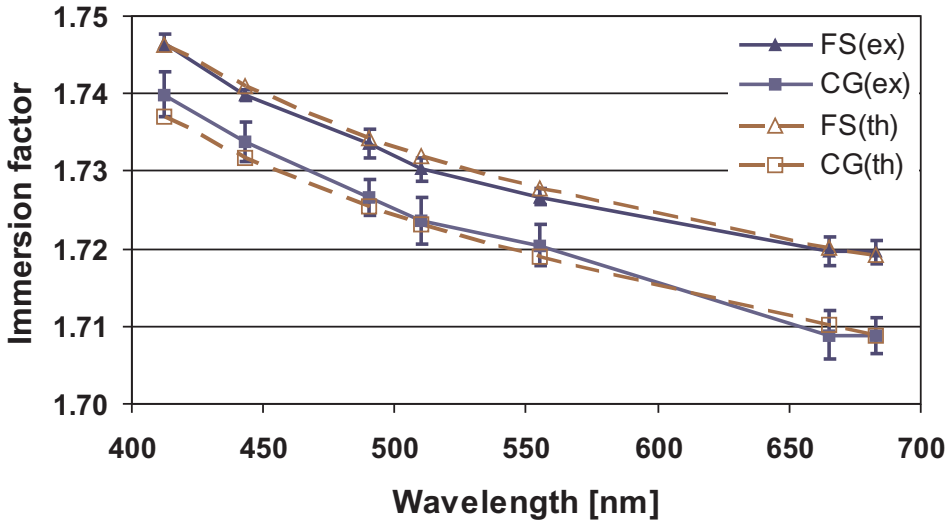


Figure 5.11: Comparison of theoretical (th) and experimental (ex) $I_f$ values for OCI-200 radiometers having Fused Silica (FS) and Optical Crown Glass (CG) windows (after Zibordi (2006)).

can satisfy the objective of assessing the newly proposed relationship to theoretically compute $I_f(\lambda)$ for the considered radiance sensors.

A comparison of results for the radiometers considered is summarized in Fig. 5.11 which plots: *i.* theoretical immersion factors computed with Eq. 5.2.9 for sensors having 13 degrees in–air half–angle field–of–view, windows made of Optical Crown Glass or Fused Silica, and detector reflectance $r_d(\lambda)$=0.15; and *ii.* average experimental immersion factors determined with the OCR-200 s/n 010 and OCR-200 s/n 051 with Optical Crown Glass windows, and, with the OCR-200 s/n 104 and OCR-507 s/n 025 with Fused Silica windows.

The repeatability of the experimental determinations of the immersion factors, indicated by error bars in Fig. 5.11 and quantified through the average of two times the variation coefficients of independent experimental $I_f(\lambda)$ values for the sensors with

windows made of the same material, $\xi(\lambda)$, exhibit larger values for the radiometers with Optical Crown Glass windows (showing spectrally averaged values of 0.32%), when compared to those of radiometers with Fused Silica windows (showing spectrally averaged values of 0.18%). This could be explained by imperfections in the windows caused by extensive field use, making less efficient the removal of bubbles in front of the window during the measurement sequences and thus leading to a decrease in the repeatability of the experimental $I_f(\lambda)$ values.

The percent differences between theoretical and experimental $I_f(\lambda)$, exhibit larger values (higher than 0.1% in the blue) for the radiometers with Optical Crown Glass windows with respect to those with Fused Silica windows (typically within 0.05%). This can probably be explained by a less tightly controlled refractive index and homogeneity of the Optical Crown Glass when compared to Fused Silica.

These results suggest the adequacy of revised relationships based on specific sensor models for the determination of $I_f(\lambda)$. They also confirm that immersion factors of radiance sensors (as opposed to irradiance sensors) can be determined with theoretical relationships and can be applied to classes of radiomters.

***a. Accuracy of the theoretical determination***

When considering Eq. 5.2.9 and its terms, the accuracies of $r_d(\lambda)$, $T_g(\lambda)$, $n_g(\lambda)$ and of water temperature affecting $n_w(\lambda)$, are the major elements that may perturb the theoretical determination of $I_f(\lambda)$. A sensitivity analysis was made on $I_f(\lambda)$ computed for pure water at 22 °C, Fused Silica window and detector with reflectance $r_d(\lambda)$=0.15. This analysis showed that changes of 0.05 (absolute) in $r_d(\lambda)$, 1% in $n_g(\lambda)$, 1% in $T_g(\lambda)$ and 1 °C in the water temperature, produce spectrally averaged uncertainties of approximately 0.15%, 0.11%, 0.01% and 0.02%, respectively. These

uncertainties lead to a quadrature sum of 0.19%, taken as an estimate of the average uncertainty for the theoretical $I_f(\lambda)$ values produced with Eq. 5.2.9.

***b. Accuracy of the experimental determination***

The accuracy of the experimental determination of $I_f(\lambda)$ is mostly linked to the possibility of creating a homogeneous, Lambertian and stable diffuse light source.

The difficulty to create an ideal diffuse source inside a water vessel increases with the size of the source. A solution was proposed by Austin and Petzold (1982) for the optical characterization of the in–water response of a radiometer based on an irradiance collector coupled with a Gershun tube. In that case, a reflectance plaque was positioned at the bottom of a tank and illuminated from above with multiple lamps operating in air. This setup, however, makes it difficult to obtain an accurate quantification of the reflection and transmission processes occurring in the tank and at the air-water interface. The alternative method proposed here (see also Zibordi (2006)) simplifies the problem by using a Plexiglas vessel and illuminating a diffuser placed in air just underneath the vessel, with a lamp located at some distance from it. With this configuration, given the symmetry of the measurement system (lamp, diffuser, vessel and the radiometer's support), any significant inhomogeneity and non-Lambertian response of the source may lead to a non-linear decrease in brightness from the center toward the edge of the diffuser. As a result, the decrease of the measured radiance with an increase of the area observed by the sensor (i.e., on $z_i$ decrease) would lead to an overestimation of $I_f(\lambda)$. This was quantified from an estimate of the radiance decay with an increase of the observed area. Specifically, the decay was determined from $L_p(d, z_i, \lambda)$ data taken with a fixed water level at progressively increased distances $d$ (see Fig. 5.9 ). These data led to the quantification of maximum

changes in $L_p(i, \lambda)$, varying from 0.8 to 1.4% as a function of wavelength over the range of areas observed by the sensors during a measurement sequence. The correction of sample measurements for this uncertainty yield a spectrally averaged overestimate of 0.05% in $I_f(\lambda)$. This result, however, could not be supported by systematic differences in the $I_f(\lambda)$ values determined with $d$=26 cm, $d$=30 cm and $d$=34 cm, and thus with different areas observed by the sensors on the diffuser. This can probably be explained by a relatively small number of characterizations performed with different distances $d$, added to a variability of the experimental $I_f(\lambda)$ values significantly larger than the bias due to the inhomogeneity and non-Lambertian response of the source.

The stability of the source was tracked by recording the voltages across the lamp and the shunt, mostly to flag measurement sequences affected by appreciable variations in $L_p(\lambda)$. This, however, did not support any quantification of the uncertainties due to the instability of the source. These uncertainties were empirically assumed lower than 0.1% in agreement with the analysis produced in the companion study focused on the characterization of the immersion factor of irradiance sensors (see previous section) and making use of a lamp and power supply identical to those applied for the characterization of $I_f(\lambda)$ for radiance sensors.

In addition to the inhomogeneity, non-Lambertian response and instability of the light source, other relevant uncertainties affecting the experimental determination of $I_f(\lambda)$ are: (*i*) the reproducibility of $L_p(0^-, \lambda)$, linked to the efficiency in removing small bubbles in front of the window; (*ii*) the perturbation induced on the light source by the radiometer immersed in the water vessel; (*iii*) changes in the water refractive index due to temperature variations during successive measurements.

The reproducibility of $L_p(0^-, \lambda)$ was explored with sequential in–water measurements made with an OCR-200 radiometer. Assuming no significant change in the source (as shown by the shunt and lamp voltages), the measurements exhibited a spectrally averaged $\xi$ value of 0.08%, affecting the derived $I_f(\lambda)$ by an equal amount. It is recalled that the radiometer used for the reproducibility analysis was new and never deployed before. It is to be expected that for optics subject to an extensive use and thus with windows very likely exhibiting imperfections at the external surface, the latter uncertainty may slightly increase due to a less efficient removal of bubbles.

The uncertainty in $I_f(\lambda)$ resulting from perturbations in the radiance field due to an immersed radiometer with a fully absorbing faceplate, was estimated from the ratio between the in-water subsurface radiance with and without the radiometer positioned just below the water surface. Specifically, this was estimated with $[1 + T_w(d, 0, \lambda) r_{wa(\lambda)} r_p(\lambda)]/[1 + T_w(d, 0, \lambda) r_{wa(\lambda)} r_p(\lambda) f_f]$ which accounts for the first order reflectance of the water subsurface area delimited by the vessel. This area has reflectance $r_{wa}$ for the fraction $f_f$ not obstructed by the radiometer and ideally null for the fraction covered by the radiometer ($r_p$ is the reflectance of the diffuser and varies linearly from 0.66 at 400 nm down to 0.62 at 700 nm). This perturbation in $L_p(0^-, \lambda)$ leads to an underestimate of 0.1% in the $I_f(\lambda)$ values determined with the OCI-200 radiometers and of 0.04% in those determined with the OCR-507s.

The uncertainty associated with changes in the water refractive index during successive measurements was estimated with a variation of 1 °C in the water temperature. This leads to a spectrally averaged uncertainty lower than 0.02% in $I_f(\lambda)$.

All the former uncertainties lead to a quadrature sum of 0.17%, taken as the typical uncertainty associated with the experimental determination of $I_f(\lambda)$.

Table 5.2: Theoretical $I_f(\lambda)$ values determined for radiometers with windows made of Fused Silica, 13 degrees in-air half-angle field-of-view and $r_d(\lambda)$=0.15, for pure water at 20 $^\circ$C with salinity $S$ of 0 and 35 psu. The values are provided as a function of wavelength $\lambda$ every 20 *nm* in the 400-500 nm range and every 40 *nm* in the 500-700 nm range (after Zibordi (2006)).

| $\lambda$ [nm] | $n_g$ | $I_f$ (S=0 psu) | $I_f$ (S=35 psu) |
|---|---|---|---|
| 400 | 1.470 | 1.752 | 1.770 |
| 420 | 1.468 | 1.748 | 1.765 |
| 440 | 1.466 | 1.745 | 1.762 |
| 460 | 1.465 | 1.741 | 1.758 |
| 480 | 1.464 | 1.739 | 1.755 |
| 500 | 1.462 | 1.736 | 1.753 |
| 540 | 1.460 | 1.732 | 1.748 |
| 580 | 1.459 | 1.728 | 1.745 |
| 620 | 1.457 | 1.726 | 1.742 |
| 660 | 1.456 | 1.723 | 1.739 |
| 700 | 1.455 | 1.721 | 1.737 |

### *c. Reference values*

The agreement observed between the theoretical and experimental $I_f(\lambda)$ values determined for various OCR-200 and OCR-507 radiometers with both types of windows, confirms that $I_f(\lambda)$ can be theoretically computed for the considered radiance sensors. As a consequence, $I_f(\lambda)$ values computed with the newly proposed theoretical relationship are given in Tab. 5.2 for the class of radiometers analyzed in this study. The reference $I_f(\lambda)$ values are provided at regular wavelength increments in the 400-700 nm range for both fresh (salinity of 0 psu) and sea (salinity of 35 psu) water at 20 °C. Values of $I_f(\lambda)$ at any different wavelength within the given spectral range, can then be extrapolated. By neglecting the dependence of $n_w(\lambda)$ on water particles (i.e., phytoplankton and detritus) and on pressure (i.e., assuming applications restricted to

within depths of a few tens of meters below the water surface) a sensitivity analysis showed that, over the temperature range of 0-30 °C (with $n_g(\lambda)$ independent of temperature) and the salinity range of 0-40 psu, $I_f(\lambda)$ varies by approximately 0.4% and 1.1%, respectively (Zibordi, 2006). These variations, not appreciably depending on wavelength in the 400-700 nm range, can be quantified by changes of approximately -0.013% per °C and 0.027% per psu within the ranges considered. This suggests that $I_f(\lambda)$ can be determined for salinities and temperatures different from those identified in Tab. 5.2, by simply applying wavelength independent correction factors. A verification of such a scheme showed the capability of determining $I_f(\lambda)$ in the 400-700 nm range for any realistic seawater salinity and temperature with differences typically lower than 0.1% with respect to the values computed with Eq. 5.2.9.

### *d. Characterization of $I_f(\lambda)$ for RAMSES radiometers*

In view of verifying the applicability of the experimental method for the determination of $I_f(\lambda)$ for radiance sensors having design different from the OCR-200 or OCR-507, RAMSES hyper-spectral radiometers manufactured by TriOS (Oldemburg, Germany) were characterized (Zibordi and Darecki, 2006). Results obtained from RAMSES-MRC-VIS radiance sensors having 20 degrees in air full-angle field-of-view showed a spectrally averaged bias of 2.4% in the theoretical $I_f(\lambda)$ values determined just using the refractive indices of the medium and of the optical window (i.e., applying Eq. 5.2.8). This bias exhibited values of 0.8% for the RAMSES-ARC-VIS radiance sensors having a 7 degree in air full-angle-field of view (i.e., uncertainty slightly higher than the 0.4% observed for the OCI-200). These results suggest the need for experimentally determining $I_f(\lambda)$ for each series of in–water radiance sensors to assess the existence of appreciable biases with respect to values determined theoretically.

## 5.3 Summary

The recent studies on the characterization of the immersion factor $I_f(\lambda)$ of irradiance sensors demonstrated the possibility of achieving an uncertainty in measurement repeatability on the average better than 0.6% (expressed by $2\sigma$). Inter-laboratory comparisons showed relative average uncertainties generally within 0.6% (absolute), while the method precision showed average uncertainty values of 1.2%. The variability in $I_f(\lambda)$, within a sample of nine OCI-200 radiometers covering about 10% of the instrument production from 1994 to 1999, showed average dispersion values on the order of 2% with spectral values as high as 5%. An attempt at producing typical $I_f(\lambda)$ values for the OCI-200 series of radiometers, showed maximum uncertainties spectrally varying from 1.4% to 3.4%. This confirms the need for ensuring a full spectral characterization of $I_f(\lambda)$ values for each in-water radiometer leading to an accurate absolute determination of irradiances (i.e., $E_u(z,\lambda)$, $E_d(z,\lambda)$) and of derived quantities (i.e., $Q_n(z,\lambda)$ and $R(z,\lambda)$).

An evaluation of methods for the experimental determination of the immersion factor for irradiance sensors suggested the need for using pure (i.e., milliQ) water, only possible through the design of a specialized water vessel, to increase both the precision and accuracy of measurements. The successive application of correction factors accounting for differences in the refractive indices between pure seawater and pure water, is required (Zibordi et al., 2003b)

A revised relationship for the determination of the immersion factor for radiance sensors – accounting for the actual solid angle field-of-view, and the reflectance and transmittance of the external and internal optical components – showed an underestimation of approximately 0.4% for $I_f(\lambda)$ computed with the basic equation, for

OCR-200 and OCR-507 radiometers having optical window made of Fused Silica, 13 degrees in air half-angle field-of-view and detector with reflectance of 0.15. This result was supported by experimental $I_f(\lambda)$ data, on the average differing by less than 0.1% from those computed with the revised theoretical relationship. An uncertainty analysis showed that both the experimental and the theoretical $I_f(\lambda)$ values determined with the newly proposed methods, have an estimated uncertainty lower than 0.2%. Additional analysis (Zibordi and Darecki, 2006) based on radiometers with different optics design, showed that the difference between $I_f(\lambda)$ determined experimentally and computed with the basic equation may become quite large (i.e., of the order of a few percent). This suggests that the experimental characterization of $I_f(\lambda)$ for sample radiance sensors of each series should become part of their quality assurance process to assess the deviation of the immersion factor from its theoretical determination.

A sensitivity analysis quantifying $I_f(\lambda)$ dependence of radiance sensors on seawater refractive index as a function of temperature and salinity, showed variations up to 0.4% and 1.1% within the 0-30 °C and 0-40 psu ranges, respectively. A scheme for the minimization of this source of uncertainty, based on wavelength independent corrections and reference immersion factors computed in the 400-700 nm range for a fixed salinity and temperature, was proposed allowing for the determination of $I_f(\lambda)$ for any realistic seawater temperature and salinity with an uncertainty increased by less than 0.1% with respect to that affecting theoretical data computed with the appropriate seawater refractive index.

# Chapter 6

# Measurement Protocols

*Of all the techniques used in ocean remote sensing, the observation of the ocean color from satellites is perhaps the most easily understood in concept, because it is the most similar to our own personal remote sensing device – the human eye.*

*Ian Robinson, 2004.*

[1]In recent years, a variety of fixed depth systems based on moorings (Antoine and Guevel (2000); Clark et al. (1997); Pinkerton and Aiken (1999)), profilers based on winched, crane and free-fall systems (Dierssen and Smith (1996); Hooker and Maritorena (2000); Zibordi et al. (1999)), and above-water systems relying on various deplyment platforms (Hooker et al. (2002b); Zibordi et al. (2002a)), were developed for the production of optical radiometric data supporting both oceanography and more specifically remote sensing applications.

Instruments on moorings can sample almost continuously in time, but their vertical resolution is quite poor (generally restricted to 2-3 discrete depths). In addition,

[1]The material presented and discussed in this chapter was mostly published in Zibordi et al. (2004a,c).

their continuous operation makes the in-water sensors very susceptible to bio-fouling, which restricts to oligotrophic regions their unattended use over relatively long time periods (generally on the order of weeks).

Winched, crane and free-fall systems provide continuous in-water profiles and permit a comprehensive characterization of the water column, but their use is generally linked to research vessels. Although oceanographic cruises can provide data with a significant spatial extent, their temporal capabilities are restricted to relatively short time periods ranging from days to a few weeks.

Above-water systems cannot provide any information on the water column, nevertheless they are not subjected to in-water sampling problems. Thus autonomous above-water systems are a valid alternative to in-water moorings and may serve as a complement to regular oceanographic cruises for the production of time series of water-leaving radiance data.

The large potential of above–water radiometry for supporting marine applications and a paucity of investigations on the related measurement methods, since the middle 1990s drove the need for new extensive research which led to the definition of the present state of the art. Developments in above–water radiometric methods combined with consolidated in-water methods are presented in this chapter largely relying on investigations previously performed and published by the author. In addition, using uncertainty analysis given in separate chapters, the equivalence of in– and above–water measurements generated by these methods is demonstrated for water–leaving radiance and the derived normalized water-leaving radiance.

## 6.1 In–water method

Current in–water radiometry based on the use of profiles of data (both continuous and discrete), mostly relies on the early method documented by Smith and Baker (1984, 1986) which assumes a linear decay with depth of the log-transformed radiometric data within a given extrapolation interval, and negligible wave focussing effects. The method was specifically proposed for radiometric profiles collected in oceanic waters which benefit from the absence of significant gradients in the vertical distribution of optically significant components within the upper sea layers. This makes possible to exclude from the extrapolation, data taken within the first few meters below the surface where the wave perturbations are the largest. However, the same assumption cannot be applied to profile data collected in coastal waters because of the likely occurrence of gradients in the vertical distribution of optically significant materials in the near surface layer.

### 6.1.1 Protocol for in–water measurements

A major objective of in–water radiometry is the determination of subsurface optical quantities at given center-wavelengths, $\lambda$, such as upwelling radiance, $L_u(0^-, \lambda)$, upward irradiance, $E_u(0^-, \lambda)$, and downward irradiance, $E_d(0^-, \lambda)$. This requires the collection of in-water optical profiles of $L_u(z, \lambda)$, $E_u(z, \lambda)$ and $E_d(z, \lambda)$ at different depths $z$ and additionally the above–water downward irradiance, $E_d(0^+, \lambda)$, at the same time as in-water data. The latter are required to correct the in-water measurements for changes in the illumination conditions during data collection.

### 6.1.2 An in-water system

An example of an in–water optical profiling system is the Wire Stabilized Profiling Environmental Radiometer (WiSPER). This is a winched system that, since 1995 has been operated at the Acqua Alta Oceanographic Tower (AAOT) in the northern Adriatic Sea within the framework of the Coastal Atmosphere and Sea Time Series (CoASTS) program (Zibordi et al., 2002b). The optical sensors of WiSPER (see Chapter 2) are mounted at approximately the same depth and distance (i.e, within a 10 cm relative depth, and 60 cm relative distance) and it is deployed through a custom-built profiling rig at a speed of 0.1 $ms^{-1}$, at 7.5 m from the main structure of the AAOT (see Fig. 6.1 displaying a schematic of the AAOT and of the WiSPER system). The rigidity and stability of the rig is maintained through two taut wires anchored between the tower and a weight on the sea bottom which prevent the movement of the rig out of the vertical plane of the wires. The wire stabilization and the relatively low deployment speed ensure a good optical characterization of the subsurface water layer. Moreover, in contrasts with winched or crane systems operated from ships, the immovability of the AAOT does not produce supplementary perturbations adding to wave effects.

### 6.1.3 Analysis of in–water data

The elements for the analysis of most of the optical profile data, are summarized through the following steps.

1. Normalize the in-water radiometric quantities (in physical units) with respect

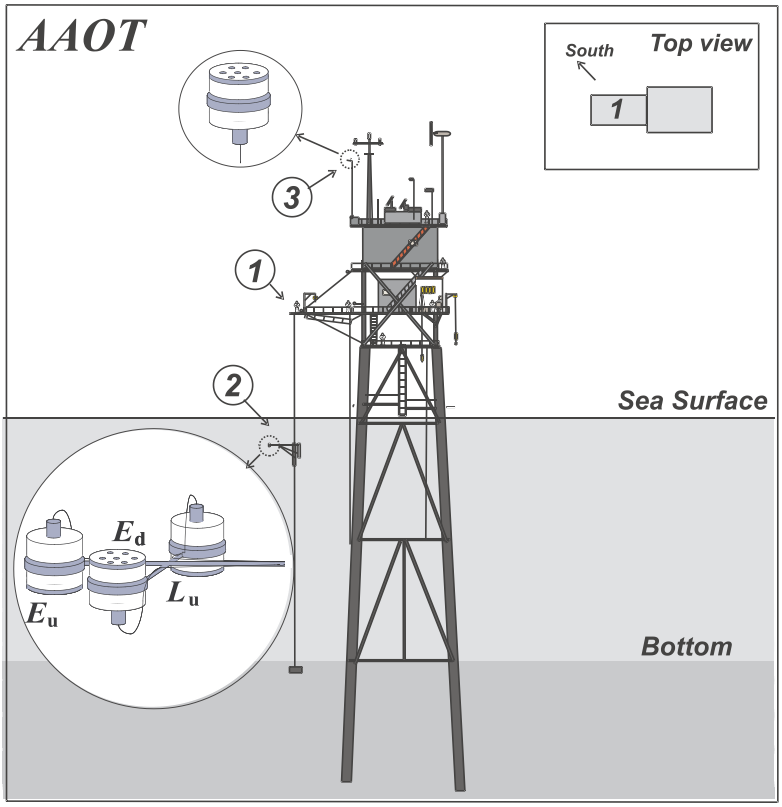


Figure 6.1: Schematic of the Acqua Alta Oceanographic Tower (AAOT): 1. the WiSPER deployment platform; 2. the WiSPER system (the inset shows the in-water radiometers used for $L_u(z,\lambda)$, $E_u(z,\lambda)$ and $E_d(z,\lambda)$ measurements); 3. the reference radiometer for $E_d(0^+,\lambda)$ measurements (after Zibordi et al. (2004c).

to $E_d(0^+,\lambda,t)$, with $t$ explicitly expressing dependence on time, according to

$$\Re(z,\lambda,t_0) = \Re(z,\lambda,t)\frac{E_d(0^+,\lambda,t_0)}{E_d(0^+,\lambda,t)} \tag{6.1.1}$$

where $\Re(z,\lambda,t_0)$ identifies the radiometric quantities (i.e., $L_u(z,\lambda,t)$, $E_u(z,\lambda,t)$ and $E_d(z,\lambda,t)$ ) as they were taken at all absolute depths $z$ at the same time $t_0$; $E_d(0^+,\lambda,t)$ is the above-water irradiance taken at the same time $t$ of the in-water $\Re(z,\lambda,t)$ data, while $E_d(0^+,\lambda,t_0)$ is the above water irradiance at time $t_0$ (where $t_0$ is generally chosen to coincide with the start of the cast). For simplicity the variable $t$ is hereafter omitted.

2. Determine the sub-surface primary quantities $\Re(0^-, \lambda)$ (i.e., $L_u(0^-, \lambda)$, $E_d(0^-, \lambda)$ and $E_u(0^-, \lambda)$) from the least-squares linear regressions of $\ln \Re(z, \lambda)$ versus $z$ (i.e., $\ln L_u(z, \lambda)$, $\ln E_d(z, \lambda)$ and $\ln E_u(z, \lambda)$), within the extrapolation interval identified by $z_0 < z < z_1$. The negative values of the slopes determined from the regressions are the diffuse attenuation coefficients $K_{\Re}(\lambda)$ (i.e., $K_l(\lambda)$, $K_d(\lambda)$ and $K_u(\lambda)$, respectively) for the extrapolation interval. Generally for WiSPER profiles collected at the AAOT coastal site, $0.3 < z_0 < 1.0$ m and $2.5 < z_1 < 4.5$ m. The appropriateness of the extrapolation interval, satisfying the requirement of linear decay of $ln\Re(z, \lambda)$, should be evaluated on a cast-by-cast basis by successive trials choosing a specific radiometric quantity (i.e. $L_u$ or $E_d$) and wavelength $\lambda$. The use of $E_d$ at $\lambda = 665$ nm is considered suitable. In fact the use of a channel in the red spectral region, where seawater has high absorption and the data show a fast drop to noise levels as a function of depth, helps in excluding irrelevant data from the extrapolation interval. The existence of large differences between subsurface $E_d(0^-, \lambda)$ and above-water $E_d(0^+, \lambda)$ values (i.e., larger than a few percent) highlights cases for which the selection of the extrapolation interval may not have been appropriate.

3. Apply corrections for self-shading, superstructure-perturbations and eventually bottom effects. These corrections are instrument, platform and site dependent. Example of correction schemes developed for the CoASTS measurements performed at the AAOT, are presented and discussed in Chapter 7. These were developed on the assumption that the various uncertainties are all independent.

4. In addition to the primary quantities $\Re(0^-, \lambda)$, $K_{\Re}(\lambda)$, and $L_W(\lambda)$ determined with Eq. 2.1.23, derived quantities like the subsurface irradiance reflectance,

$R(\lambda)$, the normalized water leaving radiance, $L_{wn}(\lambda)$, and the subsurface Q-factor at nadir view, $Q_n(\lambda)$, are computed according to equations 2.1.21, 2.1.22 and 2.1.25. The normalized water leaving radiance $L_{wn}(\lambda)$ can alternatively be computed using above-water downward irradiance values derived from $E_d(0^-, \lambda)$ values extrapolated above the surface, here defined as $\breve{E}_d(0^+, \lambda)$ and given by

$$\breve{E}_d(0^+, \lambda) = \frac{E_d(0^-, \lambda) - 0.49E_u(0^-, \lambda)}{1 - \rho_s(\lambda)}, \tag{6.1.2}$$

where the coefficient 0.49 (Mobley, 1994) is an estimate of the subsurface reflectance for upward irradiance, and $\rho_s(\lambda)$ is the sea surface reflectance for downward irradiance given by

$$\rho_s(\lambda) = \frac{\rho_0(\lambda) + 0.066I_r(\theta_0, \lambda)}{1 + I_r(\theta_0, \lambda)}, \tag{6.1.3}$$

with $\rho_0(\lambda)$ Fresnel reflectance of the sea surface at the sun zenith angle $\theta_0$, $I_r(\theta_0, \lambda)$ diffuse over direct irradiance ratio obtained from measurements of total $E_d(0^+, \lambda)$ and diffuse $E_i(0^+, \lambda)$ downward irradiance (i.e. $I_r(\theta_0, \lambda) = E_i(0^+, \lambda)/[E_d(0^+, \lambda) - E_i(0^+, \lambda)]$), and 0.066 sea surface albedo for diffuse illumination. During very clear sky characterized by low $I_r(\theta_0, \lambda)$, $\rho_s(\lambda) \rightarrow \rho_0(\lambda)$.

5. Determine the exact normalized water-leaving radiances $L_{WN}(\lambda)$[1] according to

$$L_{WN}(\lambda) = L_{wn}(\lambda)C_{f/Q}(\theta_0, \lambda, \tau_a, Chla), \tag{6.1.4}$$

where the correction term $C_{f/Q}(\theta_0, \lambda, \tau_a, Chla)$ accounts for the bidirectional effects and is defined by

$$C_{f/Q}(\theta_0, \lambda, \tau_a, Chla) = \frac{f_0(\lambda, \tau_a, Chla)}{Q_0(\lambda, \tau_a, Chla)} \left[\frac{f(\theta_0, \lambda, \tau_a, Chla)}{Q_n(\theta_0, \lambda, \tau_a, Chla)}\right]^{-1}, \tag{6.1.5}$$

[1]Using lower and upper case subscripts, the notations $L_{wn}$ and $L_{WN}$ are applied to indicate normalized water-leaving radiance and normalized water-leaving radiance corrected for bi-directional effects, respectively. The same notations are used for the remote sensing reflectance, $R_{rs}$, computed from $L_{wn}$ and for that corrected for the bi-directional effects, $R_{RS}$, computed from $L_{WN}$.

with $f(\theta_0, \lambda, \tau_a, Chla)$ a function relating the apparent optical properties (and specifically the irradiance reflectance) to the inherent optical properties (Morel et al., 2002), and $Q_n(\theta_0, \lambda, \tau_a, Chla)$ the $Q$-factor at nadir view. The quantity $f(\theta_0, \lambda, \tau_a, Chla)$ is mostly a function of $\theta_0$, $\lambda$, $\tau_a$, and chlorophyll $a$ concentration, $Chla$, (where the latter expresses the dependence on inherent optical properties). The quantities $f_0(\lambda, \tau_a, Chla)$ and $Q_0(\lambda, \tau_a, Chla)$ are the values of $f(\theta_0, \lambda, \tau_a, Chla)$ and $Q_n(\theta_0, \lambda, \tau_a, Chla)$ for $\theta_0$=0. The ratio terms $f_0(\lambda, \tau_a, Chla)/Q_0(\lambda, \tau_a, Chla)$ and $f(\theta_0, \lambda, \tau_a, Chla)/Q_n(\theta_0, \lambda, \tau_a, Chla)$ were theoretically computed for oceanic waters and are available in the form of look-up tables (Morel et al., 2002). Their application to turbid coastal waters has then to be considered with caution.

### 6.1.4 Uncertainty Budget for in–water data

The major uncertainties affecting the in-water subsurface optical data can be summarized as: $(i)$ calibration uncertainties from the absolute calibration, from the sensitivity change between successive calibrations, and finally for irradiance sensors only, from cosine errors; $(ii)$ uncertainties in the correction factors applied for removing measurement artifacts like self-shading, bottom effects and superstructure-perturbations; $(iii)$ environmental variability resulting from the combination of wave induced perturbations with seawater variability and illumination changes. Typical values of these uncertainties estimated for WiSPER data are presented in Tab. 6.1 for $L_u(0^-, \lambda)$, $E_u(0^-, \lambda)$ and $E_d(0^-, \lambda)$ at the center-wavelengths 443, 555 and 665 nm chosen as representative of the WiSPER operating range (the uncertainties estimated for $L_u(0^-, \lambda)$ are expected to equally apply for $L_W(\lambda)$).

Table 6.1: Uncertainty (in percent) in the absolute determination of $L_u(0^-, \lambda)$, $E_d(0^-, \lambda)$ and $E_u(0^-, \lambda)$ from in-water radiometry (case of WiSPER measurements).

| Source | $L_u$ | | | $E_d$ | | | $E_u$ | | |
|---|---|---|---|---|---|---|---|---|---|
| | 443 | 555 | 665 | 443 | 555 | 665 | 443 | 555 | 665 |
| Absolute calibration | 2.4 | 2.4 | 2.4 | 2.7 | 2.7 | 2.7 | 2.7 | 2.7 | 2.7 |
| Corrections | 1.9 | 1.1 | 2.8 | 0.8 | 0.4 | 0.3 | 1.8 | 1.1 | 1.8 |
| Environmental variability [1] | 2.1 | 2.2 | 3.2 | 2.0 | 2.1 | 2.9 | 3.0 | 3.3 | 4.2 |
| Quadrature sum | 3.7 | 3.4 | 4.9 | 3.5 | 3.4 | 4.0 | 4.4 | 4.4 | 5.3 |

[1] Assumed to implicitly include uncertainties in the extrapolation to $0^-$.

The uncertainties for the absolute radiometric calibration values of $L_u$(z,$\lambda$) were computed as the quadrature sum of: 2.1%, uncertainty in the in-air absolute calibration; 0.5%, assumed maximum uncertainty in the value of the immersion coefficient; and 1.0%, assumed instrument sensitivity change between calibrations. The uncertainties for the absolute radiometric calibration values of $E_u$(z,$\lambda$) and $E_d$(z,$\lambda$) were computed as the quadrature sum of: 1.5%, uncertainty in the in-air calibration (see Chapter 3); 0.5%, uncertainty in the value of the immersion coefficient for collectors individually characterized (see Chapter 5); 1.0%, assumed instrument sensitivity change between calibrations; and 2%, assumed maximum uncertainty due to cosine error.

The uncertainty values of corrections applied for self-shading (Zibordi and Ferrari, 1995), tower-shading (Doyle et al., 2003; Doyle and Zibordi, 2002) and bottom effects (Zibordi et al., 2002b) were determined assuming an arbitrary uncertainty of 25% in the overall correction factors computed for time-series (see Chapter 7). It is noted that the selection of an arbitrary uncertainty threshold somehow different from 25% would not significantly affect the overall uncertainty budget, largely depending on

environmental and absolute calibration uncertainties (see Table 6.1).

The uncertainty values related to the environmental variability were estimated from differences in $L_u(0^-, \lambda)$, $E_u(0^-, \lambda)$ and $E_d(0^-, \lambda)$ determined from pairs of consecutive profiles. The differences between the radiometric values from these consecutive profiles collected in 10 minutes delay from each other, were attributed to variability in the seawater and illumination conditions, and marginally to wave induced perturbations.

The quadrature sum of the three major sources of uncertainty for the considered radiometric quantities shows values in the range of 3–5%. The largest uncertainties are observed for $E_u(0^-, \lambda)$ and are mostly due to the high perturbations produced by environmental effects. Considering that the uncertainties caused by this latter were estimated with high depth-resolution WiSPER measurements likely minimizing the focusing and defocusing effects in the extrapolated subsurface quantities, it is of relevance to specifically determine the wave induced perturbations as a function of a varying depth-resolution to estimate their impact on the accuracy of data produced with different profiling systems. The specific problem is comprehensively addressed in Chapter 7 in conjunction with major measurement perturbing effects.

An estimate of the uncertainties affecting $L_{WN}(\lambda)$ from WiSPER profiles — which is the first estimate comprehensively presented for any $L_{WN}(\lambda)$ derived from in–water observations — is provided in Tab. 6.2 through the composition of the major uncertainties affecting its computation using Eq. 6.1.4. Specifically, these uncertainties are determined as the quadrature sum of: (*i*) uncertainty in $L_W(\lambda)$ assumed equal to that determined for $L_u(0^-, \lambda)$ and provided in Tab. 6.1; (*ii*) uncertainty in the

Table 6.2: Uncertainty (in percent) in the absolute determination of $L_{WN}(\lambda)$ from in-water radiometry (case of WiSPER measurements).

| Source | $L_{WN}$ | | |
|---|---|---|---|
| | 443 | 555 | 665 |
| $L_W$ | 3.7 | 3.4 | 4.9 |
| $C_{f/Q}$ | 0.4 | 0.9 | 0.5 |
| $E_d(0^+)$ | 1.6 | 1.6 | 1.6 |
| $E_S$ | 1.6 | 0.6 | 0.2 |
| Quadrature sum | 4.4 | 3.9 | 5.2 |

determination of the correction term $C_{f/Q}(\theta_0, \lambda, \tau_a, Chla)$ estimated as 25% of the average value computed for time series of WiSPER data; (*iii*) uncertainty in $E_d(0^+, \lambda)$ determined as the quadrature sum of 1.5% uncertainty in the absolute calibration and 0.5% additional uncertainty after the minimization of cosine error effects using individually characterized collectors and specific radiative transfer computations (see Chapter 4); *iv.* uncertainty in $E_S(\lambda)$ estimated as the percent difference between values of $E_S(\lambda)$ determined assuming a 10 nm band-width and applying $\pm 1$ nm shift in the center-wavelength, (this estimate is expected to include the intrinsic uncertainty of the tabulated spectral extra-atmospheric sun irradiance values used for computations (Thuillier et al., 1998)).

The resulting values are close to the 5% target established for the absolute radiometric uncertainty of current ocean color sensors (Hooker and Esaias, 1993). Value slightly above 5% is observed at 665 nm, mostly due to the large uncertainty in $L_W$. Notable is the uncertainty in the determination of $E_S(\lambda)$ due to the large variation characterizing its spectral value in the blue part of the spectrum.

## 6.2 Above–water method

An objective of above-water radiometry is the determination of the water-leaving radiance $L_W(\lambda)$. The method generically relies on the collection of the total radiance leaving the sea (including the water and surface contributions) and the capability of removing the surface-reflected component (i.e., glint effects) through additional measurements of the sky component or its simulation. The various proposed measurement protocols differ by the way glint effects are minimized. Among these proocols, the so-called Modified Fresnel Reflectance Glint Correction (MFRGC), outlined in the Version 1 of the SeaWiFS Ocean Optics Protocols (Mueller, 1995) is probably the most used because of its robustness (Hooker et al., 2004; Zibordi et al., 2004d).

### 6.2.1 Protocol for above-water measurements

The MFRGC protocol requires the collection of the total radiance $L_T(\varphi, \theta, \lambda)$ and sky radiance $L_i(\varphi, \theta' = 180 - \theta, \lambda)$ at viewing angle $\theta$ and relative azimuth $\varphi$ with respect to the sun azimuth. The most appropriate viewing geometry for above-water radiometry is defined by $\theta$=40 degrees and $\varphi$=135 degrees, which minimizes the sun-glint perturbations (Mobley, 1999). However, the use of $90<\varphi<135$ is still considered appropriate (Hooker et al., 2002b; Zibordi et al., 2002a). Minimization of perturbations from the superstructure of deployment platforms can be obtained by restricting or controlling the measurement geometry. Specific studies showed that perturbation effects caused by deployment platforms like ships and towers, are generally negligible when the area of the sea surface viewed by the sensor is approximately as far from the superstructure as its height (Hooker and Morel, 2003; Hooker and Zibordi, 2005).

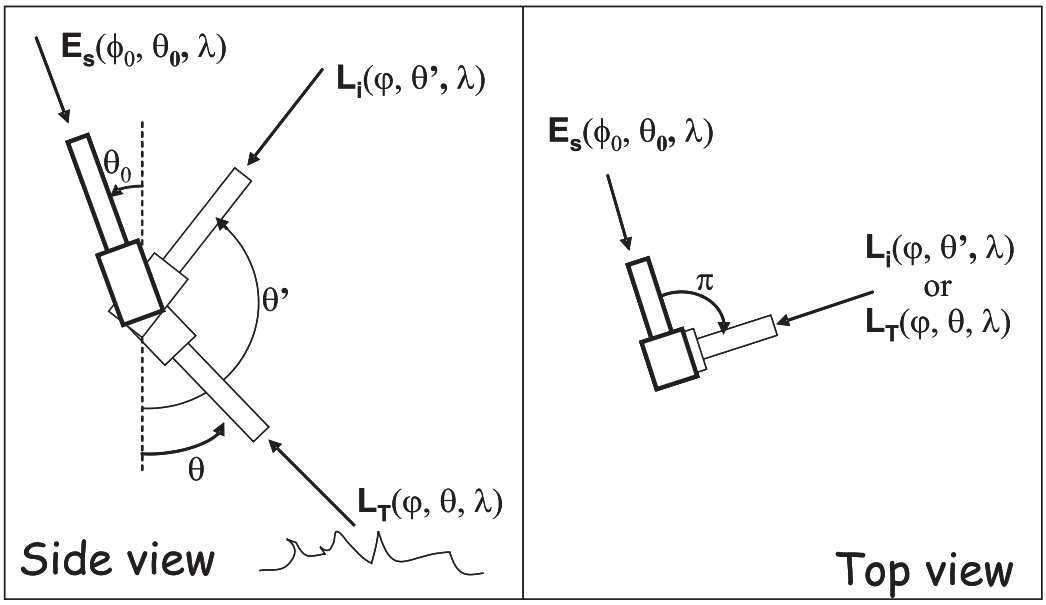


Figure 6.2: Schematic of SeaPRISM measurement geometry.

### 6.2.2 An above-water system

An example of an above–water radiometer system is provided by the SeaWiFS Photometer Revision for Incident Surface Measurements (SeaPRISM) first deployed at the AAOT in May 2002 (Zibordi et al., 2004a). With reference to the schematic displayed in Fig. 6.2, this radiometer measures: $(i)$ the direct sun irradiance $E_s(\phi_0, \theta_0, \lambda)$ as a function of sun azimuth $\phi_0$ and sun zenith $\theta_0$ at various wavelengths $\lambda$, as required for the retrieval of the atmospheric optical thickness; $(ii)$ the sky radiance $L_i(\phi, \theta, \lambda)$ in a wide range of angles identified by azimuth planes $\phi$ and viewing angles $\theta$, as required for the retrieval of the atmospheric scattering phase function; and $(iii)$ the total radiance above the sea surface $L_T(\varphi, \theta, \lambda)$, and the sky radiance $L_i(\varphi, \theta', \lambda)$, with the specific geometry required for the retrieval of the water-leaving radiance $L_W(\lambda)$.

The values of $\varphi$ and $\theta$ (and consequently of $\theta'$, being $\theta = \pi - \theta'$), the gain for each channel, and, additionally the numbers $N_T$ and $N_i$ of above-water and sky

measurements, respectively, chosen for determining $L_T(\varphi, \theta, \lambda)$ and $L_i(\varphi, \theta', \lambda)$, are independently programmable. Measurements are performed with a 1.2 degree full-angle field-of-view in eight channels within the 340–1020 nm spectral range suitable for atmospheric aerosol measurements and ocean color applications (one extra channel is used for dark measurements). Independent sun- , sky- , and sea-viewing scenarios identify the data collection sequences for direct sun irradiance, sky radiance and sea radiance observations, respectively. The sea-viewing scenario, which produces data for above–water radiometry, includes successive measurements of:

1. A series of direct sun measurements acquired at all channels for the determination of $E_s(\phi_0, \theta_0, \lambda)$;

2. A sequential set of $N_T$ total radiance measurements for determining $L_T(\varphi, \theta, \lambda)$, $N_i$ sky-radiance measurements for determining $L_i(\varphi,\theta', \lambda)$, and one dark measurement for each channel.

During clear-sky conditions, $E_s(\phi_0, \theta_0, \lambda)$ allows for the computation of the aerosol optical thickness $\tau_a(\lambda)$, required for determining the normalized water-leaving radiance $L_{WN}(\lambda)$ (see the following sub-section).

Values of $N_i$=3 and $N_T$=11 were shown to be appropriate and offer a suitable compromise with restrictions on the volume of transmitted data (Zibordi et al., 2004a). With these programmed values the execution of a complete measurement sequence of sky and sea measurements takes approximately 6 minutes (repeated at 30 min intervals). The larger number of measurements for determining $L_T(\varphi, \theta, \lambda)$, when compared to the measurements for determining $L_i(\varphi, \theta', \lambda)$, is justified by the higher environmental noise (mostly produced by wave perturbations) affecting the former measurements during clear-sky conditions.

### 6.2.3 Analysis of above–water data

The processing of above-water data collected in agreement with the current version of the MFRGC method, proceeds according to the following steps:

1. Determine $L_T(\varphi, \theta, \lambda)$ by minimizing the effects of surface roughness (Hooker et al., 2002b; Zibordi et al., 2002a). In the case of the operational SeaPRISM system, $L_T(\varphi, \theta, \lambda)$ is determined as the average of the 20% $N_T$ sea measurements exhibiting the lowest radiance levels (Zibordi et al., 2004a). Recalling that the collection of SeaPRISM data is sequential, the relative minima used for the determination of $L_T(\varphi, \theta, \lambda)$ in each channel are completely time independent. This may lead to a lower accuracy of radiance ratios or to more noisy spectra, when compared to measurements taken at the same time in all channels. The $L_i(\varphi, \theta', \lambda)$ values are determined by simply averaging the $N_i$ sky radiance data.

2. Determine $L_W(\varphi, \theta, \lambda)$ as

$$L_W(\varphi, \theta, \lambda) = L_T(\varphi, \theta, \lambda) - \rho(\varphi, \theta, \theta_0, W) L_i(\varphi, \theta', \lambda) \tag{6.2.1}$$

where $\rho(\varphi, \theta, \theta_0, W)$ is the sea surface reflectance, mostly a function of the measurement geometry (identified by $\varphi, \theta, \theta_0$) and wind speed $W$. In a first approximation $\rho(\varphi, \theta, \theta_0, W)$ can be computed neglecting the dependence on $\theta_0$ and $W$ and set to the constant value 0.028 specific for $\varphi$=90 and $\theta$=40 degrees by assuming $W < 5$ ms$^{-1}$. Alternatively $\rho(\varphi, \theta, \theta_0, W)$ at a given $\theta$ and $\varphi$, can be determined as a function of $\theta_0$ and $W$ using values from theoretical determinations (Mobley, 1999).

3. Compute the nadir-transformed water-leaving radiance, $L_W(\lambda)$, from $L_W(\varphi, \theta, \lambda)$ with

$$L_W(\lambda) = L_W(\varphi, \theta, \lambda) C_{\Im Q}(\varphi, \theta, \theta_0, \lambda, \tau_a, Chla, W) \tag{6.2.2}$$

where the correction term $C_{\Im Q}(\varphi, \theta, \theta_0, \lambda, \tau_a, Chla, W)$ minimizes the dependence associated with the viewing geometry during data acquisition and is

$$C_{\Im Q}(\varphi, \theta, \theta_0, \lambda, \tau_a, Chla, W) = \frac{\Im_0}{\Im(\theta, W)} \frac{Q(\varphi, \theta, \theta_0, \lambda, \tau_a, Chla)}{Q_n(\theta_0, \lambda, \tau_a, Chla)}. \tag{6.2.3}$$

The quantities $\Im(\theta, W)$ and $\Im_0(W)$ (i.e., $\Im$ ($\theta$=0,W)) account for surface reflectance and refraction, and primarily depend on $\theta$ and $W$.

The $\Im(\theta, W)$ and $Q(\varphi, \theta, \theta_0, \lambda, \tau_a, Chla)$ terms in Eq. 6.2.3 can be determined using look-up tables (Morel et al., 2002) produced for clear sky with aerosol optical thickness $\tau_a$=0.2 at 550 nm, for various $\varphi, \theta, \theta_0, \lambda$ and $Chla$. The value of $Chla$ is estimated from $L_W(\varphi, \theta, \lambda)$ using an empirical algorithm and then determined with the resulting $L_W(\lambda)$ by applying the same algorithm. This single iteration process applied to AAOT data showed a convergence better than 0.05% in the computed $Chla$ values used for the determination of $L_W(\lambda)$ with equations 6.2.2 and 6.2.3 (Zibordi et al., 2004a).

4. Determine the exact normalized water-leaving radiance $L_{WN}(\lambda)$ as

$$L_{WN}(\lambda) = L_W(\lambda) C_{f/Q}(\theta_0, \lambda, \tau_a, Chla) \left(D^2 t(\lambda) \cos\theta_0\right)^{-1} \tag{6.2.4}$$

where the correction term $C_{f/Q}(\theta_0, \lambda, \tau_a, Chla)$ is given by Eq. 6.1.5. The term $D^2$ accounts for the variations in the Sun-Earth distance as a function of the day of the year, while $t(\lambda)$ is the atmospheric diffuse transmittance

$$t(\lambda) = \exp\{-[(1 - \eta_R)\tau_R(\lambda) + (1 - \omega_a(\lambda)\eta_a(\lambda))\tau_a(\lambda) + \tau_O(\lambda)]/\cos\theta_0\} \tag{6.2.5}$$

where $\tau_R(\lambda)$, $\tau_a(\lambda)$, and $\tau_O(\lambda)$ are the Rayleigh, aerosol, and ozone optical thicknesses, respectively; $\omega_a(\lambda)$ is the aerosol single scattering albedo; and $\eta_R(\lambda)$ and $\eta_a(\lambda)$ are the Rayleigh and aerosol forward scattering probabilities, respectively.

5. Remove $L_{WN}(\lambda)$ data affected by cloud perturbations (Smirnov et al., 2000) or exhibiting inconsistent spectra (D'Alimonte and Zibordi, 2006). This filtering significantly diminishes the number of quality assured $L_{WN}(\lambda)$ data, but, on the other hand, leads to a systematic quality assurance of data which supports their application in calibration and validation activities.

Steps 3 and 4 could be combined together applying an iterative process relying on $R_{RS}(\lambda) = L_{WN}(\lambda)E_S(\lambda)$ for an estimate of $Chla$. This method currently applied in the operational process of SeaPRISM data from various sites (Zibordi et al., 2006c) provides the capability of choosing among those regional bio-optical algorithms proposed for satellite ocean color applications.

### 6.2.4 Uncertainty Budget of above-water data

The major uncertainties affecting above water radiomeric measurements performed with the MFRGC method can be summarized as: ($i$) radiometric calibration uncertainties resulting from the in-air absolute calibration and from the sensor sensitivity change between successive calibrations; ($ii$) uncertainties in the correction factors applied to remove the viewing angle geometry; ($iii$) environmental variability resulting from the combination of wave induced perturbations with changes in seawater optical properties and illumination conditions during measurements. Typical values for the identified uncertainties are presented in Tab. 5.3 for SeaPRISM data at 440, 555 and 674 nm chosen as representative of the instrument operating range.

Table 6.3: Uncertainty (in percent) in the absolute determination of $L_W(\lambda)$ from above water radiometry (case of SeaPRISM measurements).

| Source[1] | $L_W$ | | |
|---|---|---|---|
| | 440 | 555 | 674 |
| Absolute calibration | 2.3 | 2.3 | 2.3 |
| Viewing angle correction | 1.0 | 1.8 | 0.9 |
| Environmental variability[2] | 3.7 | 3.0 | 12.0 |
| Quadrature sum | 4.5 | 4.2 | 12.3 |

[1]The tower perturbations were not included because of the quality assurance applied to data that forces removal of measurements potentially affected by the superstructure.

[2]Estimated from the values provided by Zibordi et al. (2002b) and assumed here to include uncertainties in the determination of $\rho$ and filtering of glint perturbations.

The uncertainties for the radiometric calibration values of $L_W(\lambda)$ were computed as the quadrature sum of: 2.1%, uncertainty in the in-air absolute calibration (see Chapter 3); and 1.0%, assumed instrument sensitivity change between calibrations. The uncertainties due to viewing angle corrections were determined assuming an arbitrary 25% uncertainty in corrections applied to series of data (Zibordi et al., 2004a). The uncertainty values related to the environmental variability, assumed to include uncertainties in the determination of $\rho(\lambda)$, were estimated from differences in $L_W(\lambda)$ from successive measurement sequences (Zibordi et al., 2002a). Like in the case of in-water radiometric measurements, it is reported that the selection of an arbitrary uncertainty threshold somehow different from 25% for the viewing corrections, would not significantly affect the overall uncertainty budget largely conditioned by environmental and absolute calibration uncertainties.

The quadrature sum of uncertainties shows values varying from 4.2% at 555 nm to extreme values of 12.3% at 674 nm. The latter are mostly attributed to environmental (i.e., wave) perturbations.

Table 6.4: Uncertainty (in percent) in the absolute determination of $L_{WN}(\lambda)$ from above–water radiometry (case of SeaPRISM measurements).

| Source | $L_{WN}$ | | |
|---|---|---|---|
| | 440 | 555 | 674 |
| $L_W$ | 4.5 | 4.2 | 12.3 |
| $C_{f/Q}$ | 0.4 | 0.9 | 0.5 |
| $t_d$ | 2.0 | 2.0 | 2.0 |
| Quadrature sum | 4.9 | 4.7 | 12.5 |

An estimate of the uncertainties affecting $L_{WN}(\lambda)$ from SeaPRISM measurements — which is the first estimate comprehensively presented for any $L_{WN}(\lambda)$ derived from above–water observations — is provided in Tab. 6.4 through the composition of the major uncertainties affecting its computation with Eq. 6.2.4. Specifically, these uncertainties are determined as the quadrature sum of: (*i*) uncertainty in $L_W(\lambda)$ as provided in Tab. 6.4; (*ii*) uncertainty in the determination of the correction term $C_{f/Q}(\theta_0, \lambda, \tau_a, Chla)$ estimated as 25% of the average value computed for time series of WiSPER data at 443, 555 and 665 nm (the slight differences between WiSPER and SeaPRISM center-wavelengths are assumed to not affect the estimate of uncertainties for $C_{f/Q}(\theta_0, \lambda, \tau_a, Chla)$); (*iii*) guessed uncertainty of 2% in $t_d$ (the given value is not supported by any specific investigation and it is expected to be an underestimate).

Similarly to uncertainties determined for $L_WN(\lambda)$ derived from in–water data, the resulting values produced for $L_{WN}(\lambda)$ from above-water data are close to the 5% target established for the absolute radiometric uncertainty of current ocean color sensors (Hooker and Esaias, 1993), when excluding data at 674 nm heavily affected by wave perturbations and showing uncertainties higher than 12%.

## 6.3 Comparison of methods

The convergence of the above- and in-water methods presented and discussed in the former sections was evaluated through the comparison of SeaPRISM and WiSPER data collected at the AAOT site. Specifically $L_W^{SP}(\lambda)$ and $L_W^{WS}(\lambda)$, or $L_{WN}^{SP}(\lambda)$ and $L_{WN}^{WS}(\lambda)$, where the superscripts SP and WS indicate SeaPRISM and WiSPER data, were compared at the specific center-wavelengths 413, 440, 501, 555 and 674 nm for SeaPRISM, and at 412, 443, 501 (synthetically obtained by interpolating data between 490 and 510 nm), 555 nm and 665 nm for WiSPER. The data analysis was restricted to measurement sequences (hereafter referred to as match-ups) starting within ±5 min from each other and with sun azimuth $\phi_0$ ranging between 125 and 245 degrees. The latter constraint minimizes the tower superstructure perturbations. To ensure a direct comparison with SeaPRISM data, no correction for bottom effects was applied to $L_u(0^-, \lambda)$ values computed from WiSPER data (for the cases considered in the assessment, the corrections for the bottom effects estimated according to Zibordi et al. (2002b) would have been negligible at 412 and 665 nm, and increasing between 443 and 555 nm with average values ranging from -0.1 to -1.0%, respectively).

The data comparison was made using the relative percent difference $\psi_{j,n}$ and its absolute value $|\psi_{j,n}|$, applied to determine systematic biases and typical uncertainties, respectively. In the formulation of the relative percent differences, WiSPER data are considered the reference values, so $\psi_{j,n}$ is

$$\psi_{j,n} = 100\frac{A(j)_n - B(j)_n}{A(j)_n} \tag{6.3.1}$$

where $A$ and $B$ indicate either water-leaving radiances $L_W^{SP}(\lambda)$ and $L_W^{WS}(\lambda)$, respectively, or normalized water-leaving radiances $L_{WN}^{SP}(\lambda)$ and $L_{WN}^{WS}(\lambda)$, respectively; $n$

is the match-up number covering the range 1 to $M$, with $M$ being the total number of match-ups; and $j$ is the channel index (i.e., $j$=1–5 for the SeaPRISM center wavelengths 413, 440, 501, 555 and 674 nm).

The data analysis was carried out for the available match-ups on a channel-by-channel basis (i.e., for each single center wavelength) and across channels (through spectrally averaged values). Outliers were excluded to prevent biased estimates. The average relative percent differences were computed by removing single $\psi_{j,n}$ values exceeding the average plus or minus two times the standard deviation, $\sigma$, of the total number $N$ (i.e. $N = KM$) of the $\psi_{j,n}$ values (referred to as $2\sigma$ filtering), through

$$\psi = \frac{1}{K} \sum_{j=1}^{K} \frac{1}{M_j} \sum_{n=1}^{M_j} \psi_{j,n} \tag{6.3.2}$$

with $K$ number of channels (i.e., $K = 1$ for single channel analysis and $K = 5$ for overall spectrally averaged values) and $M_j \leqslant$M, match-ups for the $j^{th}$ channel satisfying the $2\sigma$ filtering condition. Similarly, the average absolute percent differences, $|\psi|$, were computed according to Eq. 6.3.2 using the $|\psi_{j,n}|$ values.

The data analysis was applied to measurements from CoASTS campaigns conducted between June 2002 and May 2003, and included data collected during different atmospheric and marine conditions with Case-2 water occurrence of 40% (Zibordi et al., 2004c). The results for the $L_W^{SP}(\lambda)$ versus $L_W^{WS}(\lambda)$ comparison are shown in Fig. 6.3 through a scatter plot and the distribution of relative percent differences $\psi_{i,j}$. The comparison of water-leaving radiances, instead of the normalized water-leaving radiances alone, is justified by the clear-sky conditions and the short time difference between the collection interval of SeaPRISM and WiSPER data retained for the analysis (less than 5 minutes).

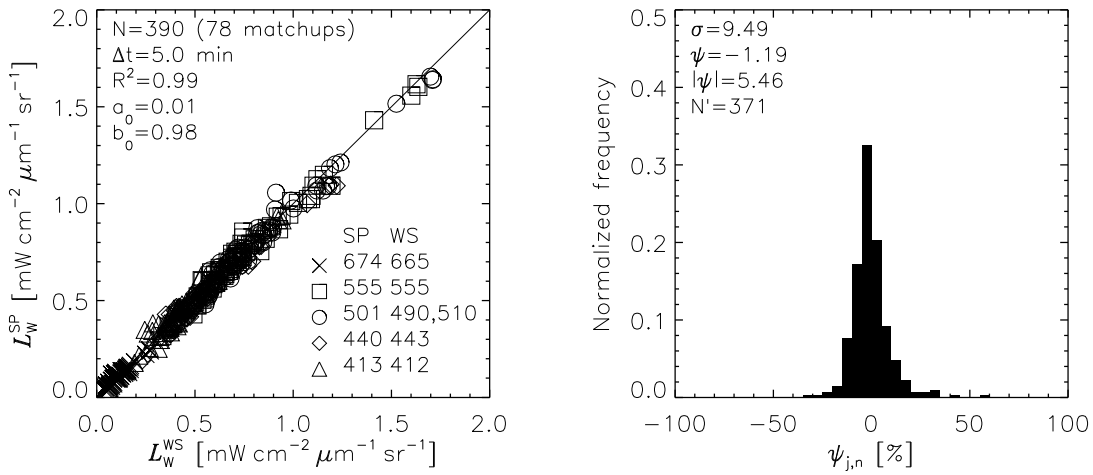


Figure 6.3: The comparison of $L_W^{SP}(\lambda)$ and $L_W^{WS}(\lambda)$ determinations showing: the scatter plot of the data (left panel), where $a_0$ and $b_0$ are the intercept and the slope, respectively, of the model II (major axis) linear regression; and the normalized frequency distribution of the $\psi_{j,n}$ values (right panel), where $\sigma$ is the standard deviation of the $N$ values of $\psi_{j,n}$, and, $|\psi|$ and $\psi$ are the averages of the N′ values of $|\psi_{j,n}|$ and of $\psi_{j,n}$ satisfying the $2\sigma$ filtering conditions (after Zibordi et al. (2004a)).

Specifically, the comparison of the water-leaving radiances comprehensively presented and discussed in Zibordi et al. (2004a) exhibits $|\psi|$ varying from 5.9% at 413 nm to 3.1% at 555 nm, with spectrally averaged value of 4.5% in the 413-555 nm interval, and of 10.2% at 674 nm. The overall spectrally averaged values in the 413-674 nm interval exhibit $|\psi|$=5.5% and $\psi$=-1.2%. The presence of a systematic bias observed at 674 nm ($\psi$=-5.9%), is explained by the difference in the center-wavelengths of the two instruments (674 versus 665 nm). A bias observed at 440 nm ($\psi$ =-3.7% ) is also attributed to a slight difference in the SeaPRISM and WiSPER center wavelengths in a spectral region characterized by high radiance gradients.

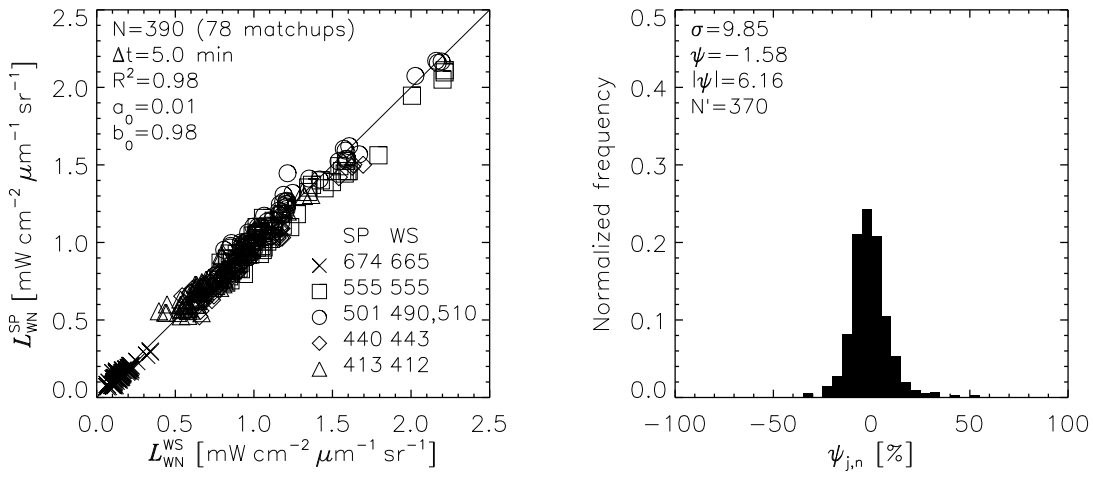


Figure 6.4: The same as in Fig. 6.3 but for $L_{WN}^{SP}(\lambda)$ and $L_{WN}^{WS}(\lambda)$ (after Zibordi et al. (2004a)).

The results from the comparison of normalized water-leaving radiance, $L_{WN}(\lambda)$, are shown in Fig. 6.4 using the same presentation scheme applied in Fig. 6.3. The spectrally averaged $|\psi|$ values for $L_{WN}(\lambda)$, when compared to those computed for $L_W(\lambda)$, increase slightly from 5.5% to 6.2%. More significant variations are on average observed for the spectral $|\psi|$ values (not presented). These results can be explained by the different methods applied in the determination of $L_{WN}^{SP}(\lambda)$ and $L_{WN}^{WS}(\lambda)$. In the case of $L_{WN}^{SP}(\lambda)$, the normalization relies on the computation of the diffuse atmospheric transmittance $t(\lambda)$, while in the case of $L_{WN}^{WS}(\lambda)$ it makes use of the $E_S(\lambda)/E_d(0^+,\lambda)$ ratio. The two methods should provide converging results during clear-sky conditions, where the impact of clouds to $E_d(0^+,\lambda)$ is negligible, and

$$\frac{E_S(\lambda)}{E_d(0^+,\lambda)} \approx \left(D^2 t(\lambda)\cos\theta_0\right)^{-1} \tag{6.3.3}$$

The formulation given in Eq. 6.3.3, however, shows that uncertainties in the

absolute values of $E_d(0^+, \lambda)$ as well as in the value of the mean extraterrestrial solar irradiance, $E_S(\lambda)$, or simply differences between the wavelengths under comparison (for instance the difference in the 674 and 665 nm center wavelengths for SeaPRISM and WiSPER), can affect $E_S(\lambda)/E_d(0^+, \lambda)$ and consequently $L_{WN}(\lambda)$.

## 6.4 Discussion on radiometric methods

The uncertainty analysis showed that in-water radiometric measurements may be still appreciably affected by self-shading and environmental effects, neglecting perturbations by deployment superstructures which can be avoided with the use of free-falls. Differently, by minimizing platform perturbations with the adoption of strict measurement geometries, above-water measurements are mostly affected by environmental effects. When restricting the discussion to comparable quantities like $L_{WN}$, the environmental perturbations specifically due to wave effects are certainly much larger in above-water radiometric measurements with values significantly increasing from the blue-green to the red. This can be explained by the different physical processes involving the two measurement methods. In the case of in-water radiometry, wave perturbations affect measurements as a function of water backscattering. In the case of above-water radiometry, they are mostly a function of surface reflectance.

A critical element for in– and above–water radiometry is the removal of the viewing angle dependence and of the effects produced by non isotropy of light distribution. Both corrections are currently applied using solutions proposed for Case-1 water. This implies that the uncertainty in these corrections may increase in presence of Case-2 waters. It is, however, out of the scope of this study to investigate uncertainties due to the application to Case-2 waters data of corrections proposed for Case-1.

## 6.5 Summary

In-water radiometric measurements are generally performed with moorings and profilers through winched or free-fall systems with the objective of producing continuous or discrete profile data to determine subsurface values. In-water systems may have different radiometric configurations. Comprehensive systems include sensors for measuring $L_u(z,\lambda)$, $E_u(z,\lambda)$ and $E_d(z,\lambda)$ in addition to an in-air sensor for $E_d(0^+,\lambda)$. Primary in-water radiometric products are the sub-surface values (i.e., $L_u(0^-,\lambda)$, $E_u(0^-,\lambda)$ and $E_d(0^-,\lambda)$) derived from the extrapolation to $0^-$ of the log-transformed measurements at depths $z$. From these, after minimizing perturbations due to self-shading, deployment superstructure and bottom reflectance, higher level products like the irradiance reflectance, $R(\lambda)$, the normalized water-leaving radiance, $L_{WN}(\lambda)$, the remote sensing reflectance, $R_{RS}(\lambda)$, and the Q-factor at nadir view, $Q_n(\lambda)$, are computed.

Above-water radiometry can now be considered a consolidated alternative to in-water radiometry. The former can use deployment platforms like ships or fixed towers for measuring the radiance emerging from the sea at given viewing and azimuth angles, in addition to sky radiance measurements to minimize glint perturbations. The primary above-water radiometric product is the water-leaving radiance, $L_W(\lambda)$, used to compute the normalized-water leaving radiance, $L_{WN}(\lambda)$, or the remote sensing reflectance, $R_{RS}(\lambda)$.

Focussed inter-comparison exercises based on a unique data set produced at the AAOT in the northern Adriatic Sea and representative of very different measurement conditions characterized by large variability in sun zenith, sea state, water type and sky conditions, showed the possibility of producing in– and above–water water-leaving

radiances with relative differences generally within 5%. On the other hand it was also shown that both in– and above–water radiometry can provide $L_W(\lambda)$ data with an uncertainty of approximately 5% below 555 nm. In contrast, in the red the uncertainties are much higher for above–water radiometry (i.e., above 12%) than for in–water radiometry (i.e., approximately 5%). As expected, uncertainties in $L_{WN}(\lambda)$ — here comprehensively addressed for the first time — exhibit slightly higher values than for $L_W(\lambda)$. Notable are the relatively high uncertainties which may affect $L_{WN}(\lambda)$ as a result of uncertainties in the determination of the extra-atmospheric sun irradiance at specific radiometer center-wavelengths in spectral regions characterized by large gradients.

Finally it must be recalled that the high level of agreement shown by the intercomparison of in– and above–water radiometric data is largely due to the respect for strict measurement protocols (which require the application of rigid measurement geometries), the adoption of correction schemes for measurement artifacts in in-water radiometric data (e.g., self-shading, deployment platform perturbations), and the application of state of the art calibration methods. It is then stressed that the application of above–water measurement methods, which rely on the position of the sun for pointing at the sea and sky, makes questionable the unmanned collection of radiometric data from ships without the aid of stabilized platforms, sun-tracking systems and the continuous control of ship heading (to minimize perturbations due to ship-superstructure).

# Chapter 7

# Measurement Perturbations

*Most in–water irradiance and radiance measurements at sea are carried out by suspending an instrument from an hydrocable located very close to the ship, the presence of which can severely perturb the in–water light field.*

*Howard Gordon, 1985.*

[1]The accuracy of radiometric measurements carried out at sea is likely to be affected by various perturbing effects. Above–water measurements may be perturbed by shading and reflection of deployment superstructures (i.e., ships, oceanographic towers), and environmental effects like wave reflections and changes in the illumination conditions during data collection. In–water measurements, in addition to the former perturbations may also be affected by instrument self-shading.

The superstructure perturbations largely vary with the illumination conditions, the seawater inherent optical properties and the deployment geometry (Doyle and Zibordi, 2002; Gordon, 1985; Hooker and Zibordi, 2005). Self-shading produces a decrease in the in–water measurements of the upward light field (Aas and Korsbø, 1997;

[1]The material presented and discussed in this chapter was mostly published in Doyle and Zibordi (2002); Zibordi et al. (1999, 2002b, 2004c).

Gordon and Ding, 1992; Zibordi and Ferrari, 1995). This effect increases with the seawater absorption and the size of the instrument case. The wave effects can produce quite large uncertainties as a function of sea state and seawater optical properties (Zibordi et al., 2004c). In addition to the former sources of uncertainty, the bottom reflectance can be a further perturbing factor in shallow waters when the collected data need to represent a semi-infinite water volume. The related perturbing effects vary spectrally as a function of the bottom reflectance, water depth and seawater optical properties (Zibordi et al., 2002a).

Minimization of measurement perturbations can be obtained through the application of measurement protocols and the implementation of correction schemes which computationally allow for an estimate of perturbation effects. In the case of above–water radiometry the minimization of perturbation effects due to deployment superstructures can be obtained through the adoption of rigid measurement geometries (Hooker and Zibordi, 2005), while environmental perturbations due to wave effects can be minimized by filtering data (Hooker et al., 2002b; Zibordi et al., 2002a). In the case of in–water radiometric measurements, quite comprehensive correction schemes were specifically developed for most of the perturbation effects.

This chapter provides an extended description of correction schemes proposed for the minimization of perturbation effects in optical radiometric measurements and additionally an evaluation of the uncertainties that still remain after these corrections have been applied. The material presented and discussed in the following sections largely relies on investigations previously performed and published by the author, but also on additional analysis required to achieve the goal of comprehensively quantifying the error budget for the major optical radiometric quantities.

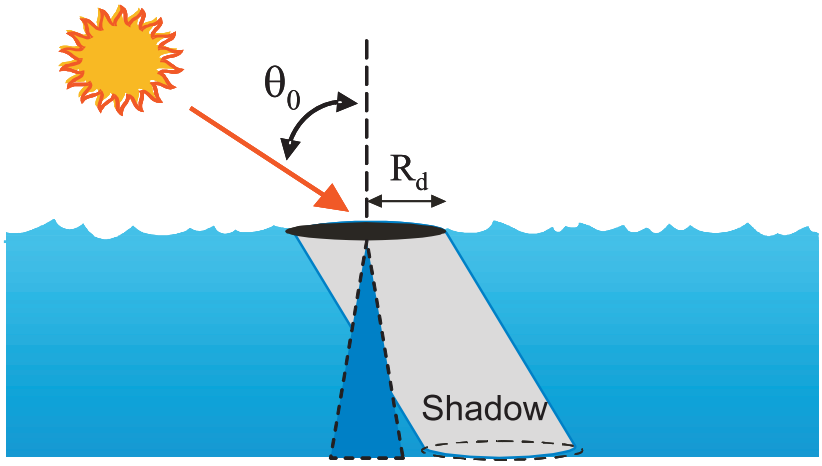


Figure 7.1: Schematic of self-shading perturbations in upwelling radiance.

## 7.1 Self-shading

The finite size of underwater radiometers affects the radiance field and induces errors in the measured upwelling radiance and upward irradiance (see schematic in Fig. 7.1). Gordon and Ding (1992) evaluated the self-shading error through numerical simulations. They estimated errors ranging from a few percent up to several tens of percent as a function of the size of the radiometer, the absorption coefficient of the medium, and the type of illumination (direct or diffuse). For a given radiometer, the error is much higher in the near infrared than in the visible because of the stronger water absorption, and the error increases with the concentration of absorbing particles and the absorption coefficient of colored dissolved organic matter.

### 7.1.1 Correction scheme for self-shading perturbations

The self-shading error $\epsilon^S_{\Re}(\lambda)$ for upwelling radiance and similarly for upward irradiance is here defined as

$$\epsilon^S_{\Re}(\lambda) = [\Re(0^-, \lambda) - \hat{\Re}(0^-, \lambda)]/\Re(0^-, \lambda) \tag{7.1.1}$$

where $\Re(0^-, \lambda)$ indicates the radiometric value that would apply in the absence of the instrument, and $\hat{\Re}(0^-, \lambda)$ indicates the radiance or irradiance measurement that is actually made and is affected by the instrument shading. Gordon and Ding (1992), hereafter simply referred as G&D, through Monte Carlo simulations showed that the correction factor $\epsilon^S_{\Re}(\lambda)$ can be expressed as a function of the radius $R_d$ of the radiometer, the absorption coefficient $a(\lambda)$ of the medium, the sun zenith $\theta_0$, and the irradiance ratio $I_r(\theta_0, \lambda)$. Using simulated data, they developed an operational scheme to compute the self-shading error for underwater radiance and irradiance measurements taken just beneath the sea surface.

According to G&D and accounting for the parameterizations suggested by Zibordi and Ferrari (1995), and Mueller and Austin (1995)

$$\epsilon^S_{\Re}(\lambda) = \frac{\epsilon_{sun}(\lambda) + \epsilon_{sky}(\lambda) I_r(\theta_0, \lambda)}{1 + I_r(\theta_0, \lambda)} \tag{7.1.2}$$

with

$$\epsilon_{sun}(\lambda) = 1 - exp[-k_{sun} a(\lambda) R_d] \tag{7.1.3}$$

$$\epsilon_{sky}(\lambda) = 1 - exp[-k_{sky} a(\lambda) R_d] \tag{7.1.4}$$

where $\epsilon_{sun}(\lambda)$ and $\epsilon_{sky}(\lambda)$ indicate the error due to the direct sun irradiance and to the diffuse radiance contributions, respectively.

The term $k_{sun}(\lambda)$ is given by

$$k_{sun}(\lambda) = (1 - f_R) k^p_{sun}(\lambda) + f_R k^e_{sun}(\lambda) \tag{7.1.5}$$

where $f_R$ accounts for the sensor-to-instrument diameter, and $k^p_{sun}(\lambda)$ and $k^e_{sun}(\lambda)$ are terms to represent the two extremes of a point sensor or a sensor having the same size as the instrument case, respectively. Functions for the computation of terms $k^p_{sun}$, $k^e_{sun}$ and $k_{sky}$ are given in Tab. 7.1.

Table 7.1: Functions for the computation of terms $k^p_{sun}$, $k^e_{sun}$ and $k_{sky}$.

| | Radiance | Irradiance |
|---|---|---|
| $k^p_{sun}$ | $(2.07 + 0.0056\theta_0)/\theta_{0w}(\lambda)$ | $3.41 - 0.0155\theta_0$ |
| $k^e_{sun}$ | $(1.59 + 0.0063\theta_0)/\theta_{0w}(\lambda)$ | $2.76 - 0.0121\theta_0$ |
| $k_{sky}$ | $4.61 - 0.87 f_R$ | $2.70 - 0.48 f_R$ |

The sun zenith in the water, $\theta_{0w}(\lambda)$, slightly dependent of wavelength and required for the computation of $k_{sun}$, is given by $\theta_{0w}(\lambda) = sin^{-1}(sin\theta_0/n_w(\lambda))$. The coefficients of the linear relationships given for $k_{sun}$ have been derived from the data published by G&D for $aR < 0.1$ and sun zenith $30 < \theta_0 < 70$ degrees.

The operational correction of the generic radiometric quantity $\hat{\Re}(\lambda)$ is then obtained by applying the multiplication factor $\eta^S_{\Re}(\lambda)$

$$\eta^S_{\Re}(\lambda) = \frac{1}{1 - \epsilon^S_{\Re}(\lambda)} \tag{7.1.6}$$

### 7.1.2 Experimental assessment of self-shading corrections

An experiment was designed to evaluate variations in upwelling radiance and irradiance as a function of the diameter of a disk in which the sensor (assumed to be a point sensor) occupies the center. Measurements were made with a SE-590 Spectron Engineering (Denver, Colorado) spectroradiometer equipped with fiber optics terminated with an interchangeable collection optics including 1 degree, 18 degrees, or $2\pi$ full angle field-of-view, having 1-cm diameter and a suitable attachment for disks used to simulate radii of the instrument ranging from 2.5 to 20 cm at 2.5-cm steps. Optics and disks were attached at the end of a pole 1.5 m long with a universal joint, ensuring exact vertical positioning of the optics. Disks and mechanical supports were

coated with black paint. The size of the collection optics was assumed not to affect the point sensor hypothesis because of the much larger size of the shading disks.

Measurements, performed in the Lake of Varese (Italy) from a floating pier, were collected for different sun zeniths during clear sky and with an almost flat water surface. Sequences of radiance and irradiance data were measured while increasing the size of the shading disk, and with the optics approximately 1.5 cm below the water surface to avoid any disturbance by capillary waves. In each measuring sequence at least two independent measurements were performed with each disk. The execution of each measuring sequence lasted approximately 10 minutes. No attempt was made to evaluate the self-shading error on overcast sky.

The absorption coefficient of lake water was computed as the sum of water, particulate, and colored dissolved organic matter absorption coefficients determined from water samples collected during the experiments applying the measurement methods proposed by Tassan and Ferrari (1995) and Ferrari and Tassan (1991), respectively.

Computation of theoretical values for $\epsilon^S_{\Re}(\lambda)$, needed for comparison with experimental data, requires estimates of $E_i(\lambda)$ and $E_d(0^+, \lambda)$ to determine $I_r(\theta_0, \lambda)$. These were determined with an atmospheric radiative transfer code with aerosol optical thicknesses $\tau_a(\lambda)$ obtained from sun photometric measurements. Data collection was always performed by sequentially increasing the size of the disk while the sun zenith was decreasing. Thus to avoid underestimating $\epsilon^S_{\Re}(\lambda)$, measured radiances and irradiances were corrected with simulated data of diffuse and direct sun irradiance accounting for their weight on $\epsilon^S_{\Re}(\lambda)$.

Figures 7.2 and 7.3, show the experimental radiance (for measurements made with l degree full-angle field-of-view in air) and irradiance $\epsilon^S_{\Re}(\lambda)$, as a function of $a(\lambda)R_d$ for

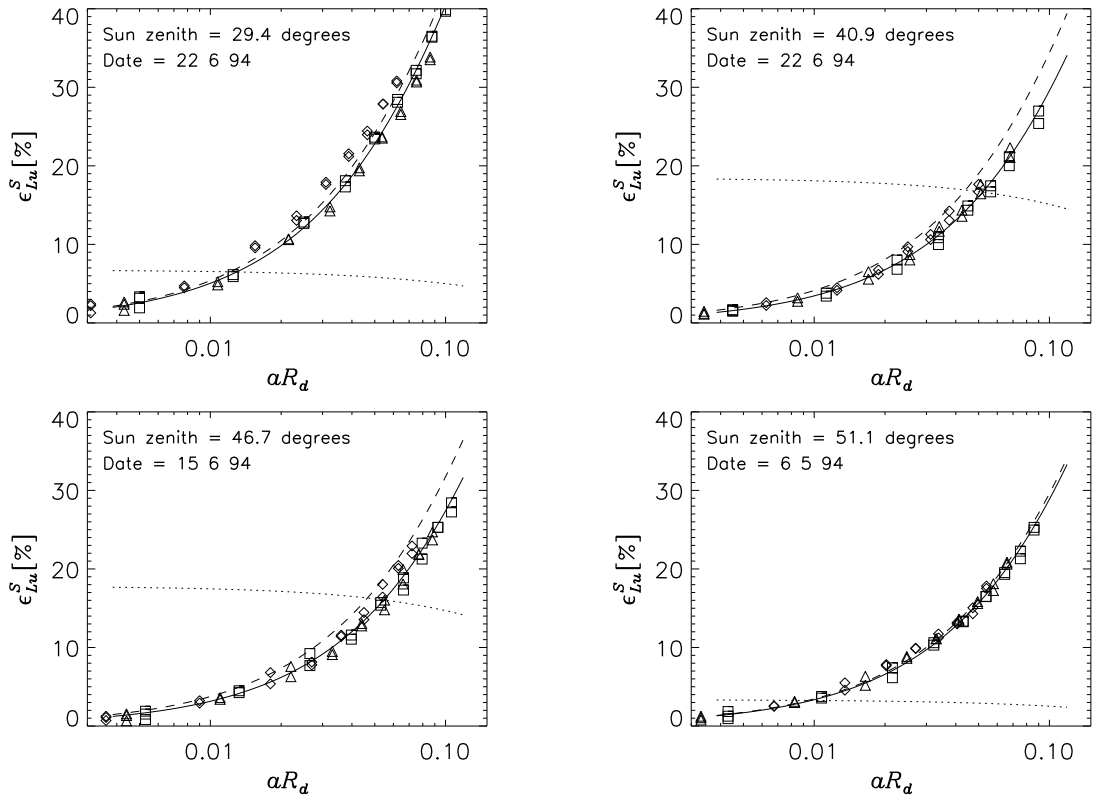


Figure 7.2: Radiance errors in percent as a function of $aR_d$ for different sun zenith angles: 29.4, 40.9, 46.7, 51.1 degrees [experimental data at 550 nm (◊), 600 nm (△), and 640 nm(□)]. The curves show the best fit of the experimental data (solid line), the theoretical error computed according to G&D (dashed line) and the relative percent difference between the theoretical and the experimental fitted data (dotted line) (after Zibordi and Ferrari (1995)).

different wavelengths at different sun zeniths. The choice of measurements made at 550, 600, and 640 nm center wavelengths (with bandwidths of 4 nm) for data analysis and presentation, was suggested by the sensitivity of the measuring system (which is too low for in-water measurements made above 700 nm) and by the need to minimize the uncertainty in the $\epsilon^S_{\Re}(\lambda)$ estimate caused by the uncertainty of total absorption coefficient (i.e., assuming that water absorption is well known, the uncertainty in total absorption coefficient is greater in the blue, where the sum of particles and yellow

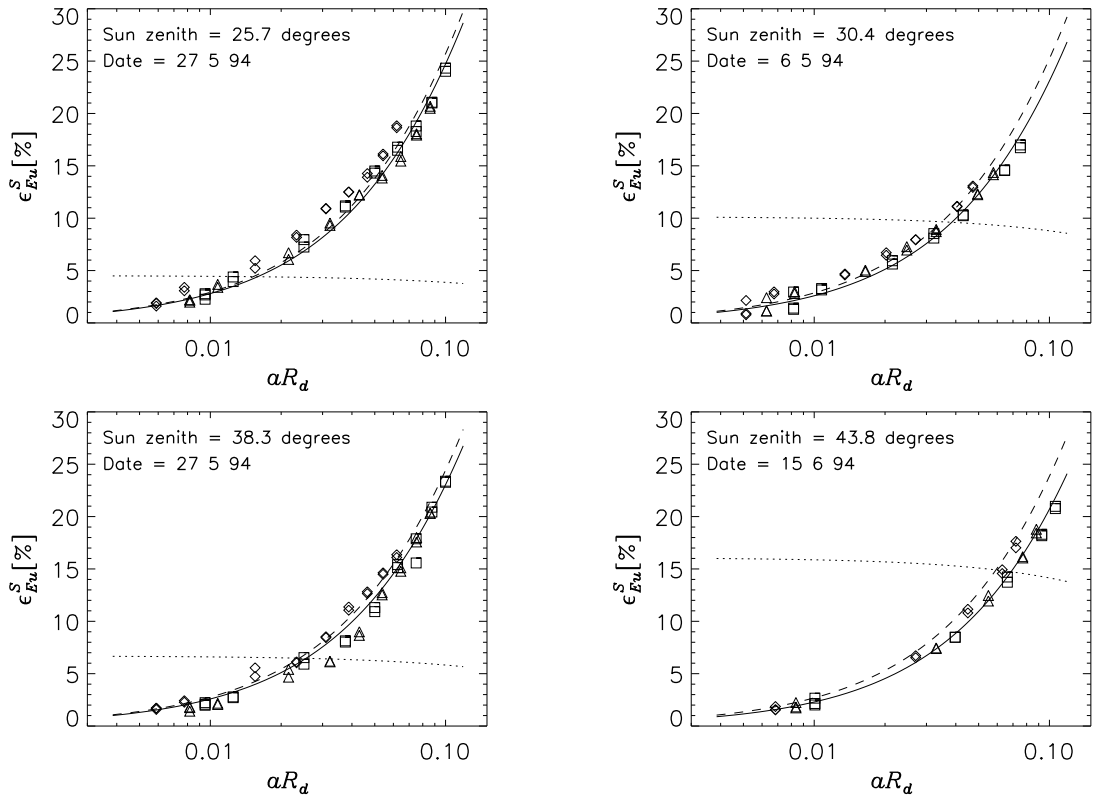


Figure 7.3: Irradiance errors in percent as a function of $aR_d$ for different sun zenith angles: 25.7, 30.4, 38.3, 43.8 degrees [experimental data at 550 nm (◊), 600 nm (△), and 640 nm(□)]. The curves show the best fit of the experimental data (solid line), the theoretical error computed according to G&D (dashed line) and the relative percent difference between the theoretical and the experimental fitted data (dotted line) (after Zibordi and Ferrari (1995)).

substance absorptions is much higher than that of water when compared with the green and the red regions of the spectrum).

The fits of experimental $\epsilon^S_{\Re}(\lambda)$ are shown in Fig.'s 7.2 and 7.3, together with theoretical $\epsilon^S_{\Re}(\lambda)$ computed with the scheme of G&D assuming a point sensor. The fits of the experimental data were computed according to the function $1 - exp(-kaR_d)$, imposing $\epsilon^S_{\Re}(\lambda) = 0$ at $R_d = 0$. Theoretical $\epsilon^S_{\Re}(\lambda)$ were computed with values of $I_r(\theta_0, \lambda)$ estimated at 600 nm only (this approximation produces relative percent

differences lower than ±2% between theoretical $\epsilon^S_{\Re}(\lambda)$ computed at 600 nm and those computed at 550 and 640 nm). Figures 7.2 and 7.3, show that the relative percent differences between fits of experimental and theoretical $\epsilon^S_{\Re}(\lambda)$ are generally lower than 20% for radiance measurements and generally lower than 15% for irradiance measurements (absolute differences in $\epsilon^S_{\Re}(\lambda)$ values are generally lower than 5% for radiance and lower than 3% for irradiances).

Most of the underwater instruments for radiance measurements have full-angle field-of-view larger than 1 degree. To evaluate the applicability of the correction scheme to radiance measurements made with a relatively large field-of-view, measurements were also collected with 18 degrees (in air) full-angle field-of-view. Results from measurements obtained at 30.7 degrees sun zenith are shown in Fig. 7.4. These data are comparable with those presented in Fig. 7.2 at $\theta_0$=29.4 degrees which were obtained with a 1 degree full-angle field-of-view at close sun zenith and with identical environmental conditions. The agreement between the experimental and the theoretical data, and between the experimental data shown in Fig.'s 7.2 and 7.4, suggests that a change in the field of view in the explored range does not significantly affect $\epsilon^S_{\Re}$ and, consequently, the capability of operationally recovering the self-shading error without accounting for the field-of-view.

The accuracy of comparisons between experimental and theoretical $\epsilon^S_{\Re}(\lambda)$ was investigated through sensitivity analysis of the parameters which more significantly affect computations. A change of $\sim$ 100% in the total absorption coefficient was shown to produce relative percentage variations on $\epsilon^S_{\Re}(\lambda)$ of approximately 4% at 550 nm and lower than 2% at 600 and 640 nm. A change of $\backsim$ 20% in aerosol optical thickness was shown to produce relative percentage variations on $\epsilon^S_{\Re}(\lambda)$ lower than

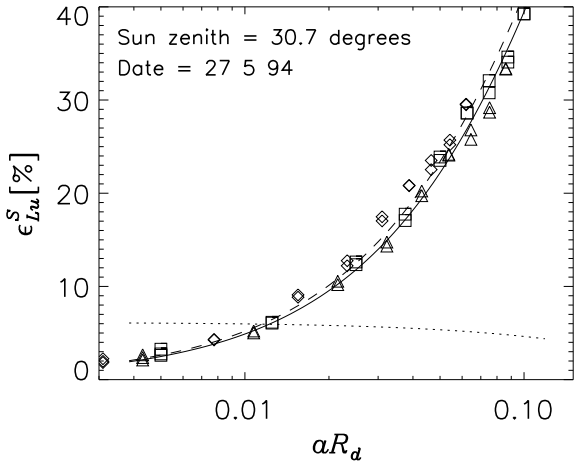


Figure 7.4: Radiance (18 degrees full angle field of view) errors in percent as a function of $aR_d$ at 30.7 degrees Sun zenith [experimental data at 550 nm (◊), 600 nm (△), and 640 nm(□)]. The curves show the best fit of the experimental data (solid line), the theoretical error computed according to G&D (dashed line) and the relative percent difference between the theoretical and the experimental fitted data (dotted line) (after Zibordi and Ferrari (1995)).

2% for radiance and 1% for irradiance.

Factors $\eta^S_{Lu}(\lambda)$ and $\eta^S_{Eu}(\lambda)$ applied to minimize self-shading perturbations in radiometric measurements performed at the AAOT in the period October 1995 - July 2005, are displayed in Fig.'s 7.5 and 7.6 for $\hat{L}_u(\lambda)$ and $\hat{E}_u(\lambda)$, respectively, at the 443, 555 and 665 nm center-wavelengths. Time series indicate a high dependence of $\eta^S_{Lu}(\lambda)$ and $\eta^S_{Eu}(\lambda)$ on sun zenith in the form of a seasonal variability (most of the observations were made around the local noon hence close to daily maximum sun zenith). This dependence appears more pronounced in the red than in the blue due to the lower variability of the total seawater absorption. The highest corrections result at 665 nm with averages of 10.0±2.9% for $\hat{L}_u$ and of 5.7±2.9% for $\hat{E}_u$. The lowest are observed at 555 nm with averages of 2.2±0.6% for $\hat{L}_u$ and of 1.3±0.2% for $\hat{E}_u$.

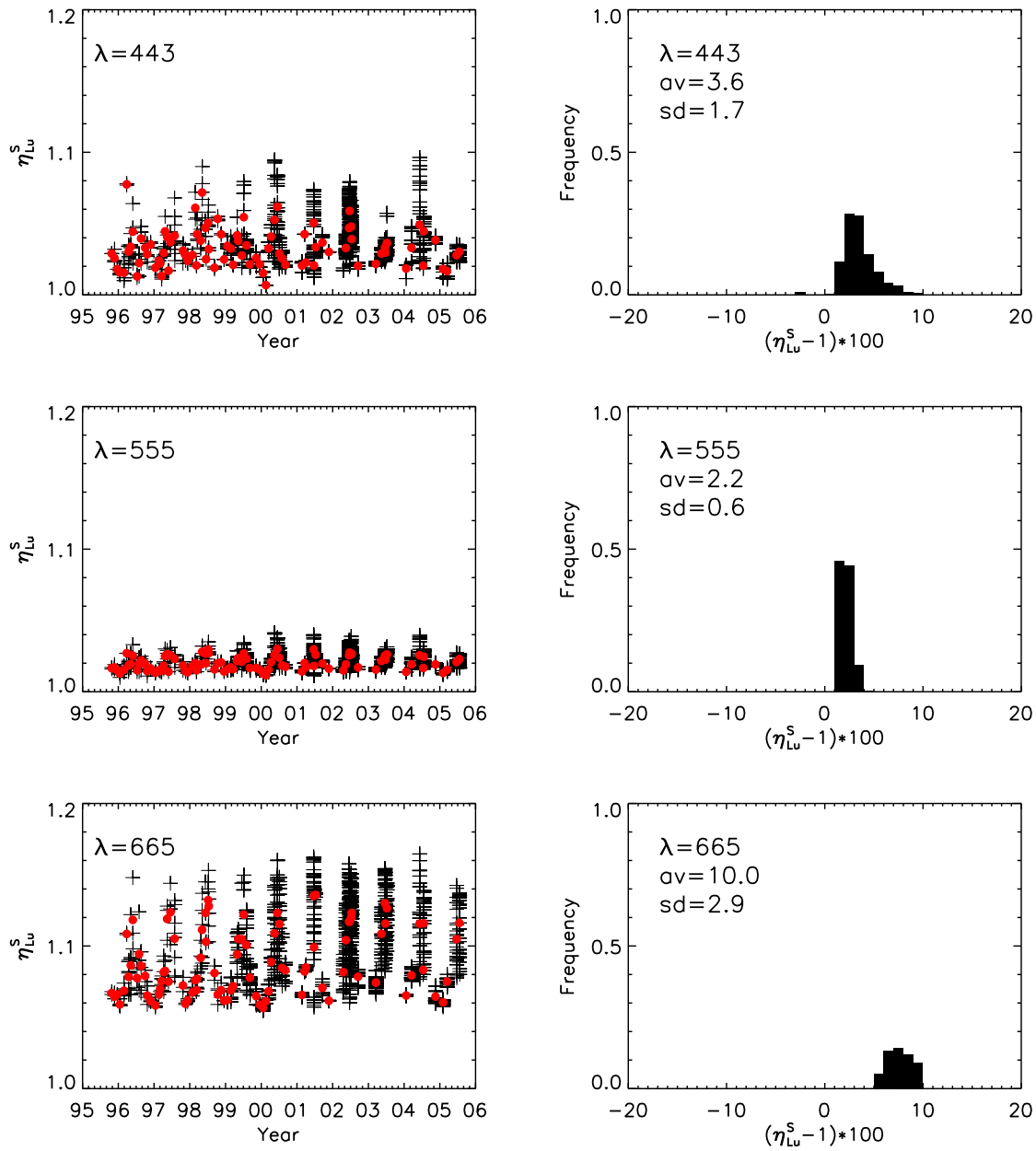


Figure 7.5: Self-shading correction, $\eta^S_{Lu}$, as a function of sampling time (between October 1995 and July 2005) and frequency distribution of its percent value $(\eta^S_{Lu} - 1) \cdot 100$, for the shadowed upwelling radiance $\hat{L}_u(\lambda)$ at 443, 555 and 665 nm (with av average value and sd standard deviation). The *bullet* symbols represent the average value per measurement campaign, symbols + indicate single measurement value (a single campaign can include as much as one week of data).

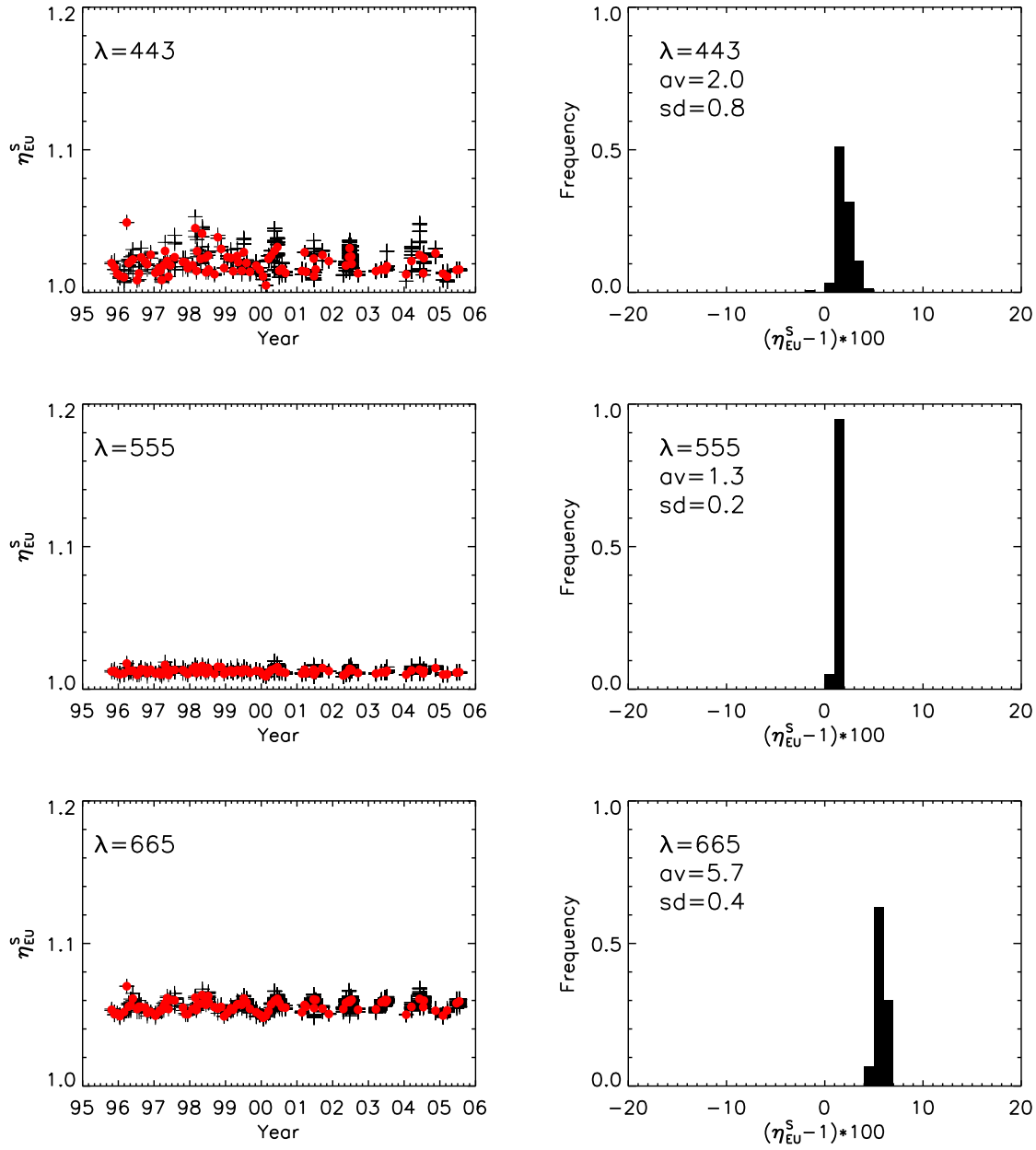


Figure 7.6: As in Fig. 7.5 but for $\eta^S_{Eu}$.

## 7.2 Superstructure perturbations

In the early 1970s data produced with a photographic system measuring the in–water radiance distribution (Smith et al., 1969), highlighted the effects of ship perturbations in light measurements (Smith, 1974). Approximately ten years later the ship-shading effects were quantitatively investigated through Monte-Carlo simulations (Gordon, 1985). This theoretical study led to the general recommendation of collecting in-water radiometric data at distances larger than 10 m from the ship to minimize the superstructure perturbations. Successive studies made by various investigators (Helliwell et al. (1990); Piskozub (2004); Saruya et al. (1996); Voss et al. (1986); Weir et al. (1994)) largely confirmed that in-water radiance and irradiance measurement uncertainties increase substantially when reducing the deployment distance of the instrument from the ship. Because of this, aiming at supporting operational optical radiometric measurements for satellite ocean color calibration and validation activities, Mueller and Austin (1995) suggested to determine the minimum ship distance from the instrument deployment point as a function of the seawater diffuse attenuation coefficient. More recently the need for accurately quantifying uncertainties in optical measurements taken nearby an oceanographic tower (i.e., the AAOT) in support of calibration and validation activities, led to the theoretical and experimental investigation of tower perturbations in optical radiometric data collected near its superstructure (Doyle et al., 2003; Zibordi et al., 1999). Results from this analysis became the rationale for the development and implementation of an operational method for the removal of superstructure effects in in-water radiance and irradiance measurements (Doyle and Zibordi, 2002).

### 7.2.1 Numerical modelling

The presence of a deployment structure at a measurement site is source of three-dimensional (3D) inhomogeneities and introduces abrupt medium changes within a predominantly plane-parallel system. Consequently, the simulation of superstructure shading effects on in–water optical radiometric measurements requires the 3D radiative transfer modelling of the ocean–atmosphere system. This is achieved by simulating radiative transfer processes using Monte Carlo methods to produce a solution of the generalized radiative transfer equation.

#### a. Principles for MC simulations

The Photon Transport (PHOTRAN) MC code, developed for the ocean–atmosphere system (Bulgarelli and Doyle, 2004; Doyle and Rief, 1998) was used to quantify the tower shading perturbations on in–water radiometric measurements. Radiances and irradiances at a specific point in the modeled system were computed using an implementation (Gordon, 1985) of Case's reciprocity relationship (Case, 1957).

Within PHOTRAN the ocean–atmosphere system is modeled on a 3D grid which delimits the macroscopic volumes (cells) each containing a medium of uniform optical properties. In each cell of the grid, the optically active components (air or water molecules, aerosols, hydrosols, etc.) are specified, and their IOPs are assigned (e.g., $c$, $\omega_0$, and $\tilde{\beta}$). Cell boundaries are spectrally characterized by transmittance and reflectance, and by the associated transmission and reflection angular distribution functions (ADFs). Specific ADFs are defined both for the source and for the detector.

Photons detected by a radiometer are a fraction of those emitted by the sun and reach the sensor after absorption, scattering, reflection, and refraction processes in the

ocean–atmosphere system. Accounting for the invariance of time-reversal processes characterizing the propagation of photons, backward MC methods are efficiently applied in the specific problem. Virtual photons initially having unitary statistical weight, are released from the detector within its field-of-view according to the predefined ADF. A free-flight optical distance to the next collision point is sampled (Lux and Koblinger, 1991), possible cell-boundary crossing processes are considered to define flight direction modifications, and finally, photon trajectory is computed taking into account possible changes in IOPs along the trajectory. At the collision point (defined as the point where the sampled optical distance is exhausted): (*i*) a scatterer is sampled and the virtual photon is re-weighted using $\omega_0$; and (*ii*) the flight direction of the re-weighted virtual photon is determined by retrieving the scattering angle from a random sampling of $\tilde{\beta}$. The latter is adequately modeled into an equal probability interval table (Lux and Koblinger, 1991). If virtual photons encounter a purely absorbing medium (i.e., the tower structure), their weight is zeroed. The single process is stopped when photons exit from the atmosphere. The weight of those virtual photons travelling in the direction of sun is then accounted for to quantify simulated measurements.

By tracking so-called *twin* virtual photons, one interacting with the tower and the other not, a *correlated sampling* scheme (Spanier and Gelbard, 1969) is produced which minimizes the score variance of differences between tower-perturbed and unperturbed signals. The number of initiated twin virtual photons defines the estimated statistical relative error on simulated data.

**b. Simulations for the AAOT**

The simulation frame consists of one large 3D box that encloses the grid defining the geometrical features of the system. The atmosphere, the ocean, and the boundaries (top of the atmosphere, sea surface, and sea floor) are modelled as horizontally plane-parallel. This plane-parallel symmetry is broken by introducing, at a specific location within the reference frame, a geometrical object schematically representing the AAOT with completely absorbing surfaces. The reference system for the simulation frame uses Cartesian orthonormal coordinates $(x, y, z)$, centered at a tower leg. The schematic of the tower structure and the relevant 3D features introduced in the PHOTRAN code are shown in Fig. 7.7.

The radiometer, located at a specific point in the reference frame, is described by its field-of-view and the associated ADF. The ADF for the direct source, as seen in a forward MC perspective, is formulated by a Dirac $\delta$ centered on the sun zenith, $\theta_0$, and sun azimuth, $\phi_0$. By modelling the atmosphere, sea surface, water column and sea floor following Zibordi et al. (1999), radiance is simulated assuming an in–water 20 degrees full-angle field-of-view with a unitary collection ADF. Irradiance is simulated assuming a $2\pi$ sr field-of-view with a cosine collection ADF.

By defining the tower shading error $\epsilon^T_{\Re}(\lambda)$ as the percent difference between the true and shading contaminated values for the specific radiometric quantity $\Re(\lambda)$, an extensive theoretical sensitivity analysis was carried out. PHOTRAN computations were performed assuming *typical* values of sea-water IOPs at the AAOT (Zibordi et al., 1999), and two extreme illumination conditions representing overcast and ideal clear sky (i.e., $\tau_a = 0$), with varying $\theta_0$ and $\phi_0 = 180$ degrees, and sensor distance from the superstructure $\chi = 7.5$ m. The value for $\chi$ was chosen to ensure exploration

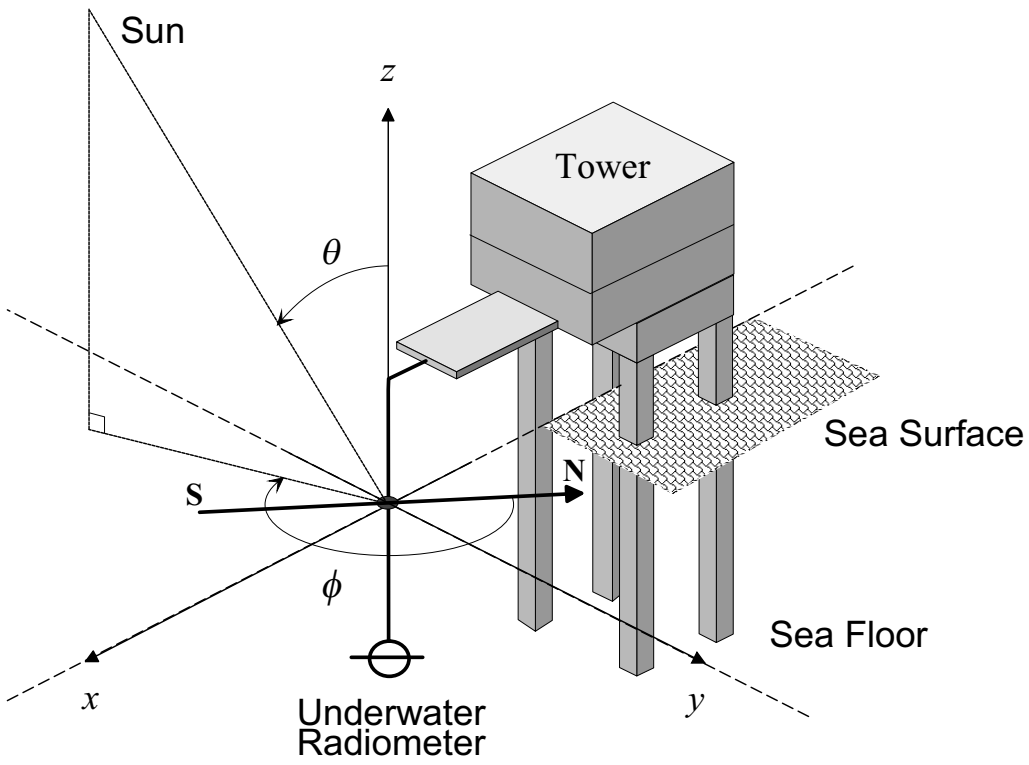


Figure 7.7: Schematic of the AAOT as defined in the PHOTRAN code (after Zibordi et al. (1999)).

of the AAOT shading effects at the location of the WiSPER radiometers; the value of $\phi_0$ was chosen to simulate the typical measurement conditions in which WiSPER is deployed from the sunny side of the tower.

Simulated downward irradiance $\epsilon^T_{Ed}(\lambda)$ and upwelling radiance $\epsilon^T_{Lu}(\lambda)$ errors, are summarized in Tab. 7.2 for overcast sky and in Fig. 7.8 for clear sky conditions at $z = 0^-$, and at the 443, 555, and 665 nm center-wavelengths.

Table 7.2: Computed tower shading errors for downwelling irradiance $E_d$ and upwelling radiance $L_u$ at $0^-$ depth and 7.5 m distance from the AAOT for a diffuse light source assuming *typical* values of inherent optical properties, at different wavelengths (in nm). Confidence intervals are given in parentheses (after Zibordi et al. (1999)).

| Parameter | Unit | 443 | 555 | 665 |
|---|---|---|---|---|
| $\epsilon_{Ed}^T$ | % | 19.8 ($\pm$0.2) | 19.9 ($\pm$0.2) | 20.1 ($\pm$0.2) |
| $\epsilon_{Lu}^T$ | % | 19.5 ($\pm$0.1) | 18.5 ($\pm$0.1) | 19.8 ($\pm$0.1) |

The data in Tab. 7.2 show values almost independent of wavelength for both $\epsilon_{Ed}^T(\lambda)$ and $\epsilon_{Lu}^T(\lambda)$. In fact, by assuming that for an overcast sky most of the perturbations are induced by interaction of the diffuse irradiance field with the superstructure of the tower, the shading error becomes closely proportional to the perturbed above–water irradiance. Consequently, $\epsilon_{Ed}^T(\lambda)$ — and analogously $\epsilon_{Lu}^T(\lambda)$ values — are very close and do not exhibit any significant dependence on $\lambda$.

Values of $\epsilon_{Ed}^T(\lambda)$ and $\epsilon_{Lu}^T(\lambda)$ in Fig. 7.8, show a strong dependence on $\theta_0$ and $\lambda$. The $\epsilon_{Ed}^T(\lambda)$ data show values increasing with $\theta_0$, while $\epsilon_{Lu}^T(\lambda)$ data show a more complex dependence on $\theta_0$ exhibiting minima close to 30 and 40 degrees, at 443 and 555 nm, respectively. The dependence on $\theta_0$ can be explained by the different perturbations induced by the AAOT on the nearby light field. During overcast sky conditions, the diffuse sky irradiance, $E_i(\lambda)$, is solely responsible for the in-water light field and the tower perturbation is uniformly cast in all directions. During clear sky conditions, when both the $E_i(\lambda)$ and the direct sun irradiance, $E_s(\lambda)$, contribute to the in-water light field, the perturbation associated with $E_i(\lambda)$ adds to that associated with $E_s(\lambda)$. The latter perturbation results in a pronounced tower shadow projected in the direction opposite to the sun, which is also opposite to the measurement side of

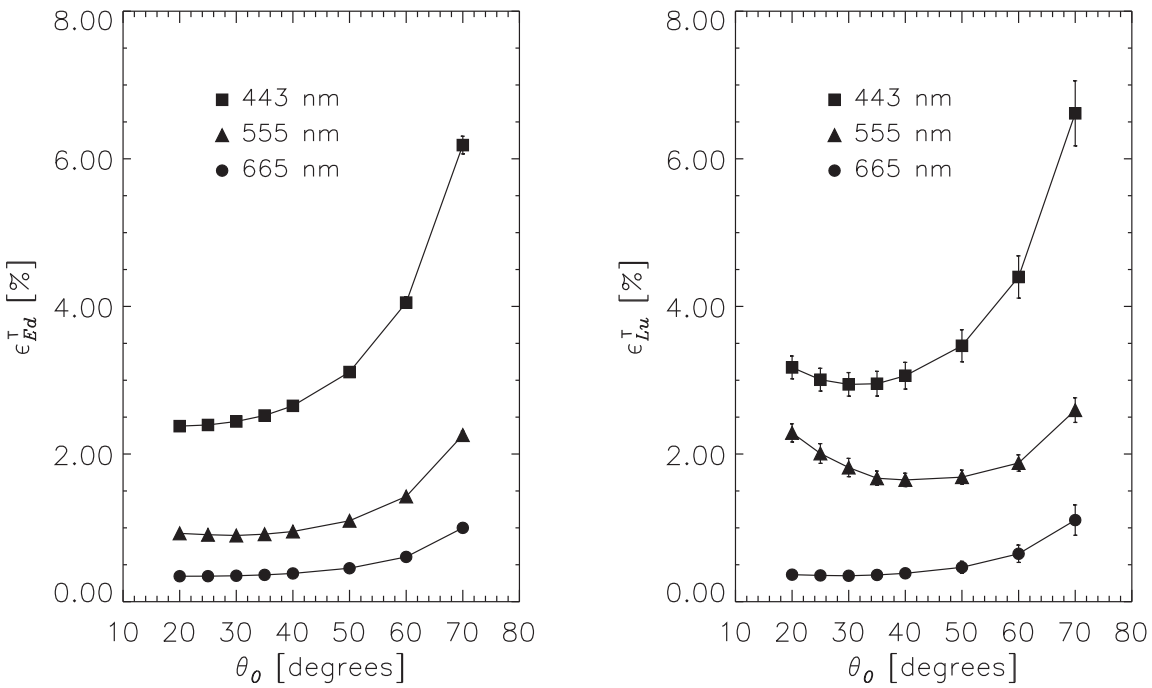


Figure 7.8: Simulated tower-shading errors $\epsilon^T_{Ed}$ and $\epsilon^T_{Lu}$ at $0^-$ depth and 7.5 m distance from the tower as a function of $\theta_0$ assuming $\phi = 180$ degrees and ideal clear-sky conditions. The vertical bars show the confidence limits for the simulation (after Zibordi et al. (1999)).

the tower. Then, during clear sky conditions, excluding cases characterized by very low values of $\theta_0$, $E_s(\lambda)$ creates perturbations that are confined at some distance from the measurement point. These perturbations produce shading errors which decrease with increasing $\theta_0$ as shown in Fig. 7.9 (the $\epsilon^T_{Ed}(\lambda)$ and $\epsilon^T_{Lu}(\lambda)$ values shown in Fig. 7.9 were computed analogously to those proposed in Fig. 7.8, but assuming no atmosphere). These errors add to those produced by $E_i(\lambda)$, which increase with $\theta_0$ (as a result of an increase of $E_i(\lambda)$ with $\theta_0$). Consequently, these errors vary significantly both with $\theta_0$ and with the ratio $I_r(\lambda)$, exhibiting the trends displayed in Fig. 7.8 for $\epsilon^T_{Ed}(\lambda)$ and $\epsilon^T_{Lu}$. The $\epsilon^T_{Ed}(\lambda)$ values shown in Fig. 7.9, contrary to the $\epsilon^T_{Lu}(\lambda)$ values, should be virtually zero at $0^-$ m. However, for computational needs, a depth of 1 mm

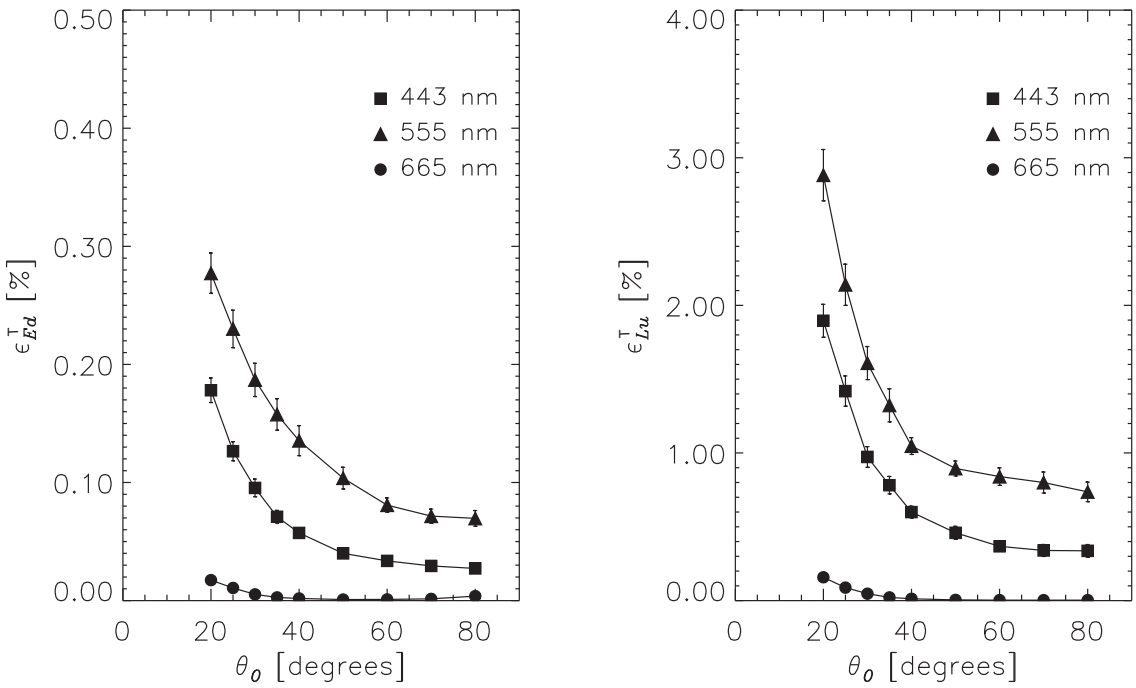


Figure 7.9: Simulated tower-shading errors $\epsilon^T_{Ed}$ and $\epsilon^T_{Lu}$ at $0^-$ depth and 7.5 m distance from the tower as a function of $\theta_0$ assuming $\phi = 180$ degrees and no atmosphere. The vertical bars show the confidence limits for the simulation (after Zibordi et al. (1999)).

is assigned to the $E_d$ sensor. This depth induces the observed nonzero $\epsilon^T_{Ed}$ at $0^-$ m, which in any case has little weight on the $\epsilon^T_{Ed}(\lambda)$ values displayed in Fig. 7.8.

### 7.2.2 Experimental assessment of simulations

An AAOT field experiment was designed to estimate shading effects on in–water radiometric data collected in close proximity to the tower. Sequential optical profiles taken with the Low Cost NASA Environmental Sampling System (LoCNESS) were used to determine the shading effects on downwelling irradiance, $\hat{E}_d(\chi, z, \lambda, t)$, and upwelling radiance, $\hat{L}_u(\chi, z, \lambda, t)$, where $\chi$ is the distance of the profiler from the tower, $z$ is the water depth, $\lambda$ is the wavelength, and $t$ is time. Concurrent with LoCNESS

data, above-water downward irradiance data at $\chi = 0$ m, $E_d(0, 0^+, \lambda, t)$, were collected with an in–air reference sensor. Different experiments were conducted during almost clear sky conditions with variable LoCNESS deployment distances ranging from 2.5 m to 22.5 m with respect to the tower.

The in–water optical measurements were normalized by the solar irradiance measured on the tower to account for temporal changes in the light field; that is, $\hat{E}_d$ and $\hat{L}_u$ values for a given profile (indicated by $\chi$) at a particular depth, wavelength and time, were divided by the corresponding above-water irradiance at the same time

$$nE_d(\chi, z, \lambda, t) = \frac{\hat{E}_d(\chi, z, \lambda, t)}{E_d(0, 0^+, \lambda, t)} \tag{7.2.1}$$

and

$$nL_u(\chi, z, \lambda, t) = \frac{\hat{L}_u(\chi, z, \lambda, t)}{E_d(0, 0^+, \lambda, t)} \tag{7.2.2}$$

The $nE_d(\chi, z, \lambda, t)$ and $nL_u(\chi, z, \lambda, t)$ profile data were binned at depths $z_i$ using depth intervals of 0.5 m (ranging from $z_i$ + 0.25 m to $z_i$ – 0.25 m) resulting in $nE_d(\chi, z_i, \lambda, t_i)$ and $nL_u(\chi, z_i, \lambda, t_i)$ values, where $t_i$ is the average time for each binning interval associated with depth $z_i$.

The data analysis was restricted to 443, 555, and 665 nm, assumed as representative wavelengths of the visible spectrum. The multiple profiles at a variety of distances from the tower (see Fig. 7.10), show almost regular and correlated variations. A careful examination of $nE_d(\chi, z_i, \lambda, t_i)$ and $nL_u(\chi, z_i, \lambda, t_i)$ values indicates higher noise in the surface data between 0–4 m depth for the former than for the latter. This is a consequence of the wave effects induced by a sea state of about 2 according to the WMO scale (WMO, 1983). Further examination of $nL_u(\chi, z_i, \lambda, t_i)$, clearly show the bottom effects which, becoming more pronounced on depth increase, induce a change in the slope of profiles. This change is not appreciable at 443 nm, but appears much

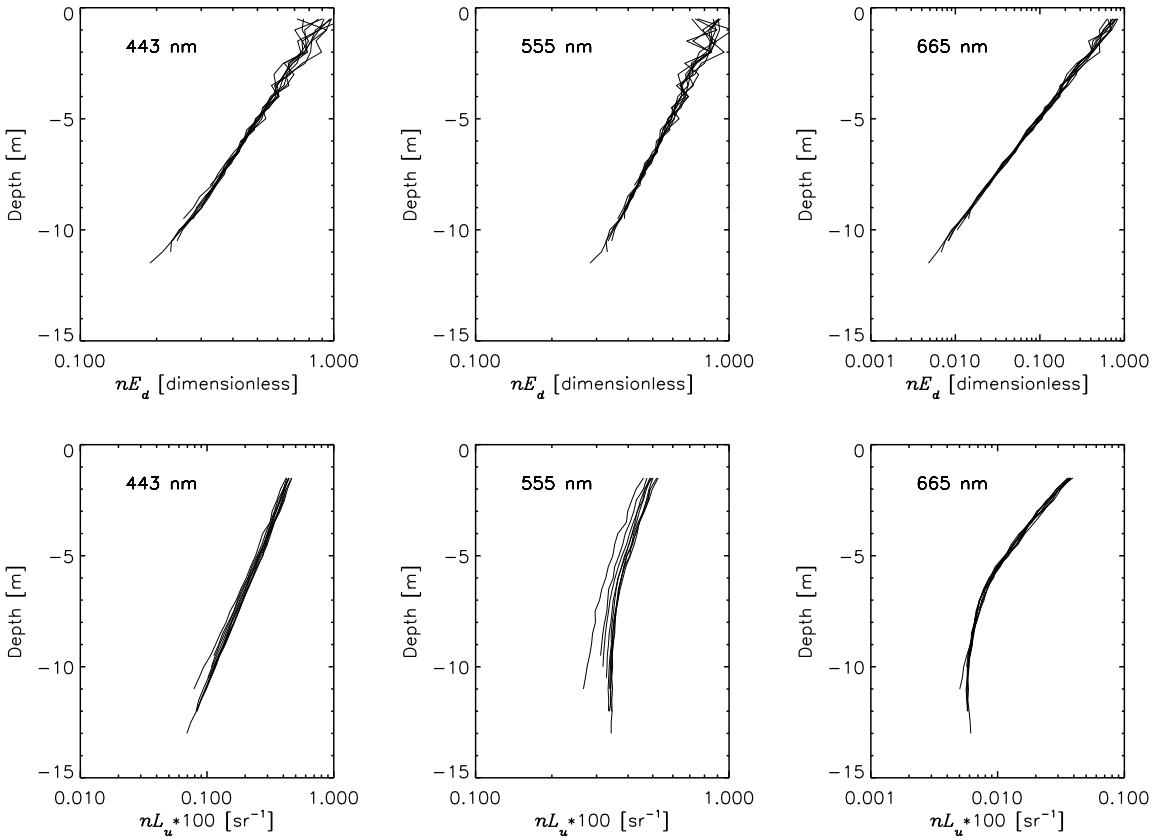


Figure 7.10: LocNESS profiles of $nE_d$ and $nL_u$. Profiles are presented at 443, 555 and 665 nm center-wavelengths at different distances from the tower. The profiles were taken with $\theta_0$ between 22–23 degrees and $\phi_0$ between 182–194 degrees (after Zibordi et al. (1999)).

more significant at 665 nm in agreement with the relatively low $\rho_b$ at 443 nm, and the much higher $\rho_b$ values 665 nm (Zibordi et al., 2002b). The percent change between radiometric quantities at different deployment distances away from the tower are discerned by choosing one deployment point as an origin, $\chi_\circ$, and then dividing the depth bin values for all deployment points by the appropriate depth bin value for the origin. Therefore, $nE_d(\chi, z_i, \lambda, t_i)$ and $nL_u(\chi, z_i, \lambda, t_i)$ series were re-normalized by the measurement taken at the origin point, $nE_d(\chi_\circ, z_i, \lambda, t_i)$ and $nL_u(\chi_\circ, z_i, \lambda, t_i)$

respectively, obtaining the following primed quantities

$$nE'_d(\chi, z_i, \lambda, t_i) = \frac{nE_d(\chi, z_i, \lambda, t_i)}{nE_d(\chi_o, z_i, \lambda, t_i)} \tag{7.2.3}$$

and

$$nL'_u(\chi, z_i, \lambda, t_i) = \frac{nL_u(\chi, z_i, \lambda, t_i)}{nL_u(\chi_o, z_i, \lambda, t_i)} \tag{7.2.4}$$

For the following analysis $\chi_0$=22.5 m was chosen as the origin, assuming the tower shading effects are negligible at this distance (so the $nE'_d$ and $nL'_u$ values at $\chi = 22.5$ m are equal to 1.0). To minimize wave effects – which can induce noise of the order of several percent in surface values – as well as to avoid intervals close to the bottom where data were not available, the analysis of $nE'_d$ and $nL'_u$ was carried out using depth bins at intermediate depths.

A plot of $nE'_d$ and $nL'_u$ experimental data (empty circles) is given in Fig. 7.11 as a function of $\chi$. These values, given at $z_i = 7$ m, result from the averaging of the five depth bins between $z_i = 6$ m and $z_i = 8$ m. The averaging was applied to smooth the relevant wave noise still present at several meters depth. The error bars on symbols associated with the experimental data represent the standard deviation of the plotted mean values. PHOTRAN simulations at $z_i = 7$ m, performed using input data measured during the experiments (i.e., $\tau_a$, $\rho_b$, plus $c$ and $\omega_0$), are also shown in Fig. 7.11 as solid circles. The related error bars represent the confidence limits resulting from the precision spread produced by the standard deviation on the mean simulated signal, which was generated with 100,000 initiated photons.

The $nE'_d$ data in Fig. 7.11 (top three panels) show that a slight trend characterizes the downwelling irradiance changes as a function of $\chi$, with the exception of experimental data at 665 nm. Simulated data show that at $\chi = 7.5$ m (i.e., at the location of the WiSPER radiometers) irradiance changes —with respect to values at

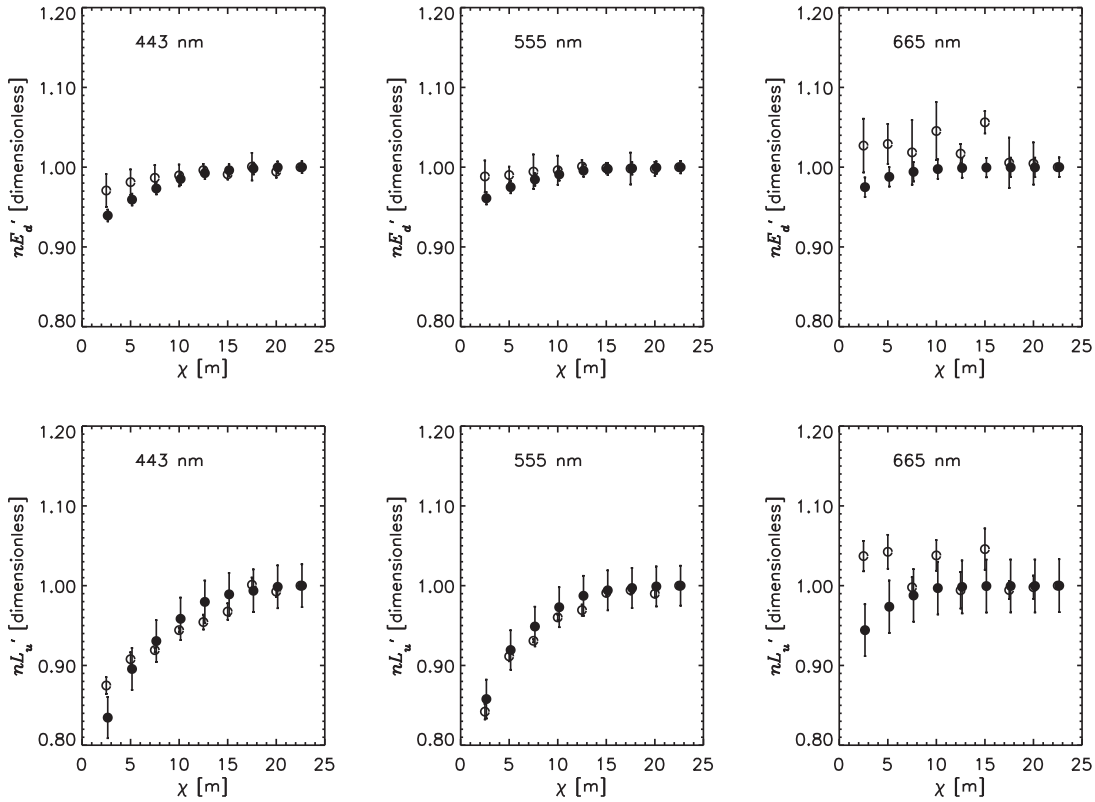


Figure 7.11: Irradiance and radiance relative variations, $nE'_d$ and $nL'_u$, respectively, as a function of distance from the AAOT as obtained from the profiles displayed in Fig. 7.10. Data are given at a depth of 7 m at 443, 555, and 665 nm. Symbols ○ and ● indicate experimental and theoretical data, respectively, with $\theta_0 = 23$ degrees and $\phi_0 = 190$ degrees. The vertical bars on symbols ○ indicate standard deviation for experimental data while on ● show the confidence limits for the simulated data.

$\chi = 22.5$ m— are less than 3%, 2%, and 1% at 443, 555, and 665 nm, respectively. The $nL'_u$ data in Fig. 7.11 (bottom three panels) show that, again with the exception of experimental data at 665 nm, the upwelling radiance has a pronounced dependence on $\chi$. Simulated data show that at $\chi = 7.5$ m, radiance changes are less than 7%, 5%, and 2% at 443, 555, and 665 nm, respectively. The $nE'_d$ and $nL'_u$ experimental data at 665 nm are, as expected, very noisy. Their high standard deviation can be mainly attributed to wave effects acting on the direct sun irradiance transmitted across the

sea surface. This direct component represents an increasingly larger percentage of the total signal at longer wavelengths.

A remarkable agreement between simulated and experimental data is observed for $nL'_u$ at 443 nm and 555 nm. The experimental data are generally within the confidence limits of the simulated data. On the contrary, a slightly different trend characterizes experimental and simulated values of $nE'_d$ at 443 nm and 555 nm. In fact, for $\chi < 10$ m, the experimental data show systematically higher values than those of simulated data. This is probably because of the approximations introduced in the description of the AAOT within the PHOTRAN code: a simplified geometry and the assumption of *completely absorbing* surfaces needed by the correlated sampling scheme. The latter assumption is likely to produce an overestimate of the shading effects. These overestimates are expected to be more pronounced in $nE'_d$ rather than in $nL'_u$ because $\hat{E}_d$ measurements are more sensitive than $\hat{L}_u$ to light reflected by the tower surfaces. It is also possible that radiance and irradiance contributions, due to reflectance of the AAOT surfaces are the source of the $nE'_d$ and $nL'_u$ experimental values higher than 1.0, observed at 665 nm for $\chi \leq 15$ m.

### 7.2.3 Correction scheme for superstructure perturbations

A tower-shading correction scheme based on MC simulations was developed for radiometric measurements taken during the differing environmental conditions found at the AAOT site. The multidimensional character of the problem supported the concept of implementing a look-up table correction scheme, rather than a general analytical approach. The computation of an extensive set of specific correction factors thus led to the construction of a look-up table designed for operational shadow

corrections.

The correction of $\hat{\Re}(\lambda)$ (i.e., $\hat{L}_u(\lambda)$, $\hat{E}_d(\lambda)$ and $\hat{E}_u(\lambda)$) is obtained through the multiplication factor $\eta^T_{\Re}$, where

$$\epsilon^T_{\Re}(\lambda) = 1 - \frac{1}{\eta^T_{\Re}(\lambda)} \tag{7.2.5}$$

For each $\lambda$, the $\eta^T_{\Re}(\lambda)$ factor was computed for a different set of discrete values of the following parameters: the solar zenith and azimuth angles, $\theta_0$ and $\phi_0$ (including independent overcast sky); the aerosol optical thickness, $\tau_a(\lambda)$, providing the corresponding diffuse to direct irradiance ratio, $I_r(\theta_0, \lambda)$; total seawater absorption coefficient, $a(\lambda)$; total seawater single scattering albedo, $\omega_0(\lambda)$; and the spectrally linked bottom reflectance $\rho_b(\lambda)$, ozone $\tau_o(\lambda)$ and and Rayleigh $\tau_R(\lambda)$ optical thicknesses. The discretization range and resolution for these parameters was chosen so that they are representative of the variability observed at the AAOT site.

The appropriate factor $\eta^T_{\Re}(\lambda)$ for a subsurface radiometric measurement is found through a matching of the actual values across the parameter grid that underlies the look-up table, with the exception of $\tau_a(\lambda)$ for which $I_r(\theta_0, \lambda)$ is used. Even though the proposed look-up table is in principle valid under clear sky conditions only, the use of $I_r(\theta_0, \lambda)$ (instead of $\tau_a(\lambda)$) as a matching parameter for indexed $\eta^T_{\Re}(\lambda)$ values better describes general illumination conditions accounting for skylight inhomogeneity. In fact, $\tau_a(\lambda)$ is less representative than $I_r(\theta_0, \lambda)$ of the actual field conditions under cloud perturbations. Appropriate $\eta^T_{\Re}(\lambda)$ correction factors are also provided for totally diffuse skylight, assuming an isotropic distribution of the sky radiance.

Corrections for tower-shading applied to radiometric measurements performed at the AAOT in the period October 1995 - July 2005, are displayed in Fig.'s 7.12 through 7.14 for $\hat{L}_u(\lambda)$, $\hat{E}_d(\lambda)$ and $\hat{E}_u(\lambda)$, respectively. These time-series of correction

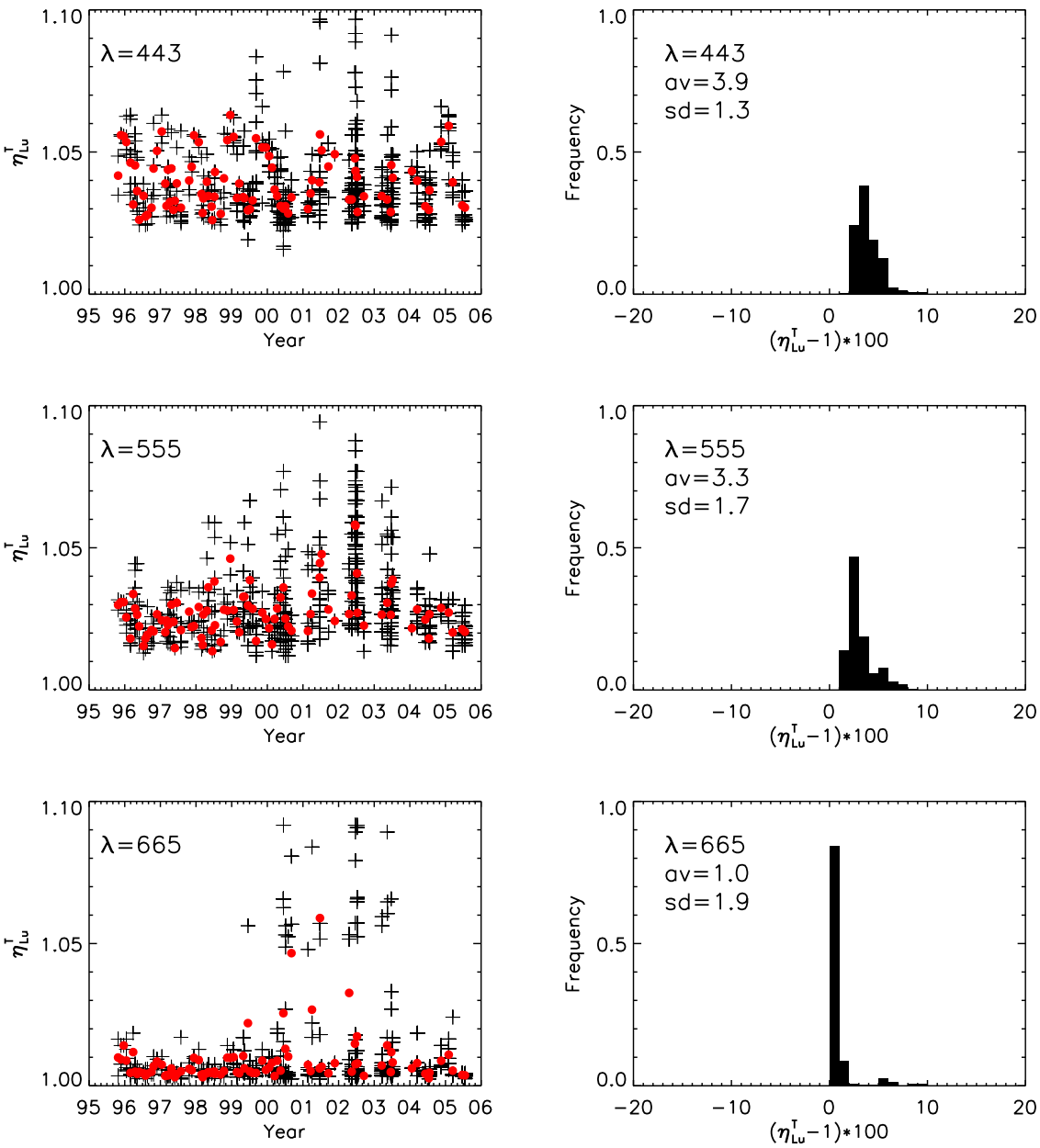


Figure 7.12: Tower-shading percent correction, $\eta^T_{Lu}$, as a function of sampling time (between October 1995 and July 2005), and the frequency distribution of its percent value $(\eta^T_{Lu} - 1) \cdot 100$ for the shadowed upwelling radiance $\hat{L}_u(\lambda)$ at 443, 555 and 665 nm (with av average and sd standard deviation). The *bullet* symbols represent the average value per measurement campaign, symbols + indicate single measurement value (a single campaign can include as much as one week of data).

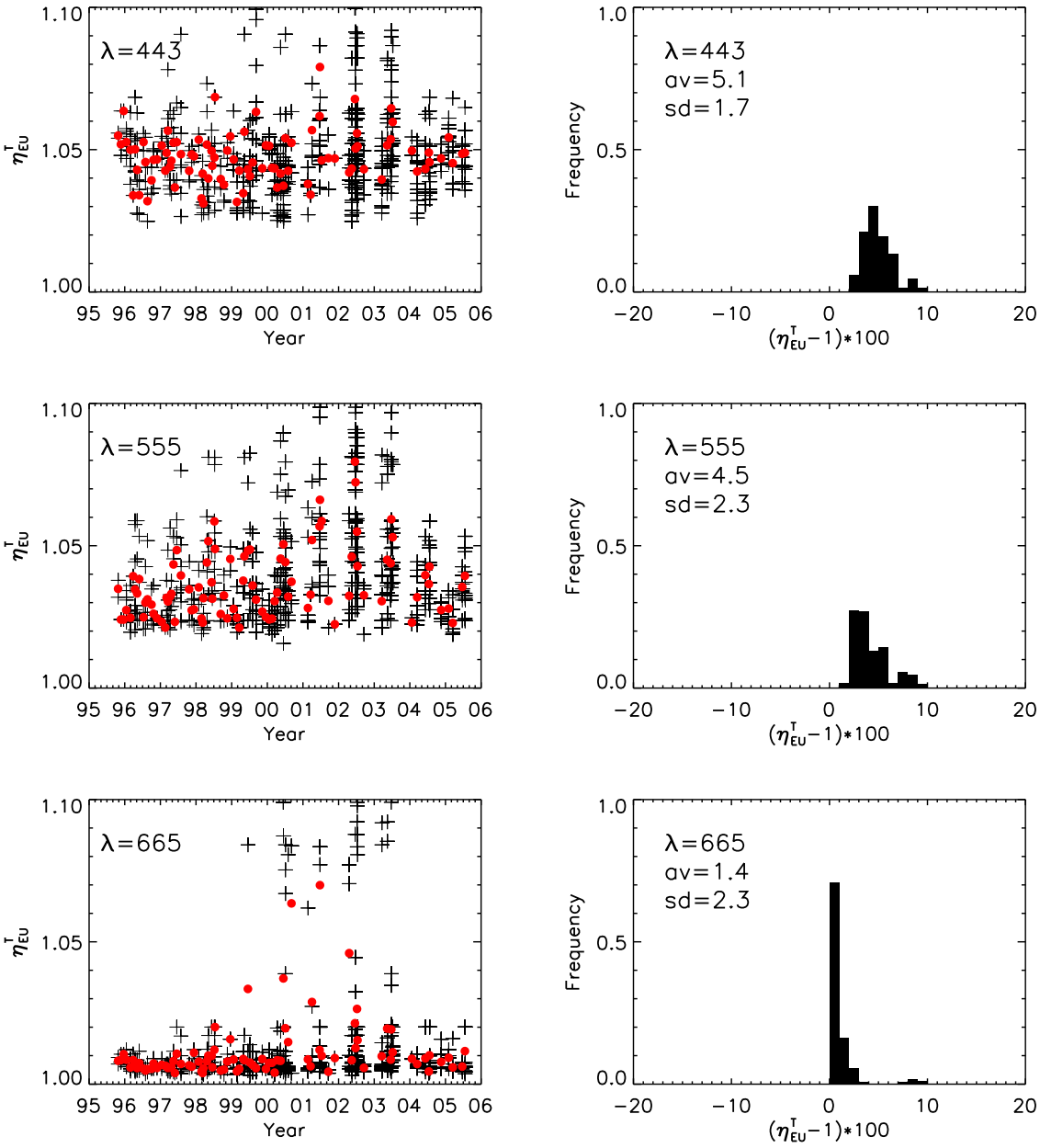


Figure 7.13: As in Fig. 7.12 but for $\eta^T_{Eu}$.

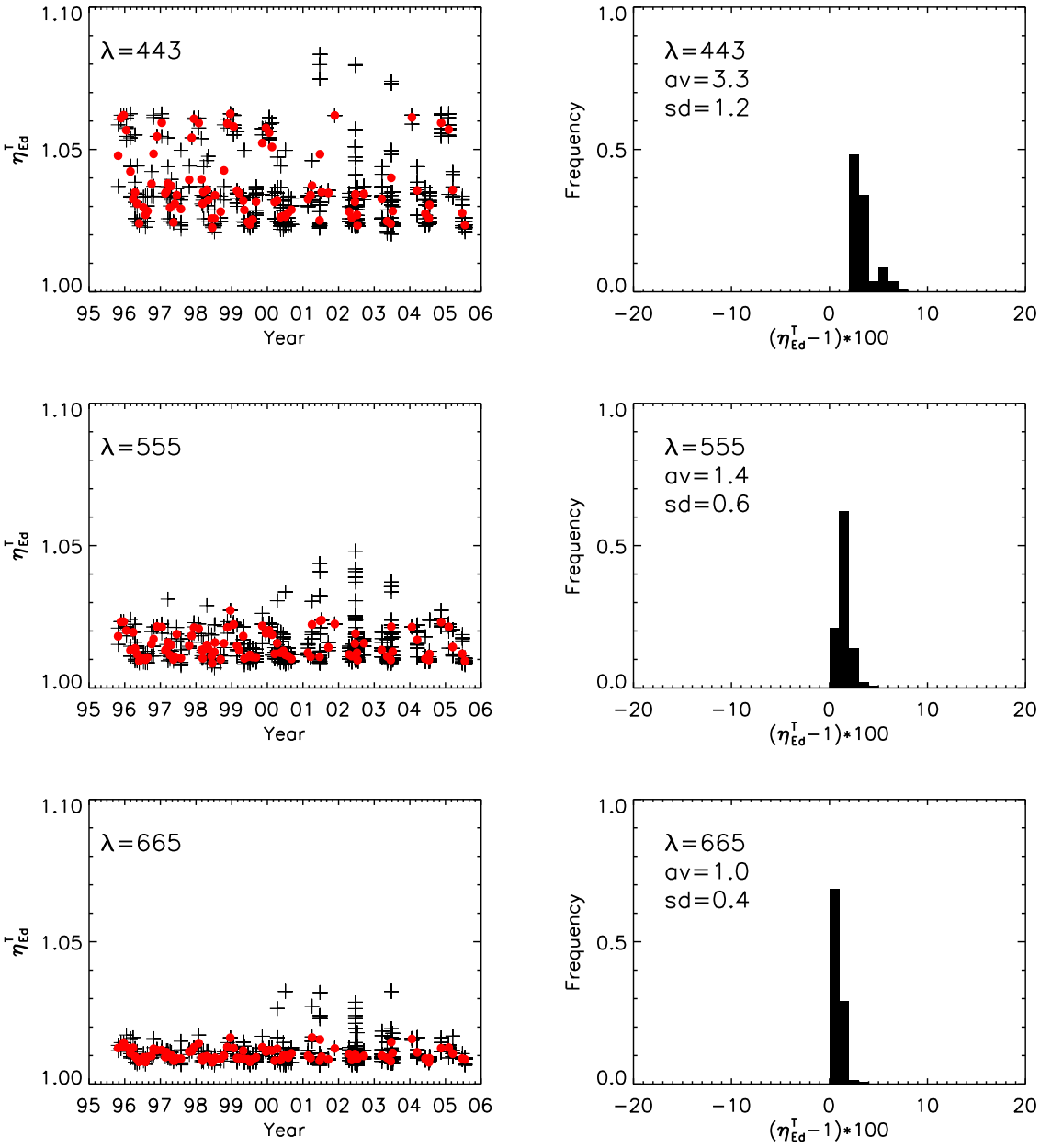


Figure 7.14: As in Fig. 7.12 but for $\eta^T_{Ed}$.

factors indicate some seasonal dependence of $\eta_{Lu}^{T}(\lambda)$, $\eta_{Ed}^{T}(\lambda)$ and $\eta_{Eu}^{T}(\lambda)$ attributed to sun zenith changes (being most of the data collected close to the daily sun zenith maximum), and random effects more likely attributed to changes in seawater inherent optical properties. The highest corrections are observed in the blue at the 443 nm center-wavelength with values of 3.9±1.3%, 5.1±1.7% and 3.3±1.2% for $\hat{L}_u$, $\hat{E}_d$ and $\hat{E}_u$, respectively.

An experimental assessment of the proposed scheme in minimizing tower perturbations, showed remarkably good results with absolute differences generally lower than 2% between measured and estimated values (Doyle et al., 2003).

## 7.3 Bottom effects

Shallow bottoms perturb the upward radiance and irradiance fields and consequently affect the determination of apparent optical properties representative of semi-infinite seawater systems.

Bottom effects in optical radiometric data have been addressed in several independent studies. Among these, Plass and Kattawar (1972) investigated the effects of the albedo of the bottom on the upward flux, Gordon and Brown (1974) explored the diffuse reflectance of a shallow ocean, Lyzenga (1978) addressed the problem of extracting water depth and bottom type information from passive multi-spectral scanner data using radiative transfer simulations, Ackleson and Klemas (1986) developed a two-flow model to simulate the light field within a canopy of bottom adhering plants, Philpot (1987) proposed a single scattering approximation for irradiance reflectance in shallow waters, Leathers and McCormick (1999) proposed a method for determining the bottom albedo from upward and downward irradiances, Mobley et al.

(2003) investigated the effects of non-Lambertian bottom reflectance in above-water remote-sensing reflectance or in in-water upwelling radiance, and Maritorena et al. (1994) developed an analytical method to estimate the reflectance of shallow waters as a function of the observation depth, bottom depth and albedo. The last approach was applied for the implementation of a correction scheme to minimize the bottom effects on in-water radiometric measurements performed at the AAOT.

### 7.3.1 Correction scheme for bottom effects

The correction for bottom effects in $\hat{L}_u(0^-, \lambda)$ and $\hat{E}_u(0^-, \lambda)$ can be accomplished using an analytical model derived from that proposed by Maritorena et al. (1994) for bottom correction of irradiance reflectance. Following Zibordi et al. (2002b), the bottom-corrected upward irradiance just below the surface, $E_u(0^-, \lambda)$, is modelled as

$$E_u(0^-, \lambda) = \frac{1}{1 - t_b(z_B, \lambda)}[\hat{E}_u(0^-, \lambda) - \rho_b(\lambda) E_d(0^-, \lambda) t_b(z_B, \lambda)] \tag{7.3.1}$$

where $t_B(z_B, \lambda)$, the transmittance for the downward plus upward normal optical paths between the surface and the bottom at depth $z_B$, is given by

$$t_B(z_B, \lambda) = exp[-2\bar{K}_d(\lambda) z_B] \tag{7.3.2}$$

with $\bar{K}_d$, so-called *operational* diffuse attenuation coefficient, assumed equal to the average diffuse attenuation coefficient obtained from the linear regression of $ln[E_d(z, \lambda)]$ versus depth $z$ between the surface and the bottom depth, $z_B$. The quantity $\rho_b(\lambda)$, indicating the bottom reflectance, is determined as

$$\rho_b(\lambda) = \frac{\hat{E}_u(z_B, \lambda)}{E_d(z_B, \lambda)} \tag{7.3.3}$$

where $\hat{E}_u(z_B, \lambda)$ and $E_d(z_B, \lambda)$ are the values of $\hat{E}_u(z, \lambda)$ and $E_d(z, \lambda)$ measurements extrapolated as a function of $z$ to the bottom depth, $z_B$.

Similar to $E_u(0^-, \lambda)$, the bottom corrected upward radiance $L_u(0^-, \lambda)$ is modelled as

$$L_u(0^-, \lambda) = \hat{L}_u(0^-, \lambda) - \frac{\rho_b(\lambda) E_d(0^-, \lambda) t_B(z_B, \lambda)}{\hat{Q}_n(0^-, \lambda)} \tag{7.3.4}$$

where $\hat{Q}_n(0^-, \lambda) = \hat{E}_u(0^-, \lambda)/\hat{L}_u(0^-, \lambda)$. The former relationship assumes that $\hat{Q}_n(0^-, \lambda)$ is not affected by bottom effects, i.e., $\hat{E}_u(0^-, \lambda)$ and $\hat{L}_u(0^-, \lambda)$ are equally affected by the bottom perturbations. Even though this assumption is only valid in isotropic conditions (i.e., when $\hat{Q}_n(0^-, \lambda) = \pi$ and the bottom reflectance $\rho_b(\lambda)$ is Lambertian) it can be shown that with corrections of 10%, an extreme uncertainty of $\pm 10\%$ in $\hat{Q}_n(0^-, \lambda)$ induces an uncertainty of approximately $\pm 0.5\%$ in $L_u(0^-, \lambda)$.

Similarly to self-shading, accounting for Eq. 7.1.6 and Eq. 7.1.1, the operational correction $\eta^B_{\Re}(\lambda)$ applied to the radiometric quantities $\hat{\Re}(0^-, \lambda)$ to minimize the bottom perturbations is given by

$$\eta^B_{\Re}(\lambda) = \frac{\Re(0^-, \lambda)}{\hat{\Re}(0^-, \lambda)} \tag{7.3.5}$$

Corrections factors $\eta^B_{Lu}(\lambda)$ and $\eta^B_{Eu}(\lambda)$ for bottom effects applied to radiometric measurements performed at the AAOT in the period October 1995 - July 2005, are displayed in Fig.'s 7.15 and 7.16 for $\hat{L}_u(\lambda)$ and $\hat{E}_u(\lambda)$, respectively. Time-series display quite close spectral correction values for both $\hat{L}_u(\lambda)$ and $\hat{E}_u(\lambda)$ with the highest average values, i.e., -1.3±2.1%, at 555 nm where light penetration is higher than in other spectral regions. As expected the corrections are negligible in the red due to the high absorption coefficient of seawater.

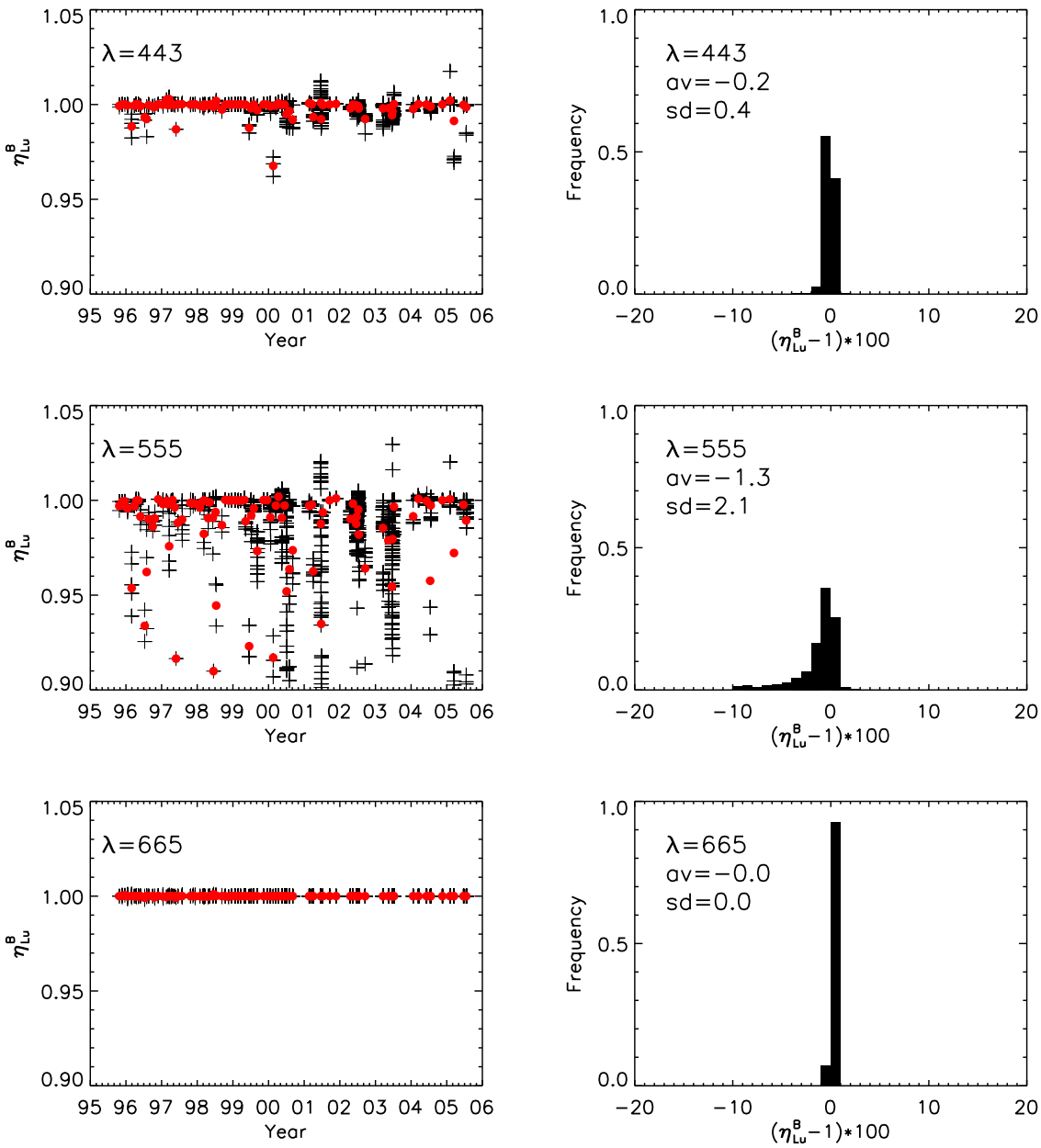


Figure 7.15: Bottom effects percent correction, $\eta^B_{Lu}$, as a function of sampling time (between October 1995 and July 2005), and frequency distribution of its percent value $(\eta^B_{Lu} - 1) \cdot 100$, for the shadowed upwelling radiance $\hat{L}_u(\lambda)$ at 443, 555 and 665 nm (with av indicating the average and sd the standard deviation). The *bullet* symbols represent the average value per measurement campaign, symbols + indicate single measurement value (a single campaign can include as much as one week of data).

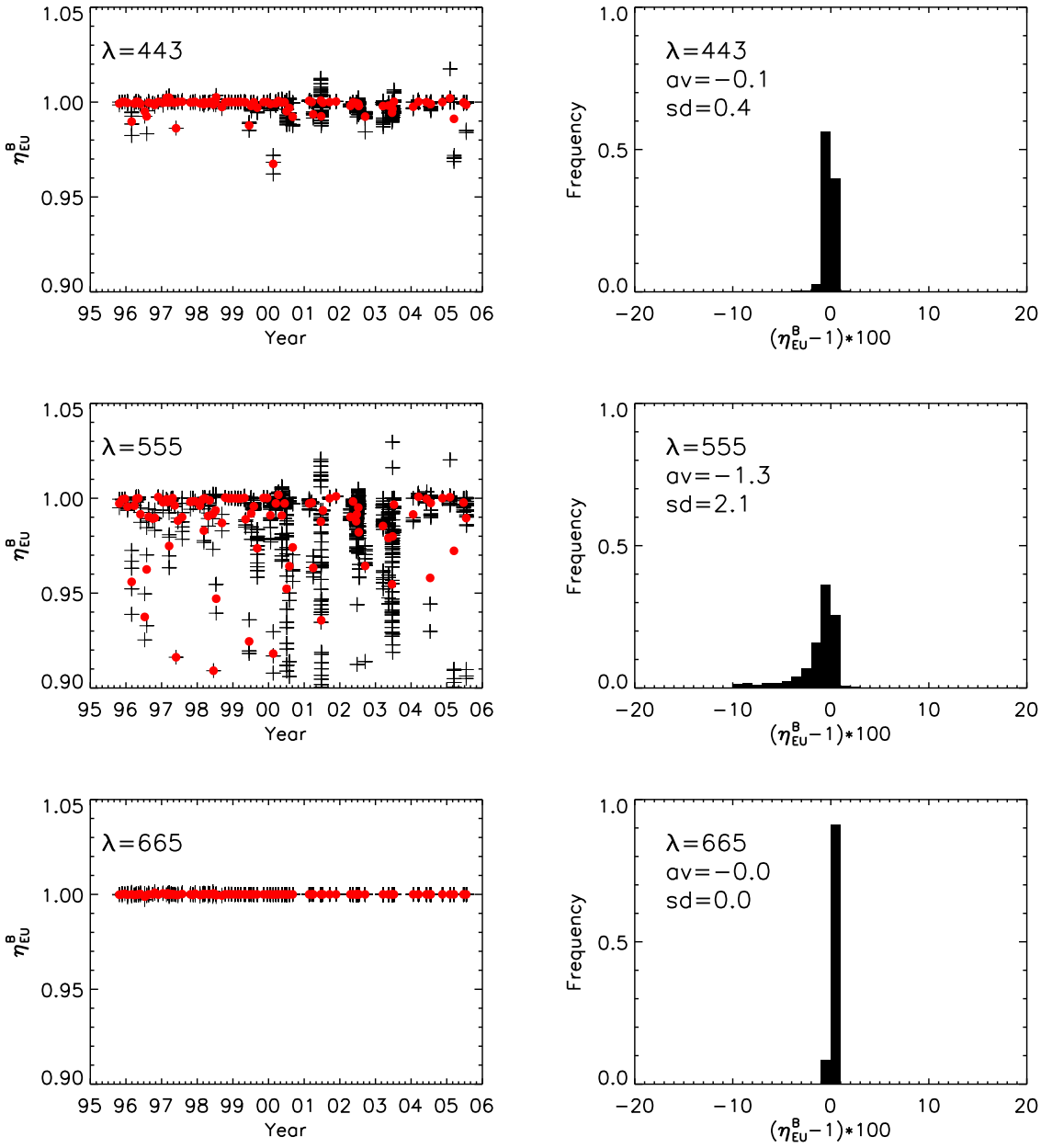


Figure 7.16: As in Fig. 7.15 but for $\eta^B_{Eu}$.

## 7.4 Wave perturbations

The focusing and defocusing of sun rays refracted by surface waves produce large light fluctuations in the upper sea layer. The origin, amplitude, frequency and depth extension of these fluctuations were addressed both theoretically (e.g., Schenck 1957, Snyder and Dera 1970, Stramski and Dera 1988, Walker 1994, Zaneveld et al. 2001) and experimentally (e.g., Dera and Olszewski 1978, Dera and Stramski 1986, Weidemann et al. 1990, and Dera et al. 1993).

Making use of measurements acquired at the 525 nm single center-wavelength and at a typical fixed depth of $\sim$1 m, Dera and Stramski (1986), showed that the frequency of the so called *light flashes* (i.e., fluctuations in intensity exceeding the mean irradiance by a factor of about 1.5) can be higher than 3 Hz and it exponentially decreases with increasing flash intensity. The most probable duration of flashes was estimated between a few and tens of milliseconds. Dera and Stramsky (1986) were also observing a reduction in the fluctuation of irradiance intensity and an increase of flashes duration on water depth increase. The wave focusing effects were also found to be more significant in clear sky conditions, clear water, low sun zenith, and relatively smooth water surface driven by a wind speed of 2-5 $ms^{-1}$. A further relevant result of their work was an analysis of wave effects in the downward irradiance data as a function of the diameter of the collector, showing a reduction in fluctuations with an increase of the diameter of the collector in the 2-6 mm range.

Weideman et al. (1990) addressed the uncertainties in the determination of the diffuse attenuation coefficient from downward irradiance measurements simultaneously taken at fixed depths in a ground tank on controlled water surface perturbations. On wave height increase, results showed uncertainties up to 30% in the computed diffuse

attenuation coefficient.

Moving to optical profiles, Zaneveld et al. (2001) presented experimental data and theoretical simulations of wave induced perturbations in downward irradiance. Their study proposed a method for the determination of the diffuse attenuation coefficient from profile data perturbed by waves. The method, suitable for optical profiles taken in the open ocean where the extrapolation interval can be quite extended, is based on the upward integration of the irradiance data starting at a depth at which the irradiance profile is only weakly affected by waves.

Intuitively, for a given optics any increase in the acquisition rate and decrease in the deployment speed is expected to produce an increase in the accuracy of the subsurface optical quantities due to a more extended averaging of the wave effects over time as a function of depth. Commercial instruments like optical free-fall profilers, however, exhibit limitations. Their deployment speed is in general higher than 0.2 $ms^{-1}$, while the acquisition rate can be as low as 6 Hz.

### 7.4.1 Perturbations in in–water radiometry

Sample WiSPER $L_u(z,\lambda)$ and $E_d(z,\lambda)$ profiles are presented in Fig. 7.17 for different measurement conditions characterized by wave height of ∼10 cm with $K_d(490)$=0.20 $m^{-1}$ determined in the 0.3–2.5 m extrapolation interval (panels *a* and *b*), and by wave height of ∼40 cm with $K_d(490)$=0.09 $m^{-1}$ determined in the 0.3–4.0 m extrapolation interval (panels *c* and *d*). The semi-logarithmic plot of $L_u(z,\lambda)$ data in panel *a* does not display relevant surface perturbation effects, but identifies the presence of a non linear change with depth. This occurs between 3 and 6 m depth and was produced by a gradient in the vertical distribution of seawater optically significant components as confirmed by simultaneous profiles of inherent optical properties. The observed

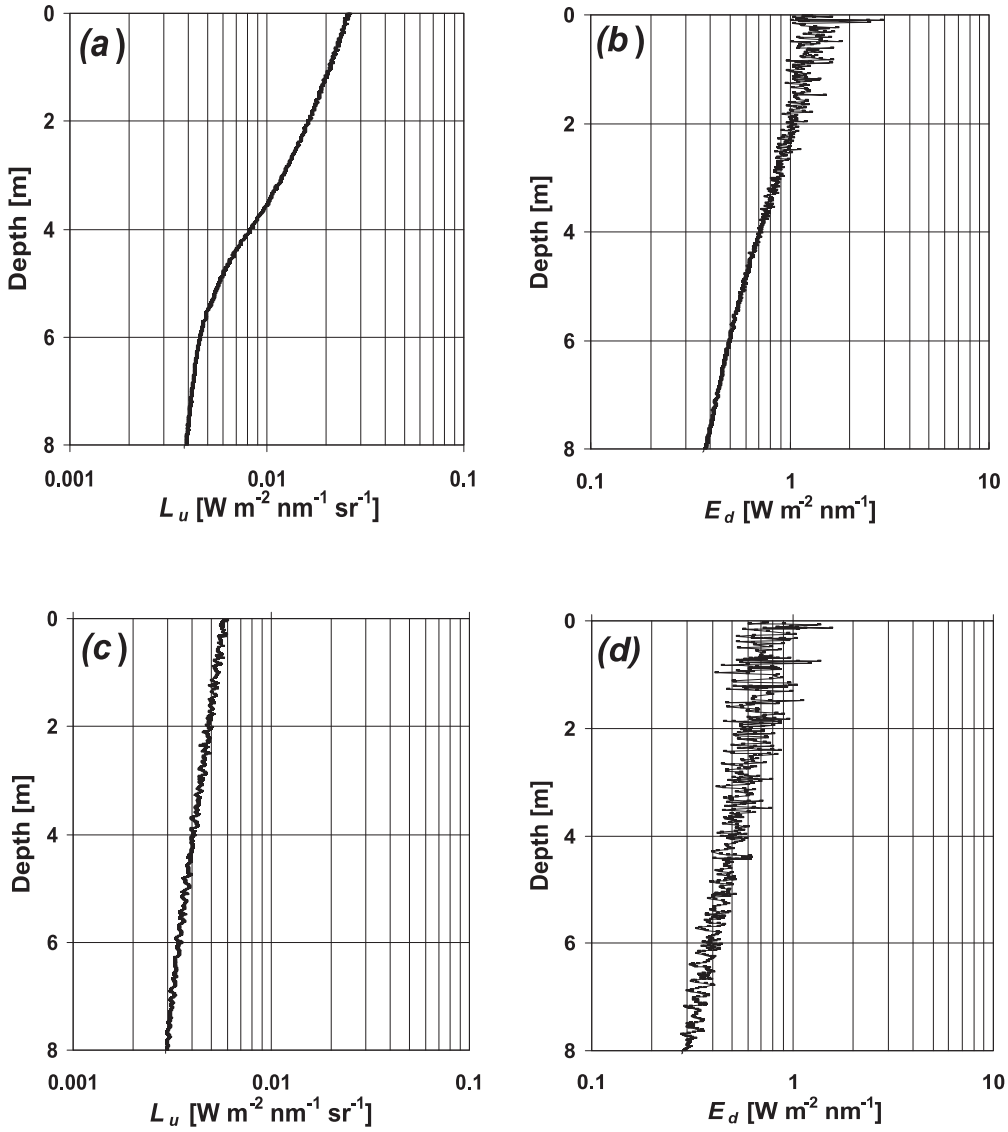


Figure 7.17: WiSPER $L_u$(z,$\lambda$) and $E_d$(z,$\lambda$) profiles at $\lambda$= 555 nm taken on July 08, 2002 with ∼10 cm average waves height and diffuse attenuation coefficient $K_d$(490)=0.20 m$^{-1}$ at 490 nm (panels *a* and *b*), and on September 17, 2002 with ∼40 cm waves height and $K_d$(490)=0.09 m$^{-1}$ (panels *c* and *d*) (after Zibordi et al. (2004c)).

changes in linearity with depth of the log-transformed $L_u(z,\lambda)$ data restrict the extrapolation interval to the first 3 m below the surface. The $E_d(z,\lambda)$ data in panel $b$ exhibit wave focusing and defocusing effects, remarked by signal fluctuations decreasing with depth. The high signal variations observed in the first tens of centimeters just below the surface, is the rationale for the removal of the related data from the extrapolation interval. The semi-logarithmic plot of $L_u(z,\lambda)$ data in panel $c$ does not display any departure from linearity with depth. However both $L_u(z,\lambda)$ and $E_d(z,\lambda)$ data in panels $c$ and $d$ show larger fluctuations extending to greater depths with respect to profiles displayed in panels $a$ and $b$. These examples, produced with a given class of commercial instruments, confirm an expected dependence of the accuracy of subsurface quantities on depth-resolution of profile data.

An uncertainty analysis was carried out by comparing the subsurface optical values computed from full resolution reference WiSPER profiles with reduced resolution profiles, keeping the same extrapolation intervals. Reduced resolution profiles were obtained by decreasing the number of measurements per meter, $N$, in the full resolution downcast profiles characterized by $\sim$64 measurements per meter corresponding to a depth-resolution $\Delta z_{No}$ greater than $\sim$1.6 cm. Specifically, profiles with $N$=32, 16, 8, 4 and 2 measurements per meter corresponding to sample depth intervals (hereafter identified as depth-resolutions) $\Delta z_N$ of 3.125, 6.25, 12.5, 25 and 50 cm, were produced by selecting data every $n$ increment steps in the full resolution profiles (that is $n$=2, 4, 8, 16, and 32, respectively). It is remarked that the time interval over which each individual sample is acquired, remains constant at 1/6 sec regardless of the depth-resolution. This is expected to reflect actual measurement conditions for decreased depth-resolution profiles on the assumption of: ($i$) random focusing and defocusing

effects; and (*ii*) comparability, over a large number of profiles, between wave perturbations affecting the single measurements related to depth intervals z$\pm 1/2\Delta z_{No}$ and those related to the larger depth intervals $z\pm 1/2\Delta z_N$.

The implicit application of the same calibration coefficients and correction factors to both full and reduced resolution profiles ensures the independence of results from any uncertainty related to the applied calibration and correction. The normalization of profile data with respect to the above–water downward irradiance by choosing the start of the cast as the reference time (see Chapter 6), makes the analysis independent of any slight change in the illumination conditions during data collection. The homogeneity of the water column in the extrapolation interval, assessed during the processing of full resolution profiles, guarantees that gradients in the vertical distribution of seawater components do not affect the analysis. In conclusion, the proposed scheme relies on the comparison of subsurface quantities determined from profile data differing by depth-resolutions, but characterized by identical: (*i*) acquisition rate; (*ii*) optical characteristics of radiometers; (*iii*) extrapolation interval; (*iv*) illumination changes and seawater characteristics. These conditions, ruling the comparisons of subsurface values from reduced and full resolution profiles, ensure that the uncertainty analysis depends of wave induced perturbations only.

**a. Uncertainties in primary radiometric quantities**

The following data analysis is presented through the most relevant primary optical quantities, i.e., those directly computed from the optical profiles, and specifically the subsurface values $L_u(0^-,\lambda)$, $E_u(0^-,\lambda)$ and $E_d(0^-,\lambda)$, and the diffuse attenuation coefficient $K_d(\lambda)$ relative to the extrapolation interval.

The data set used in the study includes 244 profiles collected in the period January

1999 – February 2001 in very different environmental conditions with 38% occurrence of Case-2 waters, and satisfying the following criteria: (*i*) cloud cover lower than 2/4; (*ii*) clear sun condition (i.e., the sun not covered by clouds); and (*iii*) wind speed lower than 10 m $s^{-1}$ (to minimize perturbations due to wave breaking). Specific quantities used to characterize the measurement conditions are: the absorption coefficient of colored dissolved organic matter, $a_y$, at 412 nm in the range of 0.02–0.26 $m^{-1}$; $Chla$ in the range of 0.21–4.74 mg $m^{-3}$; the total suspended matter, $TSM$, in the range of 0.2–3.7 g $m^{-3}$. Additional quantities are: the wind speed, $W_s$, in the range of 0.4–9.7 m $s^{-1}$; the sun zenith, $\theta_0$, in the range of 22.1–70.8 degrees; the ratio of diffuse over direct above water downward irradiance, $I_r$, at 412 nm in the range of 0.16–1.58.

The comparison of quantities obtained from full and reduced resolution profiles, are presented and summarized through average percent differences, $\psi$, average absolute percent differences, $|\psi|$, and determination coefficients, $r^2$, from least squares regressions of $M$ profiles and $L$ channels. While $\psi$ reveals the existence of a bias between the compared quantities, $|\psi|$ preserves the variance and quantifies the average uncertainty.

The values of $\psi$ were computed through

$$\psi = \frac{1}{L}\frac{1}{M}\sum_{j=1}^{L}\sum_{m=1}^{M}\psi_{j,m} \tag{7.4.1}$$

where $j$ indicates the channel index, $m$ is the profile index, and $\psi_{j,m}$ is given by

$$\psi_{j,m} = 100\frac{\Re^N(j)_m - \Re^{N_0}(j)_m}{\Re^{N_0}(j)_m} \tag{7.4.2}$$

where the superscript $N$ indicates the subsurface quantities computed from reduced resolution profiles (those defined by $N$=2–32 samples per meter), and the superscript $N_0$ indicates the reference quantities computed from full resolution profiles (those

defined by $N$=64 samples per meter). The absolute values of $\psi_{j,m}$, i.e., $|\psi_{j,m}|$, were used to compute the average absolute percentage differences $|\psi|$ according to

$$|\psi| = \frac{1}{L}\frac{1}{M}\sum_{j=1}^{L}\sum_{m=1}^{M}|\psi_{j,m}|. \tag{7.4.3}$$

The scatter plots in Fig. 7.18 display the primary quantities computed with a decreased depth-resolution defined by N=8 samples per meter versus the same quantities computed with full resolution profiles defined by N=64 samples per meter. Scatter plots show higher uncertainties for $E_d(0^-,\lambda)$ and $K_d(\lambda)$ values (panels *c* and *d*), than for $L_u(0^-,\lambda)$ and $E_u(0^-,\lambda)$ values (panels *a* and *b*). The different uncertainties are mostly explained by the direct transmission of flashes for $E_d(z,\lambda)$ and differently, by their transmission through backscattering for $L_u(z,\lambda)$ and $E_u(z,\lambda)$.

The occurrence of negative $K_d(\lambda)$ values among data computed from the reduced depth-resolution profiles (see Fig. 7.18 panel *d*) is a clear indication of appreciable perturbations affecting the computation of subsurface values. The spectral uncertainty analysis is discussed for each primary quantity as a function of $N$ at the representative center-wavelength 412, 490, 555 and 665 nm. Results from the analysis are given in Tab. 7.3. These show that all the quantities exhibit an expected increase in $|\psi|$ on $N$ decrease and confirm larger uncertainties for $E_d(0^-(\lambda)$ and $K_d(\lambda)$, in comparison to $L_u(0^-,\lambda)$ and $E_u(0^-,\lambda)$. The two last quantities exhibit close agreement with $r^2$ (not shown) always equal to 1.00. Their spectral uncertainties show almost constant $|\psi|$ values from 412 to 555 nm. They exhibit values increasing from 0.1% to 1.8% for $L_u(0^-(\lambda)$ and from 0.1% to 1.4% for $E_u(0^-(\lambda)$, as $N$ decreases from 32 to 2. More pronounced $|\psi|$ values are observed at 665 nm, increasing from 0.3% to 4.0% for $L_u(0^-(\lambda)$ and from 0.2% to 2.6% for $E_u(0^-(\lambda)$, with decreasing $N$. These slightly smaller spectral uncertainties in the blue-green, when compared to the red,

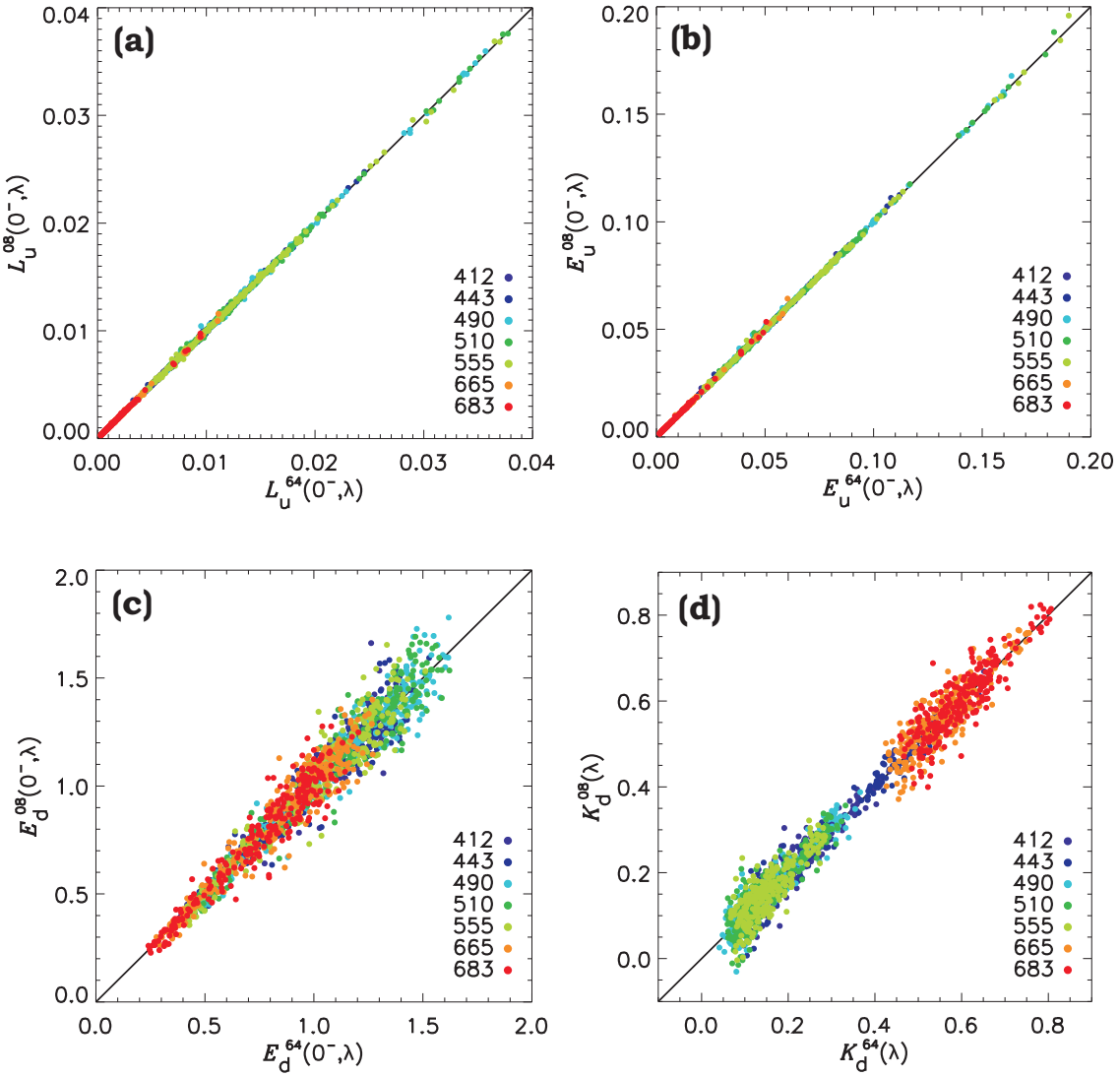


Figure 7.18: Scatter plot of primary optical quantities $L_u(0^-,\lambda)$, $E_u(0^-,\lambda)$, $E_d(0^-,\lambda)$ and $K_d(\lambda)$ (in panels *a*, *b*, *c* and *d*, respectively) obtained with decreased resolution profiles data (i.e., $N$=8) versus the reference values obtained from full resolution profile data (i.e., $N$=64). Radiances $L_u(0^-,\lambda)$ are in units of W m$^{-2}$ nm$^{-1}$ sr$^{-1}$, irradiances $E_u(0^-,\lambda)$ and $E_d(0^-,\lambda)$ in W m$^{-2}$ nm$^{-1}$, and $K_d(\lambda)$ in m$^{-1}$ (after Zibordi et al. (2004c)).

Table 7.3: Spectral uncertainty values (in percent) for different depth-resolutions (adapted from Zibordi et al. (2004c)).

| | | **412** | | **490** | | **555** | | **665** | |
|---|---|---|---|---|---|---|---|---|---|
| | $N$ | $\|\psi\|$ | $\psi$ | $\|\psi\|$ | $\psi$ | $\|\psi\|$ | $\psi$ | $\|\psi\|$ | $\psi$ |
| $L_u$ | 32 | 0.11 | 0.01 | 0.12 | 0.01 | 0.14 | 0.02 | 0.28 | 0.05 |
| | 16 | 0.36 | 0.01 | 0.34 | -0.02 | 0.41 | -0.01 | 0.97 | 0.04 |
| | 8 | 0.76 | -0.01 | 0.71 | -0.03 | 0.74 | -0.13 | 1.78 | 0.01 |
| | 4 | 1.21 | 0.00 | 1.21 | -0.02 | 1.27 | -0.10 | 2.75 | 0.44 |
| | 2 | 1.72 | -0.01 | 1.68 | 0.08 | 1.81 | 0.10 | 3.95 | 0.73 |
| $E_u$ | 32 | 0.08 | 0.01 | 0.10 | -0.01 | 0.10 | 0.01 | 00.18 | 0.01 |
| | 16 | 0.21 | -0.02 | 0.26 | -0.04 | 0.31 | -0.04 | 0.45 | 0.11 |
| | 8 | 0.45 | -0.04 | 0.49 | -0.03 | 0.51 | -0.06 | 1.02 | 0.19 |
| | 4 | 0.96 | -0.04 | 1.00 | -0.15 | 1.04 | -0.18 | 1.74 | 0.30 |
| | 2 | 1.29 | 0.02 | 1.28 | -0.05 | 1.36 | -0.04 | 2.58 | 0.64 |
| $E_d$ | 32 | 0.85 | 0.03 | 0.99 | 0.08 | 1.14 | 0.00 | 1.42 | 0.01 |
| | 16 | 2.15 | -0.09 | 2.82 | -0.01 | 3.22 | 0.30 | 3.55 | 0.31 |
| | 8 | 3.97 | 0.69 | 4.75 | 0.53 | 5.72 | 0.73 | 6.31 | 1.33 |
| | 4 | 5.80 | 0.00 | 7.29 | 0.83 | 9.02 | 1.11 | 9.97 | 1.35 |
| | 2 | 8.49 | 0.96 | 10.18 | 2.24 | 12.53 | 1.56 | 13.43 | 2.54 |
| $K_d$ | 32 | 1.50 | 0.21 | 3.37 | 0.51 | 3.52 | -0.15 | 1.13 | -0.01 |
| | 16 | 3.91 | -0.08 | 10.63 | 0.49 | 10.35 | 1.15 | 2.68 | 0.06 |
| | 8 | 8.53 | 1.66 | 17.80 | 2.48 | 18.70 | 4.00 | 5.11 | 0.71 |
| | 4 | 10.51 | 0.44 | 27.98 | 7.81 | 31.43 | 7.87 | 7.60 | 0.73 |
| | 2 | 15.30 | 3.03 | 45.71 | 15.11 | 47.75 | 10.23 | 11.02 | 3.01 |

can be explained by a higher scattering of seawater in the blue-green increasing the diffuseness of the light field and consequently decreasing the effects of wave perturbations. Different from the blue-green channels, the red channel at 665 nm shows a general increase of $\psi$ as $N$ decreases, exhibiting values reaching 0.9% with $N$=2 for both $L_u(0^-,\lambda)$ and $E_u(0^-,\lambda)$. This spectral dependence is again explained by a lower diffuseness of the light field in the red than at shorter wavelengths. The positive bias can be explained by the high weight of measurements affected by wave focusing in

the extrapolation process through an exponential function. This weight positively biases the near surface values when the measurements distribution does not adequately represent the wave perturbations, as likely occurs on depth-resolution decrease.

$E_d(0^-, \lambda)$ shows values of $|\psi|$ increasing from 0.9% at 412 nm to 1.4% at 665 nm with $N$=32, and from 8.5% at 412 nm to 13.4% at 665 nm with $N$=2. The regular increase with wavelength is again explained by the scattering properties of seawater, whose decrease produces an increase in the wave focusing and defocussing effects. The $\psi$ values for $E_d(0^-, \lambda)$ show an appreciable increase on $N$ decrease, and exhibit a general increase with wavelength (excluding data at 555 nm) from 1.0% at 412 nm to 2.5% at 665 nm. The corresponding analysis of $r^2$ (not shown) exhibits values decreasing on $N$ decrease and on wavelength increase. For $N$=2, the values of $r^2$ decrease from 0.91 at 412 nm to 0.82 at 665 nm. This is also explained by a decrease in seawater scattering, leading to more pronounced wave effects and thus increasing the dispersion of data.

$K_d(\lambda)$ shows the highest uncertainties among all analyzed quantities. The spectral $|\psi|$ values exhibit an increase from 1.5% at 412 nm to 3.5% at 555 nm with $N$=32 and from 15.3% at 412 nm to 47.8% at 555 nm with $N$=2. The red channels show much lower $|\psi|$ values, when compared to the blue-green, with an increase from 1.1% with $N$=32 to 11.1% with $N$=2. This can be explained by the fact that, assuming the same perturbations affect all wavelengths in the 412-665 nm spectral range, $K_d(\lambda)$ is subject to the smallest percent variations in the red where its value is the highest. The spectral dependence of the $\psi$ values generally reflects that observed for $|\psi|$. Specifically, with $N$=2 the analysis of $K_d(\lambda)$ data shows values of $\psi$ increasing from 3% at 412 nm up to 15% at 490 nm, and dropping to average values of 3% in the

red at 665 nm. The spectral analysis of $r^2$ for $N$=2 (not shown), indicates decreasing values from 0.9 at 412 nm to 0.6 at 555 nm, and average values of 0.7 in the red.

An appreciable increase of the spectral $\psi$ values is observed for $K_d(\lambda)$ and $E_d(0^-, \lambda)$ on $N$ decrease, as for $L_u(0^-, \lambda)$ and $E_u(0^-, \lambda)$. This can be explained by the high weight of measurements affected by wave focusing in the extrapolation process through an exponential function.

The similarity observed for both $|\psi|$ and $\psi$ values at 665 and 683 nm (non shown) suggests fluorescence does not contribute to the reduction of wave induced perturbations at 683 nm.

**b. Uncertainties in derived radiometric quantities**

Spectral ratios are of relevance in the development of bio-optical algorithms (Berthon et al., 2002; O'Reilly et al., 1998). Uncertainties in their computed values due to wave perturbations were analyzed for $L_u(0^-, \lambda_1)/L_u(0^-, \lambda_2)$, $E_d(0^-, \lambda_1)/E_d(0^-, \lambda_2)$ and, for the derived quantities $L_{WN}(\lambda_1)/L_{WN}(\lambda_2)$ and $\breve{L}_{WN}(\lambda_1)/\breve{L}_{WN}(\lambda_2)$ at center-wavelengths $\lambda_1$=443, 490 and 510 nm, and $\lambda_2$=555 nm. The last two derived quantities are those having direct application in bio-optical modeling.

The data analysis, detailed in Zibordi et al. (2004c) and summarized in Tab. 7.4, showed a reduction in the $E_d(0^-, \lambda_1)/E_d(0^-, \lambda_2)$ uncertainties with respect to those of the individual spectral quantities $E_d(0^-, \lambda_1)$ and $E_d(0^-, \lambda_2)$. A less pronounced reduction was also observed in the uncertainties determined for $L_u(0^-, \lambda_1)/L_u(0^-, \lambda_2)$ with respect to those determined for $L_u(0^-, \lambda_1)$ and $L_u(0^-, \lambda_2)$, separately. These reductions suggest the existence of a correlation between the uncertainties at the different wavelengths. An additional result was an observed decrease of uncertainties on $\lambda_1$ increase. This is explained by the design of the radiometers utilized for the

Table 7.4: Uncertainty values (in percent) for spectral-ratio quantities (after Zibordi et al. (2004c)).

| | | **443/555** | | **490/555** | | **510/555** | |
|---|---|---|---|---|---|---|---|
| | $N$ | $\|\psi\|$ | $\psi$ | $\|\psi\|$ | $\psi$ | $\|\psi\|$ | $\psi$ |
| $L_u$ | 32 | 0.09 | 0.00 | 0.08 | 0.01 | 0.05 | 0.01 |
| | 8 | 0.44 | 0.07 | 0.37 | 0.08 | 0.30 | 0.04 |
| | 2 | 0.98 | 0.16 | 0.72 | 0.05 | 0.51 | 0.00 |
| $E_d$ | 32 | 0.88 | -0.06 | 0.86 | -0.09 | 0.59 | -0.05 |
| | 8 | 3.87 | -0.13 | 3.46 | -0.11 | 2.54 | -0.03 |
| | 2 | 8.43 | 0.35 | 7.53 | 0.97 | 4.60 | 0.10 |
| $L_{WN}$ | 32 | 0.09 | 0.00 | 0.07 | 0.00 | 0.05 | 0.01 |
| | 8 | 0.43 | 0.07 | 0.38 | 0.07 | 0.30 | 0.04 |
| | 2 | 0.98 | 0.17 | 0.72 | 0.06 | 0.51 | 0.01 |
| $\tilde{L}_{WN}$ | 32 | 0.95 | 0.06 | 0.96 | 0.12 | 0.63 | 0.08 |
| | 8 | 4.16 | 0.63 | 3.79 | 0.50 | 2.77 | 0.36 |
| | 2 | 9.06 | 0.96 | 8.07 | 0.28 | 4.94 | 0.29 |

data collection (i.e., OCR-200 and OCI-200) and more specifically by the decreasing distance between the $\lambda_1$ and $\lambda_2$ entrance optics on $\lambda_1$ increase (e.g., the 510 optics is closer to that of the 555 one than is the 443). In fact the optics of the different channels for both the radiance and irradiance radiometers used in this study, are independent and distributed within a circle of $\sim$4 cm diameter. Because of this, random perturbations produced by wave focusing affect the detected signal differently in the various channels. It is reasonable to assume that the wave induced perturbations tend to become more comparable at different wavelengths when their optics are closer. This further confirms the dependence of wave induced perturbations on the geometry of optics, and implicitly on the field of view of radiance sensors and diameter of irradiance collectors.

The comparison of $\psi$ for $L_{WN}(0^-, \lambda_1)/L_{WN}(0^-, \lambda_2)$ and $L_u(0^-, \lambda_1)/L_u(0^-, \lambda_2)$

showed almost identical values because of the independence of $E_d(0^+, \lambda_2)/E_d(0^+, \lambda_1)$ from wave perturbations. Differently, the $\psi$ values for $\breve{L}_{WN}(0^-, \lambda_1)/\breve{L}_{WN}(0^-, \lambda_2)$ appeared close to the sum of those for the quantities used in their computation, i.e., $L_u(0^-, \lambda_1)/L_u(0^-, \lambda_2)$ and $\breve{E}_d(0^-, \lambda_1)/\breve{E}_d(0^-, \lambda_2)$.

Extensive analysis was also made to address the dependence of wave perturbations on quantities such as: the sea state, $S_s$, applied as a wave height index; the diffuse attenuation coefficient at 490 nm, $K_d(490)$, applied as a seawater optical index for the extrapolation layer; the sun zenith, $\theta_0$, and the diffuse over direct downward irradiance ratio at 412 nm, $I_r(\theta_0, \lambda)$, both applied as illumination indices. Results detailed in Zibordi et al. (2004c) showed an appreciable dependence of uncertainties on the first two indices with a significant decrease with $K_d(490)$ and increase with $S_s$ up to 2 (according to the WMO (1983) scale). Conversely, uncertainties exhibited a slight increase on both $\theta_0$ and $I_r$ decrease.

### 7.4.2 Depth-resolution requirements

The spectrally averaged $\psi$ values for the primary optical quantities are plotted in Fig. 7.19 as a function of $N$. The almost exponential dependence of $\psi$ on $N$ is explained by the fact that these uncertainties result from the difference of quantities determined from exponential fits. Curves like those plotted in Fig. 7.19 can be used to estimate the depth-resolution related to wave induced uncertainties at pre-defined thresholds. Setting the threshold to 2% for each primary quantity, a value comparable to absolute calibration uncertainties, the depth-resolution requirement determined from curves of $|\psi|$ is given in Tab. 7.5 at 443, 555 and 665 nm for in-water optical profiles taken with $K_d(490)$<0.14 $m^{-1}$ and $S_s$=2 (those affected by the largest wave perturbations). For completeness, estimated depth-resolutions are also provided for the 1% and 5%

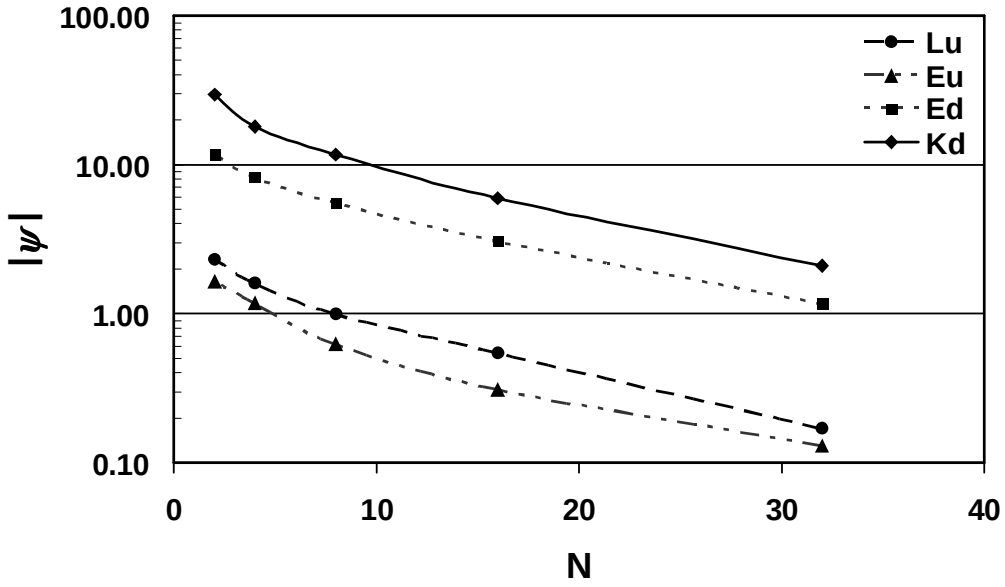


Figure 7.19: Spectrally averaged $|\psi|$ values, as a function of $N$, for the primary optical quantities $L_u(0^-\lambda)$, $E_u(0^-\lambda)$, $E_d(0^-,\lambda)$ and $K_d(\lambda)$(after Zibordi et al. (2004c)).

thresholds. Data show values varying for each primary quantity as a function of wavelength. Specifically the 2% target, for the 443-665 nm spectral range, requires depth-resolutions finer than 11, 40, 3 and 2 cm, for $L_u(0^-,\lambda)$, $E_u(0^-,\lambda)$, $E_d(0^-,\lambda)$ and $K_d(\lambda)$, respectively. By restricting the uncertainty below 1%, the depth-resolutions increase up to 5, 13, 2 and 2 cm, respectively. Conversely, by relaxing the uncertainty threshold to 5%, they decrease to values of 50 cm for $L_u(0^-,\lambda)$, $E_u(0^-,\lambda)$, and 6 and 3 cm for $E_d(0^-,\lambda)$ and $K_d(\lambda)$, respectively.

The former values confirm that the primary optical quantities determined from full resolution WiSPER data with depth-resolution better than 1.6 cm, are not significantly affected by wave induced perturbations (i.e., they are negligible in $L_u(0^-,\lambda)$ and $E_u(0^-,\lambda)$, and less than 1% in $E_d(0^-,\lambda)$ and $K_d(\lambda)$). This helps in evaluating the overall uncertainty budget in subsurface quantities determined from profiles collected in coastal waters under environmental conditions similar to those encountered

Table 7.5: Depth-resolution requirements (in units of cm) for the 1%, 2%, and 5% uncertainty values in primary optical quantities (after Zibordi et al. (2004c)).

| $\lambda$ | 443 | | | 555 | | | 665 | | |
|---|---|---|---|---|---|---|---|---|---|
| Uncertainty | 1% | 2% | 5% | 1% | 2% | 5% | 1% | 2% | 5% |
| $L_u$ | 17 | 50 | $> 50$ | 13 | 33 | $> 50$ | 5.3 | 11 | 50 |
| $E_u$ | 50 | $> 50$ | $> 50$ | 25 | $> 50$ | $> 50$ | 13 | 40 | $> 50$ |
| $E_d$ | 3.0 | 4.4 | 10 | 2.9 | 3.5 | 6.3 | 2.4 | 3.3 | 6.3 |
| $K_d$ | 2.1 | 2.6 | 3.9 | 1.8 | 2.1 | 2.9 | 2.6 | 3.7 | 9.1 |

at the AAOT site using systems having acquisition rate and optics similar to WiSPER. Specifically, the data in Tab. 7.5 suggest that the uncertainties determined with profiles collected under the stated environmental conditions with current advanced free-fall systems (having acquisition rate of 6 Hz, deployment speed of $\sim$0.25 m $s^{-1}$ and the same optics as WiSPER) are lower than 1% for $L_u(0^-, \lambda)$ and $E_u(0^-, \lambda)$, and of the order of 2% for $E_d(0^-, \lambda)$. For $K_d(\lambda)$ the uncertainties are close to 5% in the 412-555 nm interval and of the order of 2% in the red.

## 7.5 Discussion on uncertainties

Minimization of uncertainties produced by perturbations like self-shading, superstructures or bottom effects, and additionally estimation of uncertainties induced by environmental perturbations such as waves, are a major requirement to maximize the accuracy of measurements and produce an overall uncertainty budget. With this objective in mind, an attempt is made to evaluate residual uncertainties in in–water data corrected for self-shading, superstructure perturbations and bottom effects. Additionally the applicability of the proposed depth-resolution requirements is considered.

### 7.5.1 Uncertainties of correction factors

When analyzing the self-shading perturbations, sources of uncertainty in the computation of $\eta_{\Re}^{S}(\lambda)$ include assuming: $(i)$ the instrument is an ideal disc instead of a cylinder; $(ii)$ each channel sensor is located at the center of the instrument (in the case of several multi-spectral radiometers they may actually be arranged in a circle with one channel in the center); $(iii)$ the sea surface is flat.

Major limitations of the correction scheme proposed for the determination of $\eta_{\Re}^{T}(\lambda)$ for the AAOT superstructure perturbations include: $(i)$ neglecting the roughness in modelling the sea surface reflectance; $(ii)$ assuming the tower absorbs all the incident photons; $(iii)$ using discrete correction factors because of the application of a table indexed by discrete values of the input quantities (i.e., $\theta_0, \phi_0, I_r, a$ and $\omega_0$).

Uncertainties in the computation of $\eta_{\Re}^{B}(\lambda)$ for bottom perturbations, are induced by: $(i)$ applying an approximate analytical model; $(ii)$ using the operational diffuse attenuation coefficient; and $(iii)$ assuming the bottom reflectance is Lambertian.

Defining an arbitrary uncertainty of 25% in the total corrections determined as $\eta_{\Re} = \eta_{\Re}^{S}\eta_{\Re}^{T}\eta_{\Re}^{B}$ (assuming independence of correction factors), the related uncertainties were estimated from the values of $\eta_{\Re}$ applied to the CoASTS time-series composed of 1936 casts collected from October 1995 to July 2005.

Table 7.6: Estimated average uncertainties (in percent) for the total correction factors $\eta_{\Re}$ applied to various radiometric quantities.

| $\lambda$ | 443 | 555 | 665 |
|---|---|---|---|
| $L_u$ | 1.9 ± 0.6 | 1.1 ± 0.8 | 2.8 ± 0.9 |
| $E_u$ | 1.8 ± 0.5 | 1.1 ± 0.8 | 1.8 ± 0.6 |
| $E_d$ | 0.8 ± 0.3 | 0.4 ± 0.2 | 0.3 ± 0.1 |

These average uncertainty values are given in Tab. 7.6 and are an estimate of the residual uncertainties after the minimization of measurement perturbations.

### 7.5.2 Applicability of the Depth-Resolution Requirements

Results from the analysis of varying depth-resolution profiles suggest that in coastal waters the wave induced uncertainties can be reduced below 2% with a number of measurements per meter higher than approximately 9, 3, 33 and 50 for $L_u(0^-, \lambda)$, $E_u(0^-, \lambda)$, $E_d(0^-, \lambda)$ and $K_d(\lambda)$, respectively. These values are much more restrictive than the *at least 2, and preferably 6 to 8 measurements per meter* given in the Ocean Optics Protocols (Mueller and Austin, 2003) for optically deep waters and assuming the extrapolation interval equal to at least one optical depth. This difference in requirements between coastal and oceanic optical profiles highlights the superior technological needs for the former to ensure the capability of sampling with higher depth-resolution and of acquiring data as close as possible to the surface to maximize the extrapolation interval in the presence of highly inhomogeneous water columns. This suggests that, when profilers do not meet the given requirements, alternative methods should be sought. A practical solution is to add data from successive casts to produce a single profile with a higher depth-resolution. An attempt to experimentally verify this method was made using the JRC version of the miniature NASA Environmental Sampling System (JRC-miniNESS). This free-fall profiler has the same acquisition rate and radiometers as WiSPER. The data set used for the verification included 58 fully independent measurement sequences, each composed of 5 consecutive profiles collected within 10 minutes with a deployment speed of $\sim$1 m s$^{-1}$ during

clear sky and stable illumination conditions in the vicinity of the AAOT. When combining the data of the consecutive profiles for each measurement sequence and thus increasing the number of samples from ∼6 to ∼30 per meter, the comparison of primary optical quantities determined from the single mid-sequence profile versus the multicast profile, showed spectrally averaged $|\psi|$ values of 1.7, 2.7, 5.8 and 14.6% for $L_u(0^-,\lambda)$, $E_u(0^-,\lambda)$, $E_d(0^-,\lambda)$ and $K_d(\lambda)$, respectively. These uncertainties compare in magnitude with the values of 1.0, 0.6, 5.2, and 11.8% resulting from the independent comparison of WiSPER reduced resolution profiles with 8 and 32 samples per meter. The differences between the results obtained with the JRC-miniNESS and the reduced resolution WiSPER data are mostly justified by: (*i*) the environmental variability affecting the successive free-fall profiles and cancelling out in the WiSPER data; (*ii*) tilt effects present in the free-fall and not in the WiSPER data; (*iii*) slight differences in the free-fall and WiSPER depth-resolutions used for the comparison; and finally (*iv*) the mutual position of radiometers in the two profiling systems. A peculiar case in this analysis of multicast profile data, is encountered with $E_u(0^-,\lambda)$ exhibiting a higher $|\psi|$ value than that of $L_u(0^-,\lambda)$. This can be explained by the position of the $E_u$ sensor, installed on the nose of the JRC-miniNESS at approximately 0.9 m below the $L_u$ and $E_d$ sensors. Because of the adoption of a common extrapolation interval for the processing of $L_u(z,\lambda)$, $E_u(z,\lambda)$ and $E_d(z,\lambda)$, the determination of $E_u(0^-,\lambda)$ must rely on a smaller effective extrapolation layer. Thus the increase in depth-resolution through the multicast approach produces a more significant improvement in the accuracy of $E_u(0^-,\lambda)$ than $L_u(0^-,\lambda)$, determined from these specific free-fall data. This also indirectly confirms the appropriateness of the uncertainty analysis produced with the full and reduced resolution WiSPER data.

## 7.6 Summary

Optical radiometric measurements can be affected by uncertainties due to various perturbing factors. In the case of above-water radiometry, major measurement perturbations are produced by wave slopes and deployment superstructures. Wave effects can be minimized by filtering measurements, while perturbations due to deployment superstructures can be minimized with the implementation of specific measurement geometries.

In addition to wave and deployment superstructure effects, in-water radiometry can be significantly perturbed by self-shading. Perturbations due to wave effects can be minimized by collecting data with high depth-resolution in the case of profiles, or extended time intervals in the case of moorings. Self-shading and superstructure perturbations can be minimized by applying specific correction schemes.

The correction scheme suggested by Gordon and Ding (1992) for instrument self-shading was assessed using in water measurements taken at different sun zenith angles and different atmospheric and water turbidities. The application of the proposed correction scheme to radiometric data from the AAOT site in the northern Adriatic Sea characterized by moderately turbid waters, shows correction values highly varying with wavelength and sun zenith. Within the spectral range 412–665 nm the highest values result at 665 nm with averages of 10±2.9% for $L_u$, and of 5.7±2.9% for $E_u$, where the superscript $\hat{}$ indicating perturbed radiometric quantities is hereafter omitted. This confirms that for conventional radiometers, self-shading error should not be neglected.

The superstructure perturbations for in-water subsurface radiometric measurements collected at the AAOT with the WiSPER system at 7.5 m from the main body of the tower, were investigated using experimental data and Monte-Carlo simulations. The study led to the definition and assessment of a correction scheme based on a look-up table whose entries are mostly indexed values of seawater inherent optical properties, atmospheric aerosol and measurement geometry. The highest corrections are observed in the blue at 443 nm and exhibit average values of 3.9±1.3%, 5.1±1.7% and 3.3±1.2% for $L_u$, $E_u$ and $E_d$, respectively.

An additional source of perturbation is the bottom reflectance in shallow waters. The bottom effects can be minimized using an analytical relationship derived from a two-flow model. This solution requires determining the near-bottom reflectance from the in-water profile data. The application of the proposed scheme to WiSPER data collected at the AAOT site, shows correction values inversely varying with seawater attenuation with average values of -1.3±2.1% for both $L_u$ and $E_u$ at 555 nm where the light penetration is the highest. Conversely, due to the high seawater absorption, negligible corrections are observed at 665 nm.

Assuming an uncertainty of 25% in the determination of the total correction factor, the average uncertainty in the derived corrections for data collected with WiSPER at the AAOT site, exhibits values lower than 1% for $E_d(0^-, \lambda)$, 2% for $E_u(0^-, \lambda)$ and 3% for $L_u(0^-, \lambda)$.

The effects of wave perturbations on the extrapolation of subsurface radiometric values were investigated using profile data with different depth-resolutions. Results provided a figure of the expected uncertainties in deriving subsurface radiometric data as a function of the number of measurements per unit depth. These data suggest that,

under the most unfavorable condition (i.e., relatively low $K_d$ and sea state $S_s$=2) an uncertainty lower than 2% can be achieved with 50 measurements per meter for $K_d(\lambda)$, 33 for $E_d(0^-, \lambda)$, 9 for $L_u(0^-, \lambda)$ and 3 for $E_u(0^-, \lambda)$. The analysis of *in situ* optical data also showed that in the case of profilers not satisfying the given requirements, the possibility of increasing the depth-resolution by combining multiple casts collected within a short time interval (i.e., a few minutes) is still valid.

# Chapter 8

# Applications

*The problem of characterizing an unknown material in the laboratory from its reflection or transmission properties is fairly simple; it becomes progressively harder as the sensor becomes more remote from the material.*

*Philip Slater, 1980.*

[1]Optical radiometric data have direct application in the development and assessment of theoretical models describing the seawater light extintion processes (Bulgarelli et al., 2003; Chang et al., 2003) and empirical algorithms linking the seawater apparent optical properties to the water constituents expressed through their inherent optical properties or concentrations (D'Alimonte and Zibordi, 2003; D'Alimonte et al., 2004; O'Reilly et al., 1998, 2000). In addition, radiometric data are essential for the vicarious calibration of sensors in space and the validation of remote sensing products (Eplee et al., 2001; Mélin et al., 2005; Sturm and Zibordi, 2002; Zibordi et al., 2006a).

The highest accuracy is always the most desirable for any bio-optical modelling and calibration or validation activity. However, accuracy requirements impact methodological and instrumental investment which should be weighed against the specific

[1]The material presented and discussed in this chapter was mostly published in Berthon and Zibordi (2004); Zibordi and Berthon (2001); Zibordi et al. (2004a, 2006a,b).

need for each application. Because of this, several space agencies on the basis of target accuracies in derived products (i.e., 35% for *Chla* in open ocean) have specified a maximum uncertainty of 5% for radiometric measurements. This is streamlined through the so called 1% *radiometry* concept, which indicates that each major and independent source of uncertainty in *in situ* radiometric measurements should stay below the 1% level to ensure that their statistical composition (e.g., using their quadrature sum) does not exceed 5%. The achievement of this objective is based on the assumption that major uncertainties are produced by a few sources including: radiometric calibration (absolute, immersion factor, sensitivity change between calibrations); estimate of correction factors for the removal of measurement artifacts (self-shading, superstructure perturbation); and environmental variability (wave effects, changes in illumination conditions and in distribution of optically significant constituents during measurements).

Accounting for the outcome of previous chapters, examples of applications of optical radiometric data are here presented with the aim of exploring the sensitivity to uncertainty for products from such applications.

## 8.1 Bio-optical models

Bio-optical models are generally separated into analytical and empirical. Analytical models are commonly used to predict the radiometric quantities from the modelled or measured inherent optical properties of seawater constituents. In contrast, empirical models are derived from statistical analysis of field measurements and are used to describe the bio-optical state of seawater. A general example of these empirical models (usually called algorithms) is given by ratios of remote sensing reflectance at

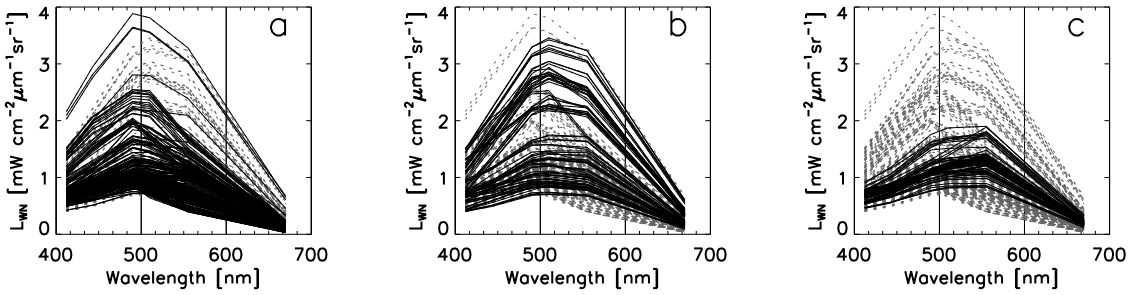


Figure 8.1: Sample $L_{WN}(\lambda)$ spectra produced within the framework of the CoASTS project from May 2002 to December 2005. Black lined in different panels highlight $L_{WN}$ spectra exhibiting maxima at different center-wavelengths $\lambda$: **a** at 490 nm; **b** at 510 nm; **c** at 555 nm.

various center-wavelengths as a function of the concentration of optically significant constituents. These specific algorithms find their rationale in the spectral variations affecting $L_{WN}$ (or $R_{RS}$) as a function of the concentration of seawater constituents: this can be evidenced by the shape of sample spectra shown in Fig. 8.1 for water types likely to be characterized by different concentrations of optically significant constituents. Unlike analytical models, which are expected to have universal applicability, empirical algorithms are mostly valid for only the specific waters where measurements were performed.

### 8.1.1 *Chla* and $K_d$ empirical modeling

In the following subsections the analysis will be restricted to various empirical algorithms in view of addressing their dependence on the accuracy of optical radiometric measurements. The *in situ* measurements used were collected within the framework of the Coastal Atmosphere and Sea Time-Series (CoASTS) program (Zibordi et al., 2002b) carried out to support ocean color calibration and validation activities through a comprehensive data collection at the AAOT. The data set, due to the peculiarity

of the AAOT site located in a frontal region representative of coastal zones (here defined as regions permanently or occasionally affected by bottom resuspension, coastal erosion, river inputs, or by relevant anthropogenic impact), include measurements in both Case-1 and Case-2 water conditions (Berthon and Zibordi, 2004). Specifically Case-1 conditions are identified for roughly 60% of cases when classified by the scheme of Loisel and Morel (1998), even though most of the data distribute around the separation threshold (Berthon et al., 2002) making their categorization somewhat speculative.

Empirical algorithms are a direct way of linking the marine reflectance to the seawater optically significant constituents and optical properties. And since the late 1970s, during experimentation for the succeeding exploitation of remote sensing data from the Coastal Zone Color Scanner (CZCS), empirical algorithms showed their robustness in the determination of $Chla$ (Clark, 1981) and $K_d$ at a given $\lambda$ (Austin and Petzold, 1981). Since then, although the development of analytical solutions applicable to all water types may appear a desirable objective, the provision and the use of purely empirical algorithms based on *in situ* measurements, has been the subject of continuous developments. This resulted in algorithms appropriate for the exploitation of remote sensing data from both global oceanic Case-1 waters and, with regional and sometimes seasonal restrictions, coastal Case-2 waters (Bricaud et al., 2002; D'Alimonte et al., 2003; Darecki et al., 2004; D'Ortenzio et al., 1994). Given this relative success, current global remote sensing products still rely on algorithms based on spectral ratios of the remote sensing reflectance for the operational determination of $K_d$ at 490 nm (Mueller, 2000) or $Chla$ (O'Reilly et al., 2000).

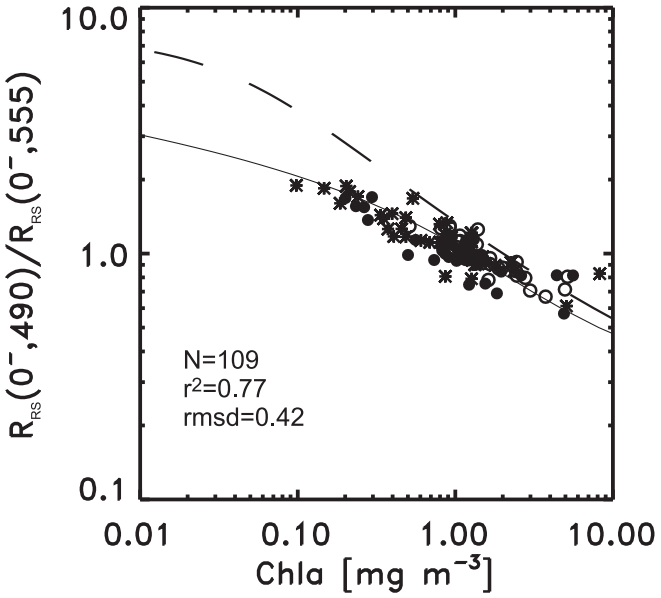


Figure 8.2: Relationships between remote-sensing reflectance ratio $R_{RS}(0^-, 490)/R_{RS}(0^-, 555)$ and $Chla$. The solid line represents the polynomial fit and the dashed line is the "SeaWiFS OC2v4" algorithm. Empty circles, bullets and stars identify Case-1, Case 2 and unidentified conditions, respectively (Berthon and Zibordi, 2004).

An additional example of empirical algorithm proposed for $Chla$ determination specific for the northern Adriatic coastal waters (Berthon and Zibordi, 2004) is displayed in Fig. 8.2. The algorithm, so called AD, provides $Chla$ in mg m$^{-3}$ as a function of the remote sensing reflectance ratio, $R_{RS}(490)/R_{RS}(555)$ (denoted as $R_{35}$), through

$$Log_{10}Chla = 0.091 - 2.620Log_{10}R_{35} - 1.148(Log_{10}R_{35})^2 - 4.949(Log_{10}R_{35})^3 \quad (8.1.1)$$

and exhibits determination coefficient $r^2$=0.77, and root mean square of differences rmsd=0.42. The OC2v4 algorithm (O'Reilly et al., 2000), identified by a dashed line in Fig. 8.2, almost systematically overestimates $Chla$ when applied to the present data set. This is particularly evident in the range 0.1-1.0 mg m$^{-3}$. For the same $Chla$ the AD reflectance ratio is lower than that given by the OC2v4 algorithm probably

because of increased absorption by dissolved and particulate matter in the blue part of the spectrum. The agreement is much better in the range 1.0-10.0 mg $m^{-3}$ when *Chla* is probably the dominating optical component.

It must be emphasized that the application of this empirical relationship outside the range used for its development (in particular for *Chla* values lower than 0.1 mg $m^{-3}$ in the above algorithm) should be considered with caution.

A further example of a regional relationship proposed for the generation of remote sensing products is that for the diffuse attenuation coefficient at 490 nm, $K_d(490)$ (Berthon and Zibordi, 2004). The algorithm developed with the same data set applied for determining the coefficients of Eq.8.1.1, is given by

$$K_d(490) = 0.016 + 0.205[\frac{L_{WN}(490)}{L_{WN}(555)}]^{-1.754} \tag{8.1.2}$$

where 0.016 $m^{-1}$ is the constant value of $K_d(490)$ for pure water. This relationship exhibits $r^2$=0.80 and rmsd=0.23.

Linear relationships in the form of $Log_{10}[K_d(\lambda)] = a_0 + b_0 Log_{10}[K_d(490)]$ were also computed for $\lambda$ = 412, 443, 510, 555, 665 and 683 nm and their parameters are provided in Tab. 8.1. The quality of these regressions, as given by $r^2$, decreases in the red part of the spectrum. An application of these algorithms is provided by their use in conjunction with semi-analytical models (see Loisel and Stramski (2000)) and marine reflectances, to derive the spectral absorption, scattering and back-scattering coefficients at corresponding wavelengths (Mélin et al., 2005).

Table 8.1: Parameters $a$ and $b$, and determination coefficient $r^2$ of the linear relationship between $K_d(\lambda)$ and $K_d(490)$ (after Berthon et al. (2002)).

| $\lambda(nm)$ | $a_0$ | $b_0$ | $R^2$ |
|---|---|---|---|
| 412 | 0.224 | 1.000 | 0.97 |
| 443 | 0.157 | 1.033 | 0.99 |
| 510 | -0.105 | 0.873 | 0.99 |
| 555 | -0.284 | 0.648 | 0.88 |
| 665 | -0.065 | 0.210 | 0.57 |
| 683 | -0.036 | 0.202 | 0.54 |

### 8.1.2 Empirical modelling of Q-factor

The capability of modeling the radiance distribution in marine water, is a basic step toward the development of advanced remote sensing techniques for the accurate determination of optically significant components dissolved or suspended in seawater. In this context, efforts were devoted to the study of the non-isotropic character of the light distribution in seawater conveniently expressed through the $Q$-factor (Tyler, 1960). In agreement with Eq.2.1.25 and applying a simplified formalism, this is defined as the ratio between the upwelling irradiance $E_u(z,\lambda)$ and radiance $L_u(z,\varphi,\theta,\theta_0,\lambda)$ at wavelength $\lambda$,

$$Q(z,\varphi,\theta,\theta_0,\lambda) = \frac{E_u(z,\lambda)}{L_u(z,\varphi,\theta,\theta_0,\lambda)}. \tag{8.1.3}$$

It is a function of: (*i*) the measurement geometry (the depth, $z$, the azimuth difference between the sun and the observation planes, $\varphi$, the viewing angle, $\theta$, and the sun zenith angle, $\theta_0$); (*ii*) the seawater inherent optical properties (the absorption coefficient, $a$, the scattering coefficient, $b$, and the scattering phase function, $\widetilde{\beta}$); (*iii*) the atmospheric optical properties generally expressed through the aerosol optical thickness, $\tau_a$, and, additionally (*iv*) sea state and cloud cover.

The anisotropy of light distribution in natural waters was already experimentally explored in the 1960s by Jerlov and Fukuda (1960); Sasaki et al. (1962); Smith et al. (1969); Tyler (1960); and more recently by Morel et al. (1995); Voss (1989); Voss and Morel (2005). Theoretical studies on $Q(z, \varphi, \theta, \theta_0, \lambda)$, specifically focused on oceanic waters and based on Monte Carlo simulations, were carried out by Morel and Gentili (1991, 1993, 1996). A related work (Morel et al., 1995) showed a good agreement between $Q(z, \varphi, \theta, \theta_0, \lambda)$ values resulting from Monte Carlo simulations and from field measurements performed at 450, 500 and 600 nm in Case-1 water off San Diego and in the Lake Pend Oreille. The latter study showed $Q(z, \varphi, \theta, \theta_0, \lambda)$ values ranging from $\sim$1 up to 5 sr with $\theta_0$ ranging from 32 up to 80 degrees. In addition to the former work, only a few others have presented experimental $Q(z, \varphi, \theta, \theta_0, \lambda)$ data. Siegel (1984) discussed $Q_n(\lambda)$ field data (i.e., $Q(z, \varphi, \theta, \theta_0, \lambda)$ at $\theta = 0$ and $z = 0^-$) ranging from 3.4 up to 6.4 sr for oceanic water, reporting almost no dependence on wavelength in the spectral interval 450 – 650 nm and a large dependence on $\theta_0$ between 25 and 80 degrees. Siegel empirically modeled the former dependence on $\theta_0$ through

$$Q_n(\lambda) = Q_{90}(\lambda) e^{-C \cos \theta_0} \tag{8.1.4}$$

where $Q_{90}(\lambda)$ defines the value of $Q_n(\lambda)$ at $\theta_0$=90 degrees and $C$ is a function of the seawater optical properties (in Siegel's formulation $C \cos \theta_0$ is expressed by $C \sin \gamma_0$, with $\gamma_0$ sun elevation, i.e., $\gamma_0 = 90 - \theta_0$). An almost identical dependence of $Q_n(\lambda)$ on $\theta_0$, was confirmed by Aas and Højerslev (1999) in the spectral interval 465-474 nm with data collected in the Mediterranean Sea.

Using CoASTS measurements, an empirical modeling of $Q_n(\lambda)$ was investigated in the 412–665 nm spectral range as a function of $\theta_0$ and of different apparent or inherent seawater optical properties (i.e., $K_d(\lambda)$, $a(\lambda)$, $b(\lambda)$ and $\omega_0(\lambda)$). Despite the

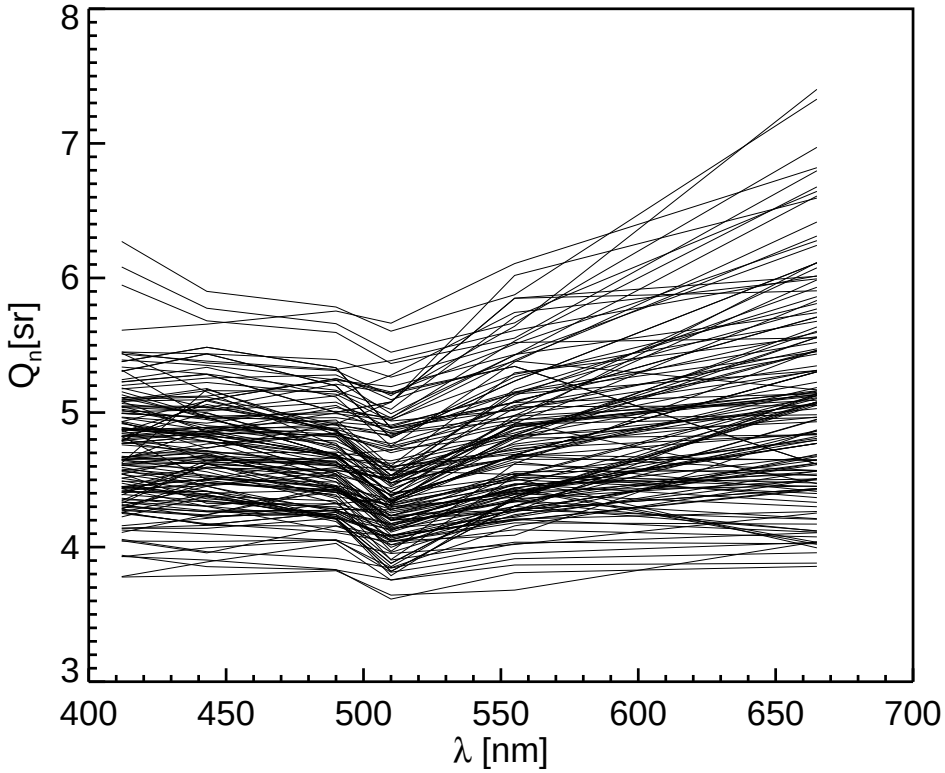


Figure 8.3: $Q_n(\lambda)$ spectra from the CoASTS (1995-1998) data set (the decrease at 510 nm is likely an artifact introduced by a miss-performance of the radiometer at the specific center-wavelength).

availability of data at 683 nm, $Q_n(683)$ was not included in the analysis so as to restrict the discussion to $Q_n(\lambda)$ at wavelengths characterized by elastic scattering only (in fact chlorophyll *a* fluorescence acts as a *source of diffuse light* and induces a more isotropic light field).

The $Q_n(\lambda)$ spectra used in the data analysis are plotted in Fig. 8.3 while the corresponding average values are given in Tab. 8.2. The spectra exhibit some dependence on $\lambda$ that, on average, shows a slight decrease from 412 to 510 nm, and an increase up to 665 nm. The decrease in $Q_n(\lambda)$ from 412 up to 510 nm does not appear in the simulated spectra proposed for oceanic waters by Morel and Gentili (1996). In fact

Table 8.2: Average $Q_n(\lambda)$ from the CoASTS (1995-1998) data set and standard deviations $\sigma_Q(\lambda)$.

| $\lambda(nm)$ | 412 | 443 | 490 | 510 | 555 | 665 |
|---|---|---|---|---|---|---|
| $Q_n \pm \sigma_Q$ | 4.7 ± 0.4 | 4.7 ± 0.4 | 4.6 ± 0.4 | 4.4 ± 0.4 | 4.7 ± 0.5 | 5.1 ± 0.7 |

these $Q_n(\lambda)$ spectra, given for $30< \theta_0 <75$ degrees and $Chla$ ranging from 0.03 to 3 mg $m^{-3}$, show a general increase with $\lambda$ from 412 to 670 nm. The different spectral behavior in the blue can probably be explained by a more pronounced absorption (in particular due to yellow substance and non-pigmented particles) characterizing the present experimental data in contrast to the theoretical data set simulated by Morel and Gentili (1996) for Case 1 water. Specifically, in the present analysis the seawater absorption coefficient $a(\lambda)$ shows an average value of 0.24±0.09 $m^{-1}$ at 412 nm against the maximum value of 0.04 $m^{-1}$ at 400 nm used by Morel and Gentili (1993).

Figure 8.4 displays the scatter plots of $Q_n(\lambda)$ v.s. $Q_n(\lambda_0)$ with $\lambda_0$=490 nm and the corresponding linear regression fits obtained according to

$$Q_n(\lambda) = A_0(\lambda) + S(\lambda)Q_n(\lambda_0). \tag{8.1.5}$$

The coefficients computed from the regressions are given in Tab. 8.3 with their 90% confidence interval. The scattering of data with respect to the regression line leads to determination coefficients $r^2$ ranging from 0.77 up to 0.94 in the spectral range 412-555 nm and $r^2$=0.50 at 665 nm. The lower correlation for $Q_n(665)$ is attributed to the lower penetration depth of light at 665 nm with respect to shorter $\lambda$. Because of this, in the presence of an optical stratification occurring just below the surface, $Q_n(665)$ could exhibit a spectral behavior different than $Q_n(\lambda)$ at shorter $\lambda$ as being related

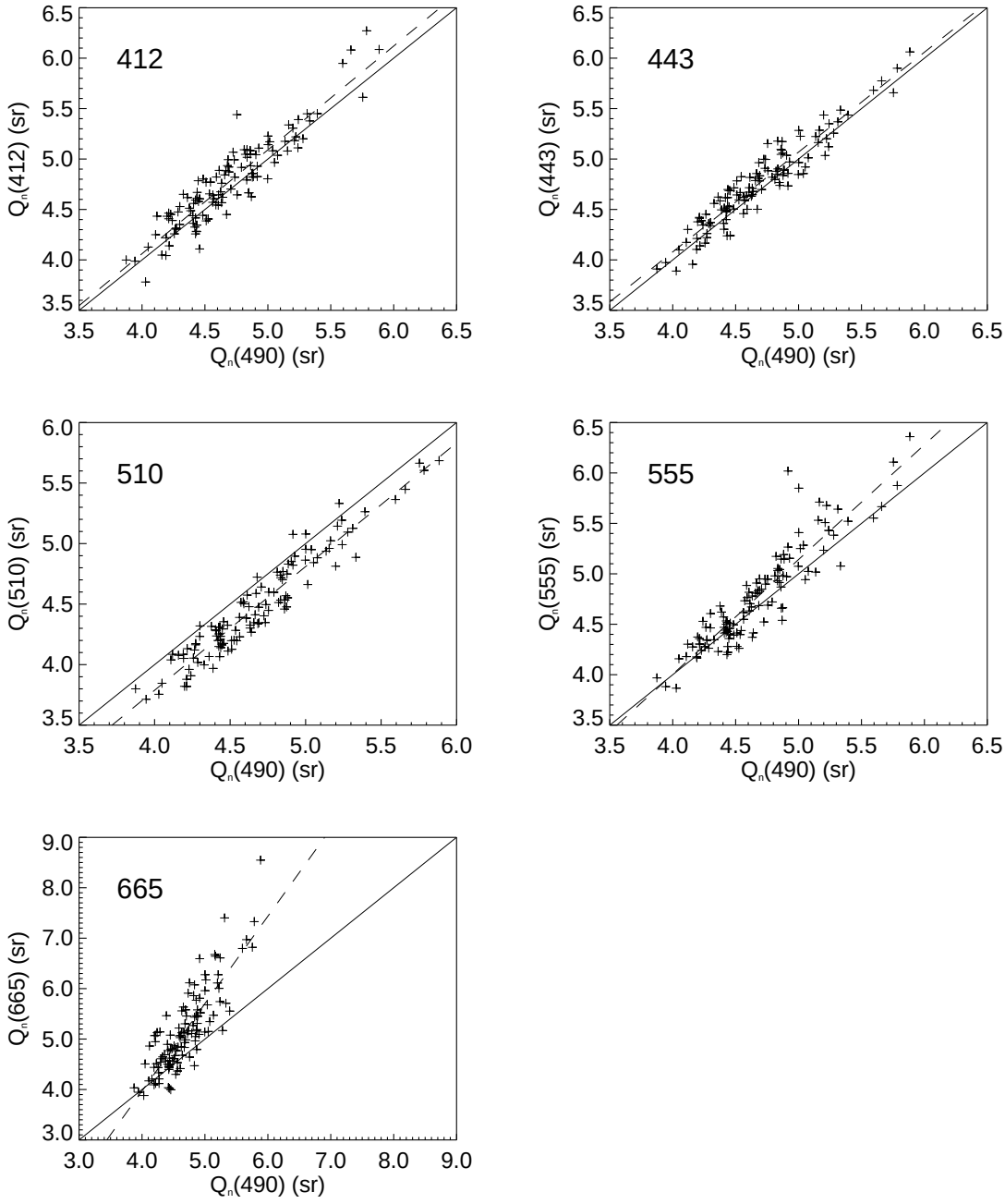


Figure 8.4: Scatter plots of $Q_n(\lambda)$ v.s. $Q_n(490)$. Dashed lines show the linear regression fits and the solid lines indicate the 1:1 ratio.

Table 8.3: Coefficients of the linear regression fits of $Q_n(\lambda)$ v.s. $Q_n(490)$ computed with Eq. 8.1.3. Values in parenthesis indicate the 90% confidence interval.

| $\lambda$ (nm) | $A_0$ | $S$ | $r^2(n = 118)$ |
|---|---|---|---|
| 412 | -0.054 (0.305) | 1.029 (0.065) | 0.85 |
| 443 | 0.120 (0.240) | 0.990 (0.051) | 0.90 |
| 510 | -0.300 (0.224) | 1.022 (0.048) | 0.91 |
| 555 | -0.544 (0.364) | 1.137 (0.077) | 0.83 |
| 665 | -2.959 (0.803) | 1.732 (0.171) | 0.71 |

to a *different* water volume. Additional uncertainty in $Q_n(665)$ could be induced by fluorescence edge effects in the presence of high chlorophyll *a* concentrations.

The use of a $\lambda_0$ different from 490 nm, could produce better or worse regressions (as actually produced by $\lambda_0$=412 or $\lambda_0$=665 nm, respectively), but this would not change the main results. The choice of $\lambda_0$=490 nm, was driven by the interest in linking $Q_n(\lambda)$ to an operational ocean color product such as $K_d(490)$.

Figure 8.5 shows scatter plots of $Q_n(\lambda)$ as a function of the sun zenith $\theta_0$ at 412, 490, 555 and 665 nm (i.e., at wavelengths considered representative for ocean color studies). The general increase of $Q_n(\lambda)$ with $\theta_0$, shows consistency with results proposed by Morel and Gentili (1996) and by Aas and Hojerslev (1999).

Among the inherent and apparent optical properties, $K_d(\lambda)$ showed the best correlations for a basic parameterization of $Q_n(\lambda)$. To investigate the dependence of $Q_n(\lambda)$ on $\theta_0$ and seawater optical properties, the $Q_n(\lambda)$ data were distributed into three different classes $i$=1-3 defined by intervals of increasing $K_d(\lambda)$ (i.e. $K_d(\lambda, i)$). These intervals were selected to constitute, for each $\lambda$, three equal logarithmic ranges within the observed $K_d(\lambda)$ span (the number of elements in each interval may change as a function of $\lambda$). The small number of classes was suggested by the need to differentiate

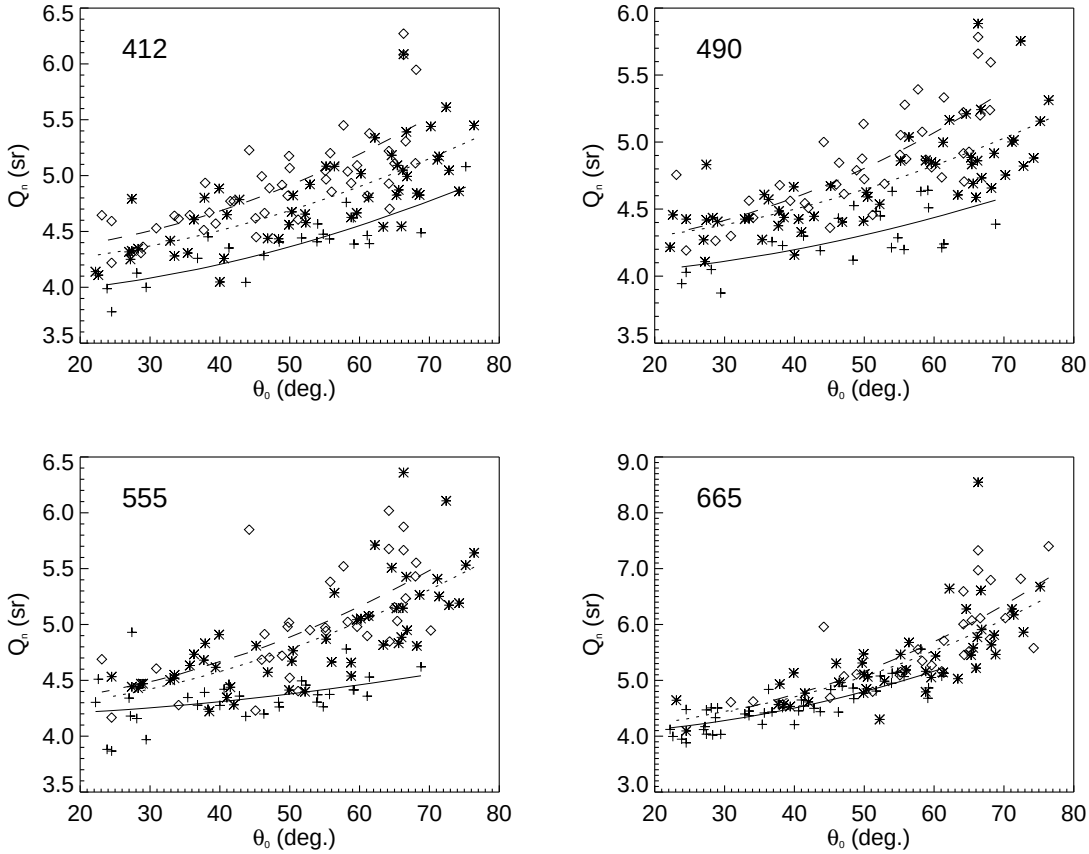


Figure 8.5: $Q_n(\lambda, i)$ plotted as a function of $\theta_0$ for the three classes $i$ defined by $K_d(\lambda, i)$ values, with the associated exponential fitting curves at 412, 490, 555 and 665 nm. + and solid lines: class 1; $*$ and dotted lines: class 2; $\diamond$ and dashed lines: class 3.

each class through a representative number of elements.

The fitting functions drawn in Fig. 8.5 for each class $i$ were computed with

$$Q_n(\lambda, i) = Q_{90}(\lambda, i) exp[-C(\lambda, i) cos\theta_0]. \tag{8.1.6}$$

For each $\lambda$, the $K_d(\lambda, i)$ interval limits and the resulting coefficients $\mathrm{C}(\lambda, i)$ and $Q_{90}(\lambda, i)$ were determined and are summarized in Tab. 8.4. $\mathrm{C}(\lambda, i)$ and $Q_{90}(\lambda, i)$ show a general increase with $K_d(\lambda, i)$ values at each $\lambda$. However, the $\mathrm{C}(\lambda, i)$ and $Q_{90}(\lambda, i)$ 90% confidence intervals (not shown) exhibit quite large values due to the

scattering of $Q_n(\lambda, i)$ data around the fitting curves. This scattering probably results from: (*i*) surface effects in $E_d(z, \lambda)$ which cause uncertainty in the retrieved $K_d(\lambda)$; (*ii*) the very different environmental conditions (i.e., sky radiance distribution and water type) characterizing the measurements; and (*iii*) the relatively small number of elements in some classes $i$. To minimize the former perturbation effects, global $\bar{C}(\lambda)$ coefficients were computed without any class separation. Then, imposing $\bar{C}(\lambda)$ constant for all $i$ classes, new exponential fits were computed to get the intercepts $\bar{Q}_{90}(\lambda, i)$.

The values of $\bar{Q}_{90}(\lambda, i)$ determined with coefficients $\bar{C}(\lambda)$, show a slight increase with respect to those computed with class dependent $\mathrm{C}(\lambda, i)$. The overall dependence of $\bar{Q}_{90}(\lambda, i)$ on $\lambda$ reflects the spectral dependence of the average $Q_n(\lambda)$ given in Tab. 8.2 with a decrease from 412 to 490-510 nm followed by an increase toward 665 nm. At each $\lambda$, the $\bar{Q}_{90}(\lambda, i)$ values show a general increase with $K_d(\lambda, i)$. $\bar{C}(\lambda)$ data show a weak spectral dependence in the 412-510 nm region with an average of $\sim$0.31, and increasing values of 0.38 and 0.70 at 555 nm and 665 nm, respectively. This is in general agreement with the trend of curves displayed in Morel and Gentili (1996) for simulations of $Q_n(\lambda)$ v.s. $\theta_0$. $\bar{Q}_{90}(\lambda, i)$ and $\bar{C}(\lambda)$ given in Tab. 8.4 at 490 nm for the first class $i$ (i.e. the class defined by the smallest $K_d(\lambda)$ values) have been compared with those proposed by Siegel (1984) and Aas and Højerslev (1999) in the same spectral region for oceanic water. $\bar{Q}_{90}(\lambda, i)$ show very close values (i.e., $\sim$5.2 sr), while $\bar{C}(\lambda)$ indicates a less pronounced dependence on $\theta_0$ (i.e., $\sim$0.30 v.s. $\sim$ 0.5 in Siegel (1984) and $\sim$0.45 in Aas and Højerslev (1999)).

Table 8.4: Coefficients $Q_{90}(\lambda, i)$ (in units of $sr^{-1}$) and $C(\lambda, i)$ (dimensionless) from the exponential fits of $Q_n(\lambda, i)$ v.s. $\theta_0$ obtained for the different classes $i$ defined by the interval limits $K_dmin$ and $K_dmax$ (in units of $m^{-1}$) at different center-wavelengths (in units of nm). Coefficients $\bar{Q}_{90}(\lambda, i)$ (in units of $sr^{-1}$) were computed with constant $\bar{C}(\lambda)$ (dimensionless).

| $\lambda$ | $K_dmin$ | $K_dmax$ | $Q_{90}(\lambda, i)$ | $C(\lambda, i)$ | $\bar{Q}_{90}(\lambda, i)$ | $\bar{C}(\lambda)$ |
|---|---|---|---|---|---|---|
| 412 | 0.107 | 0.206 | 5.284 | 0.298 | 5.382 | -0.328 |
| 412 | 0.206 | 0.352 | 5.737 | 0.315 | 5.779 | -0.328 |
| 412 | 0.352 | 0.756 | 6.303 | 0.388 | 6.072 | -0.328 |
| 443 | 0.088 | 0.160 | 5.165 | 0.257 | 5.331 | -0.307 |
| 443 | 0.160 | 0.292 | 5.667 | 0.303 | 5.680 | -0.307 |
| 443 | 0.292 | 0.688 | 6.129 | 0.349 | 5.972 | -0.307 |
| 490 | 0.058 | 0.127 | 4.925 | 0.209 | 5.228 | -0.302 |
| 490 | 0.127 | 0.219 | 5.502 | 0.263 | 5.626 | -0.302 |
| 490 | 0.219 | 0.500 | 6.123 | 0.378 | 5.851 | -0.302 |
| 510 | 0.074 | 0.123 | 4.356 | 0.126 | 4.849 | -0.293 |
| 510 | 0.123 | 0.205 | 5.240 | 0.253 | 5.362 | -0.293 |
| 510 | 0.205 | 0.446 | 5.988 | 0.395 | 5.634 | -0.293 |
| 555 | 0.096 | 0.139 | 4.758 | 0.130 | 5.677 | -0.383 |
| 555 | 0.139 | 0.202 | 5.986 | 0.350 | 6.098 | -0.383 |
| 555 | 0.202 | 0.376 | 6.250 | 0.383 | 6.252 | -0.383 |
| 665 | 0.467 | 0.567 | 6.679 | 0.514 | 7.641 | -0.699 |
| 665 | 0.567 | 0.654 | 7.501 | 0.609 | 7.857 | -0.699 |
| 665 | 0.654 | 0.819 | 8.040 | 0.691 | 8.073 | -0.699 |

In agreement with the former results, the equation for a modeled $\bar{Q}_n(\lambda, i)$ specific for the northern Adriatic Sea coastal waters, is

$$\bar{Q}_n(\lambda, i) = A_0(\lambda) + S(\lambda)\bar{Q}_{90}(\lambda_0, i)exp[-\bar{C}(\lambda_0)cos\theta_0] \tag{8.1.7}$$

where the values $A_0(\lambda)$ and $S(\lambda)$ are given in Tab. 8.3 and the values of $\bar{Q}_{90}(\lambda_0, i)$ and $\bar{C}(\lambda_0)$ are given in Tab. 8.4.

### 8.1.3 Radiometric accuracy and bio-optical modelling

Bio-optical modelling makes use of radiometric quantities like $L_{WN}$, $R$, $R_{RS}$, $Q_n$, $K_d$ and band ratios of the same quantities. Thus their uncertainties affect the accuracy of models and consequently that of the higher level products derived by applying those models to satellite ocean color data. To investigate these effects, a sensitivity analysis was carried out using estimates from uncertainties derived for individual radiometric quantities. In the case of the regional algorithms herein presented for $Chla$ and $K_d$, the analysis was carried applying an expected uncertainty of 5% in the ratios of $R_{RS}$ and $L_{WN}$, respectively. This 5% estimate results from the the combination of uncertainties affecting the individual quantities applied for the ratio (see Chapters 6), taking into account that some contributions to the individual uncertainties of each quantity are common to both and thus are not strictly additive.

Results from this sensitivity analysis for *Chla* determined with the AD algorithm for the range 0.1–10 mg m$^3$, indicate uncertainties of 0.05–1.0 mg m$^3$, respectively (corresponding to 50% and 10% of the absolute values at each end of the range). These results compare in magnitude with the intrinsic uncertainty induced by natural variability of the considered band-ratio algorithm, i.e., 33% (D'Alimonte and Zibordi, 2003) and with the target uncertainty for satellite derived products, i.e. 35% (McClain et al., 2004).

Results from the sensitivity analysis made for the diffuse attenuation coefficient at the center-wavelength of 490 nm, determined with Eq. 8.1.2 proposed for the range 0.08–0.8 m$^{-1}$, indicate that an uncertainty of 5% in the spectral ratio of $L_{WN}$ produces an average uncertainty of 8% in the computed $K_d(490)$.

The effects of uncertainties in the modelling of $Q_n$ were determined through the

uncertainties affecting the $E_u/L_u$ ratio. Given an estimate of 4% in the uncertainties of measured $Q_n$ (Zibordi and Berthon, 2001), the same uncertainty would directly translate into modelled $Q_n$ values.

These overall results confirm the need for accurate radiometric data for applications such as band-ratio algorithms. In fact, whilst these benefit from reduction in uncertainties partially cancelling out through ratios, residual uncertainties of a few percent with opposite sign at different wavelengths like those introduced by cosine errors in multi-collector radiometers (see Chapter 4), may still become the source of large uncertainties in derived products.

## 8.2 Remote sensing data validation

The primary remote sensing quantity of interest for the development of geophysical products, is the normalized water–leaving radiance, $L_{WN}(\lambda)$, from which higher level products are derived.

The accurate determination of remote sensing $L_{WN}(\lambda)$ values requires the absolute calibration of the space sensor and the removal of the atmospheric perturbing effects, i.e., the discrimination of $L_{WN}(\lambda)$ from the total radiance measured by the spaceborne sensor viewing the sea through the atmosphere. The accuracy of the absolute calibration and the effectiveness of the atmospheric correction can be determined by comparing contemporaneous satellite derived and *in situ* $L_{WN}(\lambda)$ data or, alternatively, the remote sensing reflectance, $R_{RS}(\lambda)$. The generalized process of ground truth comparison under a wide range of environmental conditions is usually called validation. The more specific process of forcing the agreement between the spaceborne sensor and sea truth observations is usually called vicarious calibration.

Both activities are major tasks of ocean color missions, and require highly accurate *in situ* data (Hooker and McClain, 2000).

Considering the difficulty of producing large individual data sets of *in situ* measurements representative of the various marine bio-optical regimes, present validation programs combine field observations from many different and fully independent sources into a single data set (Werdell et al., 2003). This combination impairs the quantification of measurement uncertainties which depend on: (*i*) the performance of different field instruments; (*ii*) the use of diverse sampling methods; (*iii*) the adoption of a variety of calibration sources and protocols; and (*iv*) the application of assorted processing schemes. Round-robin experiments (McClain et al., 2004) showed that the above differences tend to increase the total uncertainty budget well above the maximum 5% value established for $L_{WN}(\lambda)$, thus reducing the effectiveness of validation processes. Therefore, a network of standardized instruments continuously operating at different sites representative of distinct water types could produce data with minimum (or identified) uncertainties and consequently improve operational validation activities. This objective was the rationale for the development of AERONET-OC (Zibordi et al., 2006c), the ocean color component of AERONET (Holben et al., 2001), using SeaPRISM systems deployed on various offshore structures like oceanographic towers, oil platforms, navigation aids (see Fig. 8.6). Within such a context, the error budget presented in Chapter 6 provided solid basis to the operational exploitation of AERONET-OC data and supported the use of the AAOT site for ocean validation activities (Zibordi et al., 2006a,b).

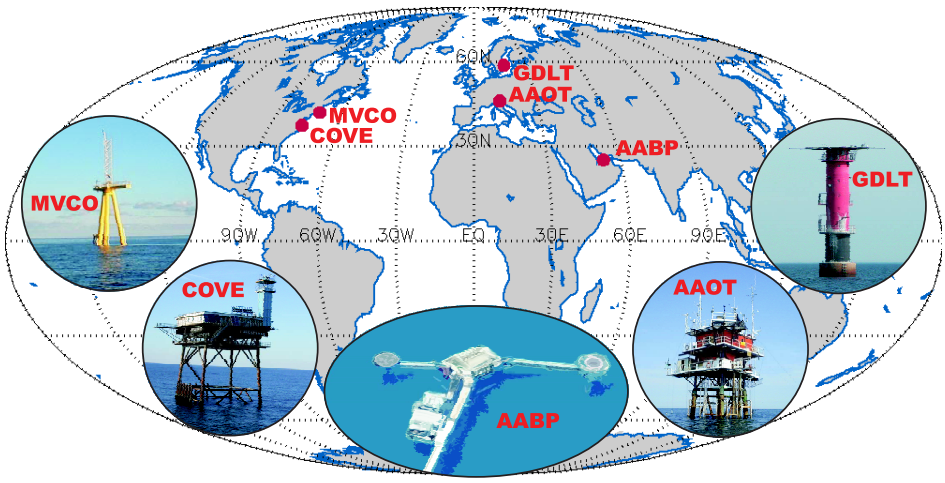


Figure 8.6: AERONET-OC test sites (After Zibordi et al. (2006c).

### 8.2.1 Assessment of remote sensing $L_{WN}$

Normalized water-leaving radiances from ocean color sensors for which products are regularly available (i.e., Sea-viewing Wide Field-of-View Sensor (SeaWiFS), Moderate Resolution Imaging Spectroradiometer (MODIS) and Medium Resolution Imaging Spectrometer (MERIS)), and normalized water-leaving radiances from SeaPRISM point measurements taken at the AAOT, were used for inter-comparisons.

The SeaPRISM measurements applied in the comparisons with remote sensing normalized water-leaving radiances were quality assured by removing data affected by clouds (as determined from triplets of sun-photometric measurements (Smirnov et al., 2000)), high variability (as determined from multiple measurements of the radiance from the sea), and potential superstructure perturbations (by accounting for the deployment geometry (Hooker and Zibordi, 2005)).

Following the methodology previously applied by Sturm and Zibordi (2002) and Mélin et al. (2003) to SeaWiFS and *in situ* data, the matchups used for the analysis were produced using the most coincident pairs of *in situ* and satellite data collected

within less than one hour of each other, to minimize perturbations induced by the temporal variability of the sea and atmosphere. Satellite data were retained for comparison only when all the pixels pertaining to the square box of 3 × 3 elements centered at the AAOT site were not: (*i*) affected by cloud and sun glint flagging; or (*ii*) characterized by excessive satellite viewing angles ($\theta \geqslant 56$ degrees) or excessive sun zenith angles ($\theta_0 \geqslant 70$ degrees).

Spectral differences between remote sensing and *in situ* data were minimized by determining synthetic $L_{WN}(\lambda)$ at the specific remote sensing center-wavelength $\lambda$ from $L_{WN}(\lambda_0)$ measured at the nearest center-wavelength $\lambda_0$ assuming ideal (rectangular), 10 nm wide, spectral bandpasses. Computations were made using

$$L_{WN}(\lambda) = L_{WN}(\lambda_0)\frac{E_0(\lambda)}{E_0(\lambda_0)}\frac{f_0(\lambda)}{Q_0(\lambda)}\frac{Q_0(\lambda_0)}{f_0(\lambda_0)}\frac{b_b(\lambda)}{a(\lambda)+b_b(\lambda)}\frac{a(\lambda_0)+b_b(\lambda_0)}{b_b(\lambda_0)} \qquad (8.2.1)$$

where: $f_0(\lambda)$ is the function relating the irradiance reflectance to the seawater inherent optical properties and $Q_0(\lambda)$ is the Q-factor describing the anisotropic distribution of the in water light field, both at $\theta_0 = 0$ and $\theta = 0$ (see also Chapter 6); $a(\lambda)$ is the total seawater absorption coefficient given by the sum of the absorption coefficients of particulate matter, $a_p(\lambda)$, colored dissolved organic matter, $a_y(\lambda)$, and pure seawater, $a_w(\lambda)$; and $b_b(\lambda)$ is the seawater backscattering coefficient given by the sum of the backscattering coefficients of particulate matter, $b_{bp}(\lambda)$, and pure seawater, $b_{bw}(\lambda)$. Synthetic values of $L_{WN}(\lambda)$ were computed assuming:

1. $\lambda$ is close to $\lambda_0$ so that $f_0(\lambda)/Q_0(\lambda) \times Q_0(\lambda_0)/f_0(\lambda_0) \approx 1$;

2. $a_p(\lambda)$ and $b_{bp}(\lambda)$ are functions only of $Chla$, as iteratively determined with the AD regional algorithm (Berthon and Zibordi, 2004) from SeaPRISM data derived at 490 nm and measured at 555 nm.

Spectral values of $a_p(\lambda)$ and $b_{bp}(\lambda)$ were estimated using the bio-optical model of

Morel and Maritorena (2001), while spectral $a_y(\lambda)$ values were obtained from

$$a_y(\lambda) = a_y(400)exp[-0.018(\lambda - 400)] \tag{8.2.2}$$

where $a_y$ at 400 nm was determined with an empirical regional algorithm applied to SeaPRISM data at 412 and 555 nm (Berthon et al., 2000).

**a. SeaWiFS Matchups**

The SeaWiFS multispectral scanning radiometer is the only Earth observing instrument aboard the OrbView-2 spacecraft launched on 1 August 1997. SeaWiFS provides data in 8 spectral channels within the 400–900 nm interval (Gordon and Wang, 1994). Specifically, it provides ocean color information in 6 bands 20 nm wide within the 400-700 nm interval, with a spatial resolution of 1100 m (at nadir).

The SeaWiFS level-1A data used in this analysis were obtained from the GSFC Distributed Active Archive Center (DAAC) and processed with the SeaDAS software package (version 4.8) relying on the atmospheric correction scheme proposed by Gordon and Castaño (1987) and its successive modifications (Patt et al., 2003; Robinson et al., 2000; Siegel et al., 2000; Wang, 2000). The SeaWiFS products analyzed here are the normalized water-leaving radiances corrected for the effects of off-nadir viewing angle and seawater anisotropy, $L_{WN}^{SWF}(\lambda)$, at 412, 443, 490, 510, 555, and 670 nm.

The comparison for 208 SeaWiFS match-ups produced between May 2002 and September 2005, is presented in Fig.'s 8.7 and 8.8 with $L_{WN}^{SWF}(\lambda)$ and $L_{WN}^{SP}(\lambda)$ indicating SeaWiFS and SeaPRISM normalized water-leaving radiances, respectively. The comparison results are summarized in Tab. 8.5 through: (*i*) the average of absolute (unsigned) percent differences, $|\psi|$, between remote sensing and *in situ* data; (*ii*) the average of relative (signed) percent differences, $\psi$; (*iii*) the root mean square

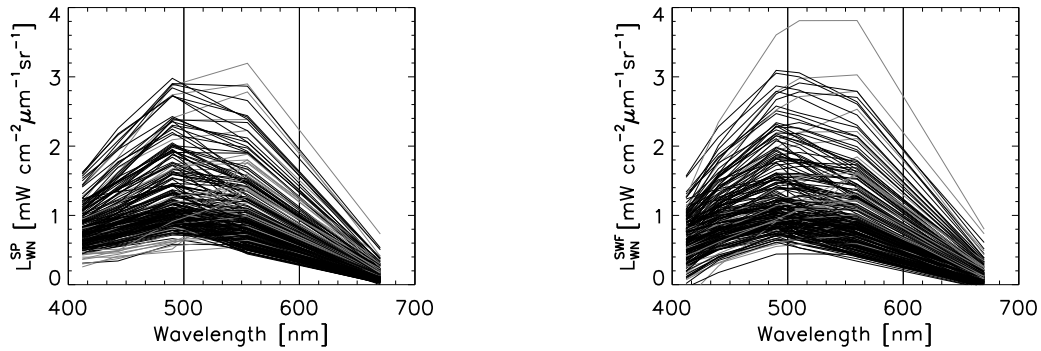


Figure 8.7: SeaPRISM $L^{SP}_{WN}(\lambda)$ (left panel) and SeaWiFS $L^{SWF}_{WN}(\lambda)$ (right panel) spectra for 208 match-ups in the 412–670 nm spectral region (note the missing center-wavelength at 510 nm in the SeaPRISM spectra).

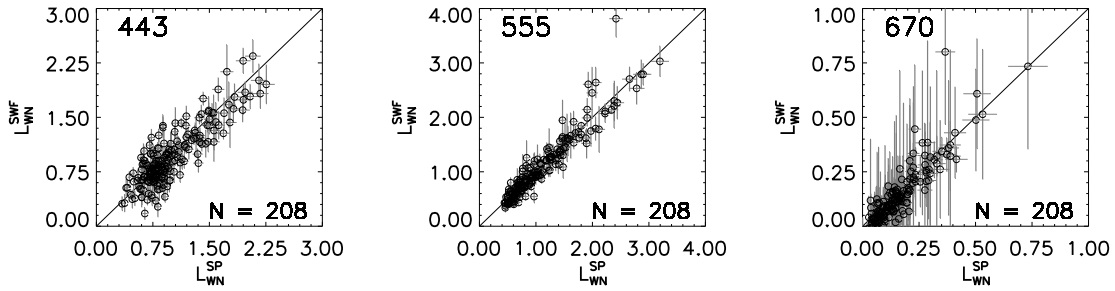


Figure 8.8: Comparison of SeaWiFS $L^{SWF}_{WN}(\lambda)$ versus SeaPRISM $L^{SP}_{WN}(\lambda)$ normalized water-leaving radiances (from left to right) at the 443, 555 and 670 nm center-wavelengths. The vertical error bars indicate the standard deviation across the 3x3 image SeaWiFS elements centered at the AAOT site, while the horizontal error bars for the SeaPRISM data indicate the expected uncertainty in $L^{SP}_{W}(\lambda)$.

of differences, rms; and *iv.* the coefficient of determination, $r^2$. Results indicate slight underestimates with $\psi$ lower than 2% (absolute) for $L^{SWF}_{WN}(\lambda)$ with respect to $L^{SP}_{WN}(\lambda)$, in the 443–555 nm interval. The poorest agreement is observed at 412 nm with $|\psi|$=30% and at 670 nm with $|\psi|$=78%. The best agreement is observed at 490 nm with $|\psi|$=0%. The spectral ratio of normalized water-leaving radiances at 490 and 555 nm shows absolute percent differences $|\psi|$=7% and bias $\psi$=-1%, explained by the differences observed at the individual channels used for the ratio.

Table 8.5: Statistical results from the comparison of SeaWiFS versus *in situ* (i.e., SeaPRISM) $L_{WN}$ data at specific center-wavelengths for the available match-ups, $N$. The data in the first column indicate the average and the standard deviation (in brackets), of the major quantities characterizing the match-up data set: *in situ* $L_{WN}$ at 555 nm in units of mW cm$^{-2}$ $\mu$m$^{-1}$ sr$^{-1}$; sun zenith $\theta_0$ in degrees; $Chla$ in $mg$ m$^{-3}$ determined with the AD regional algorithm (Berthon and Zibordi, 2004) applied to *in situ* SeaPRISM data; and aerosol optical thickness $\tau_a$ at 870 nm.

| SeaWiFS, N=208 | Stat. quantity | 412 | 443 | 490 | 555 | 670 | 490/555 |
|---|---|---|---|---|---|---|---|
| $L_{WN}(555)$=1.08 (0.55) | $\|\psi\|$ | 30 | 18 | 12 | 11 | 78 | 7 |
| $\theta_0$=40 (13) | $\psi$ | -17 | -2 | +0 | -1 | -63 | -1 |
| $Chla$=1.2 (2.5) | rms | 0.27 | 0.21 | 0.19 | 0.18 | 0.07 | 0.11 |
| $\tau_a(870)$=0.077 (0.048) | r$^2$ | 0.66 | 0.86 | 0.94 | 0.95 | 0.90 | 0.94 |

**b. MODIS Matchups**

The MODIS cross-track scanning multispectral radiometer was launched aboard the Aqua spacecraft on 4 May 2002. This sensor, frequently designated as MODIS-A and hereafter simply referred to as MODIS, provides data in 36 spectral channels within the 400–14400 nm interval (Barnes et al., 1998).

In particular MODIS provides ocean color information in 7 bands 10 nm wide within the 400–700 nm interval, with a spatial resolution of 1000 m at nadir. The MODIS level-1A data used in this analysis were obtained from the GSFC Distributed Active Archive Center (DAAC) and processed with the SeaDAS software package (version 4.8). The MODIS products analyzed here are the normalized water-leaving radiances corrected for the effects of off-nadir viewing angle and seawater anisotropy at center-wavelengths 412, 443, 488, 551 and 667 nm.

The comparison for 215 MODIS match-ups selected between May 2002 and September 2005, is presented in Fig.'s 8.9 and 8.10 with $L_{WN}^{MOD}(\lambda)$ and $L_{WN}^{SP}(\lambda)$ indicating

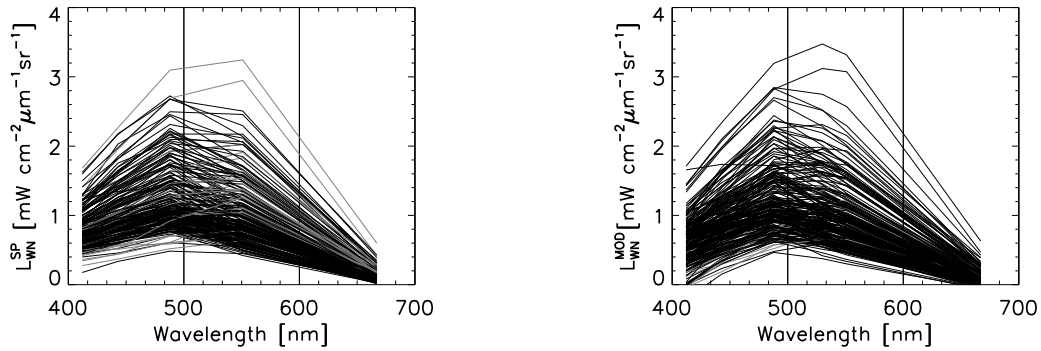


Figure 8.9: SeaPRISM $L_{WN}^{SP}(\lambda)$ (left panel) and MODIS $L_{WN}^{MOD}(\lambda)$ (right panel) spectra 215 match-ups in the 412–667 nm spectral region (note the missing center-wavelength at 530 nm in the SeaPRISM spectra).

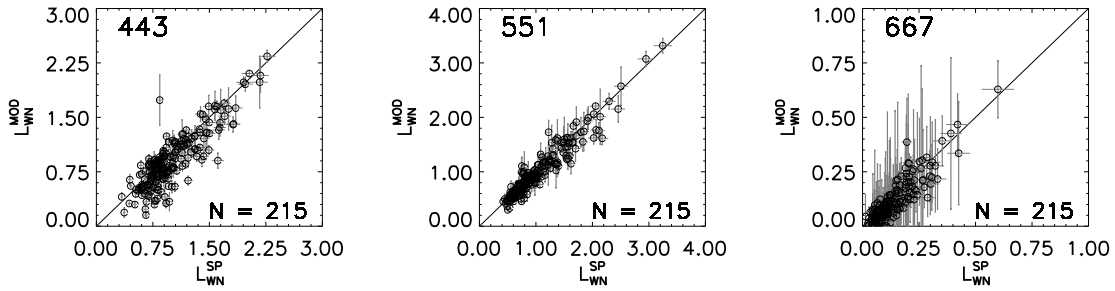


Figure 8.10: Same as in Fig. 8.8 but for MODIS (from left to right) at the 443, 551 and 667 nm center-wavelengths.

MODIS and SeaPRISM normalized water-leaving radiances, respectively. The comparison analysis between remote sensing and *in situ* data was carried out following the same scheme applied to the SeaWiFS data. The statistics on the comparison results summarized in Tab. 8.6, exhibit an underestimate of $L_{WN}^{MOD}(\lambda)$ with respect to $L_{WN}^{SP}(\lambda)$ in the 443–551 nm interval, with $\psi$ lower than 9% (absolute). Similarly to SeaWiFS matchups, the lowest agreements is observed at 412 nm with $|\psi|$=30% and at 667 nm with $|\psi|$=49%. The spectral ratio of normalized water-leaving radiances at 488 and 551 nm shows high average percent differences with $|\psi| = 6\%$ and $\psi = -1\%$. The values of $r^2$ higher than 0.7 and the values of rms ranging within 0.06–0.30 from

Table 8.6: As in Tab. 8.5 but for MODIS.

| MODIS, N=215 | Stat. quantity | 412 | 443 | 488 | 551 | 667 | 488/551 |
|---|---|---|---|---|---|---|---|
| $L_{WN}(555)$=1.01 (0.46) | $\|\psi\|$ | 30 | 18 | 11 | 11 | 49 | 6 |
| $\theta_0$=42 (12) | $\psi$ | -25 | -9 | -1 | -4 | -35 | -1 |
| $Chla$=0.76 (0.59) | rms | 0.30 | 0.22 | 0.17 | 0.15 | 0.06 | 0.10 |
| $\tau_a(870)$=0.071 (0.042) | $r^2$ | 0.70 | 0.86 | 0.94 | 0.96 | 0.88 | 0.94 |

667 to 412 nm, are generally comparable to those computed for SeaWiFS match-ups at the equivalent center-wavelengths. The overall results indicate a close agreement between SeaWiFS and MODIS radiometric products, supported by the use of a similar processor and the application of the same vicarious calibration technique with *in situ* data from the same site and measurement system (different from the AAOT site and SeaPRISM system, respectively).

### c. MERIS Match Ups

The MERIS imaging spectrometer was launched onboard the ENVISAT-1 spacecraft on March 1, 2002. MERIS provides data in 15 spectral channels typically 10 nm wide within the 400–900 nm interval (Bézy et al., 2000). Specifically, it provides ocean color information in 8 bands 10 nm wide within the 400–700 nm interval, with a full spatial resolution of 300 m or a reduced resolution of 1200 m at nadir. The reduced resolution MERIS level-2 data used in this study were delivered by the European Space Agency (ESA) and are identified by the MEGS-PC/7.4 code relying on the schemes proposed by Antoine and Morel (1999) and Moore et al. (1999).

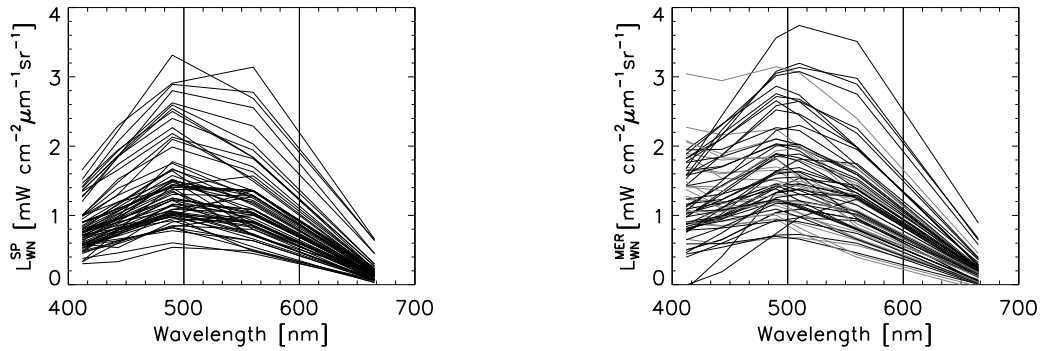


Figure 8.11: SeaPRISM $L_{WN}^{SP}(\lambda)$ (left panel) and MERIS $L_{WN}^{MER}(\lambda)$ (right panel) spectra for the considered 67 match-ups in the 412–665 nm spectral region (note the missing center-wavelength at 510 nm in the SeaPRISM spectra).

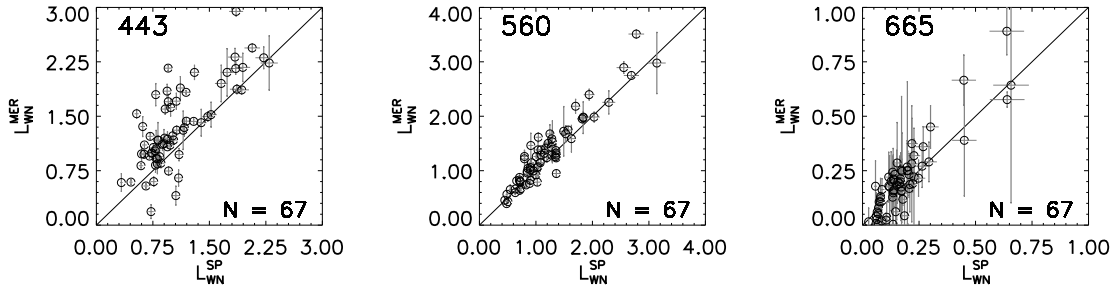


Figure 8.12: Same as in Fig. 8.8 but for MERIS (from left to right) at the 443, 560 and 665 nm center-wavelengths.

The MERIS $L_{WN}(\lambda)$ used for the assessment were determined from level-2 reflectance $R_{WN}(\varphi, \theta, \lambda)$ at center-wavelengths 412, 443, 490, 510, 560 and 665 nm, by applying

$$L_{WN}(\lambda) = R_{WN}(\varphi, \theta, \lambda)\frac{E_S(\lambda)}{\pi}\, C_{\Im Q}(\varphi, \theta, \theta_0, \lambda, \tau_a, Chla, W)\, C_{f/Q}(\theta_0, \lambda, \tau_a, Chla) \tag{8.2.3}$$

where $E_S(\lambda)$ is the mean extraterrestrial solar irradiance delivered as one of the MERIS products and determined in agreement with the values published by Thuillier et al. (1998). The quantities $C_{f/Q}(\theta_0, \lambda, \tau_a, Chla)$ and $C_{\Im Q}(\varphi, \theta, \theta_0, \lambda, \tau_a, Chla, W)$ were introduced to remove the off-nadir viewing angle dependence and the anisotropy

Table 8.7: As in Tab. 8.5 but for MERIS.

| MERIS, N=67 | Stat. quantity | 412 | 443 | 490 | 560 | 665 | 490/560 |
|---|---|---|---|---|---|---|---|
| $L_{WN}(555)$=1.30 (0.60) | $\|\psi\|$ | 80 | 43 | 22 | 18 | 46 | 9 |
| $\theta_0$=58 (14) | $\psi$ | +78 | +42 | +21 | +15 | +22 | +6 |
| $Chla$=0.87 (0.38) | rms | 0.69 | 0.50 | 0.38 | 0.27 | 0.08 | 0.16 |
| $\tau_a(870)$=0.098 (0.086) | $r^2$ | 0.59 | 0.79 | 0.92 | 0.95 | 0.91 | 0.83 |

effects of the in–water light field (see Eq. 6.1.5 and Eq. 6.2.3).

The comparison for 67 MERIS match-ups produced from March 2003 to January 2006, is presented in Fig.'s 8.11 and 8.12, with $L_{WN}^{MER}(\lambda)$ and $L_{WN}^{SP}(\lambda)$ indicating MERIS and SeaPRISM normalized water-leaving radiances, respectively. This was carried out following the same scheme applied to the SeaWiFS and MODIS data. The statistics on the comparison results summarized in Tab. 8.7 shows a significant overestimation (with $\psi$ varying from 15% and 42%) of $L_{WN}^{MER}(\lambda)$ with respect to $L_{WN}^{SP}(\lambda)$ in the 443–560 nm interval (Zibordi et al., 2006a). Once more the worst agreement is observed at 412 nm (with $|\psi| = 80\%$) and at 665 nm (with $|\psi| = 46\%$). The spectral ratio of normalized water-leaving radiances at 490 and 560 nm exhibits $|\psi| = 9\%$ and $\psi = +6\%$.

The values of $r^2$ and rms computed for MERIS match-ups generally show worse results when compared to SeaWiFS and MODIS match-ups. This finding enabled the identification of discrepancies in the MERIS processing chain probably resulting from an under-correction of the atmospheric effects due to a lack of specific aerosol models or the absence of any vicarious calibration process.

### 8.2.2 Time-Series Analysis

Time-series of *in situ* optical observations have relevance for a continuous assessment of satellite products and additionally for water quality analysis at specific sites (Zibordi et al., 2006b,d). An evaluation of the suitability of time-series of above-water radiometric products for such a purpose was made using: (*i*) a three-year time-series of SeaPRISM measurements produced from April 2002 up to March 2005 at the AAOT; (*ii*) SeaWiFS remote sensing imagery of the northern Adriatic Sea collected from January 2002 up to December 2004, and (*iii*) reference *Chla* and WiSPER in–water radiometric measurements produced at the AAOT.

The SeaPRISM normalized water-leaving radiances, $L_{WN}(\lambda)$, were produced in agreement with the method described in Chapter 6. The SeaWiFS data were processed using the SeaWiFS Data Analysis System (SeaDAS, release 4.7) software. The outputs from the processing code (i.e., $L_{WN}$ at 412, 443, 490, 510, 555 and 670 nm) saved for a 3x3-pixel square centered at the location of the AAOT site. SeaWiFS $L_{WN}$ data were excluded from the analysis if at least one of the 9 pixels was affected by one or more of the standard flags of the processing software (see the preceding subsection). Data used as an independent reference for the comparison of SeaPRISM data are $L_{WN}$ determined at 412, 443, 490, 510, 555, 665 and 683 nm from in water radiometric profiles collected with WiSPER. Further reference data included in this investigation are *Chla* from High Performance Liquid Chromatography (HPLC) analysis of surface water samples determined with an estimated uncertainty of 10% (Claustre et al., 2004).

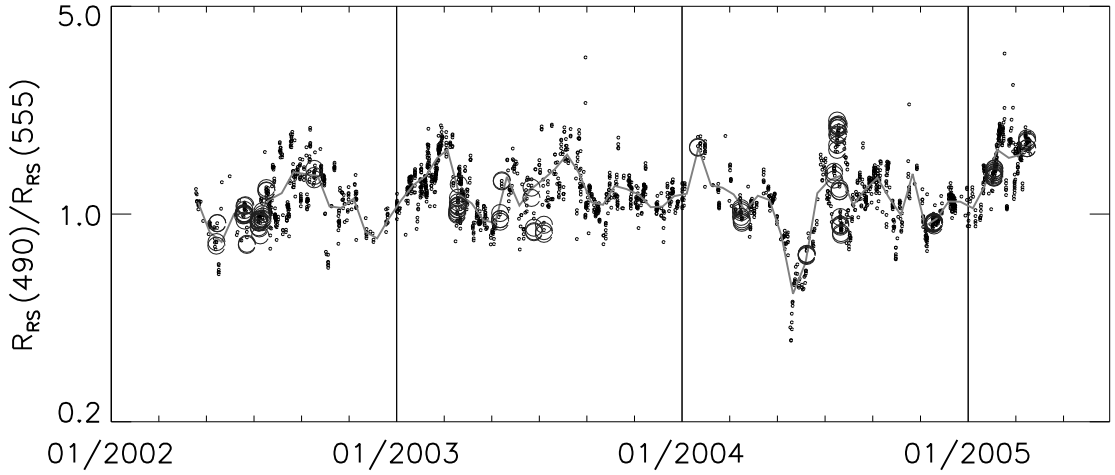


Figure 8.13: SeaPRISM $R_{RS}$ ratios at 490 and 555 nm (small circles). The continuous line indicates data averaged over 2-week periods. The large circles indicate WiSPER reference $R_{rs}$ ratios at 490 and 555 nm (after Zibordi et al. (2006b).

A time series of *Chla* values was derived from the SeaPRISM radiometric data using the AD regional bio-optical algorithm (see Eq. 8.1.1). Over the 1068 measurement days constituting the SeaPRISM time series, 45% did not produce any quality assured measurement, one single measurement was produced in 13% of the days, 2 to 12 measurements were produced in 42% of the days (see the quality assurance criteria in Chapter 6). The time-series of $R_{RS}$ ratios at 490 and 555 nm is presented in Fig. 8.13, where the $R_{RS}$ data at 490 nm (not included in the center-wavelengths of the current SeaPRISM instrument series) were linearly interpolated between the values at 443 and 501 nm as an alternative to the application of Eq. 8.2.1 to minimize effects of center-wavelength differences. The range of variation and the average of $R_{RS}(490)$ $R_{RS}(555)$ exhibits values comparable to those already reported for *in situ* measurements at the AAOT site (Berthon et al., 2002). The consistency of SeaPRISM $R_{RS}$ ratios, and implicitly of the synthetic $R_{RS}$ values at 490 nm, is supported by the comparison with reference values determined from WiSPER profile data collected within

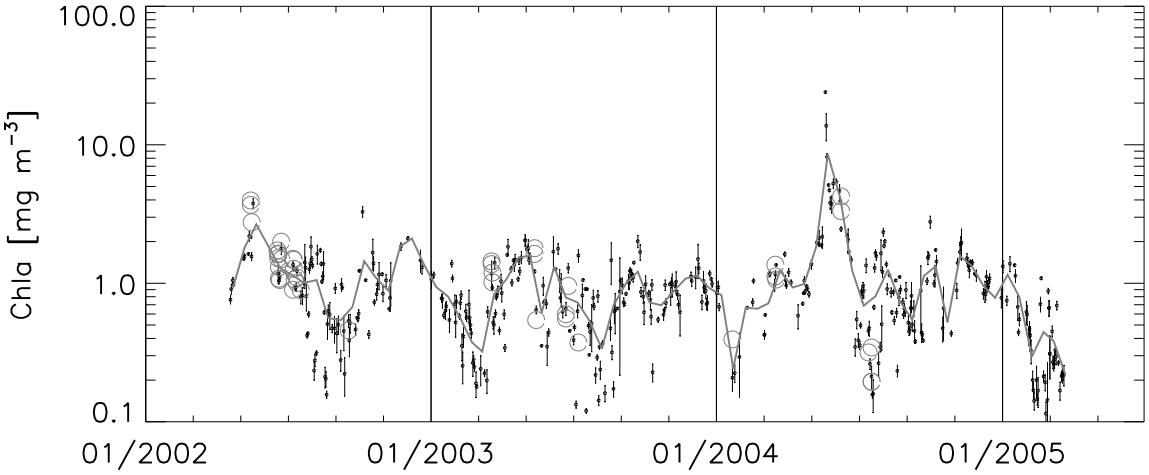


Figure 8.14: Daily averages of SeaPRISM derived *Chla* (small circles) determined for days with at least two quality assured measurements. The error bars indicate the standard deviation (the daily changes exhibit a variation coefficient of 11% with an average *Chla* of 1.1 mg m$^{-3}$). The continuous line indicates *Chla* data averaged over 2-week periods. The large circles indicate HPLC *Chla* reference values (after Zibordi et al. (2006b).

60 minutes from SeaPRISM data. The agreement between SeaPRISM and WiSPER $R_{RS}$ ratios is quantified by an average absolute difference $|\psi|$ 4.0% for the available 125 match-ups.

Figure 8.14 shows the time-series of daily average *Chla* values estimated from SeaPRISM $R_{RS}$ data by applying the AD regional algorithm, together with the *Chla* reference values from HPLC analysis. Data exhibit maxima in spring and autumn, and minima in summer and winter, in agreement with seasonal *Chla* cycles already reported for the measurement site (Berthon et al., 2002). The SeaPRISM derived *Chla* typically varies within 0.1–3.0 mg m$^{-3}$, except for a major peak reaching 25 mg m $^{-3}$ between May and June 2004. This peak corresponds to a phytoplankton bloom episode associated with traces of mucilage in the water. This occurrence is confirmed by field observations made in June 2004 during CoASTS measurements and marked

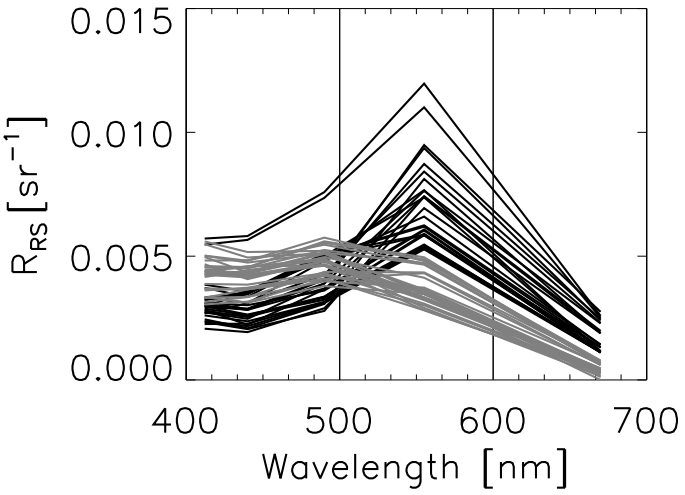


Figure 8.15: SeaPRISM $R_{RS}$ spectra from multiple observations performed during periods characterized by conditions of high (in late May 2004 and shown with black lines) and low (in early July 2004 and shown with grey lines) *Chla* (after Zibordi et al. (2006b).

by the available HPLC *Chla* data for the decaying phase of the bloom. This event is followed by low *Chla* in early July 2004, partly explained by the scavenging of particles in the water column due to sinking of mucilage material.

SeaPRISM $R_{RS}$ spectra representative of the two conditions (high *Chla* in late May 2004 and low *Chla* in early July 2004) are shown in Fig. 8.15. During the phase of low *Chla*, $R_{RS}$ at 555 nm appears significantly lower whereas $R_{RS}$ between 412 and 490 nm has slightly increased leading to a shift of the $R_{RS}$ maxima from 555 nm toward 490 and 440 nm as the *Chla* levels declines. The consistency of these spectral signatures supports the quantitative data presented in Fig. 8.14. However, the extremely high SeaPRISM derived *Chla* corresponding to the May-June 2004 peak have to be treated with some caution because of the lower accuracy of the applied algorithm for high *Chla* and the increased complexity of the seawater optical processes due to the presence of mucilage.

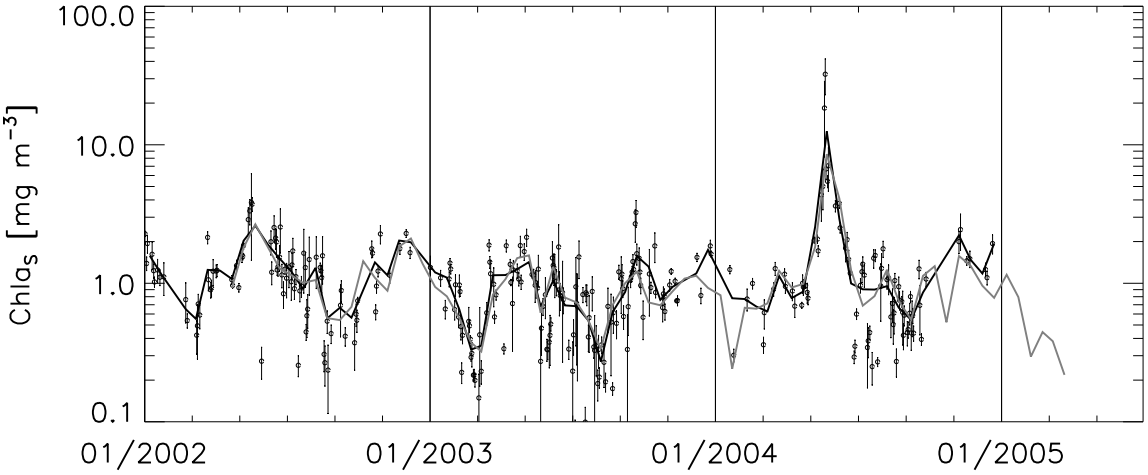


Figure 8.16: SeaWiFS derived *Chla* (small circles). The error bars indicate the standard deviation of the values from the 3x3 square pixels centered at the AAOT site. The black line indicates data averaged over 2-week periods. The gray line indicates the averaged SeaPRISM derived *Chla* (after Zibordi et al. (2006b).

Similar to the $R_{RS}$ reference values displayed in Fig. 8.13, the HPLC *Chla* reference values plotted in Fig. 8.14 also show a high qualitative agreement with the SeaPRISM derived values. This was quantitatively confirmed by the comparison of SeaPRISM versus HPLC derived *Chla* exhibiting $|\psi| = 32\%$ for the available 41 match-ups (Zibordi et al., 2006b). This result is in keeping with the expected average uncertainty of 33% reported for the AD algorithm (D'Alimonte and Zibordi, 2003). The varaibility within individual days (i.e, short-term variability) illustrated in Fig. 8.14 by the standard deviation of daily SeaPRISM derived *Chla* can vary significantly from day to day. This can be explained by the influence of regional river discharges, meteorological variability and tide effects, which may produce very short time-scale variations in the northern Adriatic Sea coastal areas (Berthon et al., 2002).

Figure 8.16 shows the time series of *Chla* values determined from SeaWiFS data at the AAOT site. The SeaWiFS and SeaPRISM data exhibit very similar trends

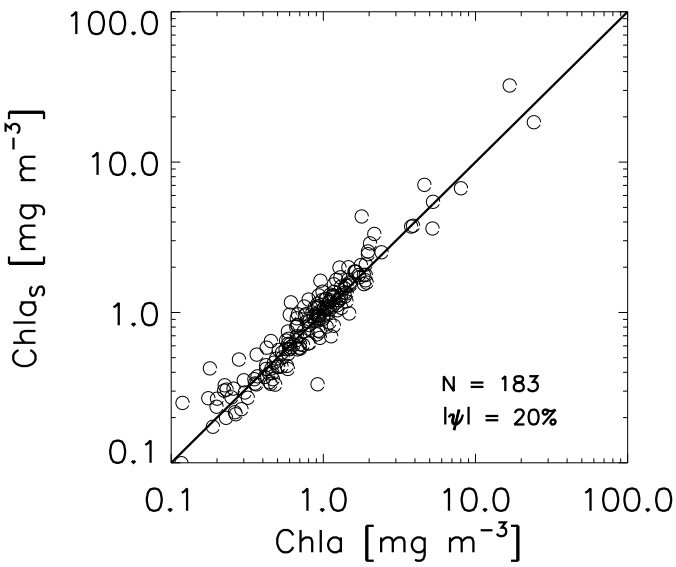


Figure 8.17: Scatter plot of concurrent SeaWiFS derived versus SeaPRISM derived *Chla* values (N is the number of match-ups, $|\psi|$ is the average absolute difference, subscript $S$ indicates SeaWiFS data and the black line indicates the 1:1 ratio) (after Zibordi et al. (2006b).

when the temporal distribution of measurements is comparable (see also Fig. 8.14). The comparison of SeaWiFS and SeaPRISM derived *Chla* shown in Fig. 8.17 for data differing by less than 60 minutes, exhibits $|\psi| = 20\%$ resulting from $|\psi| = 6.2\%$ between the SeaWiFS and SeaPRISM $R_{RS}$ ratios. These differences can be explained by expected uncertainties in the applied *in situ* and remote sensing radiometric methods and, additionally, by the spatial and temporal variability differently affecting the SeaWiFS and SeaPRISM observations.

An accurate determination of the latter uncertainties is not feasible with the available data. Nevertheless the SeaWiFS data provide a means for estimating the spatial heterogeneity of the measurement area while the SeaPRISM observations offer the capability of quantifying the variability within the time-interval chosen for selecting the match-ups. Specifically, the SeaWiFS inter-pixel variability determined from the 3x3

pixels square centered at the AAOT for the considered 183 match-ups, shows an average variation coefficient $\zeta$ (defined as the standard deviation divided by the average and expressed in percent) of 19% for $Chla$ (with average $Chla$ of 1.4 $mg\ m^{-3}$) resulting from $\zeta = 5.1\%$ for the $R_{RS}$ ratios. When restricting the analysis to SeaWiFS data exhibiting an inter-pixel variability $\zeta < 5\%$ for the $R_{RS}$ ratios, the corresponding $\zeta$ for $Chla$ drops to 10% leading to $|\psi|$=15% between SeaPRISM– and SeaWiFS–derived $Chla$ (as determined from 88 match-ups exhibiting an average $Chla$ of 1.2 mg $m^{-3}$). When considering the variability over time of the SeaPRISM observations, the analysis of 81 sequences of three successive measurements performed within one hour shows $\zeta$=8% for $Chla$ (with average $Chla$ of 1.0 mg $m^{-3}$) resulting from $\zeta$=2.5% for the $R_{RS}$ ratios. These estimates suggest that the spatial variability illustrated by the SeaWiFS products might explain a large part of the difference between SeaWiFS and SeaPRISM derived $Chla$ at the AAOT site.

### 8.2.3 Radiometric accuracy and satellite products validation

Validation activities for satellite radiometric products mostly rely on the direct comparison of *in situ* and top-of-atmosphere data corrected for the atmospheric perturbation, i.e., $L_{WN}(\lambda)$ (or the equivalent $R_{RS}(\lambda)$). Considering the requirements for remote sensing products (McClain et al., 2004), the assessment of primary products like $L_{WN}(\lambda)$ must rely on highly accurate *in situ* data. The required accuracy is achievable through the adoption of the 1% radiometry concept for *in situ* measurements. Such an objective requires that, in addition to the considered sources of uncertainty, (i.e., absolute calibration, correction factors, environmental variability), differences in spectral responses between satellite and *in situ* sensors are also accounted. In fact,

these differences may introduce biases up to a few percent in the comparison of results especially at center-wavelengths located in regions where the seawater reflectance or the extra-atmospheric sun irradiance exhibit significant spectral variations (Zibordi et al., 2006a).

The match-up analysis presented for SeaWIFS, MODIS and MERIS normalized water-leaving radiances demonstrated that a confident validation of satellite primary radiometric products is only possible when supported by a quantification of uncertainties in the applied *in situ* data. This analysis shows similar uncertainties for both MODIS and SeaWIFS, with values comparable to the estimated uncertainties of *in situ* observations in the spectral range of 443-555 nm (or equivalent). By contrast MERIS comparisons with *in situ* data exhibit higher uncertainties than those of SeaWiFS and MODIS. These MERIS uncertainties are also much higher than the estimated uncertainties of *in situ* data. This outcome unequivocally supported the identification of shortcomings in the MERIS processing chain (Zibordi et al., 2006a).

Confidence in the accuracy of *in situ* data also helps to investigate satellite radiometric products at specific center-wavelengths. For instance the uncertainties observed for $L_{WN}$ at 412 nm indicate a possible failure of the atmospheric correction process at this center-wavelength, most influenced by atmospheric multiple scattering. This can be explained by the presence of continental aerosols at the AAOT site (Mélin and Zibordi, 2005) not fully accounted for by the atmospheric correction scheme. Additional considerations provided by the match-up analysis, emerge from data at the 670 nm center-wavelength (or equivalent). In this specific case large uncertainties are explained by the relatively small values of the normalized water-leaving radiance, when compared to the atmospheric radiance in the red and near-infrared.

Because of this, relatively small perturbations affecting the atmospheric correction (e.g., uncertainties in the satellite sensor calibration, identification of the aerosol type, assumptions on the water type) may translate into significant uncertainties for the normalized water-leaving radiance.

A further outcome of this investigation supports the synergy of satellite ocean color and *in situ* data as a way of extending spatial and temporal information for a given region. The merging of the data from the two different sources is fully justified when the relative differences between satellite and *in situ* match-ups are comparable to the estimated uncertainties of the *in situ* data.

## 8.3 Summary

The application of radiometric data was presented and discussed through the development of algorithms and the validation of satellite primary products.

Algorithm development included statistical relationships for the determination of *Chla* and $K_d$. When considering the AD algorithm proposed for the determination of *Chla* in the northern Adriatic Sea coastal waters, much lower estimates are produced for *Chla* below 1.0 mg $m^{-3}$, when compared to the global OC2V4 algorithm. This further confirmed the relevance of regional bio-optical algorithms for coastal waters.

An additional application case addressed the modelling of Q-factor as a function of $\theta_0$ and $K_d$. The analysis of the proposed algorithm, like those presented for *Chla* and $K_d$, highlighted the large natural variance in the *in situ* data used for developing algorithms. This is partly accounted for by the *lack of uniqueness* between some of the considered quantities (e.g., *Chla* and $R_{RS}$ ratios) and may suggest relaxing the

radiometric constraints: larger uncertainties in radiometric measurements would not significantly affect the performance of the algorithm. Such a statement is however contradicted by the effects of relatively small radiometric uncertainties. In fact, when specifically considering the AD algorithm for the determination of *Chla*, uncertainties of 5% in $R_{RS}$ ratios may lead to uncertainties of several tens percent in the estimated *Chla*.

The validation of remote sensing products and even more the vicarious calibration of space sensors, are the applications requiring the highest radiometric accuracy. The validation of remote sensing products was addressed by comparing satellite derived products from different space sensors with *in situ* data. The specific analysis of primary satellite ocean color radiometric products highlighted the importance of comprehensively characterizing uncertainties for the *in situ* data to be applied as *truth* over a range of different bio-optical regimes. The credibility of results from validation exercises, leading to the determination of uncertainties in satellite radiometric products, relies on the evidence that uncertainties in *in situ* measurements have been comprehensively identified and minimized.

# Chapter 9

# Conclusions and Perspectives

The production of increasingly accurate *in situ* radiometric observations in support of satellite ocean color applications has become a pressing need since the early 1980s with the onset of missions for global mapping of marine biomass. Following this demand, the present work addressed the problem of uncertainties in marine optical radiometry through comprehensive investigations on absolute calibration, cosine error, immersion effects, measurement methods, field perturbations and how these impact on applications.

## 9.1 Summary and Conclusions

This work results from the combination of pre-existing studies made by the author and new specific research aimed at resolving open issues. Within this final chapter the major findings are individually summarized and discussed for each investigated topic.

### 9.1.1 Absolute Calibration

Accurate calibration of field radiometers has relevance for any application related to satellite ocean color. Because of this, several agencies defined a maximum 5% uncertainty for top-of-atmosphere radiance corrected for atmospheric perturbations. This means that when vicarious calibration processes are applied, or the accuracy of space derived products is assessed, the overall uncertainty budget of in *situ* measurements must be below 5%. This is only possible when factors contributing to the overall uncertainty budget (including calibration terms, corrections for measurement artifacts, and environmental perturbations) lead to individual uncertainties typically lower than 1% (a process known as 1% radiometry).

Investigations focussed on irradiance calibrations of state of the art field radiometers identified spectrally averaged values of uncertainties varying from 1.1 to 3.4 % based on the difficulty of reducing the size of uncertainties from different individual sources. Equivalent analysis carried out for radiance absolute calibrations, showed values ranging from 1.5 to 6.3%. These values ultimately indicate the difficulty of satisfying the 1% radiometry concept.

An element not always accounted for and strictly related to the absolute calibration of optical radiometers is their sensitivity change with time due to aging or use. This produces an increase in uncertainty that may vary spectrally. A remedy for this additional source of uncertainty is the frequent calibration of radiometers, which should include pre– and post–field calibrations. In the case of relatively long field activities, the use of a portable monitoring source provides an additional capability to track sensitivity changes.

### 9.1.2 Cosine Error

Satellite ocean color applications rely on the knowledge of the *in situ* normalized water leaving radiance $L_{WN}(\lambda)$ (or alternatively of the remote sensing reflectance $R_{RS}(\lambda)$), which is a function of the downward irradiance $E_d(0^+, \lambda)$ when applied for its computation. As a consequence, the accuracy of $L_{WN}(\lambda)$ depends on the accuracy of $E_d(0^+, \lambda)$.

Prior to this study, no major investigation had addressed the uncertainties induced in $E_d(0^+, \lambda)$ by the non-ideal cosine response of irradiance sensors. Because of this, the impact of cosine error was investigated for a sample of commercial multi-collector radiometers belonging to the same class of instruments. The analysis of inter-channel cosine errors showed values generally within ±3% below 50 degrees incidence angle within the 412-685 nm spectral range. Extreme values of 4–20% (absolute) at 50–80 degrees were however observed for the channels at the center-wavelengths 412 and 443 nm. The additional analysis of intra-channel cosine errors, probably due to differences in the manufacturing or aging of collectors, showed values generally lower than 2% for incidence angles up to 50 degrees and increasing up to 6% at 80 degrees for some center-wavelengths.

A theoretical analysis of the effects of the non cosine response for the radiometers considered, showed errors in above–water downward irradiance values varying as a function of sun zenith, wavelength and aerosol optical thickness. Results displayed values generally within ±3% reaching 4–10% (absolute) at 40–80 degrees sun zenith for the channels at the center-wavelengths 412 and 443 nm. This demonstrates that when highly accurate irradiance data are required, the adoption of a correction scheme for the minimization of the effects of cosine errors is recommended. Such a correction

is even more essential when there are appreciably different inter-channel cosine errors which may amplify uncertainties in $E_d(0^+, \lambda)$ spectral ratios and thus in the $L_{WN}(\lambda)$ or $R_{RS}(\lambda)$ spectral ratios used for the development of bio-optical algorithms.

The application of a correction method based on simulations performed with a radiative transfer code showed the capability of minimizing errors with correction values having an estimated uncertainty of 0.6%. When applying an alternative correction scheme based on a simple analytical relationship relying on the assumption of isotropic distribution of the sky radiance, the latter uncertainty increases by a bias generally lower than 1%, with extreme values of 1–2% at some zenith angles for the channels at 412 and 443 nm.

The overall results lead to the recommendation of evaluating the cosine error for each class of radiometers extensively used for satellite ocean color applications, beyond those analyzed in the present study. Additional relevant feedback from the study is the effective possibility of applying corrections for cosine error effects in irradiance measurements. Highlighted methods include the possibility of producing accurate corrections through radiative transfer simulations, or simple analytical expressions at some expense of the accuracy. The final recommendation emerging from the study is the preference for radiometers with a single collector design versus multiple collectors, to minimize intra-channel uncertainties due to differences among individual collectors.

### 9.1.3 Immersion Effects

An extensive study addressing the characterization of the immersion factor $I_f(\lambda)$ of irradiance sensors demonstrated the capability of achieving a measurement repeatability on the average better than 0.6%. Inter-laboratory comparisons showed relative

average uncertainties generally within 0.6% (absolute), while the method precision showed average values of 1.2%. The variability in $I_f(\lambda)$, within a sample of nine OCI-200 radiometers, showed spectrally averaged dispersion values on the order of 2% with individual spectral values as high as 5%. An attempt at producing typical $I_f(\lambda)$ values for the OCI-200 series of radiometers showed maximum uncertainties spectrally varying from 1.4% to 3.4%. This further confirmed the need for ensuring a full spectral characterization of $I_f(\lambda)$ values for each in-water radiometer used for accurate determination of irradiances and of derived quantities.

An evaluation of the laboratory methods for the experimental determination of $I_f(\lambda)$ for irradiance sensors demonstrated the need for using pure water to increase both the precision and accuracy of measurements. This has become possible through the design and application of a specialized laboratory water vessel enabling the characterization of radiometers with a small volume of water (i.e., a few liters).

Since the 1970's, $I_f(\lambda)$ for radiance sensors has been computed theoretically assuming a narrow field of view and negligible reflectance of the inner optics. A revised relationship for the determination of $I_f(\lambda)$ for radiance sensors – accounting for the actual solid angle field-of-view, and the reflectance and transmittance of the external and internal optical components – was conceived and investigated. Its application to OCR-200 and OCR-507 radiometers showed an underestimation of approximately 0.4% for the $I_f(\lambda)$ values computed with the basic equation. This result was supported by experimental $I_f(\lambda)$ data, on the average differing by less than 0.1% from those computed with the revised theoretical relationship. Additional analysis based on radiometers with optics design different from that of the OCR-200 or OCR-507, showed that the difference between $I_f(\lambda)$ determined experimentally and computed

with the basic equation may be quite large (i.e., of the order of a few percent). This indicates that the experimental characterization of $I_f(\lambda)$ for sample radiance sensors of each series should become part of their quality assurance process to assess the deviation of the immersion factor from its theoretical determination.

A sensitivity analysis quantifying the $I_f(\lambda)$ dependence of radiance sensors on the seawater refractive index as a function of temperature and salinity, showed variations up to 0.4% and 1.1% within the 0-30 °C and 0-40 psu ranges, respectively. A scheme for the minimization of this source of uncertainty, based on wavelength independent corrections and reference immersion factors computed in the 400-700 nm range at fixed salinity and temperature, was proposed for the OCR-200 and OCR-507 radiometers. This allows for the determination of $I_f(\lambda)$ for any realistic seawater temperature and salinity, with an uncertainty increased by less than 0.1% with respect to that affecting theoretical data computed with the exact seawater refractive index.

### 9.1.4 Measurement Methods

State of the art methods for in– and above–water measurements were extensively investigated with the objective of demonstrating their equivalence in the determination of the water–leaving radiance and derived radiometric quantities.

Primary in-water radiometric products are the subsurface values (i.e., $L_u(0^-, \lambda)$, $E_u(0^-, \lambda)$ and $E_d(0^-, \lambda)$) derived from the extrapolation to $0^-$ of the log-transformed measurements at various depths $z$. After minimizing the effects of perturbations like self-shading and deployment superstructure, higher level products such as the irradiance reflectance, $R(\lambda)$, the normalized water-leaving radiance, $L_{WN}(\lambda)$, the remote sensing reflectance, $R_{RS}(\lambda)$ and the Q-factor at nadir view, $Q_n(\lambda)$, are then computed.

Above-water radiometry was here demonstrated to be a robust alternative to in-water radiometry. The primary product of this measurement approach is the water-leaving radiance, $L_W(\lambda)$, used to compute the normalized-water leaving radiance, $L_{WN}(\lambda)$, or the remote sensing reflectance, $R_{RS}(\lambda)$. Inter-comparison exercises showed the capability of producing water-leaving radiances applying in–water and above–water methods, with relative differences generally within 5%. It was also shown that both in– and above–water radiometry can provide $L_{WN}(\lambda)$ data with an uncertainty of approximately 5% below 555 nm. By contrast, in the red the uncertainties are much higher for above–water radiometry (i.e., above 12%) than for in–water radiometry (i.e., still approximately 5%).

The high level of agreement shown by the inter-comparison of in– and above–water radiometric data is largely due to the respect for strict measurement protocols, the adoption of correction schemes for measurement artifacts for in-water radiometric data, and the application of state of the art calibration methods. The application of above-water measurement methods, which rely on the position of the sun for pointing at the sea and sky, bring into question the unmanned collection of radiometric data from ships without the aid of stabilized platforms, sun-tracking systems and the continuous control of ship heading (to minimize perturbations due to ship-superstructure).

A critical element for both in– and above-water radiometry is the removal of the viewing angle dependence and the minimization of effects produced by non-isotropy of light distribution. Both corrections are currently applied using solutions proposed for Case-1 water. This implies that the uncertainty in corrections may unpredictably increase in presence of Case-2 waters.

### 9.1.5 Field Perturbations

Minimization of measurement perturbations is obtained through the application of strict measurement protocols and the implementation of correction schemes which computationally allow for an estimate of perturbation effects. In the case of above–water radiometry the minimization of perturbations due to deployment superstructures can be obtained through the adoption of rigid measurement geometries, while perturbations due to wave effects can be minimized by filtering the data. Differently, in–water radiometry can rely on comprehensive correction schemes for perturbations due to self-shading and superstructures, while wave effects can be minimized by collecting data with a high depth-resolution. Specifically, a dedicated study indicated that in coastal waters an uncertainty lower than 2% can be achieved with 50 measurements per meter for $K_d(\lambda)$, 33 for $E_d(0^-, \lambda)$, 9 for $L_u(0^-, \lambda)$ and 3 for $E_u(0^-, \lambda)$.

Self-shading effects can be minimized by applying an experimentally assessed correction scheme requiring knowledge of the measurement geometry (i.e., sun zenith and instrument diameter) and seawater absorption coefficient. The application of the specific correction scheme to WiSPER radiometric data from the AAOT site in the northern Adriatic Sea characterized by moderately turbid waters, showed correction values highly varying with wavelength and sun zenith. Within the spectral range 412–665 nm the highest correction values were displayed at 665 nm with averages of 10% for $L_u$, and of 5.7% for $E_u$. This confirms that for conventional radiometers, self-shading error should never be neglected.

The minimization of superstructure effects requires specific schemes for each deployment configuration. In the case of AAOT, superstructure effects for in-water subsurface measurements collected with the WiSPER system at 7.5 m from the main

body of the tower, were investigated using experimental data and Monte-Carlo simulations. The study led to the definition and assessment of a correction scheme based on a look-up table whose entries are mostly indexed values of seawater inherent optical properties and measurement geometry. Average correction factors determined for WiSPER data at 443 nm are 3.9%, 5.1% and 3.3% for $L_u$, $E_u$ and $E_d$, respectively.

The additional bottom effects in in–water radiometric data can be minimized using an analytical relationship that was developed on the basis of a two-flow model. The solution requires the determination of the near-bottom reflectance from the in–water profile data. The application of the proposed scheme to WiSPER data collected at the AAOT site provided correction terms inversely varying with seawater attenuation and exhibiting average values of -1.3% for both $L_u$ and $E_u$ at 555 nm where the light penetration is the highest. Conversely, due to the high seawater absorption, almost negligible corrections were observed at 665 nm.

Assuming an heuristic uncertainty of 25% in the determination of the overall correction factors applied to WiSPER data, the average uncertainty in the applied corrections exhibits values lower than 1% for $E_d$, 2% for $E_u$ and 3% for $L_u$.

The uncertainties affecting $L_{WN}$ derived from in– and above–water radiometric measurements, in general exhibit values close to the threshold of 5% required for calibration and validation purposes by space agencies. Following the uncertainty analysis produced for the various perturbations, it is evident that a reduction of the uncertainty budget for $L_{WN}$ can only be tackled by minimizing the perturbations due to environmental and superstructure effects (in fact it is unlikely to further reduce uncertainties in calibration). This may be achieved through deployments in open sea regions characterized by negligible short-term changes in the optical properties of

seawater. When considering coastal regions, a reduction of uncertainties is envisaged through the use of deployment systems like free-falls for in–water measurements and specialized rigs for above–water measurements, both supporting observations at a suitable distance from superstructures.

### 9.1.6 Application of Radiometric Data

The impact of measurement uncertainties on different applications of optical radiometric data was explored. This included the analysis of statistical relationships (i.e., empirical algorithms) for the determination of *Chla* and $K_d$ from $R_{RS}$ or $L_{WN}$ ratios at different center-wavelengths. Another modelling case examined, was the Q-factor as a function of $\theta_0$ and $K_d$. The investigated algorithms showed relatively large intrinsic uncertainties due to the natural variance of the *in situ* data. This is partly accounted for by the lack of *uniqueness* between the considered quantities and may suggest relaxing the radiometric constraints on the assumption that larger uncertainties in radiometric measurements would not significantly affect the performance of the algorithms. The statement is however contradicted by the effects of relatively small radiometric uncertainties. In fact, when specifically considering the AD algorithm proposed for the determination of *Chla*, uncertainties of 5% in $R_{RS}$ ratios may lead to uncertainties of several tens percent in the estimated *Chla*.

Applications requiring the highest radiometric accuracy and which necessarily must rely on the 1% radiometry concept, are those related to the validation of remote sensing products and the vicarious calibration of space sensors. Exercises addressing the validation of $L_{WN}$ from SeaWiFS, MODIS and MERIS space data, showed the capability of quantifying uncertainties ranging from a few up to several tens percent

in the various spectral channels. Obviously, the credibility of results relies on the evidence that uncertainties in *in situ* measurements were comprehensively identified and minimized.

## 9.2 Research and Development Perspectives

The investigations addressed in this work indicate the need for further research and developments which would provide benefit to marine optical radiometry and to the related satellite ocean color applications. These envisaged needs are hereafter introduced for further consideration.

The definition of a comprehensive uncertainty budget for several radiometric quantities requires an estimate of the contribution of cosine errors for both in–water and in–air irradiance measurements. The results of a recent and new investigation demonstrated that the effects of cosine error are an overlooked problem which may be the source of large uncertainties in primary radiometric quantities like the normalized water-leaving radiance. This leads to the recommendation of extending the recent study on cosine errors effects to different series of radiometers for both in–air and in–water irradiance measurements with the final objective of investigating and proposing correction schemes for the minimization of the related measurement uncertainties.

The removal of the viewing angle dependence in above-water radiometric measurements and the minimization of the effects of non isotropy of light distribution in both in–water and above–water radiometric observations, largely rely on theoretical simulations of radiative transfer processes performed for Case 1 water conditions.

Thus the application of the correction schemes developed for Case 1 waters to measurements performed in Case 2 waters, may become the source of unpredictable uncertainties. This strongly suggests the need for extensive investigations on the effects of non isotropy of light distribution in Case 2 waters with a view to the subsequent implementation of correction schemes for optical radiometric data.

Hyper-spectral technology is acquiring relevance in marine optical radiometry by showing its potential in fully characterizing the radiance or reflectance spectrum of water. This improves the capability of optical radiometry to discriminate phytoplankton species as well as common seawater optically significant constituents like colored dissolved organic matter and non pigmented particles. While hyper-spectral technology appears robust in supporting above-water radiometry, its use in support of in–water applications for coastal regions requires some caution. In fact during low illumination conditions, like those characterizing observations in turbid waters, the sampling rate currently achievable (related to the integration time which is automatically adjusted on light levels by the measuring system), would not permit a comprehensive characterization of subsurface radiometric quantities due to possible gradients in the vertical distribution of optically significant constituents. This calls for the development of hyper-spectral systems with sensitivity and dynamic range capable of satisfying applications in both coastal and open sea regions.

Above-water optical radiometry showed the possibility of producing derived quantities (e.g., the normalized water-leaving radiance) with uncertainties equivalent to those characterizing the more assessed in-water radiometric products. In addition, above-water radiometry showed the capability of producing data through autonomous measurement systems from various fixed deployment platforms at different coastal

sites. This indicates that the development of stabilized deployment rigs for moving platforms like ships, capable of sun-tracking and designed for ship locations minimizing the superstructure perturbations during cruising, would provide an additional invaluable support to future satellite ocean color validation programs which could also rely on ships of opportunity for world wide radiometric observations.

Miniaturization of optical radiometers is a way forward to minimize the impact of self-shading perturbations on in–water measurements. However, it must be stated that the continuous development of smaller and smaller radiometers has to be accompanied by the improved design of deployment systems (e.g., free-falls, winches, profiling buoys) also having minimum dimensions in order to not lose the advantage of miniaturized optical devices.

Finally, the ocean color component of AERONET (i.e. AERONET-OC) demonstrated the relevance of producing highly consistent data sets comprised of standardized measurements performed at different sites with identical measuring systems and protocols, calibrated using a single reference source and method, and processed with the same code. This solution minimizes the difficulties impairing the quantification of measurement uncertainties for fully independent observations from many different sources, which clearly depend on the performance of different field instruments, diverse sampling methods, assorted calibration sources and protocols, and a variety of processing schemes. Learning from this, in addition to continuous investigations on calibration, measurement and correction methods, a substantial effort should anyway be devoted to their standardization as a viable way to minimize uncertainties and increase consistency across independent data sets.

# References


Aas, E. (1969). On submarine irradiance measurements. Technical Report 6, Institute of Physical Oceanography, University of Copenhagen, Copenhagen, Denmark.

Aas, E. and N. K. Højerslev (1999). Analysis of underwater radiance observations: Apparent optical properties and analytic functions describing the angular radiance distribution. *J. Geophys. Res. 104*, 8015–8024.

Aas, E. and B. Korsbø (1997). Self–shading effect by radiance meters on upward radiance observed in coastal waters. *Limnol. Oceanogr. 42*, 968–974.

Ackleson, S. G. and V. Klemas (1986). Two-flow simulation of the natural light field within a canopy of submerged acquatic vegetattion. *Appl. Opt. 25*, 1129–1136.

Ångström, A. (1961). Techniques of determining the turbidity of the atmosphere. *Tellus 13*, 214–223.

Antoine, D. and P. Guevel (2000). Calibration and validation of satellite ocean color observations: The boussole project. In *Proc. Ocean Optics XV, Monaco, October 16-20,2000*. [Available on CD-ROM: Office of Naval Research, Washington, DC].

Antoine, D. and A. Morel (1999). A multiple scattering algorithm for atmospheric correction of remotely sensed ocean colour (meris instrument): principle and implementation for atmospheres carrying various aerosols including absorbing ones. *Int. J. Remote Sens. 20*, 1875–1916.

Atkins, W. R. G. and H. H. Poole (1933). The photo-electric measurement of the penetration of light of various wave lengths into the sea and the physiological bearing of results. *T. Phil. Trans. Roy. Soc. London, (B) 222*, 129–164.

Austin, R. W. (1976). Air-water radiance calibration factor. Technical Memorandum ML - 76 - 004T, Scripps Institution of Oceanography, La Jolla, CA.

Austin, R. W. and T. J. Petzold (1981). *Oceanography from Space*, Volume 13 of *Marine Science*, Chapter The determination of the diffuse attenuation coefficient of seawater using the Coastal Zone Color Scanner, pp. 239–256. Plenum Press.

Austin, R. W. and T. J. Petzold (1982). Air-water radiance factor - gershun tube. Technical Memorandum DL - 82- 005T, Scripps Institution of Oceanography, La Jolla, CA.

Bais, F., S. Kazadzis, D. Balis, C. Zerefos, and M. Blumthaler (1998). Correcting total solar ultraviolet spectra recorded by a brewer spectroradiometer for its angular response error. *Appl. Opt. 37*, 6339–6344.

Barnes, W., T. S. Pagano, and V. Salomonson (1998). Prelaunch characteristics of the moderate resolution imaging spectroradiometer (modis) on eos-am1. *IEEE Trans. Geosci. Remote Sensing 36*, 1088–1100.

Berger, F. (1958). Über die ursache des "oberflächeneffekts" bei lichtmessungen unter wasser. *Wetter u. Leben 10*, 164–170.

Berger, F. (1961). Über den "taucheffekt" bei der lichtmessung ber and unter wasser. *Arch. Meteorol. Wien., (B) 11*, 224–240.

Bernhard, G. and G. Seckmeyer (1997). New entrance optics for solar spectral uv measurements. *Photochem. Photobiol. 65*, 923–930.

Berthon, J.-F., J. P. Doyle, S. Grossi, D. van der Linde, C. Targa, and G. Zibordi (2000). *Analysis of field observations and marine bio-optical modeling*, Volume EUR Report, 19515. Ispra, Italy: Joint Research Centre.

Berthon, J.-F. and G. Zibordi (2004). Bio-optical relationships for the northern adriatic sea. *Int. J. Remote Sens. 55*, 1527–1532.

Berthon, J.-F., G. Zibordi, J. P. Doyle, S. Grossi, D. van der Linde, and C. Targa (2002). *Coastal Atmosphere and Sea Time Series (CoASTS): Data analysis*, Volume 20 of *SeaWiFS postlaunch Technical Report Series*, pp. 25. Greenbelt, MD: NASA Goddard Space Flight Center, TM-2002-206892.

Bézy, J.-L., S. Delwart, and M. Rast (2000). Meris – a new generation of ocean color sensor onboard envisat. *ESA Bulletin 103*, 48–56.

Blumthaler, M., J. Groebner, M. Huber, and W. Ambach (1996). Measuring spectral and spatial varaiations of uvb and uva sky radiance. *Geophys. Res. Lett. 23*, 547–550.

Bricaud, A., E. Bosc, and D. Antoine (2002). Algal biomass and sea surface temperature in the mediterranean basin. intercomparison of data from various satellite sensors, and implications for primary production estimates. *Remote Sens. Environ. 81*, 163–178.

Bulgarelli, B. and J. P. Doyle (2004). Comparison between numerical models for radiative transfer simulation in the atmosphereocean system. *J. Quant. Spectrosc. Radiat. Transfer 86*, 315–334.

Bulgarelli, B., V. Kisselev, and L. Roberti (1999). Radiative transfer in the atmosphereocean system: the finite-element method. *Appl. Opt. 38*, 1530–1542.

Bulgarelli, B. and G. Zibordi (2003). Remote sensing of ocean color: accuracy assessment of an approximate atmospheric correction method. *Int. J. Remote Sens. 24*, 491–509.

Bulgarelli, B., G. Zibordi, and J. F. Berthon (2003). Measured and modeled radiometric quantities in coastal waters: towards a closure. *Appl. Opt. 42*, 5365–5381.

Carder, K. L. and R. G. Steward (1985). A remote sensing reflectance model of a red tide dinoflagellate off west florida. *Limnol. Oceanogr. 30*, 286–298.

Case, K. M. (1957). Transfer problems and the reciprocity principle. *Rev. Mod. Phys. 29*, 651–663.

Chandrasekhar, S. (1950). *Radiative Transfer*. Oxford University Press, London.

Chang, G. C., T. D. Dickey, C. D. Mobley, E. Boss, and S. Pegau (2003). Toward closure of upwelling radiance in coastal waters. *Appl. Opt. 42*, 1574–1582.

Clark, D. K. (1981). *Oceanography from Space*, Volume 13 of *Marine Science*, Chapter Phytoplanton pigment algorithms for the NIMBUS-7 CZCS, pp. 227–237. Plenum Press.

Clark, D. K., H. R. Gordon, K. J. Voss, Y. Ge, W. Broenkow, and C. Trees (1997). Validation of atmospheric correction over the oceans. *J. Geophys. Res. 102*, 17209–17217.

Claustre, H., S. B. Hooker, L. V. Heukelem, J.-F. Berthon, R. Barlow, J. Ras, H. Sessions, C. Targa, C. S. Thomas, D. van der Linde, and J.-C. Marty (2004). An intercomparison of hplc phytoplankton pigment methods using in situ samples: application to remote sensing and database activities. *Mar. Chem. 41*, 1508–1524.

D'Alimonte, D., F. Mélin, G. Zibordi, and J.-F. Berthon (2003). Use of the novelty detection technique to identify the range of applicability of empirical ocean colour algorithms. *IEEE Trans. Geosc. Rem. Sens. 41*, 2833–2843.

D'Alimonte, D. and G. Zibordi (2003). Phytoplankton determination in an optically complex coastal region using a multi layer perceptron neural network. *IEEE Trans. Geosc. Rem. Sens. 41*, 2861–2868.

D'Alimonte, D. and G. Zibordi (2006). Statistical assessment of autonomous radiometric data. *IEEE Trans. Geosc. Rem. Sens. 43*, 1–11.

D'Alimonte, D., G. Zibordi, and J.-F. Berthon (2004). Determination of CDOM and NPPM absorption coefficient spectra from coastal water remote sensing reflectances. *IEEE Trans. Geosc. Rem. Sens. 42*, 1770–1777.

Darecki, M., S. Kaczmarek, and S. Olszewski (2004). Seawifs ocean colour chlorophyll algorithms for the southern baltic sea. *Int. J. Remote Sensing 89*, 326–350.

de La Casiniére, A., T. Cabot, and S. Benmansour (1995). Measuring spectral diffuse solar irradiance with non-cosine flat-plate diffusers. *Sol. Energy 54*, 173–182.

Dera, J., W. Wensierski, and J. Olszewski (1972). A two-detector integrating system for optical measurements in the sea. *Acta Gephysica Polonica 20*, 3–159.

Dierssen, H. M. and R. C. Smith (1996). Estimation of irradiance just below the air-water interface. In *Proc. Ocean Optics XII, Halifax, NS, Canada*, Volume SPIE Vol. 2963, pp. 204–209.

D'Ortenzio, F., S. Marullo, M. Ragni, M. R. D'Alcala', and R. Santoleri (1994). Validation of empirical seawifs algorithms for chlorophyll *a* retrieval in the mediterranean sea: A case study for oligotrophyc sea. *Remote Sens. Environ. 99*, 7457–7466.

Doyle, J. P., S. B. Hooker, G. Zibordi, and D. van der Linde (2003). *Tower perturbation measurements in in-water radiometry*, Volume 25, pp. 33. Greenbelt, MD: NASA Goddard Space Flight Center, TM-2003-206892.

Doyle, J. P. and H. Rief (1998). Photon transport in three-dimensional structures treated by random walk techniques: Monte carlo benchmark of ocean colour simulations. *Math. Comp. Simul. 47*, 215–241.

Doyle, J. P. and K. J. Voss (2000). 3d instrument self-shading effects on in–water multi–directional radiance measurements. In *Ocean Optics XV, Monte Carlo*.

Doyle, J. P. and G. Zibordi (2002). Optical propagation within a 3-dimensional shadowed atmosphere-ocean field: application to large deployment structures. *Appl. Opt. 41*, 4283–4306.

Eplee, R. E., W. D. Robinson, S. W. Bailey, D. K. Clark, P. J. Werdell, M. Wang, R. A. Barnes, and C. R. McClain (2001). Calibration of SeaWiFS. II. Viacrious techniques. *Appl. Opt. 40*, 6701–6718.

Feister, U., R. Grewe, and K. Gericke (1997). A method for the correction of cosine errors in measurements of spectral uv irradiance. *Solar Energy 60*, 313–332.

Ferrari, G. and S. Tassan (1991). On the accuracy of dtermining light absorption by yellow substance through measurements of induced fluorescence. *Limn. Oceanogr. 36*, 777–786.

German Institute of Standardization (1978). *DIN 5032 Teil 1*. Deutsche Normen Series. Beuth Verlag, Berlin.

Gershun, A. (1939). The light field. *Journal of Mathematical Psychology 18*, 51–151. Translated by P. Moon and G. Timoshenko.

Gordon, H. R. (1985). Ship perturbation of irradiance measurements at sea. part 1: Monte carlo simulations. *Appl. Opt. 24*, 4172–4182.

Gordon, H. R. and O. B. Brown (1974). Influene of bottom depth and albedo on the diffuse reflectance of a flat homogeneous ocean. *Appl. Opt. 13*, 2153–2159.

Gordon, H. R. and D. J. Castaño (1987). The coastal zone color scanner atmospheric correction algorithm: Multiple scattering effects. *Appl. Opt. 26*, 2111–2122.

Gordon, H. R. and K. Ding (1992). Self-shading of in-water optical instruments. *Limnol. Oceanogr. 37*, 491–500.

Gordon, H. R. and M. Wang (1994). Retrieval of water leaving radiance and aerosol optical thickness over the oceans with seawifs: A preliminary algorithm. *Appl. Opt. 33*, 443–452.

Grainger, R. G., R. E. Basher, and R. L. McKenzie (1993). Uv-b robertson-berger meter charcterization and field calibration. *Appl. Opt. 32*, 343–349.

Groebner, J. (2003). Improved entrance optics for total irradiance measurements with a brewer spectrophotometer. *Appl. Opt. 42*, 3516–3521.

Groebner, J., M. Blumthaler, and W. Ambach (1996). Experimental investigation of the spectral total irradiance measurement errors due to a non cosine response. *Geophys. Res. Lett. 23*, 2493–2496.

Harrison, L., J. Michalsky, and J. Berndt (1994). Automated multifilter rotating shadow-band radiometer: an instrument for optical depth and radiation measurements. *Appl. Opt. 33*, 5118–5125.

Helliwell, W. S., G. N. Sullivan, B. Macdonald, and K. J. Voss (1990). Ship shadowing: Model and data comparison. In *Proc. Ocean Optics X, Orlando, FL*, Volume SPIE Vol. 1302, pp. 55–71.

Hengstberger, F. (1989). *Absolute radiometry: Electrically Calibrated Thermal Detectors of Optical Radiation.* Academic Press, Inc.

Holben, B. N., D. Tanré, A. Smirnov, T. F. Eck, I. Slutsker, N. Abuhassen, W. W. Newcomb, J. Schafer, B. Chatenet, F. Lavenue, Y. J. Kaufman, J. V. Castle,

A. Setzer, B. Markham, D. Clark, R. Frouin, R. Haltore, A. Karnieli, N. T. O'Neill, C. Pietras, R. T. Pinker, K. Voss, and G. Zibordi (2001). An emerging ground-based aerosol climatology: Aerosol optical depth from AERONET. *J. Geophys. Res. 106*, 12067–12097.

Hooker, S. B. and J. Aiken (1998). Calibration evaluation and radiometric testing of field radiometers with the SeaWiFS quality monitor (SQM). *J. Atmos. Oceanic Technol. 15*, 995–1007.

Hooker, S. B. and W. S. Esaias (1993). An overview of the SeaWiFS mission. *EOS, Trans., Amer. Geophys. Union 74*, 241–246.

Hooker, S. B. and S. Maritorena (2000). An evaluation of oceanographic radiometers and deployment methodologies. *J. Atmos. Oceanic Technol. 17*, 811–830.

Hooker, S. B. and C. R. McClain (2000). The calibration and validation of SeaWiFS data. *Prog. Oceanogr. 45*, 427–465.

Hooker, S. B. and A. Morel (2003). Platform and environmental effects on above–water determinations of water–leaving radiances. *J. Atmos. Oceanic Technol. 20*, 187–205.

Hooker, S. B. and G. Zibordi (2005). Platform perturbation in above-water radiometry. *Appl. Opt. 44*, 553–567.

Hooker, S. B., S. McLean, J. Sherman, M. Small, G. Lazin, G. Zibordi, and J. W. Brown (2002a). *The Seventh SeaWiFS Intercalibration Round-Robin Experiment (SIRREX-7)*, Volume 17, pp. 69. Greenbelt, MD: NASA Goddard Space Flight Center, TM-2003-206892.

Hooker, S. B., G. Lazin, G. Zibordi, and S. McClean (2002b). An evaluation of above- and in-water methods for determining water leaving radiances. *J. Atmos. Oceanic Technol. 19*, 486–515.

Hooker, S. B., G. Zibordi, J.-F. Berthon, and J. W. Brown (2004). Above-water radiometry in shallow coastal waters. *Appl. Opt. 21*, 4254–4268.

IAMAPRC (1984). A preliminary cloudless standard atmosphere for radiation computation. Technical Report WCP-112, WMO/TD-No. 24, International Association for Meteorology and Atmospheric Physics. Radiation Commission, World Climate Programme, Boulder, Colorado.

Jerlov, N. G. (1968). *Optical Oceanography*, Volume 5 of *Oceanography*. Elsevier.

Jerlov, N. G. (1976). *Marine Optics*, Volume 14 of *Oceanography*. Elsevier.

Jerlov, N. G. and M. Fukuda (1960). Radiance distribution in the upper layers of the sea. *Tellus 12*, 348–355.

Jerlov, N. G. and G. Liljequist (1938). On the angular distribution of subamrine deylight and the total sumbarine illumination. *Sven. Hydrogr. – Biol. Komm. Skr., Ny Ser. Hydrogr. 14*, 1–15.

Jerlov, N. G. and E. S. Nielsen (1974). *Optical Aspects of Oceanography*. Academic Press.

Johnson, B. C., H. W. Yoon, S. S. Bruce, P.-S. Shaw, A. Thompson, S. B. Hooker, R. E. Eplee, R. A. Barnes, S. Maritorena, and J. L. Mueller (1999). *The Fifth Sea-WiFS Intercalibration Round-Robin Experiment (SIRREX-5)*, Volume 7 of *NASA, Tech. Memo. 1999-206892*, pp. 75 pp. Greenbelt, MD: NASA Goddard Space Flight Center.

Johnston, S. F. (2001). *A history of Light and Color Measurement: Science in the Shadow*. Institute of Physics Publishing.

Kattawar, G. W. (1975). A three-parameter analytic phase function for multiple scattering calculations. *J. Quant. Spectrosc. Radiat. Transfer 15*, 839–849.

Kirk, J. T. O. (1994). *Light & Photosynthesis in aquatic Ecosystems.* Cambridge University Press.

Lambert, J. H. (1760). Photometria sive de mensura et gradibus luminus colorum et umbrae.

Le Grand, Y. (1939). La pènètration de la lumière dans la mer. *Ann. Inst. Ocèanogr. 19*, 393–436.

Leathers, R. A., T. V. Downes, and C. D. Mobley (2001). Self–shading correction for upwelling sea–surface radiance measurements made with buoyed instruments. *Optics Express 8*(10,561).

Leathers, R. A. and N. J. McCormick (1999). Algorithms for ocean-bottom albedo determination from in-water natural-light measurements. *Appl. Opt. 38*, 3199–3205.

Lenoble, J. (1986). *Radiative Transfer in Scattering and Absorbing Atmospheres: Standard Computational Procedures.* A. Deepak Pub.

Loisel, H. and A. Morel (1998). Light scattering and chlorophyll concentration in Case 1 waters: a reexamination. *Limnol. Oceanogr. 43*, 847–858.

Loisel, H. and D. Stramski (2000). Estimation of the inherent optical properties of natural waters from the irradiance attenuation coefficient and reflectance in the presence of raman scattering. *Appl. Opt. 39*, 3001–3011.

Lommel, E. (1889). Die photometrie der diffusen zuröckwerfung. *Ann. Phys. u. Chem. 36*, 473–502.

Lux, I. and L. Koblinger (1991). *Monte Carlo Transport Methods: Neutron and Photon Calculations.* CRC Press,Boca Raton, Fla.

Lyzenga, D. R. (1978). Passive remote sensing techniques for mapping water depth and bottom features. *Appl. Opt. 17*, 379–383.

Maritorena, S., A. Morel, and B. Gentili (1994). Diffuse reflectance of oceanic shallow water: Influence of water depth and bottom albedo. *Limnol. Oceanogr. 39*, 1689–1703.

McClain, C. R., G. C. Feldman, and S. B. Hooker (2004). An overview of the seawifs project and strategies for producing a climate research quality global ocean bio-optical time-series. *Deep-Sea Res. 51*, 5–42.

McCluney, W. R. (1994). *Introduction to Radiometry and Photometry*. Artech House.

Mélin, F., J. F. Berthon, and G. Zibordi (2005). Assessment of apparent and inherent optical properties derived from SeaWiFS with field data. *Remote Sensing of Environment 97*, 540–553.

Mélin, F. and G. Zibordi (2005). Aerosol variability in the po valley analyzed from automated optical measurements. *Geophysical Research Letters 32*, L03810.

Mélin, F., G. Zibordi, and J.-F. Berthon (2003). Assesment of atmospheric and marine SeaWiFS products for the north adriatic sea. *IEEE Trans. Geosc. Rem. Sens. 41*, 548–558.

Michalsky, J. J., L. C. Harrison, and W. E. Berkheiser (1995). Cosine response characteristics of some radiometric and photometric sensors. *Sol. Energy 38*, 397–402.

Mobley, C. D. (1994). *Light and Water. Radiative Transfer in Natural Waters*. Academic Press.

Mobley, C. D. (1999). Estimation of the remote sensing reflectance from above-water methods. *Appl. Opt. 38*, 7442–7455.

Mobley, C. D., B. Gentili, H. R. Gordon, Z. Jin, G. W. K. ans A. Morel, P. Reinersman, K. Stamnes, and R. H. Stavn (1993). Comparison of numerical models for computing underwater light field. *Appl. Opt. 32*, 7484–7504.

Mobley, C. D., H. Zang, and K. J. Voss (2003). Effects of optically shallow bottoms on upwelling radiances: bidirectional effects. *Limnol. Oceanogr. 48*, 337–345.

Moore, G., J. Aiken, and S. J. Lavender (1999). The atmospheric correction of water colour and the quantitative retrieval of suspended particulate matter in case ii waters: application to meris. *Int. J. Remote Sens. 20*, 1713–1733.

Morel, A. (1974). *Optical Aspects of Oceanography*, Chapter Optical properties of pure water and pure sea water, pp. 1–24. Academic Press.

Morel, A. (1980). In-water and remote measurements of ocean color. *Bound.-Layer Meteorol. 18*, 177–201.

Morel, A., D. Antoine, and B. Gentili (2002). Bidirectional reflectance of oceanic waters: Accounting for raman emission and varying particle scatering phase function. *Appl. Opt. 41*, 6289–6306.

Morel, A. and B. Gentili (1991). Diffuse refelctance of ocean waters: its dependence on sun angle as influenced by the molecular scattering contribution. *Appl. Opt. 30*, 4427–4438.

Morel, A. and B. Gentili (1993). Diffuse refelctance of ocean waters. ii. bi-directional aspects. *Appl. Opt. 32*, 6864–6879.

Morel, A. and B. Gentili (1996). Diffuse refelctance of ocean waters. iii. implication of bidirectionality for the remote-sensing problem. *Appl. Opt. 35*, 4850–4862.

Morel, A. and S. Maritorena (2001). Bio-optical properties of oceanic waters: A reappraisal. *J. Geophys. Res. 106*, 7163–7180.

Morel, A. and R. C. Smith (1982). Terminology and units in optical oceanography. *Marine Geodesy 5*, 335–350.

Morel, A., K. J. Voss, and B. Gentili (1995). Bidirectional reflectance of oceanic waters: A comparison of modeled and measured uward radiance fields. *J. Geophys. Res. 100*, 13143–13151.

Morrow, J. H., M. S. Duhig, and C. R. Booth (1994). *Design and evaluation of a cosine collector for a Sea-WiFS-compatible Marine Reflectance Radiometer*, Volume 2258, pp. 879–886. SPIE, Ocean Optics XII.

Mueller, J. L. (1995). *Case Studies for SeaWiFS Calibration and Validation, Part 3*, Volume 27, Chapter Comparison of Irradiance Immersion Coefficients for Several Marine Environmental Radiometers (MERs), pp. 46. Greenbelt, MD: NASA Goddard Space Flight Center, TM-1995-104566.

Mueller, J. L. (2000). *SeaWiFS Postlaunch Calibration and Validation Analyses, Part 3*, Volume 11, Chapter SeaWiFS algorithm for the diffuse attenuation coefficient, K(490), asing water-leaving radiances at 490 and 555 nm., pp. 24–27. Greenbelt, MD: NASA Goddard Space Flight Center, TM-2000-206892.

Mueller, J. L. and R. W. Austin (1995). *Ocean optics protocols for SeaWiFS for validation, Revision 1*, Volume 25 of *SeaWiFS Technical Report Series*, pp. 66 pp. Greenbelt, MD: NASA Goddard Space Flight Center, TM-1995-104566.

Mueller, J. L. and R. W. Austin (2003). *Ocean Optics Protocols for Satellite Ocean Color Sensor Validation, Revision 4*, Volume 3, pp. 78 pp. Greenbelt, MD: NASA Goddard Space Flight Center, TM-2003-211621/Rev4.

Nast, P.-M. (1983). Measurements on the accuracy of pyranometers. *Sol. Energy 31*, 279–282.

O'Reilly, J. E., S. Maritorena, B. G. Mitchell, D. A. Siegel, K. L. Carder, S. A. Garver, M. Kahru, and C. R. McClain (1998). Ocean color chlorophyll algorithms for SeaWiFS. *J. Geophys. Res. 103*, 24937–24953.

O'Reilly, J. E., S. Maritorena, B. G. Mitchell, D. A. Siegel, K. L. Carder, S. A. Garver, M. Kahru, and C. R. McClain (2000). Atmospheric correction for SeaWiFS imagery for turbid coastal and inland waters. *Appl. Opt. 39*, 897–912.

Patt, F. S., R. A. Barnes, R. E. E. Jr., B. A. Franz, W. D. Robinson, G. C. Feldman, S. W. Bailey, J. Gales, P. J. Werdell, M. Wang, R. Frouin, R. P. Stumpf, R. A. Arnone, R. W. G. Jr., P. M. Martinolich, V. Ransibrahmanakul, J. E. O'Reilly, and J. A. Yoder (2003). *Algorithm Updates for the Fourth SeaWiFS Data Reprocessing*, Volume 10, pp. 74. Greenbelt, MD: NASA Goddard Space Flight Center, TM-2003-206892.

Pettersson, H. and S. Landberg (1934). Submarine daylight. *Medd. Oceanogr. Inst. Göteborg 6*, 1–13.

Petzold, T. J. and R. W. Austin (1988). Chracterization of MER-1032. Tech. Memo. EN-001-88T, Visibility Laboratory of the Scripps Institution of Oceanography, University of California, San Diego.

Philpot, W. D. (1987). Radiative transfer in startified waters: a single-sacttering approximation for irradiance. *Appl. Opt. 26*, 4123–4132.

Pinkerton, M. H. and J. Aiken (1999). Calibration and validation of remotely-sensed observations of ocean colour from a moored data buoy. *J. Atmos. Oceanic Technol. 16*, 915–923.

Piskozub, J. (2004). Effect of ship shadow on in–water irradiance measurements. *Oceanologia 46*, 103–112.

Piskozub, J., A. R. Weeks, J. N. Schwarz, and I. S. Robinson (2000). Self-shading of upwelling irradiance for an instrument with sensors on a sidearm. *Appl. Opt. 39*, 1872–1878.

Plass, G. N. and G. W. Kattawar (1972). Monte carlo calculations of radiative transfer in the earth's atmosphere-ocean system. *J. Phys. Oceanogr. 2*, 139–145.

Pope, R. M. and E. S. Fry (1997). Absorption spectrum (380-700 nm) of pure water, ii, integrating cavity measurements. *Appl. Opt. 36*, 8710–8723.

Preisendorfer, R. W. (1960). Recommndation on the stardadization of concepts, terminology and and notation of hydrologic optics. Report SIO, Scripps Institution of Oceanography, University of California, San Diego.

Preisendorfer, R. W. (1976). *Hydrologic Optics*. Natl. Tech. Inform. Serv., Springfield.

Robinson, W. D., G. M. Schmidt, C. R. McClain, and P. J. Werdell (2000). *Changes made in the operational SeaWiFS processing*, Volume 10, pp. 12–28. Greenbelt, MD: NASA Goddard Space Flight Center, TM-2000-206892.

Ruddick, K. G., V. D. Cauwer, and Y.-J. Park (2006). Seaborne measurements of near infrared water-leaving reflectance: The similarity spectrum for turbid waters. *Limnol. Oceanogr. 51*, 1167–1179.

Saruya, Y., T. Oishi, K. K. M. Kishino, Y. Jodai, and A. Tanaka (1996). Influence of ship shadow on underwater iradiance fields. In *Proc. Ocean Optics XIII, Halifax, NS, Canada*, Volume SPIE Vol. 2963.

Sasaki, T. S., S. Watanabe, G. Oshiba, N. Okami, and M. Kajihara (1962). On the instrument for measureing angular distribution of underwater radiance. *Bull. Jpn. Soc. Sci. Fish. 28*, 489–496.

Seckmeyer, G. and G. Bernhard (1993). Cosine error correction of spectral uv-irradiances. In *SPIE*, Volume 2049, pp. 140–151.

Shelford, V. E. and F. W. Gail (1922). A study of light penetartion into sea water made with teh kunz photo-electric cell with particular reference to the distribution of plants. *Puget Sound Biol. Stn. Publ. 3*, 141–176.

Shifrin, K. S. (1988). *Physical Optics of Ocean Water*. AIP Translation Series, American Institute of Physics, New York.

Shuleikin, V. V. (1933). Data on the optics of a strongly scattering medium, applied to sea water, fog and cloud. *Geofizika 3*, 3–5.

Siegel, D., M. Wang, S. Maritorena, and W. D. Robinson (2000). Atmospheric correction of satellite ocean color imagery: The black pixel assumption. *Appl. Opt. 39*, 3582–3591.

Siegel, H. (1984). Some remarks on the ratio between the upward irradiance and nadir radiance just beneath the sea surface. *Beitr. Meereskd. 51*, 75.

Slater, P. N. (1980). *Remote Sensing: Optics and Optical Systems*. Addison-Wesley Publishing Company.

Smirnov, A., B. N. Holben, T. F. Eck, O. Dubovik, and I. Slutsker (2000). Cloud-screening and quality control algorithms for the aeronet database. *Remote Sens. Environ. 73*, 337–349.

Smith, R. C. (1969). An underwater spectral irradiance collector. *J. Marine Research 27*, 341–351.

Smith, R. C. (1974). *Optical Aspects of Oceanography*, Chapter Structure of solar radiation in teh upper layers of the sea, pp. 494. Academic Press Inc. (London) Ltd.

Smith, R. C., R. W. Austin, and J. E. Tyler (1969). An oceanographic radiance distribution camera system. *Appl. Opt. 27*, 341–351.

Smith, R. C. and K. S. Baker (1984). The analysis of ocean optical data. In *Proc. Ocean Optics VII*, Volume SPIE Vol. 478, pp. 119–126.

Smith, R. C. and K. S. Baker (1986). Analysis of ocean optical data ii. In *Proc. Ocean Optics VIII*, Volume SPIE Vol. 637, pp. 95–107.

Sobolev, V. V. (1956). *A Treatise on Radiative Transfer (In Russian)*. Gostekhizdat, Moscov. English translation, Von Nostrand, Princeton N.J., 1963.

Spanier, J. and E. M. Gelbard (1969). *Monte Carlo Principles and Neutron Transport Problems*. Addison-Wesley, Reading, Mass.

Spinrad, R. W., K. L. Carder, and M. J. Perry (1994). *Ocean Optics*. Oxford University Press.

Sturm, B. and G. Zibordi (2002). Seawifs atmospheric correction by an approximate model and vicarious calibration. *Int. J. Remote Sens. 23*, 489–501.

Tassan, S. and G. Ferrari (1995). An alternative approach to absorption measurements of aquatic particles retained on filters. *Limnol. Oceanogr. 40*, 1358–1368.

Thuillier, G., M. Herse, P. S. Simon, D. Labs, H. Mandel, D. Gillotay, and T. Foujols (1998). The visible solar spectral irradiance from 350 to 850 nm as measured by the solspec spectrometer during the atlas i mission. *Solar Phys. 177*, 41–61.

Tyler, J. E. (1960). Radiance distribution as a function of depth in an underwater environment. *Bull. Scripps. Inst. Oceanogr. 7*, 363–412.

Tyler, J. E. (1977). *Light in the sea*. Dowden, Hutchinson and Ross, Inc.

Tyler, J. E. and R. C. Smith (1969). *Measurements of Spectral Irradiance Underwater*. Gordon and Breach Science Publischers.

Voss, K. J. (1989). Use of the radiance distribution to measure the optical absorption coefficient in the ocean. *Limn. Oceanogr. 34*, 1614–1622.

Voss, K. J. and A. L. Chapin (2005). Upwelling radiance distribution camera system, nurads. *Opt. Express 13*, 4250–4262.

Voss, K. J. and A. Morel (2005). Bidirectional reflectance function for oecanic waters with varying chlorophyll concentrations: Measurements versus predictions. *Limn. Oceanogr. 50*, 698–705.

Voss, K. J., J. W. Nolten, and G. D. Edwards (1986). Ship shadow effects on apparent optical properties. In *Proc. Ocean Optics VIII, Orlando, FL,*, Volume SPIE, pp. 186–190.

Voss, K. J. and G. Zibordi (1989). Radiometric and geometric calibration of a spectral electro-optic "fisheye" camera radiance distribution system. *Journal of Atm. and Ocean. Tech. 6*, 652–662.

Walker, R. E. (1994). *Marine Light Field Statistics*. John Wiley & Sons, Inc.

Wang, M. (2000). *The SeaWiFS atmospheric correction algorithm updates*, Volume 9, pp. 57–63. Greenbelt, MD: NASA Goddard Space Flight Center, TM-2002-206892.

Weir, C. T., D. A. Siegel, A. F. Michaels, and D. W. Menzies (1994). In situ evaluation of a ships shadow. In *Proc. Ocean Optics XII, Bergen, Norway*, Volume SPIE 2258, pp. 815–821.

Werdell, P. J., S. Bailey, G. Fargion, C. Pietras, K. Knobelspiesse, G. Feldman, and C. R. McClain (2003). Unique data repository facilitates ocean color satellite validation. *Eos Trans. 84*, 377,387.

Westlake, D. F. (1965). Some problems in the measurement of radiation under water: a review. *Photochem. Photobiol. 4*, 849–868.

WMO (1983). Guide to the meteorological instruments and methods of observation. Technical Report WMO-8, World Meterological Organization.

Wyatt, C. L. (1978). *Radiometric Calibration: Theory and Methods*. Academic Press.

Zibordi, G. (2006). Immersion factor of in-water radiance sensors: assessment for a class of radiometers. *J. Atmos. Oceanic Technol. 23*, 302–313.

Zibordi, G. and J.-F. Berthon (2001). In situ relationships between the Q-factor and seawater optical properties in coastal regions. *Limn. Oceanog. 46*, 1130–1140.

Zibordi, G. and B. Bulgarelli (2007). Effects of cosine error in irradiance measurements from field ocean color radiometers. *Appl. Opt. Submitted*.

Zibordi, G. and M. Darecki (2006). Immersion factor for the ramses series of hyperspectral underwater radiometers. *J. Opt. A: Pure Appl. Opt. 8*, 252–258.

Zibordi, G. and G. Ferrari (1995). Instrumental self-shading in underwater optical measurements: experimental data. *Appl. Opt. 34*, 2750–2754.

Zibordi, G. and K. J. Voss (1989). Geometrical and spectral distribution of sky radiance: comparison between simulations and field measurements. *Remote Sens. Environ. 27*, 343–358.

Zibordi, G., G. Maracci, and P. Schlittenhardt (1990). Ocean colour analysis in coastal waters by airborne sensors. *Int. J. Remote Sensing 11*, 705–725.

Zibordi, G., G. P. Doyle, and S. Hooker (1999). Offshore tower shading effects on in-water optical measurements. *J. Atmos. Oceanic Technol. 16*, 1767–1779.

Zibordi, G., S. B. Hooker, J.-F. Berthon, and D. D'Alimonte (2002a). Autonomous above-water radiance measurement from an offshore platform: A field assessment experiment. *J. Atmos. Oceanic Technol. 19*, 808–819.

Zibordi, G., J.-F. Berthon, J. P. Doyle, S. Grossi, D. van der Linde, C. Targa, and L. Alberotanza (2002b). *Coastal Atmosphere and Sea Time Series (CoASTS):*

*A long-term measurement program*, Volume 19, pp. 29. Greenbelt, MD: NASA Goddard Space Flight Center, TM-2002-206892.

Zibordi, G., D. D'Alimonte, D. van der Linde, J. F. Berthon, S. B. Hooker, J. L. Mueller, S. McLean, and G. Lazin (2003a). *The Eight SeaWiFS Intercomparison Round Robin Experiment (SIRREX-8)*, Volume 21, pp. 39. Greenbelt, MD: NASA Goddard Space Flight Center, TM-2003-206892.

Zibordi, G., D. D'Alimonte, D. van der Linde, S. B. Hooker, and J. W. Brown (2003b). *New Laboratory Methods for Characerizing the Immersion Factors of Irradiance Sensors*, Volume 26, pp. 34. Greenbelt, MD: NASA Goddard Space Flight Center, TM-2003-206892.

Zibordi, G., F. Mélin, S. B. Hooker, D. D'Alimonte, and B. Holben (2004a). An autonomous above-water system for the validation of ocean color radiance data. *IEEE Trans. Geosci. Remote Sensing 42*, 401–415.

Zibordi, G., S. Hooker, J. Mueller, and G. Lazin (2004b). Characterization of the immersion immersion factor for a series of in water optical radiometers. *J. Atmos. Oceanic Technol. 21*, 501–514.

Zibordi, G., D. D'Alimonte, and J.-F. Berthon (2004c). An evaluation of depth resolution requirements for optical profiling in coastal waters. *J. Atmos. Oceanic Technol. 21*, 1059–1073.

Zibordi, G., J.-F. Berthon, B. Bulgarelli, D. D'Alimonte, D. van der Linde, F. Mélin, and C. Targa (2004d). Ocean color validation activities at the AAOT in the northern adriatic sea. *Int. J. Remote Sens. 25*, 1533–1537.

Zibordi, G., F. Mélin, and J. F. Berthon (2006a). Comparison of SeaWiFS, MODIS and MERIS radiometric products at a coastal site. *Geophys. Res. Lett. 33*, L06617.

Zibordi, G., F. Mélin, and J.-F. Berthon (2006b). A time-series of above-water radiometric measurements for coastal water monitoring and remote sensing product validation. *IEEE Geosci. Remote Sensing Lett. 3*, 120–124.

Zibordi, G., B. Holben, S. H. Hooker, F. Mélin, J.-F. Berthon, I.Sluster, D. Gilles, D. Vanemark, H. Feng, K. Rutledge, G. Schuster, and A. A. Mandoos (2006c). A network for standardized ocean color validation measurements. *Eos Trans. Amer. Geophys. Union 87*, 293,297.

Zibordi, G., N. Strömbeck, F. Mélin, and J.-F. Berthon (2006d). Tower-based radiometric observations at a coastal site in the baltic proper. *Estuar. Coast. Shelf S. 69*, 649–654.